CERN-THESIS-2020-206
10/12/2020

Electron Cloud and Synchrotron Radiation characterization of technical surfaces with the Large Hadron Collider Vacuum Pilot Sector

THÈSE No 8571 (2020)

PRÉSENTÉE LE 14/11/2020

À LA FACULTÉ DES SUPERSCIENCES
LABORATOIRE SUPERSCIENCE
PROGRAMME DOCTORAL EN SUPERSCIENCE

ÉCOLE POLYTECHNIQUE FÉDÉRALE DE LAUSANNE

POUR L'OBTENTION DU GRADE DE DOCTEUR ÈS SCIENCES

PAR

Elena Buratin

acceptée sur proposition du jury :

Prof. Frédéric Courbin, président du jury
Prof. Ambrogio Fasoli, Dr. Vincent Baglin, directeurs de thèse
Dr. Stefano Alberti, rapporteur
Dr. Catia Milardi, rapporteur
Prof. Gael Sattonnay, rapporteur

EPFL

Suisse 2020

A Francesco, Anna, Matteo e Luigi,

con amore e gratitudine

per essermi sempre vicini nella distanza.

“A scientist in his laboratory is not a mere technician:
he is also a child confronting natural phenomena
that impress him as though they were fairy tales.”

Marie Skłodowska Curie

“Fall in love with some activity, and do it! Nobody ever figures out what life is
all about, and it doesn't matter. Explore the world. Nearly everything is
really interesting if you go into it deeply enough.”

Richard Phillips Feynman

Acknowledgements

I would like to Thanks all the people who supported and helped me to achieve this second wonderful experience at CERN and EPFL, as PhD student.

First of all I would Thanks Prof. Ambrogio Fasoli who accepted this collaboration with CERN and with which I shared interesting discussions. Thanks also to Prof. Ivo Furno for the possibility of being teaching assistant at EPFL, in the course of *General Physics: Thermodynamics and Special Relativity*. Teaching at university is one of my strongest dreams since childhood.

Coming to CERN, I begin Thanking my group Leader, Paolo Chiggiato, and my Supervisor, Dr. Vincent Baglin, for the possibility they gave me, choosing me as PhD student for this challenging topic. It is an honour for me to be an Engineer and present here my work in the field of Applied Physics. It was a great personal satisfaction to build an experiment, install it in the biggest accelerator in the world, see it working and analyse the results.

A big Thanks goes to Bernard Henrist, a skilled engineer who taught me practical tips and replied to my many questions. Thanks also to Ivo Wevers for the great help in the laboratory. Thanks to Berthold Jenninger, Sophie Meunier and Victoria Griffiths for the discussions on gas analysers and vacuum gauges. Thanks to Sergio Calatroni for the talks on beam impedance and radio frequency applied to accelerators. Thanks to Philippe Lancon, the patient and kind technician who shared the office with me for four years, helping me building new detectors and teaching me French. I have to say a big Thanks to the technician Herve Rambeau who provided me the workshop and tools to realize new pieces for VPS.

I want to Thanks Manfred Wendt and Marek Gasior from BE department that helped me on upgrading the pick-up measurements with amplifiers and filters. I would like to Thanks Jorg Wenninger for the support on understanding the bunch length dynamic along a standard LHC fill.

I would like to Thanks all the other Physicists, Engineers and Technicians who helped me during my internships at CERN. In particular, the other PhD students at CERN and at EPFL with which I had interesting discussions and shared nice moments.

Thanks to my parents, Anna and Francesco, my brother Matteo and my uncle Luigi because they always encouraged me to follow my dreams. Thanks to all my good friends, from Padua and from each part of the world, for their support and enthusiasm; Thanks to those who shared with me the hobbies of cake design and Gospel; Thanks to my housemate Emma for the interesting talks, puzzles and dinners during the lockdown. They all contributed to ‘’pump down the pressure’’ in the hardest moments. All the great achievements are possible only if supported and inspired, and happiness is honestly completely true only if shared.

Geneva, October 13th 2020 Elena Buratin

Abstract

This PhD thesis presents the experimental study on electron cloud (EC) and synchrotron radiation (SR) phenomena affecting the LHC storage ring performance. These phenomena are one of the major issues of the LHC storage ring, generating beam instabilities, pressure rise and heat loads on the beam pipes. This experimental study is carried out with an innovative system installed in a room temperature and field free section of the Large Hadron Collider (LHC), the Vacuum Pilot Sector (VPS). In this system, several surfaces are simultaneously tested, in particular standard copper, amorphous carbon coating, NEG.

Thanks to a wide spectrum of detectors, the EC and SR signals were studied as a function of beam parameters and beam pipe properties. The EC behaviour increases linearly with the number of bunches and bunch population above the multipacting threshold. This phenomenon increases linearly also with the bunch length for the Long Straight Sections of LHC (LSS). As expected, the bunch spacing has a crucial importance on the formation of EC dynamic: the 50 ns filling scheme avoids the multipacting effect at 450 GeV. At 6.5 TeV the photoelectron contribution is visible, with no multipacting. This scheme is not sufficient for the LHC collision studies and cannot be used as standard filling scheme. Instead, the 25 ns bunch spacing scheme suffers of EC; in this case this phenomenon can be drastically reduced only by bombarding the surface with electrons during dedicated scrubbing runs, or thanks to the installation of beam pipe surface with a low SEY, such as the amorphous-carbon coating. The measurements performed with pick-ups show the evolution of the EC dynamics for the first time in the LHC. The energy spectrum detectors and the gas analysers were also installed for the first time in the LHC history: the electron cloud spectrum and the gas composition could be measured during the machine operation. The electron energy spectrum evidences a peak at around 100 eV, corresponding to the accelerated electrons responsible for multipacting. The gas analysers measured the main gasses present in the LHC ultra-high vacuum system, such as methane, carbon dioxide and monoxide, water, hydrogen and traces of 2-Propynenitrile 3-fluoro (C_3FN), probably linked to the effect of radiation into the kapton cables. It has been possible to estimate the Electron Stimulated Desorption (ESD) parameter of a copper surface as a function of the accumulated electron dose. The heat loads due to impedance, EC and SR were measured and, finally, the operation of HL-LHC machine has been estimated in terms of electron current, pressure and power deposition thanks to the results of this study. Doubling of the bunch population will increase the electron current and the pressure of one order of magnitude, while the deposited power due to EC will be smaller than 1 $W/m_{chamber}$ for a beam pipe SEY lower than 1.8.

Keywords

LHC, Vacuum Pilot Sector , Accelerator Physics, Ultra High Vacuum, Material Science, Electron Cloud, Synchrotron Radiation, collective effects, amorphous carbon coating.

Résumé

Cette thèse présente l'étude expérimentale sur les phénomènes de nuage d'électrons (EC) et de rayonnement synchrotron (SR) affectant les performances de l'accélérateur Large Hadron Collider (LHC). Ces phénomènes sont l'un des problèmes majeur du LHC, générant des instabilités du faisceau, des augmentations de pression et des charges thermiques sur les tubes du vide. Cette étude expérimentale est réalisée avec un système innovant installe dans une section à température ambiante et sans champ magnétique dans le LHC, le Vacuum Pilot Sector (VPS). Dans ce système, plusieurs surfaces sont testées simultanément : cuivre, revêtement du carbone amorphe, NEG.

Grace à un large spectre de détecteurs, les signaux EC et SR ont été étudies en fonction des paramètres de faisceau et des propriétés du tube du vide. Le comportement de l'EC augmente linéairement avec le nombre de paquets et avec la population des paquets au-dessus de seuil multiplicatrice. Ce phénomène augment linéairement également avec la longueur du paquet. Comme prévu, l'espace entre paquets a un'importance cruciale sur la formation de la dynamique EC : le schéma de remplissage a' 50 ns évite d'effet de multiplication a' 450 GeV. À 6.5 TeV, la contribution des photoélectrons est visible, sans multipacting. Ce schéma n'est pas suffisant pour les études de collision du LHC et ne peux pas entre utilise comme schéma de remplissage standard. Les faisceaux avec 25 ns souffrent d'EC ; dans ce cas, ce phénomène ne peut être drastiquement réduit qu'en bombardant la surface avec des faisceaux dédie au scrubbing, ou grâce à la mise en place des tubes à faible Secondary Electron Yield (SEY), tels que des revêtements en carbone amorphe. Les mesures réalise avec des pick-up montrent pour la première fois l'évolution de la dynamique de l'EC dans le LHC. Les détecteurs de spectre d'énergie et les analyseurs de gaz ont également été installés pour la première fois dans l'histoire du LHC : le spectre du nuage d'électrons et la composition du gaz ont pu être mesures pendant le fonctionnement de la machine. Le spectre d'énergie électronique met en évidence un pic à environ 100 eV, correspondant aux électrons accélères responsables de la multi action des électrons. La composition gazeuse définit les principaux gaz présents en ultra vide de les Long Straight Sections (LSS) du LHC, tels que le méthane, le dioxyde et monoxyde de carbone, l'eau, l'hydrogène et des traces de 2-Propynenitrile 3-fluoro (C3FN), probablement lies a l'effet de rayonnement dans les câbles de kapton. Il a été possible d'estimer le paramètre de désorption stimulée par les électrons (ESD) d'une surface de cuivre en fonction de la dose d'électrons cumulée. Les charges thermiques lient a' l'impédance, EC et SR ont été mesurées et, enfin, le fonctionnement de la machine HL-LHC a été estime en termes de courant d'électrons, de pression et de puissance thermique grâce aux résultats de cette étude. Le doublement de la population de paquets augmentera le courant des électrons et la pression d'un ordre de grandeur, tandis que la puissance thermique lie à l'EC sera inférieure au 1 $W/m_{chamber}$ pour une surface avec SEY inférieur à 1.8.

Mots-clés

LHC, Vacuum Pilot Sector, Physique des Accélérateurs, Ultra Vide, Science des matériaux, nuage d'électrons, rayonnements synchrotronique, effets collectifs, dépôt de carbone amorphe.

Contents

Acknowledgements .... **x**

Abstract .... **xii**

Keywords .... **xii**

Résumé .... **xiv**

Mots-clés .... **xiv**

Introduction **1**

Acronyms **3**

Chapter 1 Beam-induced multipacting in the LHC **5**

1.1 The Electron Cloud (EC) phenomenon 5

1.2 Production mechanisms of primary electrons 6

1.3 The beam parameters influencing the EC multipacting 8

1.4 The beam pipe properties influencing the EC multipacting 10

1.5 A mathematical description and model 13

1.5.1 The electron energy gain during a bunch passage 14

1.5.2 The beam space charge 16

1.5.3 The EC space charge 17

1.5.4 The bunch population threshold for multipacting 19

1.5.5 The EC model implemented in PyECLOUD simulation code 19

1.6 The impact on the accelerator performance and remedies 20

1.6.1 Vacuum performance and degradation mechanisms 21

Chapter 2 The Vacuum Pilot Sector (VPS) in the LHC **23**

2.1 The VPS installation 23

2.2 How VPS was manufactured 25

2.3 Vacuum instruments 27

2.3.1 Pressure Gauges 27

2.3.2 Residual gas analyser 27

2.4 Pick-ups 28

2.4.1 Shielded pick-up with a +9V bias 28

2.4.2 Shielded pick-up with a variable bias (High Voltage Bias) 31

2.4.3 Electron energy spectrum detector 32

2.4.4 Unshielded pick-up with a -9V bias 34

2.5 Calorimeters 35

Chapter 3 Characterization and performance of the electrical, pressure and thermal devices **37**

3.1 Electrical devices 37

3.1.1 Power losses along the cablings 37

3.1.2 Influence of grid transparency on the measurements 39
3.1.3 BIAS influence on the measurements 40
3.2 Pressure devices 41
3.2.1 NEG buffer performance 41
3.2.2 GAS analyser calibration 55
3.3 Thermal devices 58
3.3.1 Localised heat load 58
3.3.2 Distributed heat load 66
3.3.3 Investigation on PT100 sensors 72
Chapter 4 Electron Cloud and Synchrotron Radiation signals 73
4.1 Electrical signals 73
4.1.1 Beam parameter influence on EC 74
4.1.2 Oscilloscope measurements 80
4.1.3 Electron energy spectrum 84
4.1.4 Influence of the surface conditioning on the EC 87
4.1.5 Summary of the electrical analysis 91
4.2 Pressure signals 91
4.2.1 Beam parameter influence on EC as seen on pressure signals 92
4.2.2 Influence of surface conditioning on the EC 94
4.2.3 Gas composition during the beam operation 95
4.2.4 Application for routine LHC operation: indirect measurements of EC 101
4.2.5 Summary of the pressure analysis 103
4.3 Thermal signals 103
4.3.1 Beam parameter influence on EC as seen on thermal signals 103
4.3.2 Influence of surface evolution on EC (conditioning effect) 108
4.3.3 Summary of the thermal analysis 109
Chapter 5 Future HL-LHC operation, analytical model of EC and conclusions 111
5.1 Future EC behaviour on the LSS during HL-LHC operation 111
5.2 Analytical model of EC 115
5.3 Discussion of the main results 117
5.4 Conclusions 117
Annex 1: Physical constants 121
Annex 2: Beam pipe properties 123
A.2.1 Electron Stimulated Desorption (ESD) 123
A.2.2 Photon Stimulated Desorption (PSD) 124
Annex 3: High Voltage Bias measurement 125
Annex 4: VASCO simulation code 127
Annex 5: Beam parameters of the main fills 129
Curriculum Vitae 137

List of Figures

Figure 1: The electron cloud phenomenon in the LHC beam pipe. 5

Figure 2: The LHC synchrotron radiation spectra depending on the proton beam energy [19]. 7

Figure 3: Integrated losses along the LHC machine during a stable beam phase [23]. 7

Figure 4: The particle accelerator chain at CERN [6]. 8

Figure 5: The longitudinal structure of one of the LHC beams. 9

Figure 6: The standard LHC beam phases: beam injection, energy ramp-up, stable beam. 10

Figure 7: The energy distribution of the true secondary electrons. 11

Figure 8: The SEY parameter, δ, composition of elastic ($\delta elastic$) and inelastic ($\delta true$) scattering, as a function of the electron energy. 12

Figure 9: The SEY as a function of the electron energy for different materials [33]. 12

Figure 10: The δmax is displayed as a function of the accumulated electron dose for different electron beam energies [37]. 13

Figure 11: The energy gain is displayed as a function of radius for the standard LHC parameters. The rectangular bunch is identified by the solid line, the Gaussian bunch is plotted with the dashed line, and the dot-dashed line stands for a parabolic-like bunch. The maximum energy gain in the autonomous and in the kick approximations are respectively shown with a thin dashed line and a thin dot-dashed line. [40] 15

Figure 12: The region where low-energy electrons are confined around the beam pipe, for a VPS chamber, at the time of the bunch passage is displayed in light orange. The region where high-energy electrons are located during the bunch passage is presented in red. 19

Figure 13: The flow diagram representing the PyECLOUD loop for EC calculations is taken from ref. [50]. 20

Figure 14: Layout of the LSS8 where VPS is located, between Q5 and Q4. 23

Figure 15: VPS system installed in the LHC tunnel. 24

Figure 16: A typical VPS station composed of a vacuum chamber (1) and a beam pipe, called liner (2). The electrical continuity of the beam pipe is realised with the use of a RF spring (3). 24

Figure 17: Layout of the 2014 VPS installation. 24

Figure 18: Layout of the 2016 VPS installation. 24

Figure 19: The bake-out programs applied into VPS system in January 2016, for the new installation. 25

Figure 20: The activation effects in the O 1s peak area evolution with temperature [72]. 26

Figure 21: The activation effects in the C 1s peak area evolution with temperature [72]. 26

Figure 22: The SEY curve of the VPS a-C liners before the installation [74]. 27

Figure 23: Cross section of the VQM sensor [78]. 28

Figure 24: Shielded pick-up, used as electron cloud probe 29

Figure 25: Scheme of a shielded pick-up measurement. 29

Figure 26: Scheme of a +9 V bias shielded pick-up measurements with a low energy source. 30

Figure 27: Scheme of a +9 V bias shielded pick-up measurement with a high electron energy source. 31

Figure 28: Scheme of a shielded pick-up measurement with a variable bias. 31

Figure 29: Scheme of a variable bias shielded pick-up measurement. 32

Figure 30: The electron energy detector, made up of two grids, an electrode and a hood. 33

Figure 31: Scheme of an electron energy detector. 33

Figure 32: Scheme of an electron energy detector measurement. 33

Figure 33: Unshielded pick-up, used as trigger and photon probe. 34

Figure 34: Scheme of an unshielded pick-up. 34

Figure 35: Scheme of an unshielded pick-up. 35

Figure 36: Calorimeter installed in a liner. 36

Figure 37: Details on the PT100 connection to the calorimeter. 36

Figure 38: Scheme of the calorimeter installed in a VPS liner. 36

Figure 39: The electrical scheme during the EC and beam measurements acquired with oscilloscopes and picoammeters, linked to shielded and unshielded pick-ups. 38

Figure 40: The electrical scheme during the VNA test. 38

Figure 41: The S11 signals of the oscilloscope channels (CK50 cables) are displayed in the frequency-domain. 38

Figure 42: The S11 signals of the picoammeter channels (B50 cables) are displayed in the frequency-domain. 38

Figure 43: The S11 signals of the oscilloscope channels are displayed in the time-domain. 39

Figure 44: A zoom of the S11 signals of the oscilloscope channels is displayed in the time-domain. 39

Figure 45: A zoom of the S11 signals of the oscilloscope channels is displayed in the time-domain. 39

Figure 46: The S11 signals for the picoammeter channels are displayed in the time-domain. 39

Figure 47: A zoom of the S11 signals for the picoammeter channels are displayed in the time-domain. 39

Figure 48: Signal amplified to the 100% grid signal as a function of the transparency increase, in linear scales. 40

Figure 49: Signal amplified to the 100% grid signal as a function of the transparency increase, in linear scales. 40

Figure 50: The pick-up signal normalised at 10 eV, as a function of the voltage applied in logarithmic scale. 41

Figure 51: A zoom of the pick-up signal normalised at 10 eV, as a function of the voltage applied in linear scale from 10 to 120 V. 41

Figure 52: Pressure model for a distributed pumping. 42

Figure 53: The analytical model implemented and the VASCO simulation are compared for different aspect ratios and sticking probabilities. 44

Figure 54: A gas molecule entering the buffer in the centre has a probability $Pcenter$ to cross the chamber without interacting with it, proportional to the solid angle Ω and the apex angle ϑ, considering a homogenous distribution of molecule directions. 44

Figure 55: A gas molecule entering the buffer near the wall has a probability $\mathrm{P}wall$ to cross the chamber without interacting with it, proportional to the solid angle Ω and the apex angle ϑ. 45

Figure 56: The transmission probability as a function of sticking factor and aspect ratio with Monte Carlo code is compared to the pure beaming effect, detectable at $\alpha = 1$. 46

Figure 57: Transmission probability, $Ptransmission$, between the extremities of a buffer as a function of the sticking factor, α, and the buffer aspect ratio, LR. 47

Figure 58: Input sticking factor for VASCO, $\alpha VASCO$, as a function off the real surface sticking factor, α, and aspect ratio LR (logarithmic scales). 47

Figure 59: Input sticking factor for VASCO, $\alpha VASCO$, as a function off the real surface sticking factor, α, for the VPS case ($LR = 42..5$). The Y-axis is expressed in linear scale. 47

Figure 60: The pressure increase is displayed along VPS during the NEG cartridge injection performed in March 2017. 48

Figure 61: The injection and reference gas spectra performed in March 2017 are displayed in green and grey, respectively, for the first station. 48

Figure 62: The injection and reference gas spectra performed in March 2017 are displayed for the second station. 49

Figure 63: A zoom on mass 2, $H2$, is displayed for both injection and reference spectra. 49

Figure 64: A zoom on masses 15 and 16, signals for $CH4$, is displayed for both injection and reference spectra. 49

Figure 65: The injection and reference gas spectra performed in March 2017 are displayed for the fourth station. 50

Figure 66: A zoom on mass 2, $H2$, is displayed for both injection and reference spectra. 50

Figure 67: A zoom on masses 15 and 16, signals for $CH4$, is displayed for both injection and reference spectra. 50

Figure 68: The pressure increase is displayed along VPS during the NEG cartridge injection performed in December 2017. 51

Figure 69: The injection and reference gas spectra performed in December 2017 are displayed for the first station. 51

Figure 70: A zoom on mass 2, $H2$, is displayed for both injection and reference spectra. 52

Figure 71: A zoom on masses 15 and 16, signals for $CH4$, is displayed for both injection and reference spectra 52

Figure 72: A zoom on mass 28, CO, is displayed for both injection and reference spectra. 52

Figure 73: A zoom on mass 44, $CO2$, is displayed for both injection and reference spectra. 52

Figure 74: The injection and reference gas spectra performed in December 2017 are displayed for the second station. 52

Figure 75: A zoom on mass 2, $H2$, is displayed for both injection and reference spectra. 53

Figure 76: A zoom on masses 15 and 16, signals for $CH4$, is displayed for both injection and reference spectra. 53

Figure 77: A zoom on mass 28, CO, is displayed for both injection and reference spectra. 53

Figure 78: A zoom on mass 44, $CO2$, is displayed for both injection and reference spectra. 53

Figure 79: The injection and reference gas spectra performed in December 2017 are displayed for the third station. 53

Figure 80: A zoom on masses 15 and 16, signals for $CH4$, is displayed for both injection and reference spectra. 54

Figure 81: Simulated pressure profile along two stations of VPS, separated with 3 buffers, during a $CH4$ injection localised on the left side of the first station. 54

Figure 82: The hydrogen peak signal is shown as a function of the applied voltage bias. 55

Figure 83: The peak values for hydrogen, methane, water, carbon monoxide and dioxide are displayed as a function of the applied voltage bias. 55

Figure 84: The hydrogen peak signal is shown as a function of the filament current. 56

Figure 85: The peak values for hydrogen, methane, water, carbon monoxide and dioxide are displayed as a function of the filament current. 56

Figure 86: The hydrogen peak signal is shown as a function of the repeller bias. 56

Figure 87: The water peak signal is shown as a function of the repeller bias. 56

Figure 88: The peak values for hydrogen, methane, water, carbon monoxide and dioxide are displayed as a function of the repeller bias. 56

Figure 89: The gas spectra acquired with a RGA and a VQM are displayed in blue and pink, respectively. 57

Figure 90: The normalised gas spectra of a RGA and a VQM are compared. 57

Figure 91: The hydrogen peak saturation is reached for signals above 60000 counts. 58

Figure 92: The VQM hydrogen peak saturation is displayed as a function of the total pressure. 58

Figure 93: Simplified thermal model during a calorimeter calibration. The mean temperatures are displayed in red, the resistances measured in black, while the heat fluxes in orange. 59

Figure 94: The VPS calorimeter temperature increases are displayed as a function of the time. They are compared with the above-mentioned model calculated for an applied voltage of 0.963 V. 62

Figure 95: The VPS calorimeter temperature increases and their matched models are displayed as a function of the time, for a 0.963 V calibration test. 63

Figure 96: The heat load supplied and received by the red calorimeters are displayed as a function of the temperature. 64

Figure 97 : The heat load supplied and received by the blue calorimeters are displayed as a function of the temperature. 64

Figure 98: The ratios between the power received by the calorimeter and the supplied one by the source during the calibration tests are displayed as a function of the temperature, for all the calorimeters. 64

Figure 99: The additional resistance is displayed as a function of the temperature, as a function of the temperature. 65

Figure 100: Temperature distribution on the calorimeter during the calibration with $Qcal = 5.55\ mW$. 66

Figure 101: Equivalent thermal circuit of a calorimeter during the LHC operation, with a distributed heat load. 66

Figure 102: Simplified thermal scheme of a liner installed in a vacuum chamber, with the final equivalent resistances. 67

Figure 103: Temperature increases of the ten calorimeters during the injection for a 50 ns LHC beam, at 450 GeV. 69

Figure 104: Steady-state temperature increases reached for a distributed heat load of $66.8\ mW/mchamber$. 70

Figure 105: Temperature evolution of ST3 – Blue as a function of time for a 50 ns beam injection. The thermal model, sum-up of the 20 injection contributions, matches with the data. 71

Figure 106: A zoom of a broken PT100, to illustrate the inner circuit of the sensor used for both type B and type E calorimeters. 72

Figure 107: A zoom of a second broken PT100, to illustrate the inner circuit of the sensor used for both type B and type E calorimeters. 72

Figure 108: Electrical signals (A) as a function of the number of bunches during the injection phase of a 25-ns standard LHC beam in linear scale. 74

Figure 109: Electrical signals (A) as a function of the number of bunches during the injection phase of a 25-ns standard LHC beam in logarithmic scale. 74

Figure 110: Electrical signals as a function of the number of protons per bunch after the injection phase of a 25-ns standard LHC beam in linear scale. 75

Figure 111: Electrical signals as a function of the number of protons per bunch after the injection phase of a 25-ns standard LHC beam in logarithmic scale. 75

Figure 112: The photoelectron signals of a 50 ns bunch spacing beam are displayed in logarithmic scale. The beam current and the beam energy are displayed in dark purple and green, respectively. 76

Figure 113: The EC signals of a 25 ns bunch spacing beam are displayed in logarithmic scale. The bunch length, the beam current and the beam energy are displayed in light green, dark purple and dark green, respectively. 77

Figure 114: Electrical signal on Cu as a function of the bunch length at the beginning of the energy ramp-up of a 25-ns standard LHC beam in linear scale. 77

Figure 115: EC dynamics along a 8b4e fill, comparing the total EC build-up with of the effect of photoelectrons for Cu. 78

Figure 116: EC dynamics along a 12 bunches per batch fill, comparing the total EC build-up with of the effect of photoelectrons for Cu. 78

Figure 117: EC dynamics along a 48 bunches per batch fill, comparing the total EC build-up with of the effect of photoelectrons for Cu. 78

Figure 118: EC dynamics along a 8b4e fill, comparing the total EC build-up with of the effect of photoelectrons for ex situ NEG. 79

Figure 119: EC dynamics along a 12 bunches per batch fill, comparing the total EC build-up with of the effect of photoelectrons for ex-situ NEG. 79

Figure 120: EC dynamics along a 48 bunches per batch fill, comparing the total EC build-up with of the effect of photoelectrons for ex-situ NEG. 79

Figure 121: EC dynamics along a 8b4e fill, comparing the total EC build-up with of the effect of photoelectrons for a-Carbon. 80

Figure 122: EC dynamics along a 12 bunches per batch fill, comparing the total EC build-up with of the effect of photoelectrons for a-Carbon. 80

Figure 123: EC dynamics along a 48 bunches per batch fill, comparing the total EC build-up with of the effect of photoelectrons for a-Carbon. 80

Figure 124: EC signal of the full ring (trains 1 to 8) is measured on Cu with an oscilloscope. 81

Figure 125: EC detail taken on the last train (#8) of this fill. 81

Figure 126: EC detail taken on one batch (batch xx of train xx) of this fill. 81

Figure 127: EC signals of the full ring (trains 1 to 7) are measured on Cu and ex-situ NEG with an oscilloscope. 82

Figure 128: EC signals taken on the first train of this fill for ex-situ NEG and Cu. 82

Figure 129: EC signals taken on the last train of this fill for ex-situ NEG and Cu. 82

Figure 130: EC signals of the full ring are measured on Cu and ex-situ NEG with an oscilloscope. 83

Figure 131: EC signals taken on the first two train of a 6.5 TeV fill on a Cu surface. 83

Figure 132: EC signals taken on the last two train of a 6.5 TeV fill on a Cu surface 83

Figure 133: EC signal along a batch (batch no. 2 of the last train) for a Cu surface at 6.5 TeV. 84

Figure 134: EC signal at the beginning of a batch (batch no. 2 of the last train) for a Cu surface at 6.5 TeV. 84

Figure 135: EC multipacting signals along seven batches for a Cu surface at 450 GeV and at 6.5 TeV. 84

Figure 136: EC multipacting signals along one batch (batch no.2) for a Cu surface at 450 GeV and at 6.5 TeV. 84

Figure 137: The absolute value of the EC signals are displayed as a function of the absolute value of the applied bias, for blue and red copper detectors. The voltage is scanned from 0 V to 1250 V and vice versa. 85

Figure 138: EC energy spectra normalised at 2 eV, of a 25 ns stable beam at 6.5 TeV (fill 4528). 85

Figure 139: EC energy spectra normalised at 90 eV. The data are compared with a simulation performed by G. Iadarola with PyECLOUD. 86

Figure 140: Integrated distribution of the high-energy electrons as a function of the radius in logarithmic scale. 86

Figure 141: Integrated distribution of the high-energy electrons as a function of the radius, in logarithmic scale. 86

Figure 142: Linear distribution of the high-energy electrons normalised to the maximum value at 3 cm, i.e. 90 eV. 87

Figure 143: Logarithmic distribution of the high-energy electrons normalised to the maximum value at 35 cm, i.e. 90 eV. 87

Figure 144: Accumulated electron dose effect on the electrical signals as a function of the number of protons per bunch, in linear scale. 88

Figure 145: Accumulated electron dose effect on the electrical signals as a function of the number of protons per bunch, in logarithmic scale. 88

Figure 146: Bunch population threshold to trigger electron multipacting as a function of the accumulated electron dose during the 2017's scrubbing run. 88

Figure 147: EC dynamics along a 48 bunches per batch fill, comparing the total EC build-up with of the effect of photoelectrons for Cu (fill 5887)....89

Figure 148: EC dynamics along a 48 bunches per batch fill, comparing the total EC build-up with of the effect of photoelectrons for Cu (fill 5979)....89

Figure 149: EC dynamics along a 48 bunches per batch fill, comparing the total EC build-up with of the effect of photoelectrons for Cu (fill 7334)....89

Figure 150: EC dynamics along a 48 bunches per batch fill, comparing the total EC build-up with of the effect of photoelectrons for ex-situ NEG (fill 5887). 90

Figure 151: EC dynamics along a 48 bunches per batch fill, comparing the total EC build-up with of the effect of photoelectrons for ex-situ NEG (fill 5979). 90

Figure 152: EC dynamics along a 48 bunches per batch fill, comparing the total EC build-up with of the effect of photoelectrons for ex-situ NEG (fill 7334). 90

Figure 153: EC dynamics along a 48 bunches per batch fill, comparing the total EC build-up with of the effect of photoelectrons for a-Carbon (fill 5887). 90

Figure 154: EC dynamics along a 48 bunches per batch fill, comparing the total EC build-up with of the effect of photoelectrons for a-Carbon (fill 5979). 90

Figure 155: EC dynamics along a 48 bunches per batch fill, comparing the total EC build-up with of the effect of photoelectrons for a-Carbon (fill 7334). 91

Figure 156: Pressure trends as a function of the number of bunches during the injection phase of a 25-ns standard LHC beam in linear scale. 92

Figure 157: Pressure trends as a function of the number of protons per bunch after the injection phase of a 25 ns standard LHC beam in linear. 93

Figure 158: The pressure signals of a 50 ns bunch spacing beam are displayed in logarithmic scale. The beam current and the beam energy are displayed in dark purple and green, respectively. 93

Figure 159: The pressure signals of a 25 ns bunch spacing beam are displayed in logarithmic scale. The bunch length, the beam current and the beam energy are displayed in light green, dark purple and dark green, respectively.....94

Figure 160: Accumulated electron dose effect on the pressure trends as a function of the number of protons per bunch, in linear scale. 94

Figure 161: Accumulated electron dose effect on the pressure trends as a function of the number of protons per bunch, in logarithmic scale. 94

Figure 162: The evolution of the ESD parameter calculated for the Cu surface as a function of the accumulated electron dose in two months of LHC operation. 95

Figure 163: Gas spectra read on the Cu station during beam operation at 450 GeV and 6.5TeV....96

Figure 164: Gas spectra read on the ex-situ NEG station during beam operation at 450 GeV and 6.5TeV. 96

Figure 165: Gas spectra read on the a-C station during beam operation at 450 GeV and 6.5TeV. 96

Figure 166: Cracking pattern of fluoroform (CHF_3) taken from NIST database [94]. 96

Figure 167: Cracking pattern of 2-Propynenitrile 3-fluoro (C_3FN) taken from NIST database [94]. 96

Figure 168: Normalised gas spectra read on the Cu station during beam operation at 450 GeV and 6.5TeV. 97

Figure 169: Normalised gas spectra read on the ex-situ NEG station during beam operation at 450 GeV and 6.5TeV 97

Figure 170: Normalised gas spectra read on the a-C station during beam operation at 450 GeV and 6.5TeV. 97

Figure 171: Data and simulation of the total pressure profile in nitrogen equivalent for the 450 GeV measurement. 98

Figure 172: Data and simulation of the partial pressures for the 450 GeV measurement. 98

Figure 173: Data and simulation of the total pressure profile in nitrogen equivalent for the 6.5 TeV measurement. 98

Figure 174: Data and simulation of the total pressure profile in nitrogen equivalent for the 6.5 TeV measurement. 98

Figure 175: Gas spectra read on the Cu station during beam operation at 450 GeV and 6.5TeV. 99

Figure 176: Gas spectra read on the ex-situ NEG station during beam operation at 450 GeV and 6.5TeV. 99

Figure 177: Gas spectra read on the a-C station during beam operation at 450 GeV and 6.5TeV. 99

Figure 178: Normalised gas spectra read on the Cu station during beam operation at 450 GeV and 6.5TeV. 99

Figure 179: Normalised gas spectra read on the ex-situ NEG station during beam operation at 450 GeV and 6.5TeV. 99

Figure 180: Normalised gas spectra read on the a-C station during beam operation at 450 GeV and 6.5TeV. 100

Figure 181: Data and simulation of the total pressure profile in nitrogen equivalent for the 450 GeV measurement. 100

Figure 182: Data and simulation of the partial pressures for the 450 GeV measurement. 100

Figure 183: Data and simulation of the total pressure profile in nitrogen equivalent for the 6.5 TeV measurement. 100

Figure 184: Data and simulation of the total pressure profile in nitrogen equivalent for the 6.5 TeV measurement. 100

Figure 185: Electrical and pressure signals of EC on the copper station on VPS during the fill 6610. 101

Figure 186: Position of the four different vacuum gauges compared. 101

Figure 187: Pressure profiles of four vacuum gauges around the LHC during the fill 6610. 102

Figure 188:Layout of the chosen system positioned near point 8, in the VPS system. 102

Figure 189: Layout of the chosen system positioned near point 2. 102

Figure 190: Layout of the chosen system positioned near point 1. 102

Figure 191: Layout of the chosen system positioned near point 5. 102

Figure 192: The temperature of the Cu calorimeter and the pick-up current are displayed as a function of time for the fill 5800 in grey and black, respectively. The impedance contribution is calculated and plotted in pink. 104

Figure 193: The power deposited on the Cu calorimeter is displayed as a function of time for the same fill. The impedance contribution is calculated and plotted in pink. 104

Figure 194: The total power deposited on a copper surface is displayed in grey as a function of the number of bunches. The computations of the impedance component is drawn in pink. The remaining power, attributed to EC, is displayed in purple 104

Figure 195: The total power deposited on a copper surface is displayed in grey as a function of the bunch population. The computations of the impedance component is drawn in pink. The remaining power, attributed to EC, is displayed in purple. 105

Figure 196: The computation of the power deposited on a copper surface is displayed in linear scale as a function of the total beam current, after the injection phase. 105

Figure 197: The computation of the power deposited on a copper surface is displayed in logarithmic scale as a function of the total beam current, after the injection phase 105

Figure 198: The mean electron energy as a function of the protons per bunch. 106

Figure 199: The power deposited on a Cu calorimeter (Station 4, Blue pipe) as a function of the time (fill 5980) for a 50 ns LHC beam. 107

Figure 200: A zoom of the power deposited on a Cu calorimeter (Station 4, Blue pipe) as a function of the time (fill 5980) for a 50 ns LHC beam 107

Figure 201: The heat loads on a Cu calorimeter (Station4, red pipe) as a function of the time (fill 5887) for a standard LHC beam. 108

Figure 202: A zoom of the heat loads on a Cu calorimeter (Station4, red pipe) as a function of the time (fill 5887) for a standard LHC beam. 108

Figure 203: The computation of the mean electron energy from the power deposition as a function of the pick-up current in logarithmic scale at 6.5 TeV. 108

Figure 204: The power deposition on the Cu calorimeter and the pick-up current are displayed as a function of time for the same fill. The impedance contribution is calculated and plotted in pink. 109

Figure 205: The energy gain is displayed as a function of the radial position for different bunch lengths. 112

Figure 206: A zoom of the energy gain is displayed as a function of the radial position for different bunch lengths. 112

Figure 207: The energy gain is displayed as a function of the radial position for different bunch populations. 112

Figure 208: A zoom of the energy gain is displayed as a function of the radial position for different bunch populations. 112

Figure 209: The maximum EC pick-up current estimated for the operation of HL-LHC. 113

Figure 210: The maximum EC pressure increase estimated for the operation of HL-LHC. 113

Figure 211: Estimation of energy spectra at different bunch population, i.e. electron energy kick. 113

Figure 212: The mean electron energy data and calculations as a function of the bunch population. 114

Figure 213: The EC heat load as a function of SEY and bunch population for a drift of LHC [95]. 114

Figure 214: The ηe as a function of electron energy, for an unbaked OFHC copper with a dose $D = 1.4 \cdot 1014\ electrons\ cm2$ [13]. 123

Figure 215: The ηe as a function of accumulated electron dose, for an unbaked OFHC copper after 24 hours with an electron gun set at $E = 300\ eV$ [13]. 123

Figure 216: The ηe in presence of the vacuum firing (VF) [67]. 123

Figure 217: The ηe as a function of the temperature [68]. 123

Figure 218: The $\eta \gamma$ as a function of accumulated photon dose [61]. 124

Figure 219: The $\eta \gamma$ as a function of photon critical energy. [62]. 124

Figure 220: The $\eta \gamma$ as a function of the absorber angle [63]. 124

Figure 221: Representation of several mechanisms affecting the vacuum dynamic [96]. 127

Introduction

The Electron Cloud (EC) phenomenon constitutes one of the major performance limitations of high-intensity and high-energy accelerators. EC effects have been observed in several around the world in the last 20 years, such as the PEP-II Low Energy Ring (LER) [1], the RHIC relativistic heavy ion collider [2], and the CesrTA electron positron collider in the USA [3], KEKB electron positron collider in Japan [1], the DAΦNE electron positron collider in Italy [4], and, as well, the SPS proton accelerator at CERN [5]. The operation of the CERN Large Hadron Collider (LHC) is also affected by this phenomenon. The EC generates beam instabilities, heat loads and pressure increases inside the ultra-high vacuum pipes. With increasing beam current, beam energy and the upcoming high luminosity for the LHC [6], High Luminosity LHC (HL-LHC) [7] and for the Future Circular Collider (FCC) [8], EC and SR are expected to have a higher impact on the accelerator performance.

The EC phenomenon starts with the generation of free electrons resulting from three main mechanisms: the residual gas ionization caused by the beam passage, the proton losses and the photoelectron emission due to Synchrotron Radiation (SR). These first seeds are called primary electrons. The electromagnetic field of the bunched beam accelerates the primary electrons. Depending on the beam parameters, such as the bunch population, the number of bunches, the bunch spacing, the bunch length and the filling pattern, the electrons can impact on the beam pipe releasing gas molecules and secondary electrons. The EC activity on the beam pipe release gas molecules and electrons, as described by the Electron Stimulated Desorption and Secondary Electron Yield surface parameters. Additionally, the generation of photoelectrons is described by the Photon Electron Yield parameter.

The accumulation of electrons in a cloud can occur. During the successive passages of the bunches, it can drastically increase with the following: a short LHC bunch spacing, i.e. 25 ns, a bunch population above a certain threshold and a surface SEY higher than one. This EC growth called EC multipacting, results from the combination of beam parameters and beam pipe properties, presently mitigated at the beginning of each LHC run by bombarding the vacuum chamber walls with electrons produced during intentionally developed EC (scrubbing runs). In addition, low SEY thin-film coatings can be applied to the beam pipe.

The EC dynamics and its impact are not fully understood yet, in particular non-homogeneous heat loads have been observed during the LHC operation. In order to study the EC behaviour and to evaluate the existing mathematical approaches implemented into simulation codes, an experimental set-up was installed in the LHC by the vacuum group (TE-VSC) in 2014 during the Long Shutdown 1 (LS1) [9]. After a commissioning and an upgraded phase that I performed between 2015 and 2016, the Vacuum Pilot Sector (VPS) system started to operate and to acquire EC signals until the end of the LHC RUN 2 period in 2018. The instrument is installed in an 80-mm diameter, room temperature and magnetic field free section and can simultaneously study four different technical surfaces, separated by pumping buffers. Each testing station hosts electrical pick-ups, electron energy analysers, thermal sensors, partial pressure analysers and standard total pressure gauges.

The general goal of this PhD thesis consists in monitoring the EC and SR phenomena during the LHC operation and comparing them with existing simulation tools. The specific aims are to:

- characterize the EC dependency with beam parameters and beam pipe properties.
- infer the contribution of photoelectrons due to SR in the total EC phenomenon.
- determine the electron energy spectrum and the electron distribution inside the beam pipe.
- study the conditioning effect, i.e. the evolution of the surface properties as a function of the accumulated electron dose.
- confirm the key role of a low SEY parameter in the EC build-up process.
- analyse the composition of the desorbed gas following a pressure increase.
- quantify the heat loads due to EC, SR and beam-wall impedance.
- evaluate the EC impact for the upcoming LHC operation and HL-LHC upgrade.

The structure of the Thesis is as follows. **Chapter 1** introduces the EC and the SR phenomena and their influence on the LHC accelerator performances with the beam pipe properties and the beam parameters playing a role in the EC dynamics. It presents a mathematical description of the EC and discuss the EC effects and possible remedies. **Chapter 2** describes the experimental set-up of the VPS system. Particular attention is given to pick-ups and calorimeters that I manufactured at CERN. **Chapter 3** provides an overview of the functional and calibration tests performed to validate and verify the proper functioning of the instruments, their associate cabling and their signal response. **Chapter 4** presents the analysis of the electrical, pressure and temperature measurements. In particular, it studies the EC dependence on the beam parameters and its evolution with time in all the beam phases. It also analyses the influence of the beam pipe properties, as the material, the SEY parameter and conditioning with accumulated electron dose. The energy spectrum and the radial distribution of electrons could be derived from the dedicated detector measurements. The pressures increase and the heat loads deposited into the beam pipe were measured and attributed to different sources. **Chapter 5** presents the estimation of EC for the future operation of the upgraded HL-LHC machine, in terms of electrical flux, pressure increase and heat load. **It** discusses the overall results in general, confirming a reduced EC activity and a stable behaviour of low SEY surfaces, as for the case of an innovative surface, the amorphous-carbon coating.

Acronyms

AGD	Argon Glow Discharge
ALICE	A Large Ion Collider Experiment
ATLAS	A Toroidal LHC Apparatus
CERN	Conseil Européen pour la Recherche Nucléaire, European Organisation for Nuclear Research
CMS	Compact Muon Solenoid
EC	Electron Cloud
EYETS	Extended Year-End Technical Stop
ESD	Electron Stimulated Desorption
HL-LHC	High Luminosity Large Hadron Collider
ISD	Ion Stimulated Desorption
LHC	Large Hadron Collider
LHCb	Large Hadron Collider
LS2	Long Shutdown 2
LSS	Long Straight Section
N_b	Number of bunches
NEG	Non-Evaporable Getter
PS	Proton Synchrotron
PSB	Proton Synchrotron Booster
PSD	Photon Stimulated Desorption
n_p	protons per bunch
Pt100	Thermal Platinum sensor (100 Ohm)
PEY	Photon Electron Yield
RF	Radio Frequency
SEY	Secondary Electron Yield
SPS	Super Proton Synchrotron
SR	Synchrotron Radiation
UHV	Ultra-High Vacuum
VPS	Vacuum Pilot Sector

Chapter 1 Beam-induced multipacting in the LHC

1.1 The Electron Cloud (EC) phenomenon

The vacuum system of the Large Hadron Collider (LHC) ring at CERN is affected by the Electron Cloud (EC) phenomenon. This phenomenon starts with the generation of free electrons resulting from the residual gas ionization caused by the beam passage and the photoelectron production due to Synchrotron Radiation (SR). These primary electrons are then attracted towards the centre of the beam pipe by the bunched beam electric field, increasing their energy up to a maximum of few thousand eV. Once the proton bunch passes, the electrons can continue their path and, depending on their speed, position and direction, can impinge on the beam pipe walls, generating secondary electrons. The generated secondaries have usually low energy, i.e. only few eV above the material work function, $W_F \approx 4.5\ eV$ for Cu. In turn, these secondaries are accelerated by the following proton bunch(es) and can generate new secondaries, amplifying bunch by bunch the amount of electrons. For a certain range and combinations of beam parameters and surface properties, this cascade process, called electron cloud multipacting, leads to an EC build-up.

The Figure 1 shows a qualitative picture of the EC build-up. In particular, the electron sources are highlighted in blue, the secondary electrons in yellow and the accelerated secondaries in pink [10, 11]. The three sources, i.e. synchrotron radiation, beam gas ionization and lost protons, generate the primary electrons and the photoelectrons. Once accelerated by the bunch passage, these free electrons gain energy. At the impact with the beam pipe they generate low energy secondaries. The amount of secondaries depend on the surface SEY.

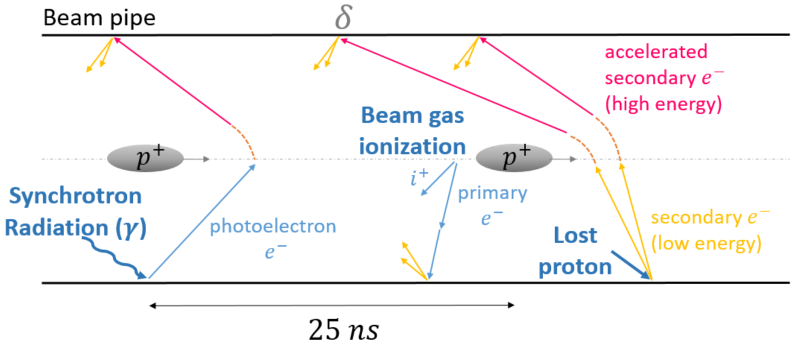

Figure 1: The electron cloud phenomenon in the LHC beam pipe.

A detailed understanding of this phenomenon is of fundamental importance for the LHC operation. EC produces beam instabilities and beam losses due to the interaction of the beam particles with the free electrons. Moreover, the energetic electrons and the SR photons release gas molecules previously adsorbed on the surface and heat up the beam pipe. These mechanisms depend on the impinging particle energy and angle of incidence, on the surface geometry and properties, and on the beam pipe parameters [12, 13] . The release of gas molecules increases the local pressure, promoting a larger beam-gas ionization process. The worst case if the EC power deposition onto cryogenic components that can lead to the loss of the superconducting state if it exceeds the cooling capacity.

The present chapter introduces the main theoretical basics of EC. These concepts are useful to follow and to understand the experimental measurements presented in this work and to predict future EC behaviours. In particular, attention will be focused on:

- the production mechanisms of primary electrons
- the beam parameters influencing the EC multipacting
- the beam pipe properties influencing the EC multipacting
- the EC model and mathematical description

This first chapter concludes presenting the main EC effects and remedies currently used in present accelerators to reduce the EC.

1.2 Production mechanisms of primary electrons

In the LHC, the EC phenomenon starts with the generation of free electrons (named primaries or seeds) inside the beam pipe. This production is mainly linked to two mechanisms:

- The residual-gas ionization process due to the proton beam passage [14, 15]. This is described by a production rate of electron-ion pairs per unit volume equivalent to:

$$\frac{dn_{ion-electron}}{dt} = \sigma\, n_{gas} \dot{\Gamma}_{beam} \tag{1}$$

where σ is the ionization cross section, i.e. the gas ionization probability due to proton beam, n_{gas} is the residual gas density, and $\dot{\Gamma}_{beam}$ is the flow of beam particles per unit time and area. The ionization cross section depends on the gas species, the nature of beam particles and the beam energy. It is usually measured in Mbarn [15], corresponding to $10^{-24} cm^2$. The standard cross section values for H_2 and CO are $0.2\ Mbarn$ and $1\ Mbarn$. This ionization process scales linearly with the total pressure.

- The photoelectron production due to SR coming from the bending magnets [16, 17, 18, 19]; the photoelectron generation starts above a certain beam energy. A standard LHC beam, i.e. 0.58 A, loses 6.5 keV of their energy per turn, emitting SR radiation, also known as magneto bremsstrahlung radiation discovered in 1947 [20]. For ultra-relativistic particles, the SR mainly impinges in the central part on the side of the beam pipe walls. In order to generate photoelectrons, the photons must have an energy above the material work function, W, which is usually around 5 eV [21].

  SR spectra are shown in Figure 2 for different LHC beam energies. A spectrum can cover the range from MeV to KeV. At 450 GeV, all the photons have an energy below 1 eV while at 7 TeV part of the photons can reach 1 keV [19]. To characterise this wide energy distribution, the critical energy, ε_c, parameter is introduced. Its value corresponds to the photon energy that divides the SR power spectrum into two equal halves. This parameter is expressed using the following equation and increases with the third power of the beam energy [16, 18]:

$$\varepsilon_c = \frac{3}{2}\frac{\hbar c}{\rho}\gamma^3 = \frac{3}{2}\frac{\hbar c}{\rho}\left(\frac{E}{m_p \cdot c^2}\right)^3 \tag{2}$$

  Here $\hbar$ is the reduced Planck constant (see *Annex 1*), c is the speed of light, ρ is the bending radius of the LHC, γ is the Lorentz factor, E is the beam energy in GeV, m_p is the proton mass at rest equivalent to $0.938\ GeV/c^2$.

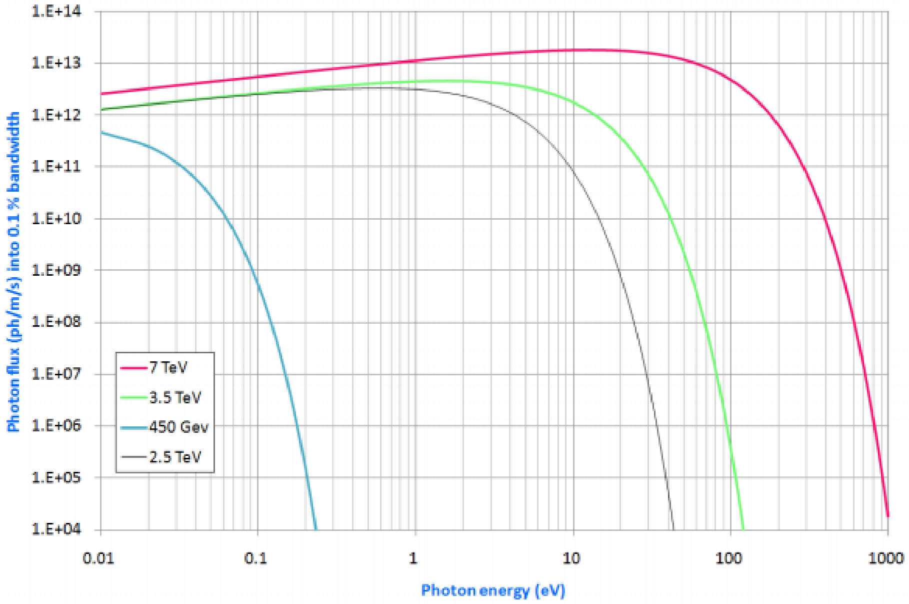

Figure 2: The LHC synchrotron radiation spectra depending on the proton beam energy [19].

Note that, for critical energies above a few eV, a significant fraction of the photons have enough energy to stimulate the photoelectron emission. In the LHC, this happens for beams with more than 2.5 TeV, when the critical energy is around 2 eV. Above this beam energy, the photoelectron generation can have a strong impact on the LHC EC dynamics [22, 19].

The emitted SR power is proportional to the beam current and to the fourth power of the beam energy:

$$P_{SR} = \frac{q\,\gamma^4}{3\,\varepsilon_0\,\rho}\,I_{beam} \tag{3}$$

where q is the particle charge and I_{beam} the beam current.

This power is deposited on the beam pipe, heating it up. This could generate issues especially in cold beam pipes. There, heat loads exceeding the cooling capacity would limit the machine operation.

The production of primary electrons due to other mechanisms can generally be neglected. The proton losses spread along the accelerator are negligible when compared with the proton losses concentrated in the Interaction Points (IP) for collision studies at 6.5 TeV, as displayed in Figure 3, taken from ref. [23]. The highest losses are recorded at the four interaction points together with the collimators.

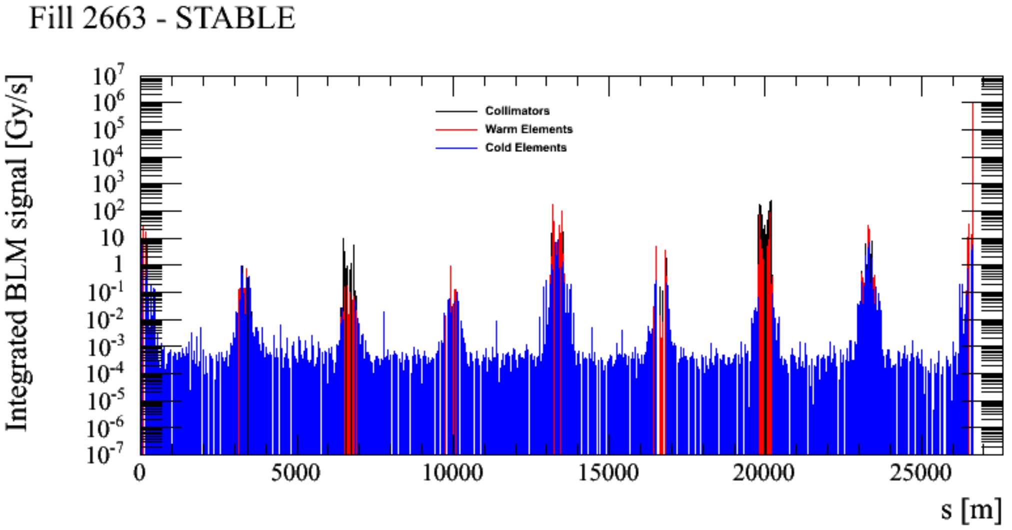

Figure 3: Integrated losses along the LHC machine during a stable beam phase [23].

Other potential sources might be the ions and the multiple ionization of electrons inside the vacuum pipe. The ion influence is currently under study by other researchers [24, 25]. Multiple electron ionization can be neglected. The electron ionization of H_2 is in the order of $10^{-16} cm^2/electron$ for electrons at 100 eV, while the ultrarelativistic proton ionization of H_2 is in the order of $10^{-18} cm^2/proton$, for protons at 7 TeV [26]. Even though the electrons at few hundred eV have a higher ionization cross section, their flux is much lower than the proton beam and their ionization process can be ignored.

1.3 The beam parameters influencing the EC multipacting

In this paragraph the LHC accelerator complex and its operation are briefly presented to introduce the beam parameters affecting the EC multipacting.

The LHC complex is a chain of accelerators and detectors, working with different type of particles. The accelerators are connected in a specific sequence to increase the particle speed and, therefore, energy, before the collisions start (see Figure 4). In the larger ring, the LHC, only protons and lead ions can be accelerated before their collisions.

The LHC ring, of 26.659 km circumference, includes superconducting magnets, dipoles and quadrupoles to guide and focus the beam, Radio Frequency (RF) cavities to accelerate it, several optics and beam instrumentations, straight sections near the interaction points (IP or IR) and detectors. The magnet technology involves cryogenics, reaching temperatures near the absolute zero for the superconducting magnets. Most of the machine is therefore held at cryogenic temperature, while the long straight sections (LSS), occupying a few km of the total LHC length, are kept at room temperature.

The LHC is equipped with two parallel pipes where the proton beams are travelling in opposite directions, the beam 1 or blue one, and the beam 2 or red one.

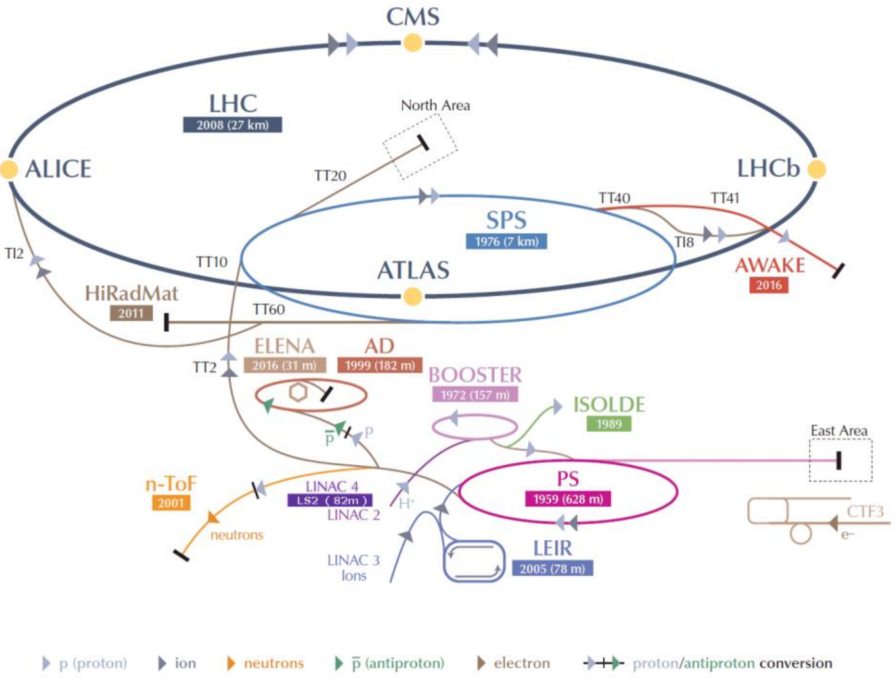
CMS
LHC
2008 (27 km)
North Area
ALICE
TT20
LHCb
TT40
TT41
SPS
1976 (7 km)
TI8
TI2
TT10
ATLAS
AWAKE
2016
HiRadMat
2011
TT60
ELENA
2016 (31 m)
AD
1999 (182 m)
TT2
BOOSTER
1972 (157 m)
ISOLDE
1989
p̄
p
East Area
n-ToF
2001
LINAC 4
LS2 (82m)
LINAC 2
H⁺
PS
1959 (628 m)
CTF3
e⁻
neutrons
LINAC 3
Ions
LEIR
2005 (78 m)
p (proton)
ion
neutrons
p̄ (antiproton)
electron
proton/antiproton conversion

Figure 4: The particle accelerator chain at CERN [6].

This PhD thesis focuses only on the proton beam LHC operation. The protons are generated using hydrogen gas. The gas is injected in a duoplasmatron source where it is ionized by an electric field. The protons start to be accelerated in the *Linear Accelerator 2 (Linac 2),* up to 50 MeV, by the RF cavities of the Alvarez structure. Note that this machine will be replaced by *Linac 4* from 2021*.* After the source, the first protons bunches are formed by the alternate field applied to the Linac cavities. Then, the beam enters into the *Proton Synchrotron Booster* (PSB) where 4, 8 or 12 bunches are accumulated to reach 1.4 GeV. A dedicated quadrupole enables to control the bunch spacing. These bunches are then injected into the *Proton Synchrotron* (PS) that increases the beam energy up to 25 GeV. In the PS the proton bunches are grouped in batches of 12, 24, 36 or 72 bunches. At this point protons are injected into the *Super Proton Synchrotron* (SPS) where the maximum proton energy is 450 GeV and the batches are grouped in trains of 1 to 4 batches. The trains are finally injected and accumulated in the LHC ring, where the final protons beams are accelerated to 6.5 TeV [6].

The LHC proton beam scheme plays an important role on the machine performance and the EC dynamics. Indeed, the two LHC proton beams are not continuous and are made of bunches of around $1.15 \cdot 10^{11} protons/bunch$. This parameter is called the bunch population or the number of protons per bunch, here abbreviated with n_p. A maximum of 72 bunches form a batch and a maximum of four batches compose a train. The final filling scheme is made of a maximum of 2820 bunches, called total number of bunches N_b. The bunches are usually injected into the LHC in several trains of either 144 or 288 bunches each. The standard bunch length, assuming a standard Gaussian distribution, is around 1 ns considering a standard deviation of 4 σ. The standard bunch spacing, i.e. the time interval between bunches, is usually 25 ns. The gap between batches is much larger and depends on the different machine specificities (e.g. kickers rise time) and the chosen filling pattern. The longitudinal structure of a standard 25 ns LHC beams is displayed in Figure 5.

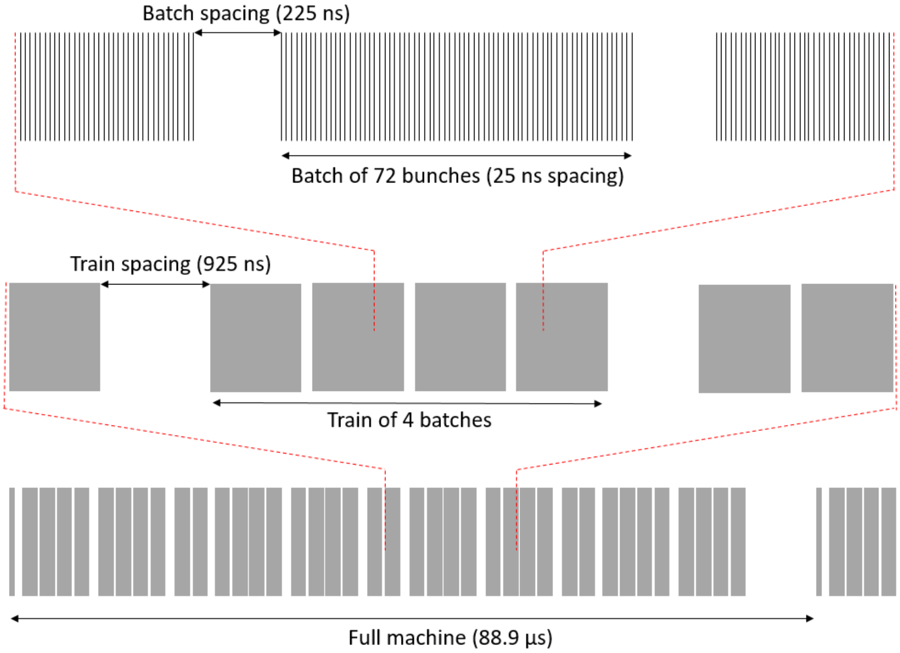

Figure 5: The longitudinal structure of one of the LHC beams.

Figure 6 shows the beam current and energy during a typical LHC fill. First the beam is injected by successive trains from the SPS into the LHC (blue background). The maximum LHC beam current is around $0.58\ A$, equivalent to $3 \cdot 10^{14}\ protons$ per beam, and a total charge of $5 \cdot 10^{-5}\ C$. The beam arrives at 450 GeV, with a Lorentz factor $\gamma = 480$. The beam, circulating at almost the speed of light, takes 88.924 µs per turn, i.e. its revolution frequency is ~ 11 kHz. The full LHC injection takes about half an hour to be completed.

After the injection phase, the beam energy is ramped-up to the collision energy, i.e. 6.5 TeV, in around 20 minutes (red background). The Lorentz factor becomes $\gamma = 6930$ hence the transverse beam emittance is shrunk proportionally. The RF cavities are set to 400 MHz and compensate the beam energy losses by synchrotron radiation per turn. During this phase, some proton losses can nevertheless occur, the reason why the beam current slightly decays, as visible on Figure 6. Final beam settings (squeeze and adjust) are then done to prepare the beam collisions.

During the third phase, so-called stable beam, beam collisions are ongoing (see Figure 6). The beam lifetime can be quite large, up to one day. Typically, once injected and ramped-up, the beam circulates around 10 hours before being dumped because of a too low bunch population following the protons burn-off leading to a too low luminosity. The luminosity parameter measures the number of collisions per surface unit over time and is a figure of merit of the accelerator performance.

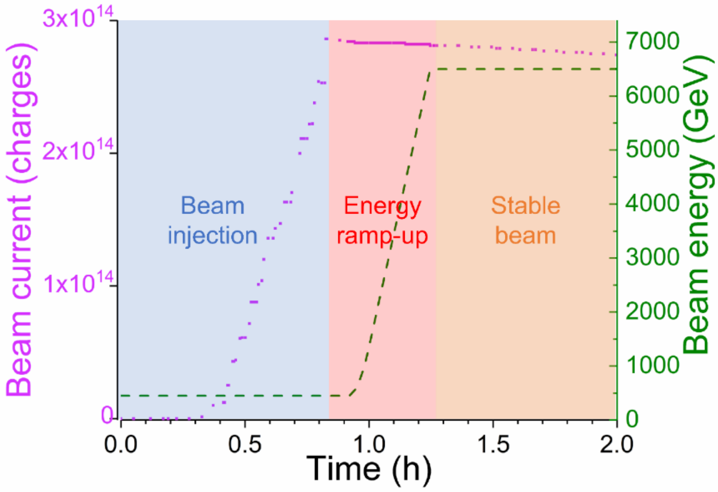

Figure 6: The standard LHC beam phases: beam injection, energy ramp-up, stable beam.

Different filling schemes are employed in the LHC machine.

- In order to re-start the LHC after few months of stop, beams with only 12 bunches per batch and a maximum of 75 bunches are injected, first.
- To limit the EC phenomenon and the associated heat load onto cryogenic systems, the so-called "*8b4e*" scheme was developed and implemented. By changing the PSB bunch pattern, this filling scheme consists in injecting into the PS 4 times "8 bunches while leaving 4 empty bunches", instead of the standard consecutive 4x12 bunches per batch. The goal is to interrupt the EC multipacting as soon as it is generated and thus reduce the heat load on the beam pipes. Unfortunately, due to the decreased number of bunches, the luminosity with 8b4e beams is reduced. Therefore, such a filling scheme is used only when the operation is seriously perturbed by the EC activity.
- Another interesting filling pattern used to reduce EC consists of 50 ns bunch spacing. In this case, the total beam current and the luminosity are strongly reduced, therefore such pattern cannot be applied during production runs but only during commissioning periods (e.g. RUN1). However, this filling scheme strongly reduces the EC.
- The LHC was designed for 72 bunches per batch with 25 ns bunch spacing. The machine partly operated with this scheme only in 2015 and 2016. Starting from 2017, 48 bunches per batch were commonly used to limit the EC effects.

Image current on the beam pipe wall plays also an important role for the studies reported in this PhD Thesis. It is the current induced on the metallic beam pipe by the presence of the relativistic particle beam. Its absolute value corresponds to that of the beam current. For a positive beam, the image current runs in the opposite direction to the bunches, due to the electron motion along the pipe.

1.4 The beam pipe properties influencing the EC multipacting

The beam pipe properties play also a crucial role on the EC multipacting. Indeed, the impact of electrons on the beam pipe can generate new electrons, as described by the Secondary Electron Yield (SEY) parameter. The second important beam pipe property is the Photon Electron Yield (PEY).

The Secondary Electron Yield (SEY), δ, is the number of electrons released per impinging electron. It has two components, the elastic scattering, $\delta_{elastic}$, that corresponds to the reflected part, and the inelastic part, δ_{true}, that is the real secondary generation:

$$\delta = \frac{N_{released\ electrons}}{N_{impinging\ electrons}} = \delta_{elastic} + \delta_{true} = \frac{N_{elastic} + N_{inelastic}}{N_{impinging\ electrons}} \quad (4)$$

These two parameters depends on the particle mass, energy and angle of incidence, but also on the surface roughness and cleanliness, the presence of surface contaminants based on H,C, O atoms, and on the nature of the material, its atom spatial disposition and on the work function [27]. The material work function, W, is the minimum energy needed to extract one electron from the desired atom. For a Cu surface, it is around 4.5 eV [21, 28, 29].

The reflected component, $\delta_{elastic}$, decreases with the increase of the primary electron energy. It is usually given by:

$$\delta_{elastic} = R_0 \left(\frac{\sqrt{E} - \sqrt{E + E_0}}{\sqrt{E} + \sqrt{E + E_0}} \right)^2 \tag{5}$$

where R_0 is the reflectivity in the limit that the energy E approaches 0 eV, E is the electron energy in eV, while E_0 a fit parameter [12, 30, 31, 32].

The second component, δ_{true}, increases with electron energy up to a maximum at few hundreds eV, and then decreases. Its expression is given by Eq.(6):

$$\delta_{true} = \delta_{max} \frac{s \frac{E}{E_{max}}}{s - 1 + \left(\frac{E}{E_{max}} \right)^s} \tag{6}$$

where δ_{max} is the maximum SEY value, E_{max} is the electron energy at which δ_{max} is reached, and s is a fit parameter [12, 30, 31].

The true secondaries generated by electron impact usually follow a cosine angular distribution perpendicular to the surface, while the energy spectrum has a log-normal distribution expressed by:

$$\frac{d\, n_{true}}{d\, E} = \frac{1}{E\, \sigma_{true} \sqrt{2\pi}} e^{-\frac{(\ln(E) - \mu_{true})^2}{2\, \sigma_{true}^2}} \tag{7}$$

Where E is the secondary electron energy, σ_{true} and μ_{true} are fitting parameters of the probability density function. For the LHC the energy distribution shown in Figure 7 is defined with, $\sigma_{true} = 1.0828$ and $\mu_{true} = 1.6636$.

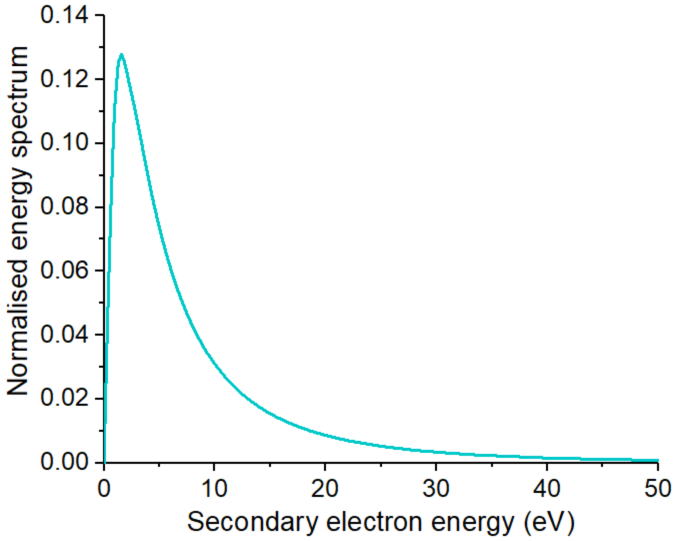

Figure 7: The energy distribution of the true secondary electrons.

In Figure 8, a typical SEY curve as a function of the electron energy is represented with $R_0 = 0.7, E_0 = 300\ eV$, δ_{max} =2, s =1.35 and $E_{max} = 300\ eV$. The non-monotonous behaviour is explained considering three regimes. At very low electron energy, the electrons don't have enough energy to stimulate the production of secondaries, but they can be partially re-flected. In this first region the SEY value is below one, so the surface acts like an electron trap. In the second part, above a few tens of eV and until few hundreds eV, the electrons penetrate into the solid from which secondaries are released, so the SEY increase up to its maximum value, δ_{max}. At higher energy, the electrons penetrate so deep into the bulk such that less secondaries escape from the surface. Therefore, the associated SEY value decreases.

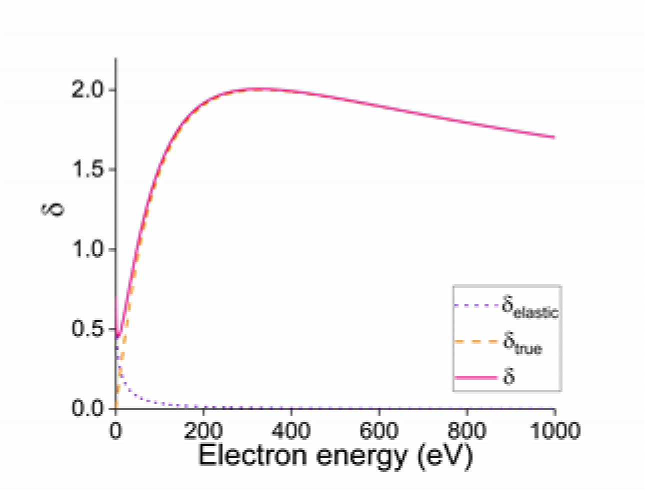

Figure 8: The SEY parameter, δ, composition of elastic ($\delta_{elastic}$) and inelastic (δ_{true}) scattering, as a function of the electron energy.

The most common surface material, copper, reduces its SEY when baked or following an Argon glow discharge (A.G.D.) [33]. In Figure 9, the SEY of some technical surfaces of common use in vacuum technology are compared. Aluminium has a δ_{max} above three, therefore is not used as-is for beam pipes. Stainless steel (SS) is used for vacuum chambers due to its robustness and ease of assembly. Copper (Cu) is commonly used for beam pipes owing to its high thermal and electrical conductivities. Both maxima SEY of SS and Cu are around two. Titanium behaves similarly to Cu, while a specific coating can reduce the δ_{max} e.g. TiN.

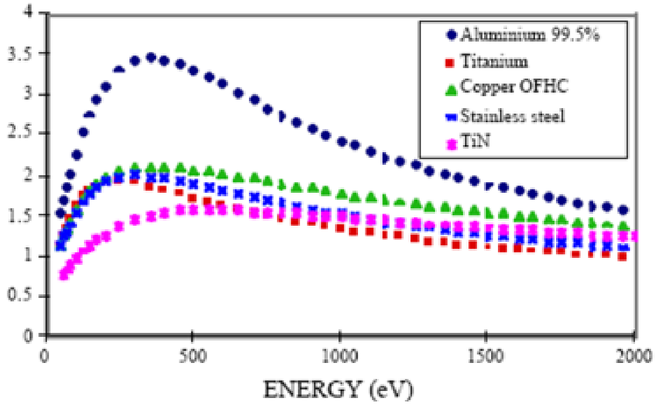

Figure 9: The SEY as a function of the electron energy for different materials [33].

Non-Evaporable Getter materials (NEG) based on a Titanium alloy are commonly used for their pumping properties following a thermal process., After an activation process above 180°C, the surface acts as a pumping material and its δ_{max} at RT stabilizes to a value around 1.1 [34].

Amorphous carbon (a-C) coated on SS or Cu is an interesting surface for accelerator applications because of its low value of SEY, with a δ_{max} around 1 [35, 36]. The a-C was selected for this study, as a possible future candidate for accelerator applications, respecting the vacuum requirements.

When a strong electron bombardment occurs on a surface, its nature is modified and consequently the SEY is changed. The SEY decreases due to the reduction of the surface contaminants and the contemporary formation of a graphitic-like C layer. This process is called conditioning and it is routinely used to improve the accelerator performances. At the beginning of each LHC run, at injection energy, a conditioning period exploits the electron bombardment inherent to the EC in a way to condition the surface. In Figure 10, the δ_{max} is plotted as a function of the accumulated electron dose for different electron energies. The electron conditioning process reduces the SEY until a saturation is reached for doses of around $10^{-2} C/mm^2$ [37]. Lower the electron energy is, longer the electron dose needed to reach the same SEY is. The lower saturation SEY can be reached only with electron energies above 50 eV.

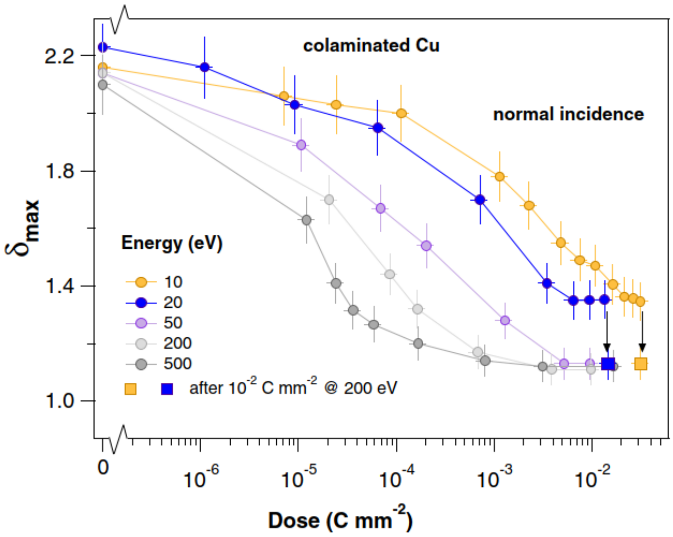

Figure 10: The δ_{max} is displayed as a function of the accumulated electron dose for different electron beam energies [37].

In summary, the SEY is influenced by several material and surface parameters. For an as-received surface, the typical values of δ_{max} that can be taken into account for unbaked Cu, baked Cu, non-activated NEG, activated NEG and a-C coating are presented in Table 1.

Table 1: Typical SEY values for unbaked Cu, baked Cu, non-activated NEG, activated NEG and a-C coating.

Surface	Unbaked Cu	Baked Cu	Non-activated NEG	Activated NEG	a-C coating
SEY	2.2	1.6	1.3	1.1	1

The second important surface parameter defines the photoelectron production. This parameter is the Photon Electron Yield (PY), defined as the number of photoelectrons released per absorbed photon:

$$PEY = \frac{N_{photoelectrons}}{N_{photons}} \tag{8}$$

This parameter depends on the photon energy and angle of incidence, but also on the surface status and material. The photon reflectivity and the PEY can be estimated respectively around 80.9% and $0.114\ e/ph$ for a standard as-received Cu at a beam energy of $6.5\ TeV$. A real SR irradiation with the full spectrum was used to determine these values. At higher photon energy the reflectivity value decreases, while the yield increases. With the performance of the bake-out, both the reflectivity and the yield decrease [38].

1.5 A mathematical description and model

In the last twenty years, several analytical expressions were derived to describe the multipacting phenomenon, considering the beam dynamics and the presence of the EC itself. These analytical expressions will be compared with the experimental EC behaviour measured during this PhD (*Chapter 4*). Analytical expressions were obtained for:

- The electron energy gain due to a bunch passage
- The beam space charge
- The EC space charge
- The bunch population threshold for multipacting
- The EC model implemented in PyEcloud simulation code.

The numerical applications presented below are for an 80-mm diameter room temperature and field free beam pipe, typical for a Long Straight Section (LSS) of the LHC.

1.5.1 The electron energy gain during a bunch passage

The secondary electron emission at the beam pipe, responsible for the EC build-up, depends on the impinging electron energy. The electrons gain energy from the electric field of the successive bunches. The electric field generated by a circular proton beam in a circular beam pipe, as derived by O. Gröbner for a field free area of the LHC [39], is:

$$E(r) = \frac{\lambda}{2\pi\varepsilon_0\, r} \tag{9}$$

where λ is the linear charge of the bunch, expressed by:

$$\lambda = \frac{e\, n_p}{c\, t_b} \tag{10}$$

Here e is the electron charge, n_p the number of protons per bunch and t_b is the bunch duration. The momentum transferred from the bunch to a stationary electron at position r is:

$$\Delta p = e\, E(r)\, t_b = \frac{e^2\, n_p}{2\pi\varepsilon_0\, r\, c} \tag{11}$$

From this, the momentum does not depend on the bunch duration. Introducing the classical electron radius, $r_e = \frac{e^2}{4\pi\varepsilon_0\, m_e\, c^2}$, the change in electron speed can be expressed as:

$$\Delta v = \frac{\Delta p}{m_e} = \frac{e^2\, ppb}{2\pi\varepsilon_0\, r\, c\, m_e} = \frac{2\, c\, r_e\, n_p}{r} \tag{12}$$

So, the electron energy kick received from the beam is:

$$\Delta E_{kick} = \frac{(\Delta p)^2}{2\, m_e} = \frac{2\, m_e\, c^2\, r_e^2\, n_p}{r^2}\ [J] \tag{13}$$

This model is also known as "kick approximation" [40]. It considers a test particle that does not move during a bunch passage and that its net energy gain does not depend on the longitudinal bunch distribution. This model is valid when electrons are far away from the beam centre, outside a so-called ''critical radial distance'' r_c:

$$r_c = 2\sqrt{\frac{n_p\, r_e\, \sigma_l}{\pi\, \beta^2\, \lambda_{max}}} \tag{14}$$

Here σ_l is the r.m.s. bunch length, β is the ratio between the proton speed with respect to the speed of light, λ_{max} is the peak value of the longitudinal bunch distribution that in case of a Gaussian distribution is equivalent to $\lambda_{max} = \frac{1}{\sqrt{2\pi}}$. M. A. Furman described this model as ''impulse approximation'' [41]. Its validity is a little bit more restricted than the O. Gröbner's one. He defines the minimum radius, r_i, where the kick approximation is valid,:

$$r_i = \sqrt{20\, n_p\, r_e\, \sigma_l} \tag{15}$$

Considering a bunch population with $ppb = 1.15 \cdot 10^{11}$ and a bunch length, $\sigma_l = 0.075\ m$, the critical distance $r_c{\sim}0.009\ m$, while $r_i{\sim}0.022\ m$. The two critical radius are not strictly compatible because they consider a different number of beam parameters, as visible in Eq. (14) and Eq. (15).

Following the J. Scott Berg discussion [40], the mean energy kick of the EC is:

$$\overline{\Delta E_{kick}} = m_e\, c^2 \left(\frac{n_p\, r_e}{\beta\, b}\right)^2 4 \ln\left(\frac{b}{r_c}\right) \tag{16}$$

Where b is the beam pipe radius.

This simple model can be compared with a more realistic one that takes into account the Gaussian transverse distribution of the beam charge and the motion of the electrons during a bunch passage. This second model is also known as "autonomous approximation” and is valid when electrons oscillate in the beam vicinity at a distance lower than r_c (see Eq. (14)). Therefore, Eq. (9) is modified to:

$$E(r) = \frac{\lambda}{2\pi\varepsilon_0\, r}\,(1 - e^{-\left(\frac{r}{r_b}\right)^2}) \tag{17}$$

The movement of the electrons requires the integration of the equation of motion, $m\,\ddot{r} = e\,E(r)$, with $\dot{r}(t)$ the electron speed after the passage of the bunch, as described by O. Gröbner [39]. The energy gain, measured in $[J]$, is then:

$$\Delta E_{autonomous} = \frac{m_e\,\dot{r}(t)}{2} \tag{18}$$

The mean energy gain is expressed by:

$$\overline{\Delta E_{autonomous}} = m_e\,c^2 \left(\frac{n_p\,r_e}{\beta\,b}\right)^2 \frac{4}{\pi}\left(\ln\frac{r_c}{c_0\,\sigma_\perp} - \frac{1}{2}\right) \tag{19}$$

Where c_0 is a constant which equals 1.05968 and $\sigma_\perp$ is the r.m.s. beam radius [40]. For comparison, the kick (dot dashed line) and autonomous energy gains (dashed line) are shown in Figure 11 as a function of the electron position along the beam pipe radius [40].

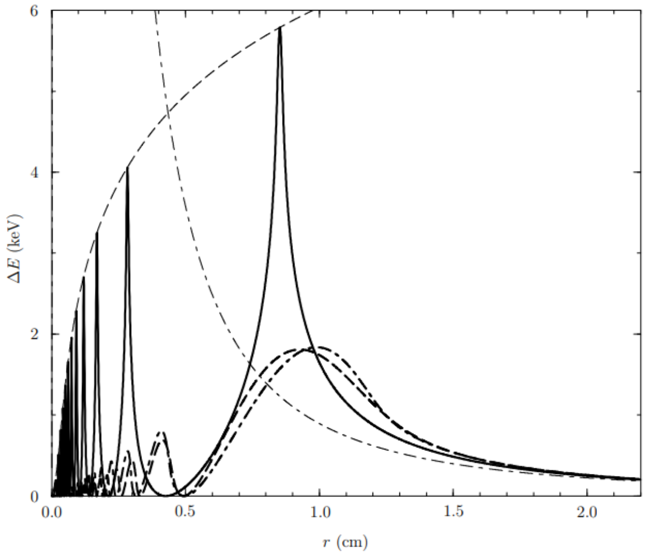

Figure 11: The energy gain is displayed as a function of radius for the standard LHC parameters. The rectangular bunch is identified by the solid line, the Gaussian bunch is plotted with the dashed line, and the dot-dashed line stands for a parabolic-like bunch. The maximum energy gain in the autonomous and in the kick approximations are respectively shown with a thin dashed line and a thin dot-dashed line. [40].

The total energy gained by an autonomous electron that receives the next bunch kick is defined ΔE_{total}, as the sum up of autonomous and kick energies. The maximum energy gain is expressed by:

$$\Delta E_{max} = m_e\,c^2 \left(\frac{n_p\,r_e}{\sigma_l}\right)^2 \lambda_{max}\,(\ln\frac{r_c}{c_0\,\sigma_\perp}) \tag{20}$$

The kick received by the photoelectrons that are generated at the beam pipe, in phase with the beam passage, is given by:

$$\Delta E_{wall} = 2\,m_e\,c^2 \left(\frac{n_p\,r_e}{\beta\,b}\right)^2 \tag{21}$$

Another interesting expression concerns the minimum energy required by an electron to cross the vacuum chamber before the arrival of the next following bunch, as derived by M. A. Furman [41]:

$$E_{\min to\, cross} = \frac{1}{2}\, m_e\, v_{min}^2 = \frac{1}{2}\, m_e \left(2b\, \frac{c}{s_b}\right)^2 = 2\, m_e\, c^2 \left(\frac{b}{s_b}\right)^2 \tag{22}$$

The minimum secondary electron speed, v_{min} , is calculated considering the beam pipe diameter, $2b$, and the bunch distance, $\frac{s_b}{c}$. Using the above-mentioned equations, the different energy gains for an 80-mm diameter beam pipe are calculated and summarised below in Table 2. These calculations estimate the boundaries of the electron energy spectrum and will be compared to the experimental data. The accelerated electrons gain a minimum of 67 eV if their position at the time of a bunch passage is near the beam pipe wall, up to a maximum of around 6600 eV. The electrons generated at the beam pipe wall in between bunches do not receive an energy boost and they need at least 7 eV to manage to cross the beam pipe before the arrival of the following bunch and generate new electrons.

Table 2: Summary of the above-mentioned electron energy gain parameters for an 80-mm diameter room temperature and field free beam pipe of the LHC, with $ppb = 1.15 \cdot 10^{11}\ protons\ per\ bunch$. The first parameter, r_c, is the critical radius above which the kick approximation is valid, following the J. Scott Berg formulation (see Eq. (14)). It is followed by the calculation of the mean energy of autonomous (see Eq. 19)); and kick approximations (see Eq. (16)); their sum is defined by ΔE_{total}. After, the maximum and minimum energy gain are calculated as ΔE_{max} and ΔE_{wall}, respectively at the center and near the beam pipe. The last parameter is the minimum energy needed to transversally cross the vacuum chamber between two bunches separated by the standard $25\ ns$

$\boldsymbol{r_c}$	$\overline{\Delta \boldsymbol{E}_{autonomous}}$	$\overline{\Delta \boldsymbol{E}_{kick}}$	$\Delta \boldsymbol{E}_{total}$	$\Delta \boldsymbol{E}_{max}$	$\Delta \boldsymbol{E}_{wall}$	$\boldsymbol{E}_{\min to\, cross}$
$0.9\ cm$	$139\ eV$	$202\ eV$	$341\ eV$	$6590\ eV$	$67\ eV$	$7\ eV$

Another theoretical consideration is related to the deflection of the electrons during the bunch passage. Following L. Vos discussion [42], beams with a “large” bunch spacing deflect the electrons after an average time, $\overline{dt}$:

$$\overline{dt} \approx 2b \sqrt{\frac{m_e}{2\,\bar{E}}} \tag{23}$$

Where $\bar{E}$ is the mean energy kinetic energy of the secondaries generated at the vacuum chamber. For an 80-mm diameter beam pipe, $\overline{dt} \approx 102\ ns$. So, for closely spaced bunches, the electrons perform transverse oscillation, with a frequency, f_e, equals to:

$$f_e \approx \frac{1}{b} \sqrt{\frac{e\, Z_0\, I}{2\, \pi\, m_e}} \tag{24}$$

Where, Z_0 is the impedance of free space and I the total beam current. For an 80-mm diameter beam pipe, $f_e \approx 62\ MHz$. L. Vos defines the beam closely bunched when $f_e \cdot s_b < 1$, where s_b is the bunch distance, i.e. $25\ ns$ for a standard LHC beam; sparsely bunches if $f_e \cdot s_b > 1$. A LHC drift, as the VPS, corresponds to a $f_e \cdot s_b > 1$, therefore to the sparsely bunched case. A threshold beam intensity, i_{th}, is also introduced to define the closely or sparsely bunched beam regime. This condition is also known as wall-to-wall transit time condition:

$$i_{th} \approx \frac{2\, \pi\, m_e}{e\, Z_0} \left(\frac{b}{s_b}\right)^2 \tag{25}$$

For an 80-mm diameter beam pipe, the threshold current is $i_{th} \approx 0.24\ A$. The LHC drift case corresponds to the sparsely bunched case.

1.5.2 The beam space charge

The charge distribution of the proton beam determines the bunch electric field, and therefore, influences the EC dynamics. Hence, it is important to quantify the inner dynamics of the proton bunch to define if there is an effect also on the EC mechanism.

In an accelerator, the beam particles motion is driven by external electromagnetic (e.m.) fields, generated in bending magnets and Radio Frequency (RF) cavities. Another important source of e.m. field is generated by the charged beam itself. This additional e.m. field is called “self-field” and depends on the beam current and on the charge distribution. The study of selffields is usually divided in charge fields and wakefields. The charge fields correspond to the space charge forces, which are produced by the charge distribution and the wall image current. The wakefields are generated by geometric variation of the beam pipe or wall conductivity limitations [43]. For charge fields, two regimes can be defined:

- The collisional regime: the intrabeam single particle scattering, known as Touschek effect, originating from particles motion internally to the bunch, can lead to limitations on beam lifetime.
- The collective regime or space charge regime: the self-field produced by a variable charge distribution over large distances leads to collective behaviours.

To determine the relative importance of these two regimes, the plasma Debye length parameter, λ_D, is introduced:

$$\lambda_D = \sqrt{\frac{\varepsilon_0 \gamma^2 k_B T}{e^2 d}} \tag{26}$$

Where ε_0 is the vacuum permittivity, γ the relativistic factor, k_B the Boltzmann constant, T the beam temperature, and d the particle density. The electric potential produced when a test particle is added to the beam is screened off at a distance λ_D, due to the charge redistribution. This concept of Debye shielding was developed in plasma physics. In fact, the beam as a whole can be viewed as a non-neutral plasma. So, collective effects are visible and dominant in the beam pipe when the Debye length is smaller than the beam radius and, therefore, the EC dynamics happening outside the bunch region can be studied globally. Note that the Debye length is proportional to the relativistic factor (energy and particle mass), so at high beam energy the transition from space charge to collisional regime might occur [43].

For relativistic charges moving on parallel trajectories at constant velocity, the field lines are confined on a perpendicular plane with respect to the direction of motion. It is can be shown that the e.m. forces between the bunch charges vanish, following $1/\gamma^2$, due to the cancellation of the electric and magnetic forces [43]. Therefore, for a LHC beam we can neglect the beam space charge effect. Indeed, the calculation of the Debye length for a $450\ GeV$ and $6.5\ TeV$ LHC beam gives $\lambda_{D_{450\ GeV}} \approx 7 \cdot 10^3\ m$ and $\lambda_{D_{6.5\ TeV}} \approx 4 \cdot 10^5\ m$, and the beam space charge can be neglected from injection to top energy. Therefore, the EC dynamic cannot be affected by beam space charge in the LHC. However, low energy machines are affected by proton beam space charge, this is the case of the LINAC.

1.5.3 The EC space charge

The presence of additional charges inside the beam pipe, as in the case of the EC, can generate an additional electric field perturbing the beam dynamics and the EC itself. Indeed, the electric field generated by the presence of many free electrons inside the beam pipe is not negligible for the motion dynamic of the low energy electron. In particular, the low energy secondaries generated at the beam pipe are affected by the space charge field of the EC itself [44]. The Debye radius of the EC can be estimate as:

$$\lambda_{D_{EC}} = 740 \sqrt{\frac{\overline{E_{cloud}}}{n_e}} \tag{27}$$

Where $\overline{E_{cloud}}$ is the mean kinetic energy (eV) in the cloud and n_e the electron density $(1/cm^3)$. Considering an electron density of the order of $n_e \sim 10^5 \frac{1}{cm^3}$ and an energy $\overline{E_{cloud}} \sim 15\ eV$, the EC Debye length is in the order of $9\ cm$. This means that the collective behaviour is expected for distances beyond these values. For the VPS beam pipe with beam pipe radius of 4 cm, this regime is not expected, so the EC space charge has no effects on our observations.

It is also possible to estimate the maximum electron energy for which the EC space charge has a dominant effect at the beam pipe [44]:

$$\bar{E} = \frac{b^2 n_e}{740^2} \tag{28}$$

Assuming an electron density in the order of $n_e \sim 10^5 \frac{1}{cm^3}$ and a 4 cm radius beam pipe, the space charge fields are relevant for the electrons with an energy below $3\ eV$. Therefore, the EC space charge concerns only the low energy electrons, mainly generated by the secondary emission process at the beam pipe wall.

- **Low secondary electron confinement near the beam pipe during multipacting**

Following the discussion presented by S. Heifets [45] [46], the electrons are divided in two groups: primary impinging electrons and secondary electrons. The primary impinging electrons interacts with the parent bunch and their speed increases proportionally to the number of proton per bunch as shown in Eq. (12). The secondary electrons do not interact with the parent bunch and move at a speed proportional to the square root of its energy. The EC formation depends on two parameters, κ and ς, representing the distance (in units of b) that each of the two electron groups can cross between two bunches. The first parameter, κ, concerns the primary electrons and is defined as:

$$\kappa = \frac{v_{primaries}}{c}\frac{s_b}{b} = \frac{2\,n_p\,r_e\,s_b}{b^2} \tag{29}$$

Where $\frac{s_b}{b}$ corresponds to the ratio between the bunch distance and the beam pipe radius and the speed is given by Eq. (12). The second parameter, ς, concerns the secondary electrons and is defined as:

$$\varsigma = \frac{v_{secondaries}}{c}\frac{s_b}{b} = \sqrt{\frac{2\,E_0}{m_e\,c^2}}\frac{s_b}{b} \tag{30}$$

At low bunch intensities, $\kappa \ll 1$ and the electrons interact with many bunches before they reach the beam pipe walls. In this ''neutrality'' regime, the sum averaged in time of the beam field and the EC space charge is zero at the beam pipe. The secondaries remain in the cloud for a long time after the bunch passage.

At high bunch intensities, $\kappa > 2$ and all the electrons reach the wall in one bunch spacing.

For $\kappa > 1$ and $\varsigma < 1$, secondary electrons are confined near the beam pipe, in particular within $\varsigma < \frac{r}{b} < 1$, where r is the radial position of the electron. This regime describes a typical multipacting in LHC for highly populated bunches: the density of secondaries grows until the secondary space charge potential is below E_0.

For a $80\ mm$ diameter beam pipe, with a bunch population, $ppb = 1.15 \cdot 10^{11} protons\ per\ bunch$, the calculations give $\kappa \cong 3.04$ and $\varsigma \cong 0.83$. Therefore, this computation confirms the confinement of low energy electron near the beam pipe for a standard LHC beam in a room temperature and field free beam pipe. The radius at which these electrons are confined is given by $r_{\min} = \varsigma \cdot b \cong 0.033\ m$. It means that in the VPS, the low secondary electrons are mainly confined around the beam pipe, between $3.3\ cm$ and $4\ cm$, i.e. at the beam pipe radius (see light orange ring in Figure 12).

- **High primary electron confinement near the bunch during the seed generation**

At $450\ GeV$, the few most energetic electrons are produced near the beam by beam-gas ionization and their initial distribution is spatially confined around it as shown by K. Kanazawa et al. [47]. To measure the energy distribution, he used several Retarding Field Analysers (RFA). The RFA is a device where different bias grids are applied to separate charged particles by their speed to analyse the particle energy. The speed is related to the initial position of each electron at the moment of the kick, therefore it is possible to reconstruct the electron distribution as a function of the radius. The radius of the region with a highly populated high-energy electrons is given by [47]:

$$r_{\max} = r_e\,n_p\,\sqrt{\frac{2\,m\,c^2}{eV_b}} \tag{31}$$

Where V_b is the retarding bias of the RFA. Considering a bunch population of $ppb = 1.15 \cdot 10^{11}\ protons\ per\ bunch$, and an energy kick of around $E = eV_b \cong 100\ eV$, the computed radius is: $r_{max} \cong 0.033\ m$. This concerns the high energy electrons around the beam at the time of the bunch passage. This computed value for high-energy electron confinement is in line with the low-energy one found above (see red region in Figure 12).

From these two considerations, we conclude that at the time of the bunch passage the high-energy electrons at around few hundreds eV are confined near the bunch, within a maximum radius r_{max}, while the secondaries at few eV mainly stay in the complementary region near the beam pipe, with a distance above r_{min}.

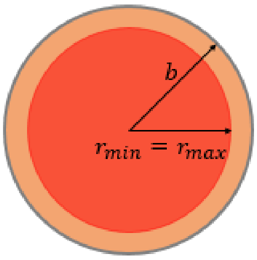

Figure 12: The region where low-energy electrons are confined around the beam pipe, for a VPS chamber, at the time of the bunch passage is displayed in light orange. The region where high-energy electrons are located during the bunch passage is presented in red.

1.5.4 The bunch population threshold for multipacting

Electrons that move synchronous with the bunch and cross the vacuum chamber before the arrival of a second bunch can multipact [39]. This condition can be expressed as:

$$\frac{2\, r_{pipe}}{\Delta v} \leq t_{bb} \tag{32}$$

where r_{pipe} is the pipe radius and t_{bb} the time interval between two successive bunches. The distance between two bunches is defined as:

$$s_b = c\, t_{bb} \tag{33}$$

Replacing the Eq.(12) and (33) into Eq. (32), and considering an electron with an initial position at $r = r_{pipe}$, the bunch intensity threshold above which the multipacting is triggered equals :

$$n_{p_{th\,G}} = \frac{r_{pipe}^2}{r_e\, s_b} \tag{34}$$

For a room temperature LHC straight, with $r_{pipe} = 0.04\ m$, and for a standard LHC beam, where $s_b = 7.5m$, the n_p threshold settles around $7.6 \cdot 10^{10}\ protons\ per\ bunch$. This simple calculation gives an indication of the minimum bunch population to generate EC multipacting [39]. The same multipacting condition is expressed by M. A. Furman [48], defining a resonance state at $G = 1$, where the G parameter is equal to:

$$G = \frac{n_p\, r_e\, s_b}{r_{pipe}^2} \tag{35}$$

However, as underlined by F. Zimmermann *et al.* [49], this condition is far too stringent. Since the majority of the electrons have low energy, they survive for a long time after the bunch passage, thereby interacting with several bunches and gaining sufficient energy to have a mean secondary yield higher than one when impinging on the surface. Following this reasoning, the bunch population threshold becomes:

$$n_{p_{th\,Z}} = \frac{E_0\, s_b}{m_e\, c^2\, r_e} \tag{36}$$

For the same kind of beam pipe and a $E_0 \sim 2 \div 5\ eV$, $ppb_{th\,Z} \approx 1 \cdot 10^{10} \div 3 \cdot 10^{10}\ protons\ per\ bunch$. Hence, the Zimmermann estimation gives a lower value than the Gröbner-Furman one.

1.5.5 The EC model implemented in PyECLOUD simulation code

However, the bunch population threshold and the bunch spacing are necessary but not sufficient conditions for multipacting. The other requirement to stimulate the EC multipacting concerns the effective surface SEY, called δ_{eff}, higher than one. This last parameter is the mean value of the beam pipe SEY multiplied by the energy distribution of the cloud. The low energy electrons, in fact, have a $SEY < 1$, therefore they don't directly participate to the multipacting process. The multipacting is driven by the activity of the accelerated electrons at few eV that extracts more electrons at the beam pipe wall.

The EC build-up process and the evolution of the electron density can be modelled using numerical simulation tools based on 2D macroparticle (MP) approach, such as PyECLOUD, WARP-POSINST and BI-RME/ECLOUD. The cloud is a dynamic phenomenon with electron productions and losses. The electron productions are calculated considering the primary creation and the secondaries generated at the beam pipe surfaces for SEY above 1. Conversely, the large amount of secondaries have low energy and, therefore, their SEY is lower than one, generating electron losses.

In particular, the PyECLOUD code has been developed at CERN. The dynamics of the MP system follows the flow diagram sketched in Figure 13 taken from ref. [50]. The first seeds are generated by gas ionization or SR at a certain time step. The electric field is evaluated at each MP location followed by the electron space charge. The position and momenta of all the macroparticles are recomputed by integrating the dynamics equation. External magnetic field are taken into account in this fourth step. At each time, a certain number of particles hit the wall. The SEY parameter is applied to the beam pipe surface to generate secondaries, accordingly with their energy and angle of emission.

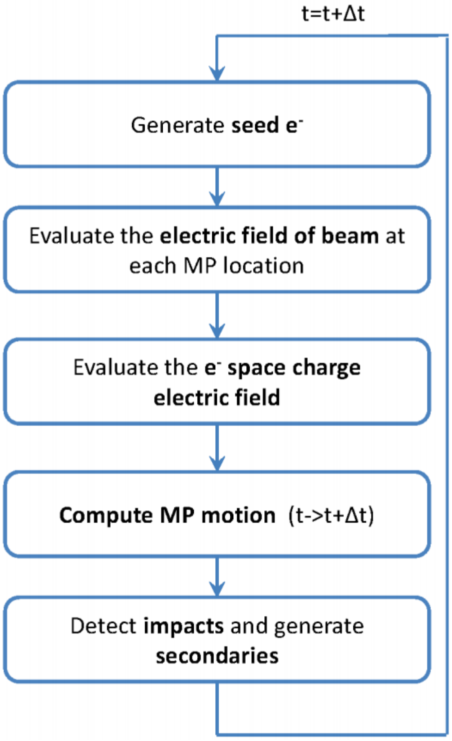
t=t+Δt
Generate **seed e⁻**
Evaluate the **electric field of beam** at each MP location
Evaluate the **e⁻ space charge electric field**
Compute MP motion (t->t+Δt)
Detect **impacts** and generate **secondaries**

Figure 13: The flow diagram representing the PyECLOUD loop for EC calculations is taken from ref. [50].

The electron density can be described as:

$$n_{i+1} = \delta_{eff}\, n_i + n_0 \tag{37}$$

Where n_i is the electron density before a bunch passage and n_0 the primary electrons generated by a single bunch passage, due to gas ionization or photoelectron generation. The "multipacting regime" occurs only when $\delta_{eff} > 1$ for which the electron density increases rapidly. After a certain amount of consecutive bunches, when the electron gain balances the electron loss, and equilibrium regime starts, also called "seed accumulation regime" [11].

1.6 The impact on the accelerator performance and remedies

The EC and SR phenomena affect the vacuum system and they produce several effects. In particular:

- Vacuum degradation, i.e. pressure increase, due to the gas desorbed by the impact of electrons, photoelectrons, photons and protons lost on the beam pipe. Beam lifetime reduction and the possibility of breakdown in high voltage devices, such as kickers.
- Heat load due to the power deposited by the electrons and photons, particularly crucial for a cryogenic installations, with the possibility to trigger a beam dump following the loss of the cryogenic condition
- Transverse beam instabilities, such as "coupled bunch" and "intra-bunch" motion resulting in transverse emittance blow up and beam losses, and incoherent beam effects, such as the tune spread, ultimately leading to a luminosity reduction hence loss of Physics time.
- Beam diagnostics aging following the bombardment by the electron of different instruments, hence risk for the machine operation.

To prevent or reduce these effects, specific actions are taken on LHC. Notice that the first EC seeds cannot be completely avoided, due to SR and residual gas. Concerning the operation parameters, two techniques can be applied during the operation. The first is a standard procedure at the beginning of each LHC run, the scrubbing, which allows the reduction of the SEY by electron bombardment (introduced in the *Section 1.4.1)* [51]. The second technique is applied when the heat loads cannot be supported by the cryogenic system. It consists in running LHC with "8b4e" beams, as performed in 2017 (*Section 1.3)* [52].
Other vacuum technology actions can be taken to reduce or stop the electron and radiation activities, by acting on the potential, the geometry and the surface material of the beam pipe [44, 53, 54, 55, 56, 33].

- The choice of a material, a surface treatment, or a coating with low SEY and PY can improve the accelerator performance, as for example amorphous carbon and NEG coatings.
- A particular surface geometry can be grooved, as in the case of the "saw teeth", to reduce the PY and the photon reflectivity
- The use of clearing electrodes that apply a positive voltage up to 1kV on the beam pipe to trap the secondaries generated and avoid the multipacting [57].
- The use of solenoidal magnetic field that confines the free electrons near the beam pipe walls, avoiding their interaction and acceleration with the passing beam.

1.6.1 Vacuum performance and degradation mechanisms

The vacuum performance is crucial for the LHC beam operation. The LHC vacuum system is complex and consists of more than 100 km of pipes [6]. Vacuum reduces the interaction between the beam particles and the gas molecules. In this PhD we concentrate only on the EC interaction with the beam pipe vacuum system.

The LHC beam pipe base pressure is in the order of 1 and 10^{-10} mbar, i.e. Ultra-High Vacuum (UHV), corresponding to a mean free path of the molecules between 500 and 5000 km. To reach such a low pressure, several pumps are used: sputter ion pumps, NEG coatings and cartridges, together with cryopumps or cryotraps. Pirani, Penning and Bayard-Alpert gauges are used to measure the total pressure on different pressure ranges.

A thermal treatment is applied for room temperature beam pipes. It consists on a bake-out to heat up the full vacuum system, usually for 24 hours, in order to stimulate the outgassing of the surfaces and instruments and release the majority of the adsorbed gas, especially water vapour. Before the end of this first step, the activation process can be launched for NEG components, and, just after, the system can be cooled down to room temperature [58]. This procedure is repeated every time a vacuum system is vented. Moreover, the venting procedure is usually performed with an overpressure of dried air, Argon, Neon or Argon in order to avoid the air humidity to enter in the system when the intervention time is short.

The choice of the material is critical for the performance of the vacuum system. The most common material used for vacuum chambers is stainless steel (SS), while for the beam pipes NEG coatings and copper (Cu) are used. After bake-out, their outgassing rates, i.e. the quantity of gas released in UHV per second and per square centimetre, are, respectively, $3 \cdot 10^{-12} \frac{mbar\cdot l}{s\cdot cm^2}$, $3 - 7 \cdot 10^{-12} \frac{mbar\cdot l}{s\cdot cm^2}$ and $3 \cdot 10^{-14} \frac{mbar\cdot l}{s\cdot cm^2}$, [59] [60] . For amorphous carbon coatings (a-C), never used in the LHC ring before this PhD study, the outgassing value is around 3.5 times higher than stainless steel [36].

The pressure measured during the LHC operation is influenced not only by the outgassing rate, A, and pumping speed, S, but also by the beam dynamics, i.e. the surface desorbs molecules stimulated by electrons, $\eta_e N_e$, and photons, $\eta_{ph}\Gamma_{ph}$., bombardment.

$$P = \frac{A}{S} + \frac{RT}{V}\left(\eta_e N_e + \eta_\gamma \Gamma_{ph}\right) \tag{38}$$

The main desorption parameters are:

- the Photon Stimulated Desorption (PSD) yield, characterised by η_γ. The PSD yield is defined as the number of gas molecules desorbed per impinging photon on the surface:

  $$\eta_\gamma = \frac{N_{molecules}}{N_{photons}} \tag{39}$$

  Where $\Gamma_{molecules}$ is the flux of molecules desorbed under photon irradiation [Pa m^3/s], $\Gamma_{photons}$ is the photon flux [photons/s]. The PSD yield decreases with photon dose and increases with photon energy [61, 62, 63, 64, 65, 66].

- the Electron Stimulated Desorption (ESD) yield, characterised by η_e. This is defined as the number of gas molecules desorbed per electron impinging on the surface:

  $$\eta_e = \frac{N_{molecules}}{N_{electrons}} \tag{40}$$

  where $\Gamma_{molecules}$ is the flux of molecules desorbed due to electron bombardment [Pa m^3/s], q_e the electron charge [C], k_B the Boltzmann constant [J/K], T the temperature [K], $I_{electron}$ the electron current [A]. The ESD increases with higher electron energy and decreases with accumulated electron dose [13]. Moreover, the ESD decreases if the vacuum firing process is performed and increases with the temperature [67, 68].

These parameters depend on the particle mass, energy and incident angle, but also on the surface material and conditions such as the temperature, the applied thermal treatment and the conditioning process taking place with particle bombardment [61, 64].

Chapter 2 The Vacuum Pilot Sector (VPS) in the LHC

2.1 The VPS installation

The Vacuum Pilot Sector (VPS) is an 18 meter long experimental area installed in a room temperature and magnetic field free region of the LHC Long Straight Section (LSS). It is located on the left side of point 8, 150 m away from the LHCb experiment. This position was selected to provide an easy access and a low radiation level [9]. The VPS is composed of two parallel 80 mm inner diameter beam pipes, where two proton beams circulates in opposite directions (see Figure 15). The external line hosts the so-called blue or B1 beam, coming from the arc 7-8 and passing across the quadrupole Q5. The internal line houses the so called red or B2 beam, coming from the LHCb experiment and passing through the dipole D2 and the quadrupole Q4. a picture of the VPS is displayed in Figure 14.

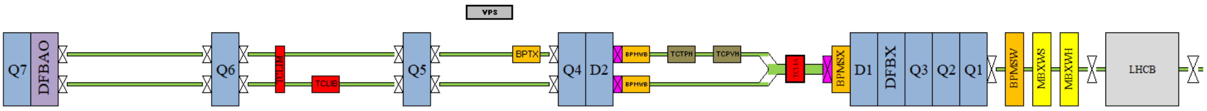

Figure 14: Layout of the LSS8 where VPS is located, between Q5 and Q4.

The two dipoles, D1 and D2, are located next to the triplet magnets (Q1-Q2-Q3) and before Q4. D1 is a 9.45 m long single bore superconducting magnet, while the second one is double bore. Both magnets operates at 4.5 K [6]. The parameters of the seven quadrupole magnets installed in LSS8 are displayed in Table 3. These quadrupoles are positioned between the interaction point (IP8) and the dispersion suppression (DS), just before the arc.

Table 3: Quadrupole magnet parameters in in the LSS8.

	low-β triplet			**MS**			
Magnet	**Q1**	**Q2**	**Q3**	**Q4**	**Q5L**	**Q6**	**Q7**
Type: MQ	XL	X	XL	Y	M	M	
L [m]	6.3	5.5	6.3	3.4			
T [K]	1.9			4.5		1.9	
B [T/m]	215/220			160		200	
r [mm]	22.2	28.95		27.2	20.6		22.2
	17.3	24.05		22.3	15.75		17.3

As shown in Figure 18, the VPS is made of four 1.3 meter long stations, separated by 1.7 meter long activated NEG buffers. The buffers provide a distributed pumping system to isolate in terms of pressure one station from another. In addition, ion pumps and NEG cartridges are placed at the each extremities of a station. The modified LEP ion pump (model: Nobel VacIon Pump 911-5034, Starcell, 60 l/s, Varian) accommodates a NEG cartridges (model: CapaciTorr D 400-2, Saes Getters)

Each station is composed of a vacuum vessel and a 1-mm think OFE liner that can be exchangeable. The liner surface can be treated with different coatings or thermal processes. Windows are curved on the liner to host detectors and to pump (see

Figure 16). The stainless steel vacuum vessel host several flanges to connect the station to the buffers and the different instruments.

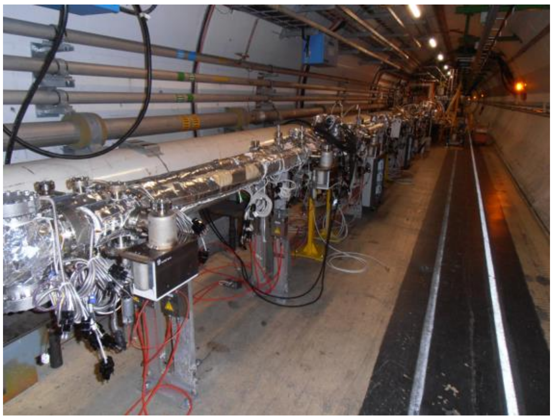

Figure 15: VPS system installed in the LHC tunnel.

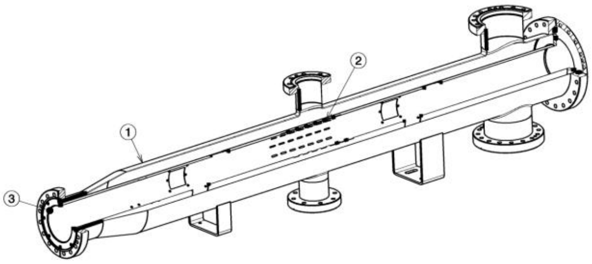

Figure 16: A typical VPS station composed of a vacuum chamber (1) and a beam pipe, called liner (2). The electrical continuity of the beam pipe is realised with the use of a RF spring (3).

The first VPS installation was achieved in 2014 during Long Shutdown 1 before the LHC Run 2. The installed surfaces were non-activated NEG, activated NEG, baked copper and unbaked copper (see Figure 17). A non-activated NEG station was chosen to study the impact of a fast intervention in the machine without NEG activation. The other surfaces are LHC baseline materials. Activated NEG is deployed in the Long Straight Sections. Baked copper is used for the LHC room temperature transitions while the unbaked copper is installed in the cold parts of LHC. A full bake-out process was carried out in the NEG buffers separating the four stations. The activated NEG and the baked copper stations were respectively baked out to 230ºC and to 250ºC for 24 h. A moderate bake out to 80 ºC was applied to the non-activated NEG and unbaked copper stations to degas the water trapped in the kapton cables used for electrical and thermal measurements.

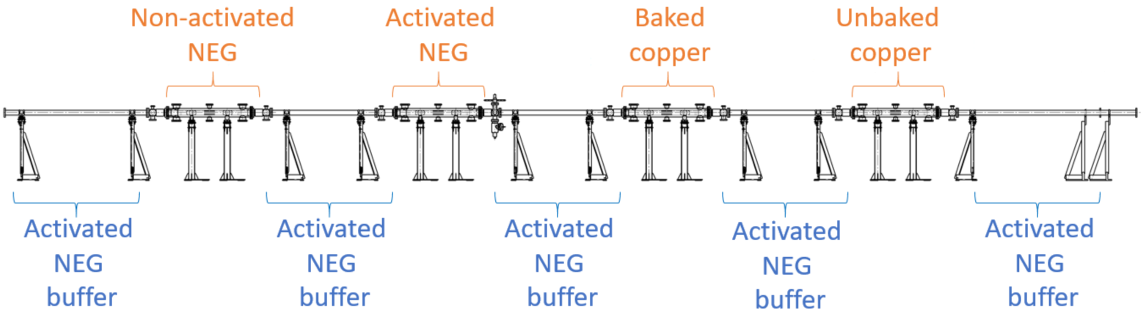
Non-activated NEG
Activated NEG
Baked copper
Unbaked copper
Activated NEG buffer
Activated NEG buffer
Activated NEG buffer
Activated NEG buffer
Activated NEG buffer

Figure 17: Layout of the 2014 VPS installation.

A second version of VPS was built and installed in January 2016, during my master thesis internship at CERN. During this upgrade, three stations were modified. Ex situ NEG, amorphous-Carbon coating (a-C) and a new unbaked copper (Cu) were installed in the first three positions from the left (see Figure 18). In this version, all the liners were baked at 80ºC to partially degas the water to preserve the LHC performances. The NEG buffers were baked out to 230ºC for 24 h.

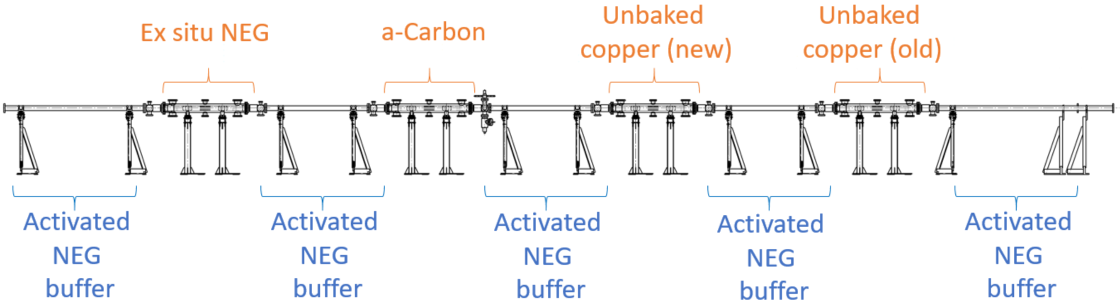
Ex situ NEG
a-Carbon
Unbaked copper (new)
Unbaked copper (old)
Activated NEG buffer
Activated NEG buffer
Activated NEG buffer
Activated NEG buffer
Activated NEG buffer

Figure 18: Layout of the 2016 VPS installation.

A typical sequence of the bake-out procedure is displayed below. This bake-out was the one applied to VPS in 2016, for the second version. The first plateau corresponds to the mild bake-out of the stations, that was kept for few days along the weekend. The second plateau corresponds to the degassing of the gauges (SVT and Penning), gas analysers (VQM), inox components, the so-called 'magic box" (BM) installed to control the bake-out, the beam position monitors (BPM). After one day there is a flashing of the ion pumps, followed by the third ramp-up to activate the NEG buffers. At the end of the activation, a second flashing of the ion pumps takes place together with the degassing of the gauges. The NEG cartridges are activated just at the end when the system reaches room temperature.

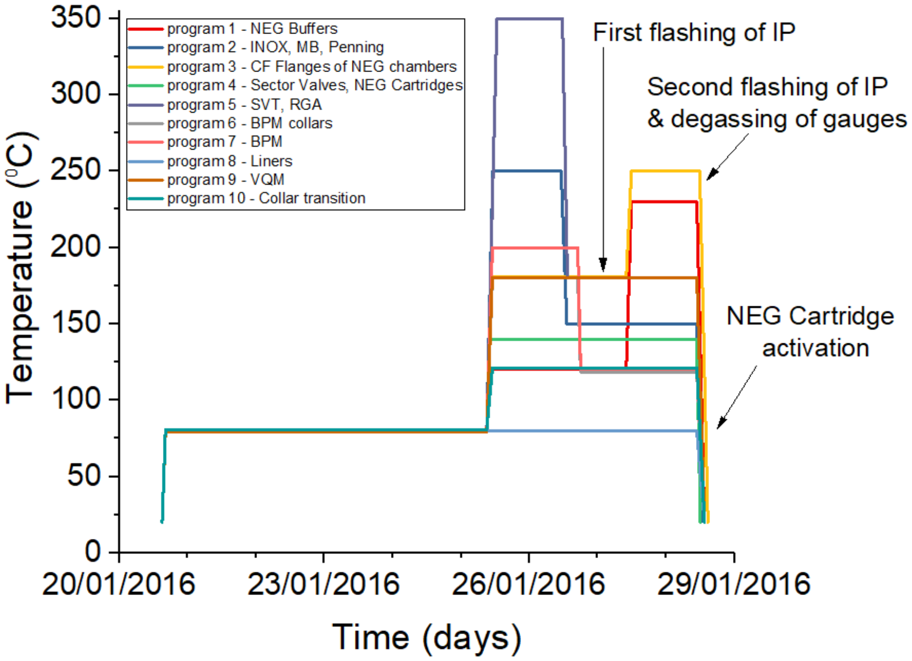

Figure 19: The bake-out programs applied into VPS system in January 2016, for the new installation.

2.2 How VPS was manufactured

The 2016 VPS update of six new liners supposes several manufacturing steps: the design, the production, the cleaning, the coating and the installation. This update took around seven months, from the previous design modifications to the final installation in the tunnel, in January 2016.

Concerning the design, the layout was slightly changed from the 2014 version, in particular the position of the detectors on the liner. This modification was done to increase the separation from $5\ cm$ to $16\ cm$, between the different detectors to avoid their mutual influence, The production of the OFE copper liners and stainless steel vacuum chambers was performed in the CERN main workshop. The production of non-standard detectors, i.e. pick-ups and calorimeters, was carried out at CERN. This phase including building, welding, assembling and installing the detectors into each liner took me around two months during my internship [69].

The cleaning and coating of these pieces was performed by the colleagues of the Surfaces, Chemistry and Coatings section (TE-VSC-SCC) at CERN. For the cleaning, the standard procedures were applied to have detergent cleaned copper and stain-less steel vacuum pieces [70]. The NEG and amorphous carbon coatings were produced by magnetron sputtering, using an argon plasma.

- **NEG coating liners**

After the magnetron sputtering NEG coating process [71], the X-ray photoelectron spectroscopy (XPS) shows the following parameters, (see Table 4) [72]. The VPS sample is compared to a reference and min/max values accepted for an installation in the LHC. As reported, the sample is generally good, apart for a contamination with N (3.22) and Cu (6.257), that doesn't harm the performance of the NEG coating.

Table 4: The activation characteristics of the different samples of NEG, extracted from the XPS analysis [72]

Chamber	Surface C [at. %]	Surface O [at. %]	Surface pollutant [at. %]	Surface metallic composition [at. %]			Activation (carbon area decrease) ΔC(RT250° C)/C(RT)	Activation Carbide/total C (250 C)	Activation (oxigen area Decrease) ΔC(RT250° C)/C(RT)
				Ti	Zr	V			
Reference (LSS 16-4 CR000044)	23.4	52.9	---	24.2	41.7	34.1	52.7	78.8	74.5
VPS sample (S0115_b-20151210)	11.9	53.6	N(3.22), Cu(6.257)	28	38	34	38.4	83.6	82.9
min ref. values	---	---	---	16	30	25	---	40	66
max ref. values	40	---	---	35	51	42	---	---	---

The following two figures show the activation effects in the O 1s and C 1s peak area evolution with temperature. The VPS sample is displayed in blue, while the reference is in red. The NEG sample activates well, since the metal is fully reduced and the oxygen decrease is sufficient.

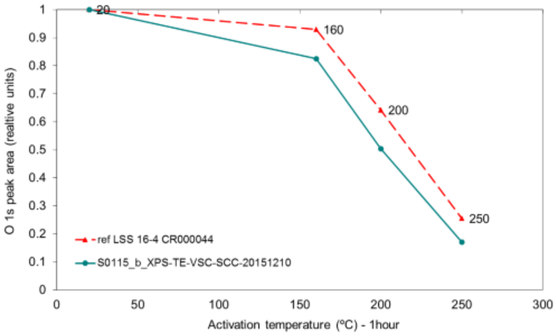

Figure 20: The activation effects in the O 1s peak area evolution with temperature [72].

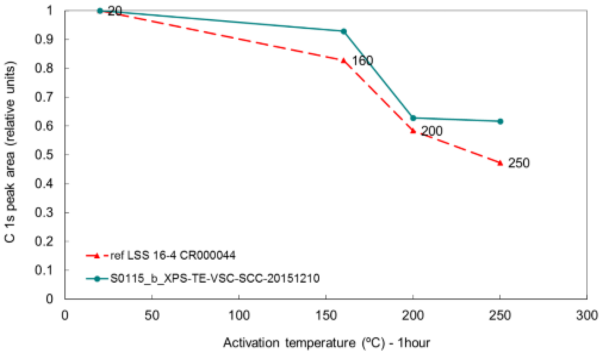

Figure 21: The activation effects in the C 1s peak area evolution with temperature [72].

The two NEG liners were placed inside vacuum chambers and the internal vacuum cabling connection followed in September-October 2015. The NEG chambers were activated and stored under vacuum at the end of 2015, then vented with Nitrogen and installed in the LHC in January 2016.

- **a-C coating liners**

The a-C coating is performed by DC Cylindrical Magnetron sputtering (DCCM) in the same solenoids used for the NEG coating [73]. After the coating, the SEY was measured on a-C coating as a function of electron energy (see Figure 22) [74]. The maximum SEY, δ_{max}, is included between 0.97 and 1.05, positioned at an electron energy of around 300 eV.

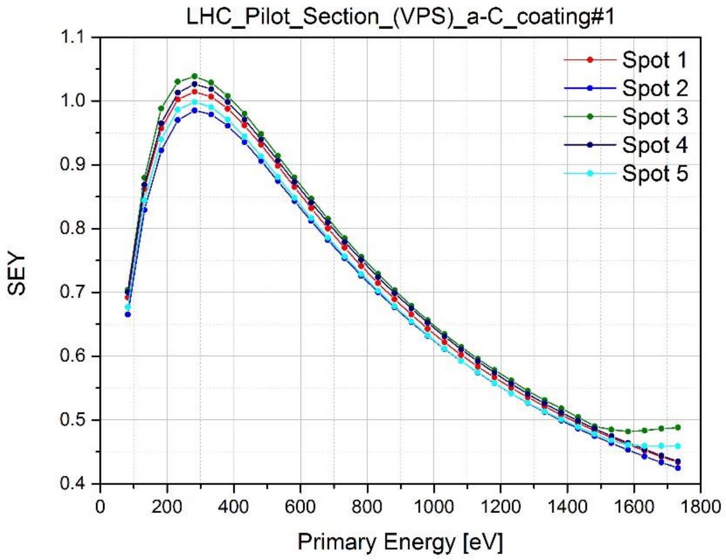

Figure 22: The SEY curve of the VPS a-C liners before the installation [74].

The installation of the two a-C liners inside each vacuum chamber and the internal vacuum cabling connection followed in September-October 2015. The liners were finally installed in the LHC together with the NEG and Cu chambers in January 2016.

The NEG buffers were activated following the standard LHC procedure. After the bake-out, all the detectors were externally connected to their controller, positioned in the radiation-free tunnel areas on dedicated electronic racks.

2.3 Vacuum instruments

The stations are equipped with several vacuum instruments. Total pressure gauges, such as Bayard-Alpert gauges (BAG), penning gauges and Pirani, are installed all along the system. Additionally, some gas analysers are measuring the partial pressures.

2.3.1 Pressure Gauges

The pressure gauges are used to monitor the LHC vacuum system. Different gauges are used to measure from atmospheric pressure to ultra-high vacuum (UHV) pressure.

A Pirani gauge (model: TPR 018 from Pfeiffer) is installed in the middle of both beam pipes in order to the pressure during the pump down [75]. The Penning gauges (model: IKR 070, Pfeiffer) are installed on the left side of each station and also on the right side of the ex situ NEG stations since the 2016 upgrade [75]. The Bayard-Alpert gauges (model: Nude-UHV Ion Gauge, SVT 305) are installed in the middle of each station, for a total of 8 gauges, plus two in the central modules of VPS [76].

The distribution of a large number of gauges allows us to control the pressure profile along VPS during the gas injections and the LHC runs. If not specified, all the pressure readings are intended as nitrogen equivalent.

2.3.2 Residual gas analyser

The Granville-Philippe 835 Vacuum Quality Monitor System (MKS instruments) was chosen among the residual gas analysers. This choice was driven by the electronic remote connection possible with a 50 meter cable [77]. The radiation level in the LHC tunnel would not permit any electronic system to work if directly connected on the head of the analyser.

The use of this autoresonant ion trap for low-mass range spectroscopy is new at CERN. During the first installation, the gas analysers were positioned only on the second and fourth stations, while since 2016 also the first station was equipped. The VQM analysers are positioned at the top flange present in the middle of each vacuum vessel, facing the BAG gauge.

The sensor consists of an ionizer, an ion trap and an ion detector (see Figure 23). The ioniser is composed of a repeller and a filament which generates electrons ionizing the residual gas. Then, the ions are trapped in the mass separator, composed of an electron multiplier to amplify the signal [77, 78].

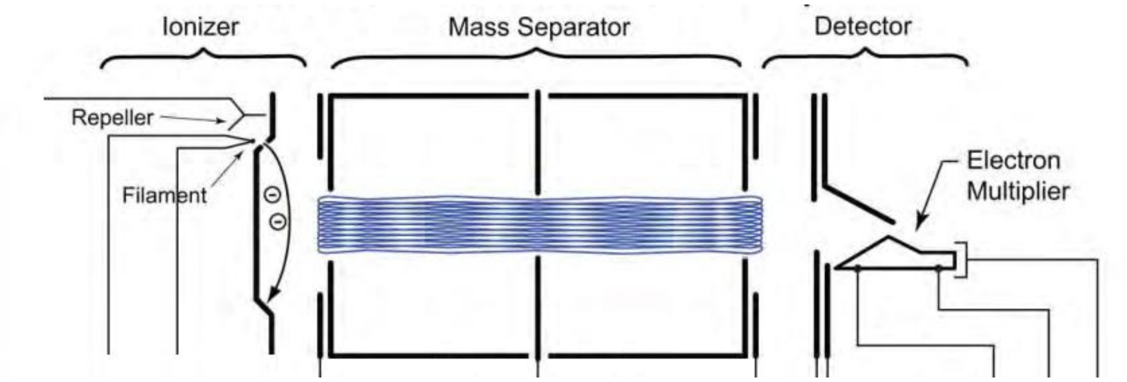

Figure 23: Cross section of the VQM sensor [78].

The parameters use for the analyser operation are:

- The filament emission current, which default value is around 0.07 mA,
- The repeller bias, by default -31 V,
- The electron multiplier bias, by default around -900 V.

Concerning the bake-out, the recommended temperature cannot exceed 200 ºC. It was then set 180 ºC.

2.4 Pick-ups

The stations are also equipped with dedicated probes to study EC and SR. In this section, I discuss the homemade pick-ups utilised to investigate the electron density into the VPS beam pipe. The electrical measurements are acquired with these instruments designed, manufactured and realised at CERN. In particular, three kind of detectors are used: the shielded pick-ups for electron measurements, the electron energy detectors to scan the electron energy distribution and the unshielded pick-ups to monitor the beam passage [9, 79].

2.4.1 Shielded pick-up with a +9V bias

The shielded pick-ups measure the electron flux arriving at the beam pipe. Each detector is composed of a grounded grid attached on the VPS beam pipe, a +9V polarised copper electrode and a grounded copper cover (see Figure 24). The bias is applied to re-collect the secondary electrons generated at the electrode [80]. The grid is used not to perturb too much the measurement. Different grids are employed to study the transparency influence on the measurement. In general, the grids used to compare different stations have a transparency of 7%, but lower and higher transparencies are also available on both unbaked copper liners. In the first VPS version, 0.2%, 5%, 10% were compared to 7%, while in the second installation 0.2%, 15% and 50% are tested.

The measurements are acquired with picoammeters (model: 6485, Keithley) and oscilloscopes (model: WR620Zi, bandwidth: 2GHz, Teledyne Lecroy). Pick-ups with transparency other than 7% are only connected with picoammeters. A LabVIEW program records automatically the integrated currents read by the picoammeters. The oscilloscopes, instead, acquire and display voltage signals that follow the nanosecond timescale.

A scheme of a shielded pick-up measurement read by a picoammeter is displayed in Figure 24. The 7% grid is grounded and directly connected to the liner. The +9 V electrode is mounted with screws and isolated with alumina. The copper cover is mounted on top of the electrode and electrically isolated as well.

We neglect the signal perturbation due the measurement itself.

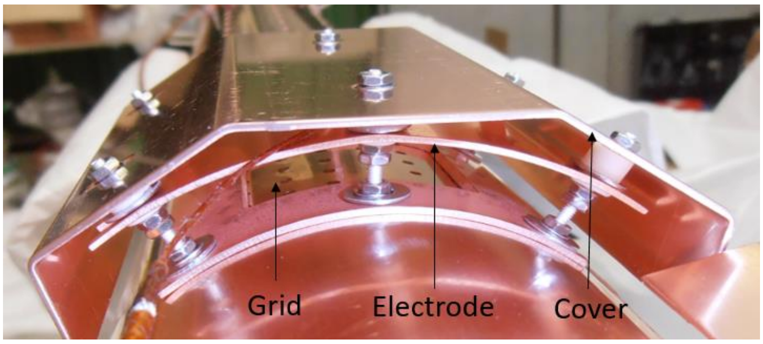

Figure 24: Shielded pick-up, used as electron cloud probe

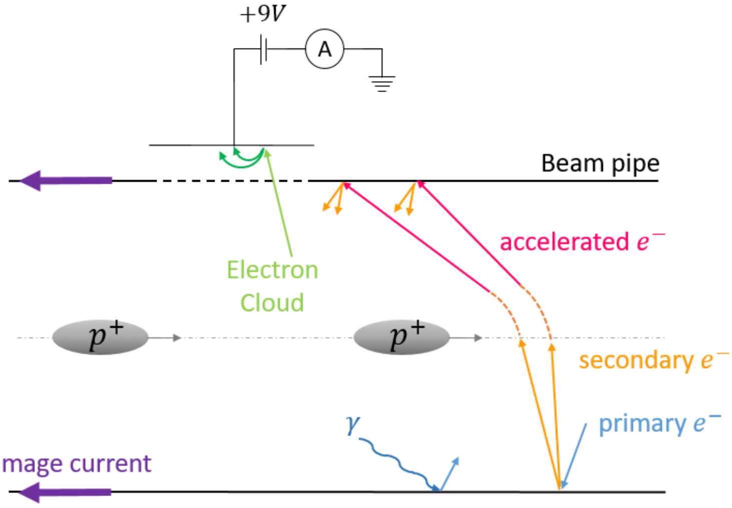

Figure 25: Scheme of a shielded pick-up measurement.

The effective collecting area of each detector is calculated as the multiplication between the electrode surface and the grid transparency. For a 7% grid, the effective area is around $0.8\ cm^2$. This parameter will be useful while converting the Amperes measured per detector into electron density.

During the electron build-up and the photoelectron generation, the +9 V shielded pick-up collects a current $I_{pick-up}$. The measurement quantifies the net balance of the charged particle fluxes at the electrode surface. The fluxes can be related to electrons, of any energy, or positive ions, with more than $9\ eV$. In this analysis, we neglect the effect of ions. As first hypothesis, one can consider insignificant the ion collection at the electrode because ions are heavier than electrons, therefore they gain a lower speed and their effect at the collector itself is limited.

By convention for a positive charge, we define as positive a current entering the picoammeter and negative a current leaving the surface. Measuring negative charge carriers, i.e. electrons, instead, their measured currents will be negative if entering, and positive if escaping the electrode.

The input current, I_{input}, i.e. the EC signal in the LHC, can be written as the sum of: (a) electrons with an energy below the electrode bias, and (b) the electrons with an energy above the bias:

$$I_{input} = I_{E<9eV} + I_{E>9eV} \tag{41}$$

The measurement of these two components will be analysed separately.

- Case a): electron energies below the electrode bias, $I_{E<9eV}$

This case considers coming electrons with low energy, with $E < 9\ eV$. These low energy electrons are mainly collected between batches, when no beam acceleration occurs. The reflectivity properties of the beam pipe surface increases with low electron energy and sustain the EC process between bunches.

These low energy electrons collected at the electrode split into: the electrons with an energy below the electrode's work function W, $I_{0<E<W}$, and the energy above, $I_{W<E<9eV}$. Electron with energy below the work function do not have enough energy to release secondaries and it is very likely that these electrons are reflected or back-scattered, $I_{refl,0<E<W}$. The higher energy group, $I_{W<E<9eV}$, can be partially reflected and back-scattered, $I_{refl,W<E<9eV}$, but can also generate secondaries, $I_{sec,W<E<9eV}$. Both the secondary and the elastic electrons are consequently trapped by the positive bias owing low energy.

The mathematical description of the pick-up measurement can be cast into Eq.(42). When the incoming electrons have an energy below the applied bias of 9 V as this case, this measurement is a good approximation of the impinging electron flux.

$$I_{pick-up_a} = I_{0<E<W} + I_{W<E<9eV} = I_{E<9eV} \tag{42}$$

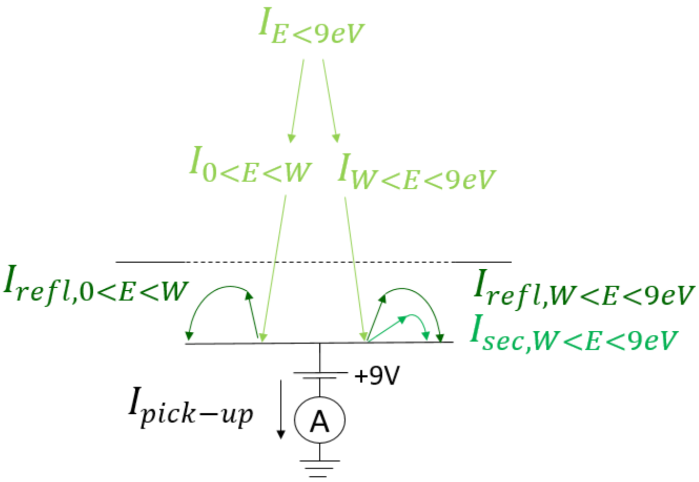

Figure 26: Scheme of a +9 V bias shielded pick-up measurements with a low energy source.

- Case b): electron energies above the electrode bias, $I_{E>9eV}$

As shown in Figure 27, the second case considers electrons coming from a high energy source, with $E > 9eV$. This high-energy component is attributed to the electron acceleration during the passage of the bunch.

The secondaries with less than 9 eV, $I_{sec<9eV,E>9eV}$, are re-collected at the electrode, while the more energetic ones, $I_{sec>9eV,E>9eV}$, are not collected. Nevertheless, the amount of secondary electrons with more than 9 eV, $I_{sec>9eV,E>9eV}$, can be neglected (see Figure 7), reason for which a 9 V bias was chosen. In a first approximation, one can neglect also the elastic component because for high electron energies $\delta_{elastic}$ is low (see Figure 8). With these approximations, the pick-up current read results to be equivalent to the EC signal input.

$$I_{pick-up_b} = I_{E>9eV} - I_{refl,E>9eV} - I_{sec>9eV,E>9eV} \approx I_{E>9eV} \tag{43}$$

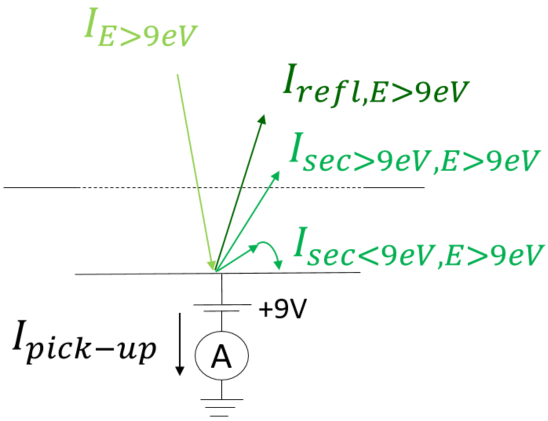
$I_{E>9eV}$
$I_{refl,E>9eV}$
$I_{sec>9eV,E>9eV}$
$I_{sec<9eV,E>9eV}$
+9V
$I_{pick-up}$
A

Figure 27: Scheme of a +9 V bias shielded pick-up measurement with a high electron energy source.

- Case c): low and high energy electrons, $I_{input} = I_{E<9eV} + I_{E>9eV}$

In a real EC dynamics, both low and high energy electrons are present. Therefore, the total current read by shielded pick-ups becomes the sum of the two cases a) and b). A first approximation, the current read by this pick-up can be considered the total EC signal impinging at the electrode, following the previous simplification.

In order to evaluate the hypothesis, i.e. how much the reflectivity and the high energy secondary components influence the measurement, a shielded pick-up with a variable bias was installed.

2.4.2 Shielded pick-up with a variable bias (High Voltage Bias)

One of the shielded pick-up was connected to a high voltage bias (model: 6485, Keithley), instead of a +9V DC battery. This allows changing the electrode bias from 0 V to +120 V and scanning the energy of the electrons leaving the electrode (see Figure 28).

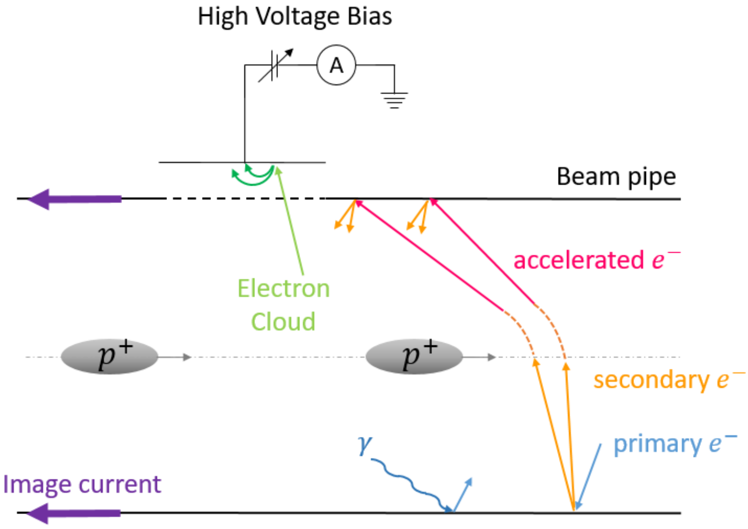
High Voltage Bias
A
Beam pipe
accelerated e^-
Electron Cloud
p^+
p^+
secondary e^-
primary e^-
γ
Image current

Figure 28: Scheme of a shielded pick-up measurement with a variable bias.

In this paragraph I explore the influence of positive bias only, from 0 V to few hundreds Volts. The higher is the bias, the more secondary, reflected and back-scattered electrons are at the electrode, and so the more reliable the measurement. The measurement is sketched in Figure 29 and Eq.(44).

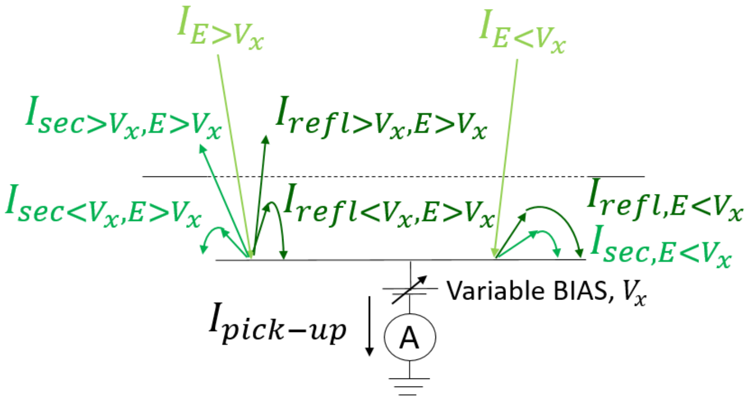

Figure 29: Scheme of a variable bias shielded pick-up measurement.

$$I_{pick-up\ (V_x)} = I_{E<V_x} + I_{E>V_x} - I_{refl>V_x,E>V_x} - I_{sec>V_x,E>V_x} \tag{44}$$

If one varies the bias with a defined input source and compares the values with the 9 eV measurement usually applied to the electrode with a battery, the difference should give the information on the reflected, back-scattered and secondary components. The higher the applied bias, the bigger the amount of secondaries trapped at the electrode, so the higher the absolute value of the current read. The complete derivation is given in *Annex 3*.

Considering a similar approach to the previous discussion for a $V_x > 9\ V$, the final equation becomes:

$$I_{pick-up\ (V_x)} - I_{pick-up\ (+9V)} = \delta \cdot I_{9eV<E<V_x} \tag{45}$$

The pick-up current difference between a general V_x and the standard $+9V$ applied to the bias measures the reflected, back-scattered and secondary electrons generated for electrons impinging with an energy, E, between the two voltage values, $9\ eV < E < V_x$. This mathematical description will be useful to understand the high voltage bias measurements presented in *Chapter 4.1.2*.

2.4.3 Electron energy spectrum detector

The electron energy spectrum detector is made of two grids, an electrode and a cover (see Figure 30). The first grid is attached to the liner, grounded, and has 7% transparency. The second grid is 75% transparent, with a variable negative bias from 0 V to -1250 V. The third element is the electrode, with a +9 V bias applied, to trap the majority of the secondaries generated at the electrode. The last component is a grounded cap to protect the electrode from the other electrical connections inside the vacuum chamber. (Figure 31).

The lower the voltage of the second grid, the lower the number of electrons that can reach the electrode. In fact, only the electrons with higher energy than the negative bias can arrive to the electrode [81] [82] [83] [84].

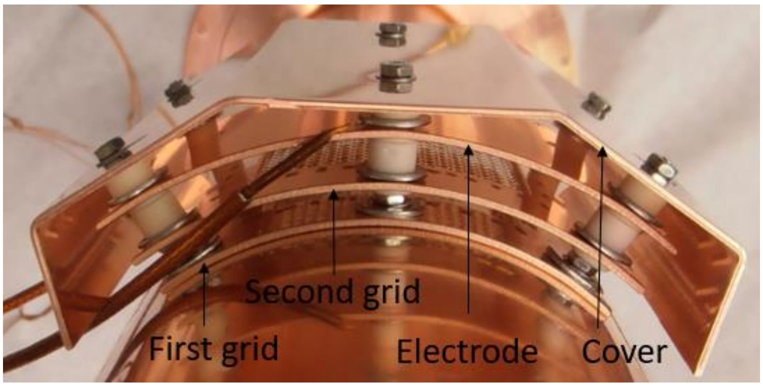
Second grid
First grid
Electrode
Cover

Figure 30: The electron energy detector, made up of two grids, an electrode and a hood.

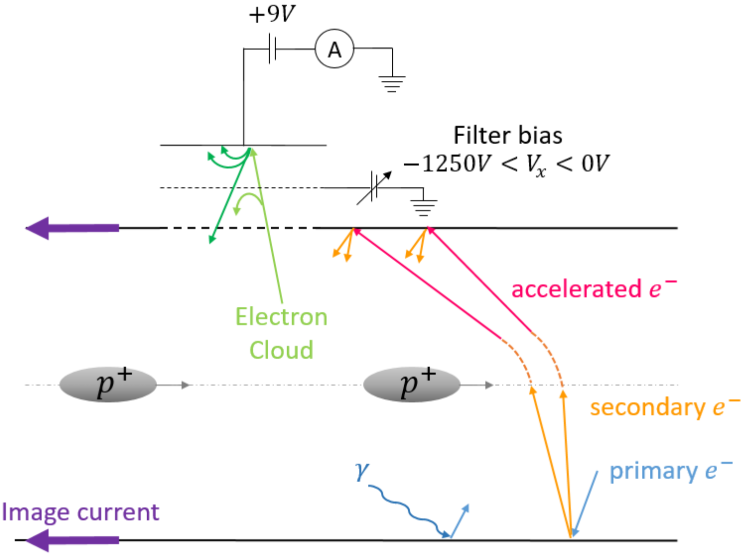
$+9V$
A
Filter bias
$-1250V < V_x < 0V$
accelerated e^-
Electron Cloud
p^+
p^+
secondary e^-
γ
primary e^-
Image current

Figure 31: Scheme of an electron energy detector.

A schematic of the measurement is shown in Figure 32. The electrons with an absolute energy value smaller than the one of the negative variable bias do not cross the second grid. The higher energetic electrons can reach the electrode, generating secondaries or being reflected and back-scattered. At this point, only the electrons with a remaining energy above V_x can escape and cross again the second grid, for the second time. Therefore, only the secondary and elastic electrons with an initial energy above $2 \cdot V_x$ cannot be trapped, i.e. respectively $I_{sec>2\cdot|V_x|,\ E>|V_x|}$ and $I_{refl>2\cdot|V_x|,\ E>|V_x|}$ components.

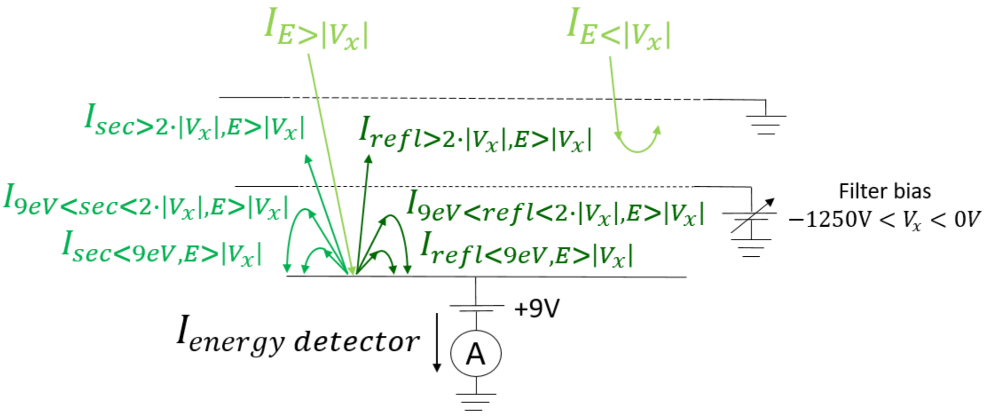
$I_{E>|V_x|}$
$I_{E<|V_x|}$
$I_{sec>2\cdot|V_x|,E>|V_x|}$
$I_{refl>2\cdot|V_x|,E>|V_x|}$
$I_{9eV<sec<2\cdot|V_x|,E>|V_x|}$
$I_{9eV<refl<2\cdot|V_x|,E>|V_x|}$
$I_{sec<9eV,E>|V_x|}$
$I_{refl<9eV,E>|V_x|}$
Filter bias
$-1250\text{V} < V_x < 0V$
+9V
$I_{energy\ detector}$
A

Figure 32: Scheme of an electron energy detector measurement.

The reflected, the back-scattered and the most energetic part of the secondary electrons can be considered such a small quantity such that the total current measured represents only the electron flux above the applied bias:

$$I_{energy\ detector} = I_{E>|V_x|} - I_{refl>2\cdot|V_x|,\, E>|V_x|} - I_{sec>2\cdot|V_x|,\ E>|V_x|} \approx I_{E>|V_x|} \tag{46}$$

The pick-up current (A) acquired applying a certain voltage (V) on the grid corresponds to the integration of the number of electrons above the equivalent electron energy (eV). The derivative of the detector current describes the energy distribution of the collected signal, $S_{electron}$. Hence, the energy distribution of the electrons (A/V) is:

$$S_{electron} \approx \frac{dI_{energy\ detector}}{dE} \approx \frac{d(I_{E>|V_x|})}{dE} \tag{47}$$

This measurements will be discussed in *Chapter 4.1*.

2.4.4 Unshielded pick-up with a -9V bias

When connected to an oscilloscope, the unshielded pickup is used to trigger the beam passage, or used to acquire the signals of the photoelectrons, when connected to the picoammeter. The detector is made of a copper plate facing the beam where a hole is cut out, a circular golden coated button facing the beam and a cover sheet (see Figure 33). A -9 V bias applied to the button prevents the majority of the electrons from impacting on its surface (see Figure 34). The measurement is done through a very simple electrical circuit, with 1 MΩ resistance.

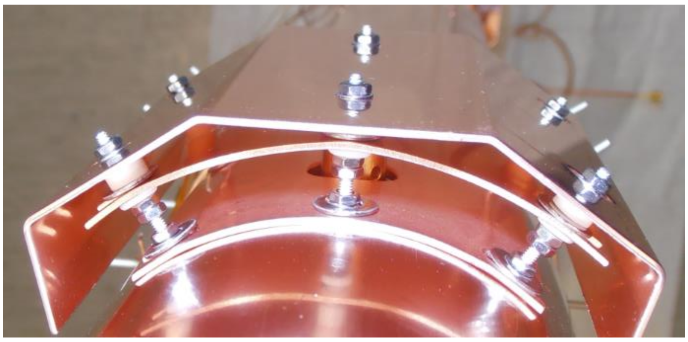

Figure 33: Unshielded pick-up, used as trigger and photon probe.

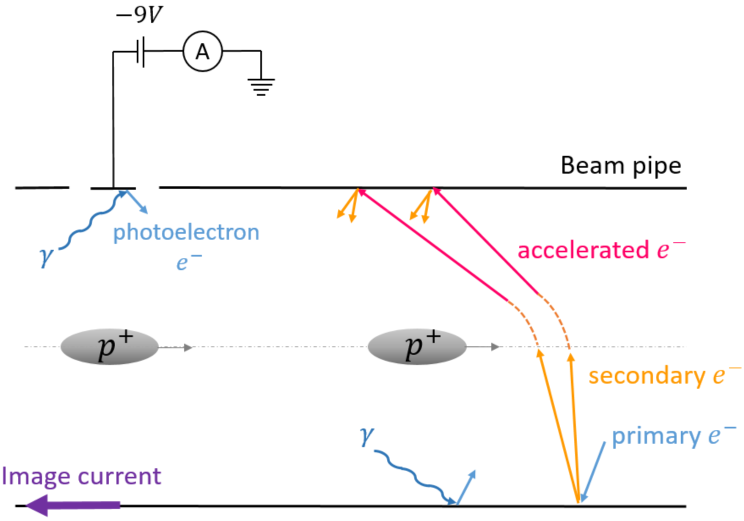

Figure 34: Scheme of an unshielded pick-up.

A schematic of the unshielded pick-up is shown in Figure 35. The electron flux with an energy below the electrode bias, $I_{E<V_{bias}}$, cannot reach the surface. The electrons with a minimum energy, E_0, defined as the sum up of the electrode bias and the gold work function, W, can reach the electrode and release secondary electrons. They are indicated with $I_{E>E_0}$. A typical gold W value is around 5.3 eV [85]. This minimum energy needed by the electrons to reach the electrode and generate secondaries is defined by the following equation:

$$E_0 = V_{bias} + W = 9\ eV + 5.3\ eV \approx 14.3\ eV \tag{48}$$

The electrons with an energy in between can only be reflected and are indicated with $I_{V_{bias}<E<E_0}$. The last impinging flux is the SR represented by γ. This produces photoelectrons, I_{pe}, as explained in *Chapters 1.3.5* and *1.4*.

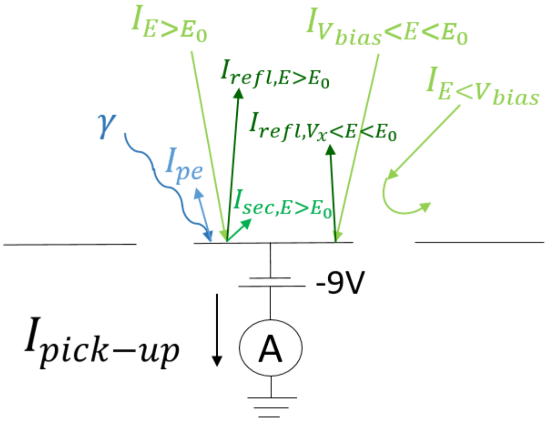

Figure 35: Scheme of an unshielded pick-up.

If the majority of the electrons are below 15 eV and the presence of high energy electrons can be neglected, at first glance the main current reading is related just to the photoelectrons, as expressed by the following equation:

$$I_{pick-up\ (-9V)} = -I_{pe} + I_{E>E_0} - I_{refl,E>E_0} - I_{sec,E>E_0} + I_{V_{bias}<E<E_0} - I_{refl,V_x<E<E_0} \approx -I_{pe} \tag{49}$$

The photoelectron current, I_{pe}, is related to the photon yield, PEY, and the photon flux, γ:

$$I_{pe} = PEY \cdot \gamma \tag{50}$$

This unshielded pick-up is inserted directly on the beam pipe and also collects the beam signal interference due to an induction process. This parasitic effect is here used to record and trigger the beam structure for the EC measurements acquired with the oscilloscope.

2.5 Calorimeters

The VPS calorimeters measure the heat loads deposited into the beam pipe. In particular, these calorimeters investigate the power deposition linked to beam-wall impedance, SR and EC phenomena. The first two components are well known in the literature, while the EC there is not fully understood yet. In addition, the beam-wall impedance and the EC heat loads can be considered homogeneously distributed along one field free VPS station, while the SR depends on the exact position and the distance from the LHC arcs and magnets.

As for the case of pick-ups, these dedicated calorimeters were built and installed. They are composed of a squared $0.2\ \mathrm{mm}$ thick copper plate, measuring around $30\ mm$ per side. This thin plate is linked to the copper beam pipe through 6 stainless steel ribbons, with much higher conductive resistance. Their dimensions are respectively 0.05 mm in thickness, 5 mm in width and around $10\ \mathrm{mm}$ in length. A VPS calorimeter, installed in a dedicated window carved into the liners, is visible in Figure 36.

The thermal measurements are performed with Resistance Temperature Detectors (RTDs), in particular thin-film PT100, i.e. platinum thermal sensors with $100\ \Omega$ resistance (model: CRZ2005R-100 class A, Hayashi Denko). The PT100 connected with a four-wire circuit was chosen because it provides good accuracy, stability, repeatability for room temperature UHV vacuum systems. Two PT100 were positioned on the calorimeter plate: the first sensor was used for the calibration, while the second one for the measurements. A third sensor was attached to the liner. An additional PT100 was connected to a vacuum chamber flange, in station 4, to control the vacuum chamber temperature, usually between $18\ °C$ and $20\ °C$. The PT100 were fixed to the copper surfaces using a small stainless steel ribbon welded all around. This detail is presented in Figure 37. Kapton cables were used to transmit the current and voltage signals up to the data logger (model: 34970A, Keysight Technologies). In order to calibrate the sensors, a voltage power supply was used (model: EX355, TTi) .

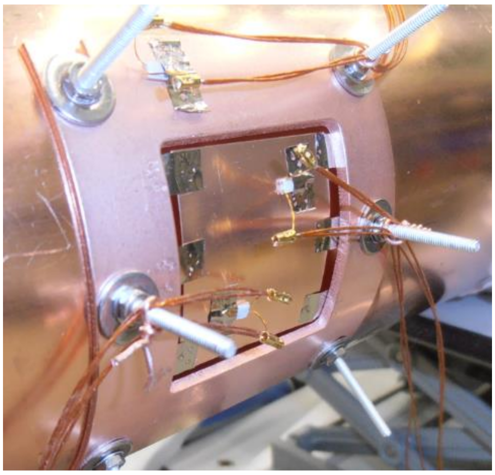

Figure 36: Calorimeter installed in a liner.

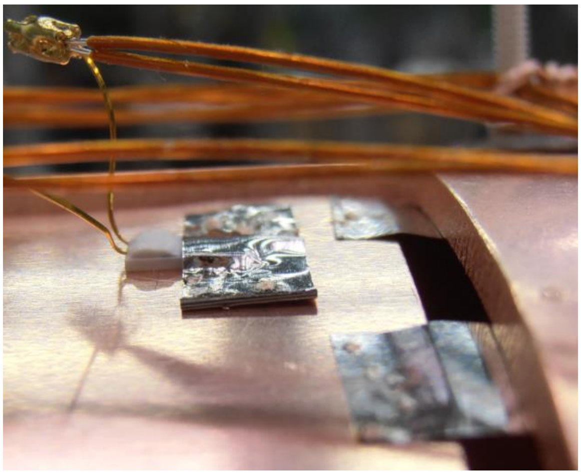

Figure 37: Details on the PT100 connection to the calorimeter.

The PT100 sensors measure different temperatures, as shown in Figure 38. In particular:

- T_{cal} is the temperature of the calorimeter plate.
- $T_{calibration}$ is the equivalent temperature of the PT100 used to calibrate the calorimeter. Its values corresponds to T_{cal}.
- T_{liner} is the temperature of the liner, measured near the calorimeter.
- $T_{chamber}$ is the temperature measured in one of the vacuum chamber flanges.

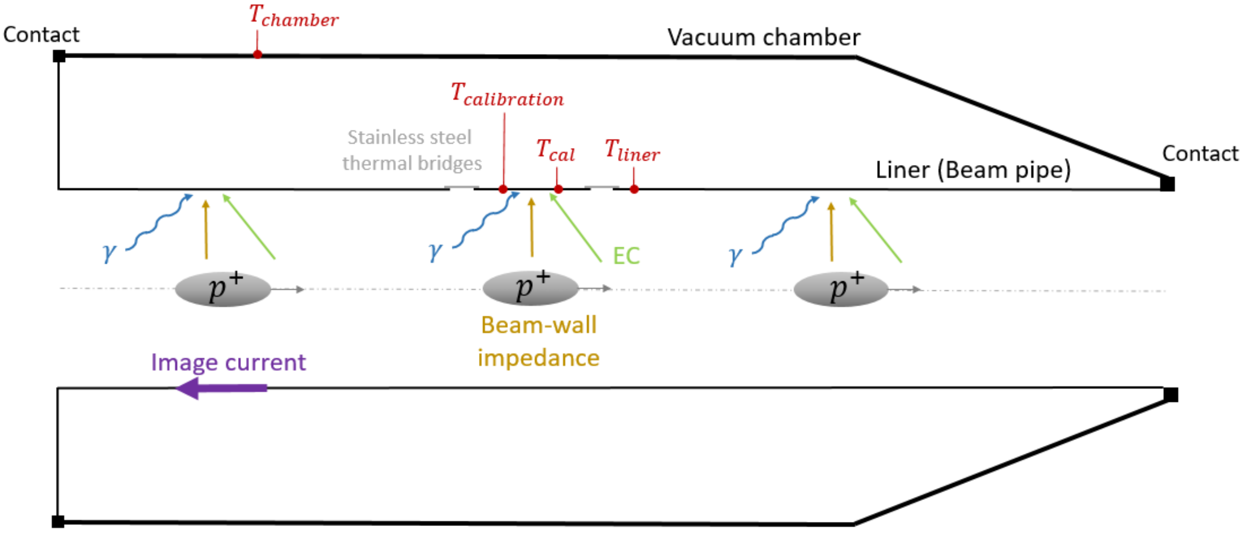

Figure 38: Scheme of the calorimeter installed in a VPS liner.

Under vacuum, the heat loads on the liner, the calorimeter and the stainless links are transferred towards the vacuum chamber by conduction and radiation mechanisms. In order to model the thermal behaviour of the full vacuum system and define its equivalent electrical circuit, each component has to be considered. Analytical calculations, an ANSYS simulation and the relevant calorimeter calibration will be presented in *Chapter 3.2* to define the characteristics of the thermal circuit, i.e. the conduction resistances, R_{cond}, the radiative resistances, R_{rad}, the thermal capacitances, C, and the thermal fluxes, $\dot{Q}$.

Chapter 3 Characterization and performance of the electrical, pressure and thermal devices

Several tests have been performed to validate the measurements acquired by electrical, pressure and thermal devices. In particular, electrical and thermal detectors were homemade and needed different tests to prove their reliability and accuracy.

Firstly, tests were carried on the pick-up circuits with a Vector Network Analyser (VNA) to verify the response and to identify the higher losses and their position (*Chapter 3.1.1*). This study was followed by the influence of grid transparency and electrode bias into the EC measurements (*Chapter 3.1.2* and *Chapter 3.1.3).* These two analyses were important steps to define if the measurement itself strongly perturbed the phenomenon studied and influenced the readings.

Concerning the total pressure measurements, the VPS NEG buffer status was analysed through injections in order to infer the NEG performance with the LHC operation (*Chapter 3.2.1)*. A possible saturation of the NEG buffers would increase the pressure influence between the VPS stations and reduce the accuracy of the EC estimation from pressure readings. Concerning the partial pressure measurements, a Vacuum Quality Monitor (VQM) gas analyser was calibrated in the laboratory to study its limitations in terms of dynamic range and resolution (*Chapter 3.2.2*).

Thirdly, the thermal model of a calorimeter was compared with calibration tests and ANSYS simulation with localised heat load (*Chapter 3.3.1*) and distributed heat load (*Chapter 3.3.2*). A small investigation on the PT100 orientation was carried out in *Chapter 3.3.3.*

3.1 Electrical devices

3.1.1 Power losses along the cablings

The first commissioning test was performed on the pick-up electrical circuit. It concerned the analysis of the reflected signals, through connections and cablings. A Vector Network Analyser (VNA) was used to identify the S11 parameter of the electrical open circuit, also called reflection coefficient or return loss. When the S11 is equal to $0\ dBm$ in an open circuit, all the power is reflected back. The frequency was varied from $10^5\ Hz$ to $2 \cdot 10^9\ Hz$. The goal of this test was to identify the signal losses in the frequency-domain and in the time-domain, from the electronic rack to the detectors. The tested cables are of two types: CK50 coaxial cables linked to the oscilloscope and B50 cables connected to the picoammeter. The circuit layout for oscilloscope and picoammeter are schematized for a normal operation (Figure 39) and during the VNA test (Figure 40). A bias of -9 V was applied to the shielded pick-up, while 9V were applied to the unshielded pick-up circuits. While testing the cablings, the VNA was connected instead of oscilloscope and picoammeter.

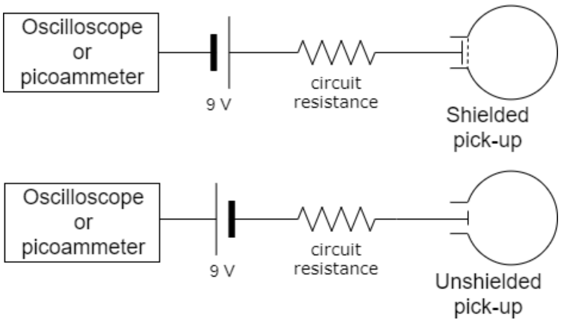

Figure 39: The electrical scheme during the EC and beam measurements acquired with oscilloscopes and picoammeters, linked to shielded and unshielded pick-ups.

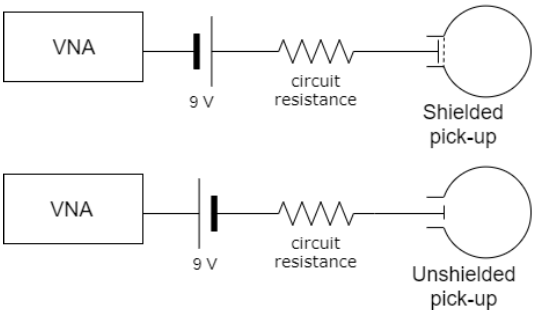

Figure 40: The electrical scheme during the VNA test.

The frequency-domain signals for the CK50 cables are displayed in Figure 41. These cables are used to carry the signals up to the oscilloscopes. The signal amplitude in Y-axis corresponds to S11, the power ratio between the input and the reflected signals, measured in dBm. The signals have a similar behaviour and drop at around $1\ GHz$. The minimum reflected power signal is in the order of $-60\ dBm$, that corresponds to a power ratio of 10^{-6}. This means that the higher the frequency, the higher the losses. Despite these losses at high frequency, this circuit allowed to acquire signals of EC with the oscilloscope and the picoammeter. The EC bandwidth is wide and the higher EC frequency probably exceeds $1\ GHz$, corresponding to 1 ns, i.e. the bunch length. Nevertheless, the bandwidth applied was large enough to detect the main components of the EC signals. The frequency-domain signals for the B50 cables are displayed in Figure 42. These curves show more distributed losses, included between $10^7\ Hz$ and $10^9\ Hz$.

The CK50 cables used for the oscilloscope measurements have lower losses, if compared to the B50 ones. They are coaxial cables with higher transmission quality, therefore more expensive and installed only into the oscilloscopes.

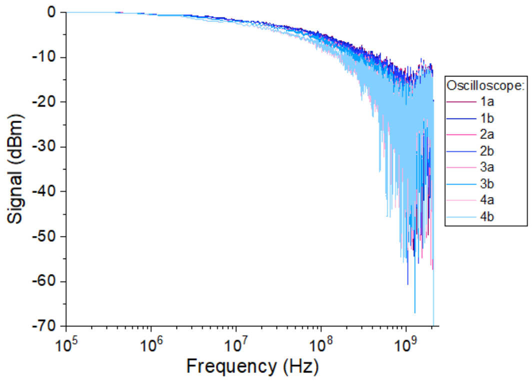

Figure 41: The S11 signals of the oscilloscope channels (CK50 cables) are displayed in the frequency-domain.

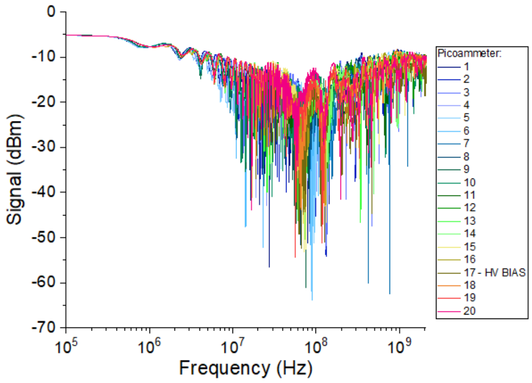

Figure 42: The S11 signals of the picoammeter channels (B50 cables) are displayed in the frequency-domain.

The time-domain signals for the oscilloscope channels during the VNA test on shielded and unshielded pick-ups (see Figure 40) are displayed in Figure 43. A zoom of the signals is presented in Figure 44 and Figure 45 to identify the position of the major losses. They all identify the connections between different cables, mainly attributed to BNC and SMA connectors at different locations along the circuit. In particular, the main connectors are situated at $2\ m, 3\ m, 40\ m, 45\ m\ or\ 46\ m, 48\ m, 53\ m.$

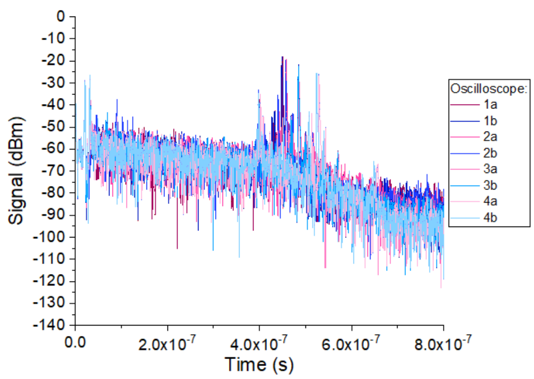

Figure 43: The S11 signals of the oscilloscope channels are displayed in the time-domain.

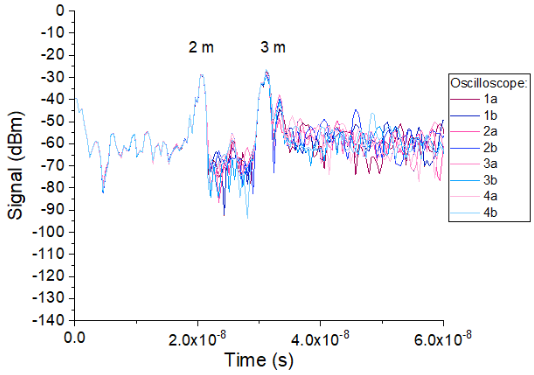

Figure 44: A zoom of the S11 signals of the oscilloscope channels is displayed in the time-domain.

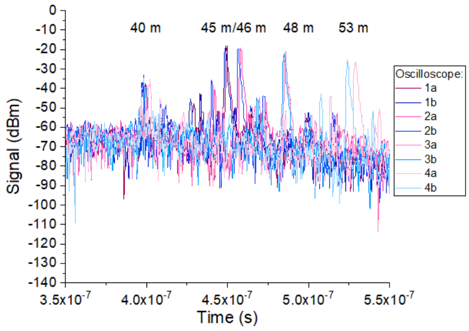

Figure 45: A zoom of the S11 signals of the oscilloscope channels is displayed in the time-domain.

The time-domain signals of the picoammeter channels during the VNA test on shielded and unshielded pick-ups (see Figure 40) are displayed in Figure 46. A zoom of the signals is presented in Figure 47, identifying the major losses at $2\ m$, $3\ m$ and, for the HV bias, at $4\ m$.

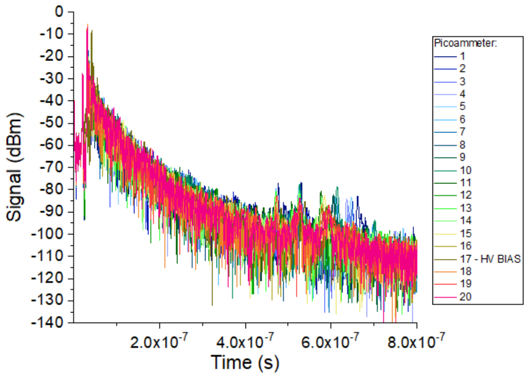

Figure 46: The S11 signals for the picoammeter channels are displayed in the time-domain.

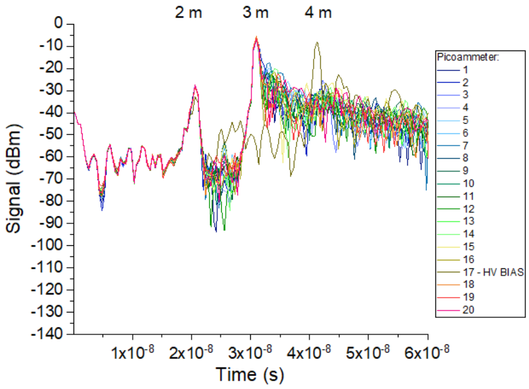

Figure 47: A zoom of the S11 signals for the picoammeter channels are displayed in the time-domain.

In conclusion, these tests studied the losses distribution of two different circuits: the one of the pick-ups connected to the oscilloscope by CK50 cables and the one connected to the picoammeter by B50 cablings. The loss distribution along the circuits is different for the two cablings, therefore the amplitude of the two measurements cannot be directly correlated. It can still give an indication of the EC phenomenon from two different points of view: the fast-time behaviour measured with the oscilloscopes and the integrated signal acquired with picoammeters.

3.1.2 Influence of grid transparency on the measurements

The impact of the grid transparency applied to shield the pick-ups, i.e. the proportion of free passage over the full detector area, has been investigated. The following data are acquired with different beams during 2015 and 2017. In 2015 the 5%, the standard 7% and

10% transparencies were studied, while in 2017 the comparison is between 0.2%, the reference 7%, 15% and 50%. All the holes drilled on the grids have 2 mm diameter, therefore the transparency is only proportional by the number of holes.

Each measurement, as we know, perturbs the studied phenomenon. In theory, the higher the transparency, the more the signal is compromised because a large fraction of the total electrons is extracted and does not sustain anymore the EC phenomenon inside the beam pipe. On the other hand, the lower the transparency, the lower the current signal and the resolution: the signal must be high enough to be detected above the noise signal. Therefore, both cases, i.e. too low or too high transparencies could compromise the reading.

The EC signals recorded for several fills of 2015 are shown in Figure 48 for different transparencies. In order to compare them, the row signals have been normalised to the full transparency, i.e. the signals were divided by the pick-up transparency and multiplied by 100% aperture. Concerning the comparison between 5%, 7% and 10% for a same fill, we can notice that in general the 5% grid underestimates the signal; the 7% and 10% have compatible behaviours.

The EC signals registered in five fills in 2017 are shown in Figure 49. In this case, the transparencies installed were from 0.2% to 50%. One can notice that the 0.2% grid signals are always much above the normalised value registered with the other detectors. This could be attributed to a better measurement with the 0.2% pick-up thanks to a minimum distortion during the measurement. From the other hand, the measurement error becomes very large while amplifying the signal from 0.2% to a 100% transparency. The behaviour of the 50% transparency signals are in line with the estimation of 7% and 15%. Therefore, the 50% grid does not strongly perturb the EC phenomenon inside the beam pipe.

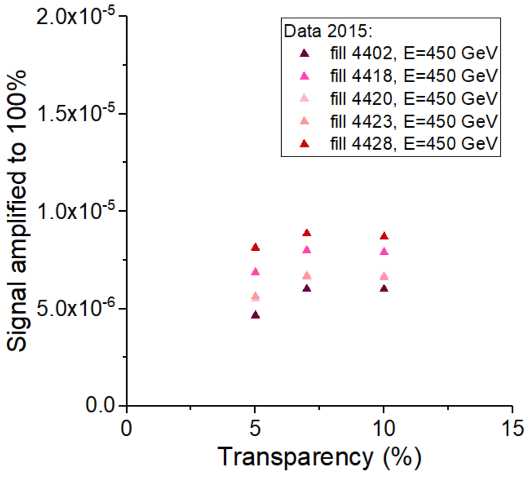

Figure 48: Signal amplified to the 100% grid signal as a function of the transparency increase, in linear scales.

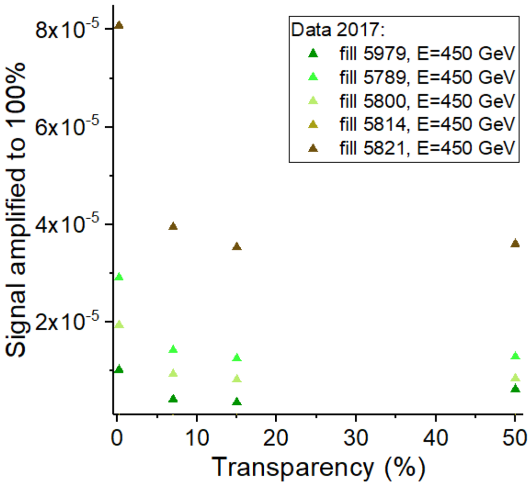

Figure 49: Signal amplified to the 100% grid signal as a function of the transparency increase, in linear scales.

As conclusion, the grid transparency seems not to have too much impact on the measurement, a part from the 0.2% grid case.

3.1.3 BIAS influence on the measurements

A battery of 9 V is applied to the electrode of the shielded pick-ups in order to collect the secondaries generated locally. This value was chosen in order to collect the majority of the low-energy secondaries. It is known from previous studies that the secondaries have an energy below 20 eV [12]. In order to verify that the 9 V bias is a good compromise for good EC measurements, voltage scans were performed on a dedicated 7% grid pick-up, the High Voltage Bias, installed on the blue pipe, on station 4, i.e. Cu surface, during the LHC run from 0 to 130 V. Increasing the bias voltage, it is possible to trap higher energy secondaries and, as consequence, the pick-up current increases. The scan are arbitrarily normalised by the 10 V value, being the nearest to the standard bias (9 V) applied to the shielded pick-ups.

The scans presented concern the fills 4963 to 4965, in 2016, at both 450 GeV and 6.5 TeV (see Figure 50 and Figure 51). The measurements show the normalised current increase as a function of the voltage applied. In particular, Figure 50 shows the abscissa values in logarithmic scale, while Figure 51 is a zoom of the linear behaviour above 10 V. The scans performed at a beam energy of 450 GeV and 6.5 TeV, respectively, follow the same trend.

Looking in details into Figure 50, a voltage decrease from 10 V to 1 V is equivalent to a current reduction of 60%. Therefore, the 60% of the secondaries generated at the electrode has an energy between 1 and 10 eV.

A voltage increase from 10 V to 20 V corresponds to a current rise of around 7% (see Figure 51). A voltage increase from 10 V to 50 V corresponds to a current growth of around 12%. A voltage increase of one order of magnitude, from 10 V to 100 V, corresponds to a current increase of around 17%. This means that the kinetic energy of an important part of the total number of electrons leaving the surface, considering secondary, reflected and back-scattered electrons, is higher than 10 eV. Since the copper work function is around 5 eV, their total energy must be at least equivalent to 15 eV.

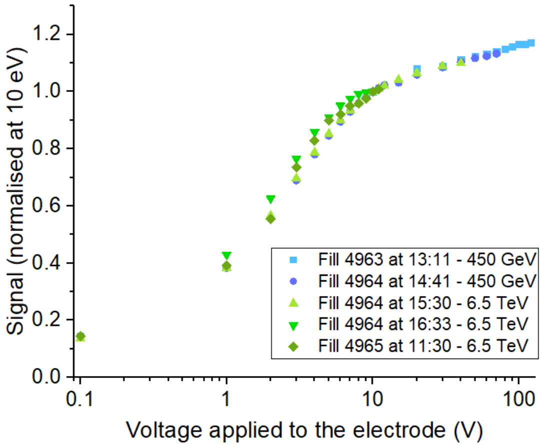

Figure 50: The pick-up signal normalised at 10 eV, as a function of the voltage applied in logarithmic scale.

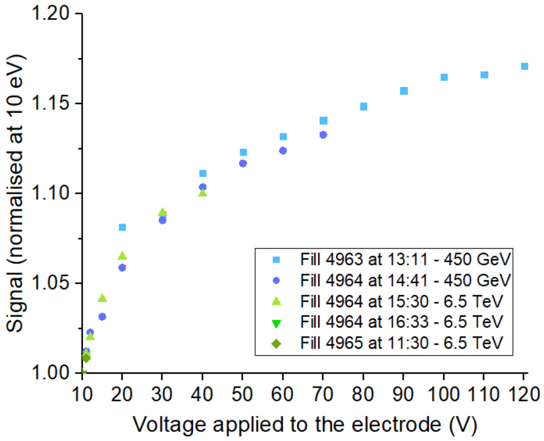

Figure 51: A zoom of the pick-up signal normalised at 10 eV, as a function of the voltage applied in linear scale from 10 to 120 V.

For future LHC and HL-LHC applications and studies, it could be appropriate to increase the voltage applied to the VPS pick-ups in order to grab the total amount of electrons generated at the electrode, including the backscattered and reflected electrons, to a value of 50 V to gain 12% higher signal.

3.2 Pressure devices

Concerning the pressure devices, both the NEG buffers and the gas analysers were characterised. The NEG coated buffers are the main pumping system along VPS, together with NEG cartridges and IP pumps (see Figure 18). Their pumping status along the years is essential to the machine operation and their behaviour was characterised with injection tests, compared with VASCO, a one dimension gas diffusion equation solver, and Monte Carlo simulations and sketched with analytical models. A VQM gas analyser was calibrated in the lab to outline its intrinsic limitations.

3.2.1 NEG buffer performance

The analytical model of the gas interaction with the buffer surface is carried out to describe a standard NEG buffer vacuum performance. This first simplified model, describing only the gas-surface interaction, is the base of the VASCO code (see *Annex 4*), used for vacuum simulations. The parameter that describes the NEG buffer pumping speed is called sticking factor, α, that defines the probability for a certain gas molecule to be trapped by the getter. The standard molecules present in an Ultra-High Vacuum (UHV) system are usually hydrogen, methane, carbon monoxide (CO), carbon dioxide (CO_2) and, in case of an unbaked system, also water (H_2O). Among these gasses, CH_4 is not pumped by NEG, while CO and CO_2 are strongly pumped (α=0.7) if compared to H_2 (α=0.008) [86].

The second model describes the beaming effect, i.e. the gas directly transmitted at the end of a tube without touching the beam pipe walls. An important parameter introduced in this model is the ratio between pipe length and radius, called aspect ratio $\frac{L}{R}$. The radius of all the LHC NEG buffers is constant and equivalent to $40\ mm$. This study was performed changing the standard buffer length from $0.4\ m$ to $14\ m$, therefore, with an aspect ratio included between 10 and 350. The VPS buffers are equivalent to an aspect ratio of 42.5. This effect is not considered into VASCO code, while it is taken into account by Monte Carlo simulations.

Due to this intrinsic VASCO limitation, the results of the first code are compared with a Monte Carlo code. This comparison allows to correct VASCO that does not consider the direct transmission of the gas to the end of the tube. A new VASCO input parameter is therefore specified, α_{VASCO}, to take into account this additional effect, in order to use VASCO and get meaningful results that includes the beaming effect. This comparison study was performed for different beam pipes dimensions, in order to determine the input α_{VASCO} for any standard LHC NEG pipe.

The second part of this section consists on the data analysis of gas injections performed in the VPS system in order to cross check the pumping status of the NEG buffers and the pressure influence between stations. The gas injections were carried out heating up one NEG cartridge, already installed in the VPS, using it as source of gas. In this case, no vacuum intervention was required and the injections could be performed faster, in an easier way, just before the beginning of the LHC run and right after the end of the beam operation.

Among the different injections, I selected the last two tests performed with NEG cartridges, precisely before and after the LHC run 2017 (March and December 2017). They are representative of the last VPS layout and configuration, where a total of 16 NEG cartridges were installed, one per side of each station. The first NEG cartridge from the left was used as source of gas for the example reported below. The data of March and December are analysed and compared considering both the total pressure measured with BAG and Penning gauges and the partial pressures acquired with the VQM gas spectrometer.

- **Analytical model for the gas interaction with the buffer**

As mentioned above, VASCO consider only the gas interaction with the beam pipe tube, ignoring the direct gas transmission at the end of the tube. The VASCO model calculates the steady-state pressure profile, as defined in *Annex 4*. It considers the equilibrium of beam pipe thermal outgassing, localised and distributed pumping, electron and ion activities at the wall that release gas molecules. The analytical model for a beam pipe is presented in the following figure. The finite element method is applied, considering small elements with outgassing rate Adx and distributed pumping speed $TPdx$. These gas fluxes add to an existing gas flow, q, simulating an injection.

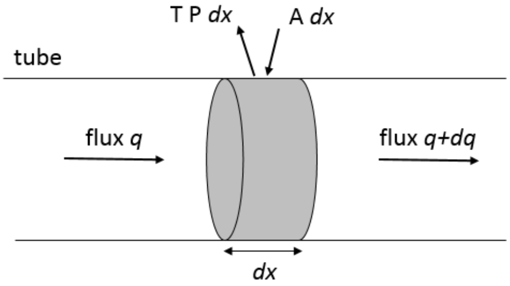

Figure 52: Pressure model for a distributed pumping.

The contribution to the gas flow is expressed by dq, as following:

$$dq = [A - T\,P(x)]\,dx \tag{51}$$

Consider a conductance per meter of vacuum chamber, C/dx, and a pressure difference, dp. The gas flow becomes:

$$q = \frac{C}{dx}\,dp \tag{52}$$

Deriving this flow, the previous equation becomes:

$$\frac{dq}{dx} = -C\frac{d^2p}{dx^2} \tag{53}$$

Therefore, from Eq.(51) and Eq. (53) we get the following differential equation:

$$C\frac{d^2p}{dx^2} = T\,P(x) - A \tag{54}$$

Its solution is described by:

$$p(x) = P_\infty + k_1e^{\omega x} + k_2e^{-\omega x} \tag{55}$$

With:

$$\omega = \sqrt{\frac{T}{C'}} \tag{56}$$

$$P_\infty = \frac{A}{T} = 0 \tag{57}$$

Consider the case of an activated NEG buffer: $p(0)$ is the pressure reached in the injection point during gas injection, the vacuum components outgassing A can be considered zero, and therefore the pressure at the end extremity is $P_\infty = 0$. The pumping speed per meter of buffer, T, is given by the sticking coefficient α, the tube surface $S\ [cm^2]$ and the conductance of an surface C'', expressed in $\left[\frac{l}{s \cdot cm^2}\right]$, divided by the buffer lenght:

$$T = \frac{\alpha\, S\, C''}{L} = \alpha\ 2\pi RL\ \frac{C''}{L} = \alpha\ 2\pi R\ C'' = \alpha\ 2\pi R \sqrt{\frac{R_{gas} \cdot Temp}{2\pi\ M}} \qquad \left[\frac{l}{s \cdot cm}\right] \tag{58}$$

This parameter is linearly proportional to the radius. Instead, the beam pipe conductance per meter of chamber, C', is equivalent to:

$$C' = C \cdot L = \frac{1}{6}\sqrt{\frac{2\pi k \cdot Temp}{m}}\ \frac{D^3}{L} \cdot L \approx 3.81 \sqrt{\frac{Temp}{m}} D^3 \qquad \left[\frac{l}{s} \cdot cm\right] \tag{59}$$

For the VPS buffers, ω is proportional to the cube of the radius and to the temperature-to-mass ratio:

$$\omega = \sqrt{\frac{T}{C'}} = \sqrt{\frac{\alpha\ 2\pi R \sqrt{\frac{R_{gas} \cdot Temp}{2\pi\ M}}}{\frac{1}{6}\sqrt{\frac{2\pi k\, Temp}{m}} \frac{d^3}{L} L}} = \sqrt{\frac{\alpha\ 2\pi R \sqrt{\frac{R_{gas}}{2\pi}} \cdot \sqrt{\frac{Temp}{M}}}{\frac{1}{6}\sqrt{2\pi\ R_{gas}} \cdot \sqrt{\frac{Temp}{M}}\, d^3}} = \sqrt{\frac{3\,\alpha}{4\,R^2}} \qquad \left[\frac{1}{cm}\right] \tag{60}$$

Note that ω is not related to the beam pipe length. It is just linked to α and to the beam pipe radius R for this case study. Let consider an outgassing A, therefore there is a certain minimum pressure reached by the system, P_∞. In order to determine the constant $k_1$and k_2, I have to define boundary conditions. The minimum pressure is reached in $x = L$, where $p(L) = P_\infty$ in $x = L$. The minimum pressure is described by a zero-derivative:

$$\left.\frac{dp}{dx}\right|_{x=L} = \omega\ k_1 e^{\omega L} - \omega\ k_2 e^{-\omega L} = 0 \tag{61}$$

Therefore:

$$k_2 = k_1 e^{2\omega L} \tag{62}$$

Applying it to the pressure value $p(L) = P_L$, I get:

$$P_L = p(L) = k_1\ (e^{\omega L} + e^{-\omega L} e^{2\omega L}) = k_1\ \left(e^{\omega L} + e^{-2\omega^2 L^2}\right) \tag{63}$$

The pressure value in $x = 0$ becomes:

$$P_0 = p(0) = k_1\ (e^{\omega 0} + e^{-\omega 0} e^{2\omega L}) = k_1\ (1 + e^{2\omega L}) \tag{64}$$

So:

$$k_1 = \frac{P_0}{(1 + e^{2\omega L})} \tag{65}$$

Setting the maximum pressure reached, P_0, the equation is defined. The final solution of the differential equation becomes:

$$p(x) = \frac{P_0}{(1+e^{2\omega L})}\left(e^{\omega x} + e^{-2\omega^2 L\, x}\right) \tag{66}$$

The so-called transmission rate $P_{transmission}$ is defined as the pressure ratio between the injection and the extremity of the tube:

$$P_{trasmission} = \frac{p(0)}{p(L)} = \frac{1+e^{2\omega L}}{e^{\omega L} + e^{-2\omega^2 L^2}} \tag{67}$$

It describes the pressure ratio between entrance and the end of the tube, as represented in Figure 53, by the above-mentioned analytical model and by VASCO simulations. The analytical model and the computation match and I reconstructed what VASCO does.

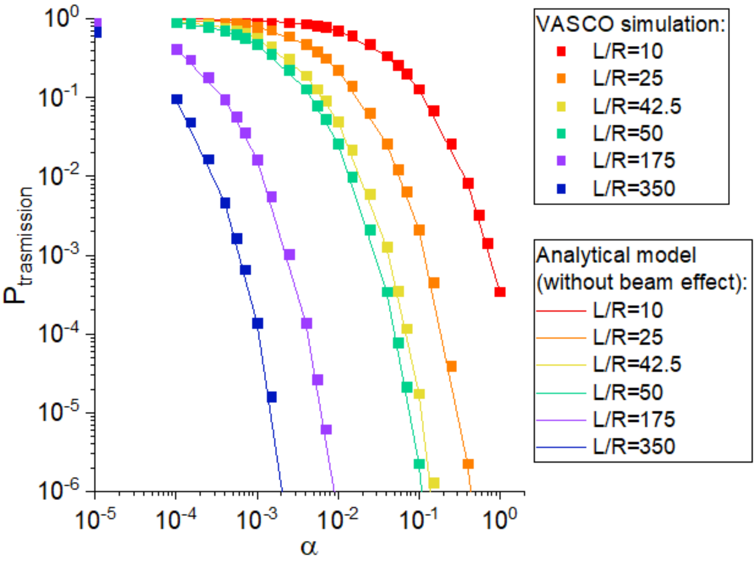

Figure 53: The analytical model implemented and the VASCO simulation are compared for different aspect ratios and sticking probabilities.

This analytical model described in this paragraph does not consider the beaming effect. In the next paragraph, the beaming effect will be estimated and compared with the Monte Carlo simulations.

- **Analytical model for the beaming effect**

Consider a NEG buffer (see Figure 54). A gas molecule entering the buffer has a small change to go through without interacting with the beam pipe, known as beaming effect. In order to calculate this probability, the apex angle ϑ and the solid angle Ω need to be calculated. At first approximation, let consider a homogenous distribution of molecule directions.

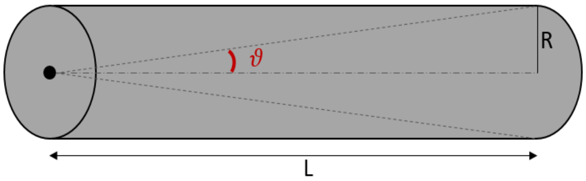

Figure 54: A gas molecule entering the buffer in the centre has a probability P_{center} to cross the chamber without interacting with it, proportional to the solid angle Ω and the apex angle ϑ, considering a homogenous distribution of molecule directions.

The apex angle ϑ is given by:

$$\vartheta = \arctan\left(\frac{R}{L}\right) \tag{68}$$

The cone solid angle Ω is:

$$\Omega = 2\pi\,(1-\cos\vartheta) \tag{69}$$

For a VPS buffer with $r = 0.04\,m$ and $L = 1.7\,m$, these angles correspond to $\vartheta_{dt} = 1.35° = 0.024\,rad$ and $\Omega_{\mathrm{dt}} = 0.00174\,sr$. Knowing that the solid angle of an half sphere in the direction of the flow is $\Omega_{\text{half sphere}} = 2\pi$, I can calculate the beaming effect probability, P_{center}through a geometrical ratio, when a gas molecule is injected at the center of the beam pipe:

$$P_{center} = \frac{\Omega}{\Omega_{\text{half sphere}}} = \frac{2\pi\,(1-\cos\vartheta)}{2\pi} = (1-\cos\vartheta) \tag{70}$$

For a VPS buffer geometry, $\mathrm{P_{center}} = 0.014\%$. This would mean that around a molecule every 7000 molecules is not touching the beam pipe, while is directly transmitted at the end of the 1.7 m buffer.

Consider the same model of a NEG buffer where the molecule enters the beam pipe close the wall (see Figure 55). At first approximation, let consider a homogenous distribution of molecule directions.

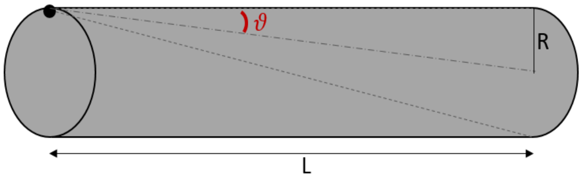

Figure 55: A gas molecule entering the buffer near the wall has a probability P_{wall} to cross the chamber without interacting with it, proportional to the solid angle Ω and the apex angle ϑ.

The transmission probability, P_{wall}, is given by:

$$\mathrm{P}_{wall} = \frac{\Omega}{\Omega_{\frac{1}{4}\text{sphere}}} = \frac{2\pi\,(1-\cos\vartheta)}{\pi} = 2(1-\cos\vartheta) \tag{71}$$

These two simplified formulas, P_{center} and P_{wall}, consider the particle velocity directed according to a homogenous distribution.

In order to consider a more realistic behaviour, the cosine law for the velocity direction needs to be implemented. This description was carried out by G. Smith and G. Lewin [87]. The beaming probability is described by:

$$\mathrm{P}_{\mathrm{B}_{\text{Smith \& Lewin}}} = 1 - \frac{L}{R}\left\{\left[\left(\frac{L}{2R}\right)^2 + 1\right]^{\frac{1}{2}} - \frac{L}{R}\right\} \tag{72}$$

This solution is derived from a general expression for the probability that a particle enters within the elementary solid angle $d\omega$, and ϑ and φ the polar and azimuthal angles:

$$\mathrm{P}_{\mathrm{B}_{\text{general}}} = \int_{\Omega} p\,d\omega \tag{73}$$

Performing the integral, I obtain that the solution can be written as:

$$\mathrm{P}_{\mathrm{B}_{\text{general}}} = \int_0^{\vartheta}\int_0^{2\pi} \frac{1}{\pi}\cdot\cos\vartheta\cdot sin\,\vartheta\cdot d\vartheta\cdot d\varphi = \int_0^{\vartheta} 2\cdot\cos\vartheta\cdot sin\,\vartheta\cdot d\vartheta = sin^2\,\vartheta \tag{74}$$

For small angles: $\sin\vartheta \approx \vartheta$, $\cos\vartheta \approx 1 - \frac{\vartheta^2}{2}$, and $\vartheta = \arctan\left(\frac{R}{L}\right) \approx \frac{R}{L}$, I can approximate:

$$P_{B_{\text{general}}} = \sin^2\vartheta \approx \vartheta^2 \approx 2(1-\cos\vartheta) \approx \left(\frac{R}{L}\right)^2 \tag{75}$$

These approximated formulas are valid for aspect ratios included between $0.1 < \frac{L}{R} < 10^5$. This is reasonable, being a single LHC beam pipe included between cm and km.

I can compare this calculation with the Monte Carlo computation for $\alpha = 1$, where the transmission probability is due only to the beaming effect, because all the gas touching the beam pipe is pumped by the NEG coating (see Figure 56). The beaming effect computation matches the Monte Carlo simulations for all the aspect ratios.

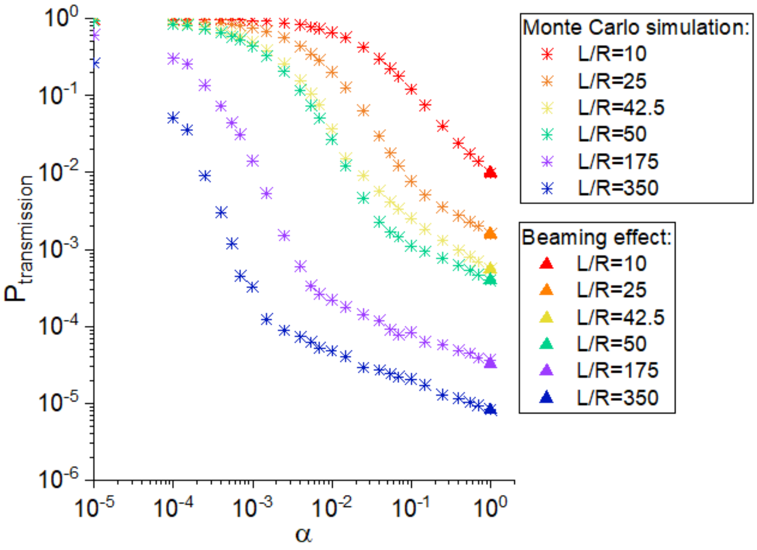

Figure 56: The transmission probability as a function of sticking factor and aspect ratio with Monte Carlo code is compared to the pure beaming effect, detectable at $\alpha = 1$.

- **VASCO vs Monte Carlo simulations**

VASCO code has an intrinsic limitation because it doesn't consider the beaming effect. This has a big impact mainly for high sticking factors in the case of VPS buffers. In order to understand the limitations of VASCO, I compare its results with a Monte Carlo simulation code, provided by a colleague of the vacuum group.

For low α the transmission probability tends to one, case in which the pressure is homogenously distributed along the buffer because no localised pump is installed in this case study. For high α the gas transmission probability tends to smaller values because the gas is mainly pumped by the distributed pumping surface. For long tubes. i.e. high aspect ratios, the chance for gas molecules to reach the end of the tube is reduced. The VASCO computations match the Monte Carlo ones for low α, because VASCO does not consider the above-mentioned beaming effect (see Figure 57). For an aspect ratio of 42.5, as for VPS, the beaming effect has an impact for gasses with $\alpha > 0.01$, i.e for molecules other than H_2 and CH_4.

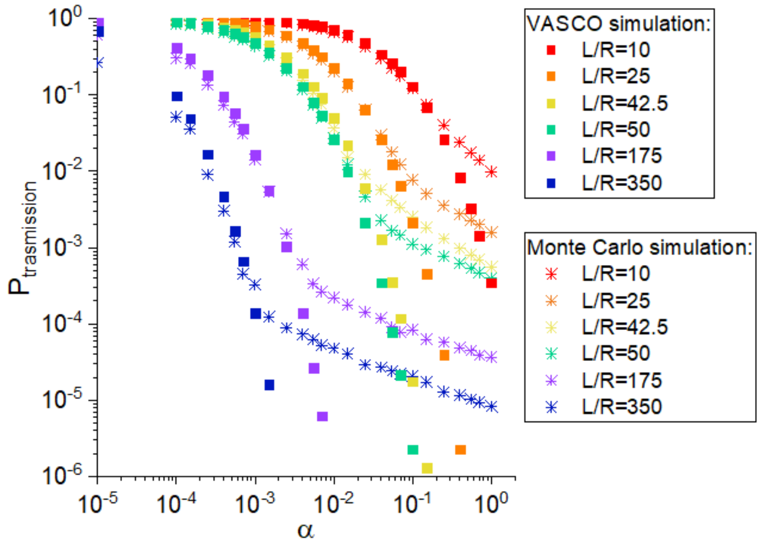

Figure 57: Transmission probability, $P_{transmission}$, between the extremities of a buffer as a function of the sticking factor, α, and the buffer aspect ratio, $\frac{L}{R}$.

Due to its simplicity of use, the VASCO code is still used among the vacuum group but it is needed to correct this wrong behaviour to continue to use it properly. The following plot relates the input for VASCO, α_{VASCO}, with the real α, input for Molflow+ (see Figure 58) in order to consider the beaming effect. For a VPS station, α_{VASCO} is correct below 0.01. This limitation has to be taken into account while simulating gas with high sticking coefficients, as CO and CO_2. A zoom of the curve valid for the VPS geometry is presented below in linear scale (see Figure 59).

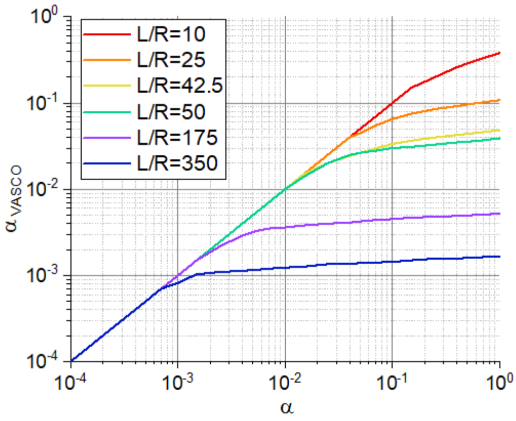

Figure 58: Input sticking factor for VASCO, α_{VASCO}, as a function off the real surface sticking factor, α, and aspect ratio $\frac{L}{R}$ (logarithmic scales).

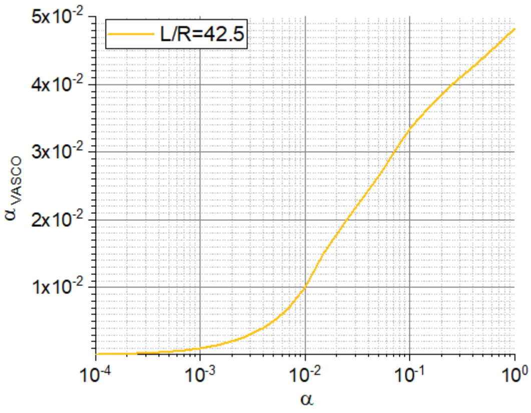

Figure 59: Input sticking factor for VASCO, α_{VASCO}, as a function off the real surface sticking factor, α, for the VPS case ($\frac{L}{R} = 42..5$). The Y-axis is expressed in linear scale.

For CO and CO_2 the standard NEG sticking factor is around $\alpha \approx 0.7$. Their input for the VPS simulation in VASCO corresponds to $\alpha_{VASCO} \approx 0.046$ (see Figure 59). It is clear that a small error on the estimation of the pressure increase ratio generates a big error on α and, therefore, on α_{VASCO}.

- **Pressure profile during a NEG cartridge injection before the LHC run 2017: hydrogen transmission**

The first injection presented is the one performed in March 2017, on the left side of station 1 and on the external beam pipe. The following figure shows the pressure increase, i.e. total pressure measured during injection without the reference pressure registered before injection, as a function of the position along VPS. Both Penning gauges and BAG gauges are displayed. The BAG gauges are positioned in the centre of each station and an additional one is placed in the centre of the full system (right side of station 2, see Figure 18). The position along VPS of the four stations corresponds to 3 m, 7 m, 11 m and 15 m, respectively. The gas is injected at the left side of the first station, where the second Penning gauge is installed. The injection point corresponds to the highest pressure reading. The gas is then transmitted and pumped by the IP pumps, the NEG cartridges and the NEG buffers. As displayed in Figure 60, the pressure measured at the right extremity is more than three orders of magnitude lower than the maximum one. A pressure difference of one order of magnitude is registered between station no. 1 (positioned at 3 m) and station no. 2 (at 7 m), and between each couple of adjacent stations.

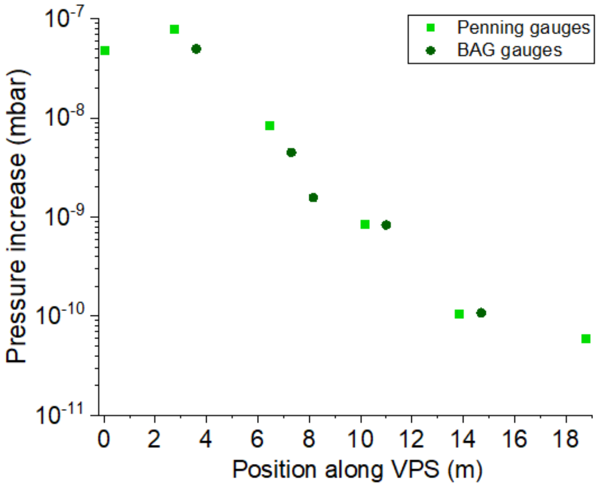

Figure 60: The pressure increase is displayed along VPS during the NEG cartridge injection performed in March 2017.

In addition to the total pressure measurement, the gas analysers were used to measure the gas spectra at station 1, 2 and 4. The following VQM spectra display the signal as a function of the atomic mass unit (amu). During these initial measurements, the reference spectra were not recorded before each injection. Due to the limitations of the instrument, the background drifted, therefore it is not possible to directly subtract the reference spectrum from the injection spectrum for this first batch of measurements.

The first plot (see Figure 61) shows the spectra acquired at the first station, before and during injection. The vacuum pressure during injection, using NEG cartridge heating, is dominated by mass 2 (H_2), followed by a small increase of masses 28 (CO) and 16 (CH_4). The peak 44 (CO_2) is almost constant. These gasses were released by the conditioning of the NEG cartridge and its metallic body.

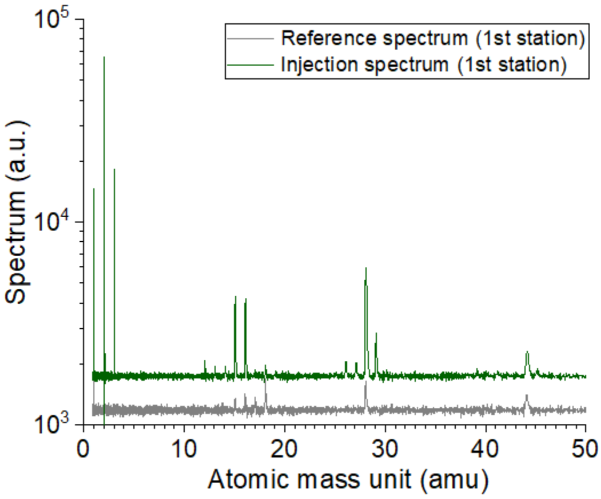

Figure 61: The injection and reference gas spectra performed in March 2017 are displayed in green and grey, respectively, for the first station.

Figure 62 shows the spectra acquired at the second station located downstream to the gas injection. From the total pressure gauges (see Figure 60), a pressure reduction of a factor 10 is measured at the second station (positioned at around 7 m) from the first one (positioned at around 3 m). This pressure ratio is in line with VASCO and Monte Carlo simulations for a 0.7%

sticking factor gas, such as H_2, in excellent agreement with literature data, showing that the buffer is still fully activated The vacuum is, in fact, dominated by hydrogen, followed by methane and carbon monoxide.

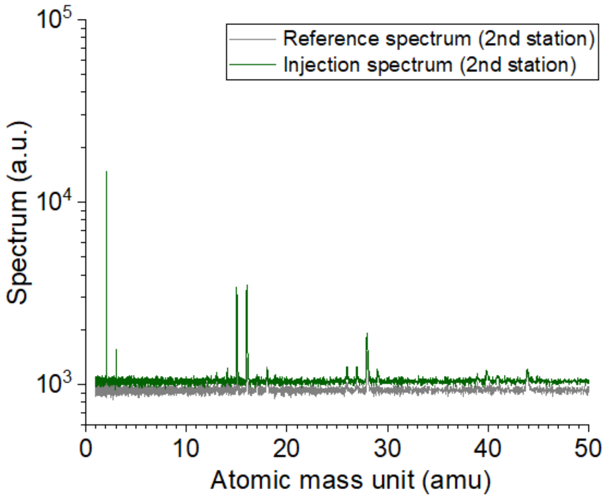

Figure 62: The injection and reference gas spectra performed in March 2017 are displayed for the second station.

In Figure 63 the zoom on the hydrogen peak is displayed. Methane slightly increases (see Figure 64), while carbon monoxide and dioxide are almost constant.

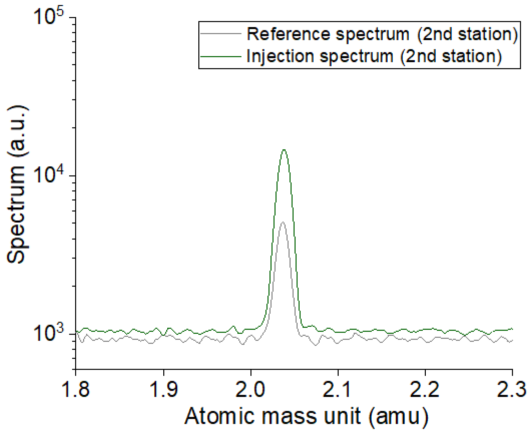

Figure 63: A zoom on mass 2, H_2, is displayed for both injection and reference spectra.

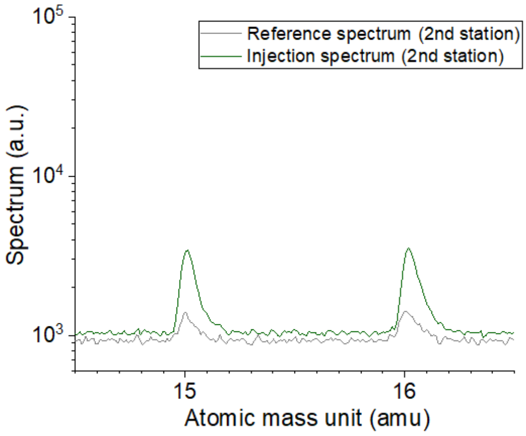

Figure 64: A zoom on masses 15 and 16, signals for CH_4, is displayed for both injection and reference spectra.

Figure 65 shows the spectra acquired at the fourth station. The total pressure reduced of a factor 500 if compared to the first station (see Figure 60). The vacuum is now dominated by hydrogen and methane increase.

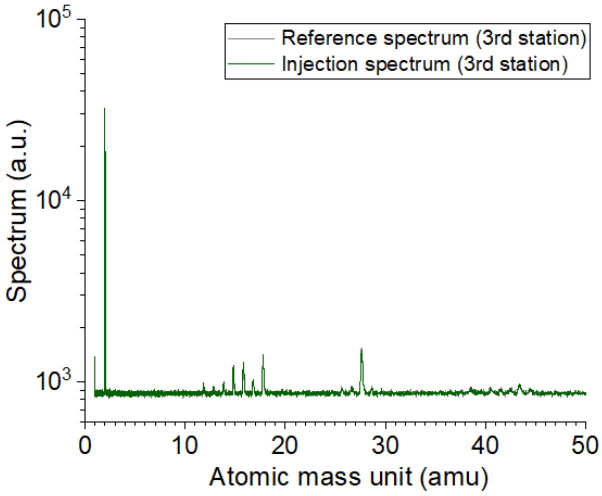

Figure 65: The injection and reference gas spectra performed in March 2017 are displayed for the fourth station.

Hydrogen and methane signals are increasing (see Figure 66 and Figure 67). No evident increase of carbon monoxide or dioxide is present.

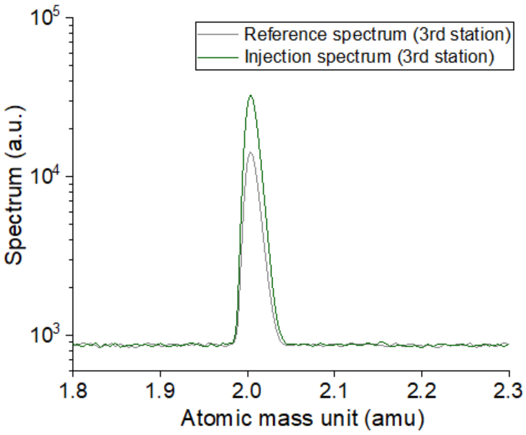

Figure 66: A zoom on mass 2, H_2, is displayed for both injection and reference spectra.

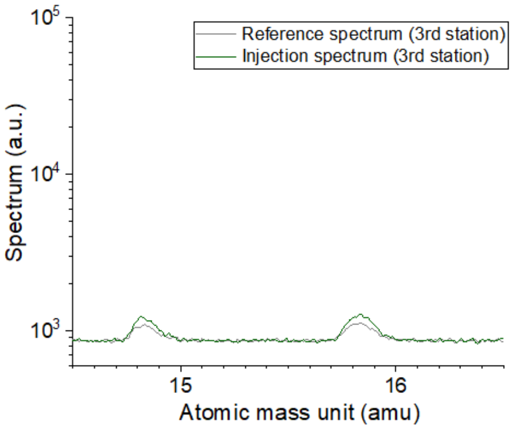

Figure 67: A zoom on masses 15 and 16, signals for CH_4, is displayed for both injection and reference spectra.

In summary, the injection can be considered as hydrogen dominated near the injection point (station 1). Far from the injection point (station 4), only an increase of hydrogen and methane is measured. Methane, in fact, is not pumped by NEG cartridges and buffers, and it can diffuse long distances in vacuum.

This injection was useful to study the hydrogen transmission between stations and to compare it with simulations (see Figure 57). The standard hydrogen sticking factor used to evaluate the pumping speed of NEG buffers, i.e. 0.7%, can explain a pressure ration of 10 between station 1 and 2.

- **Pressure profile during a NEG cartridge injection at the end of the LHC run 2017: influence of methane**

The second injection presented was performed in December 2017, at the same position along VPS. The following figure shows the pressure increase, as a function of the position along VPS. The maximum pressure reached in this case is much lower than the previous injection. This can be attributed to the variation of the input current of the power supply from 4 to 3 A. This has an effect of the quantity of gas released as well. As for the previous case, the pressure reached at the right extremity is three orders of magnitude lower, after a year of LHC operation.

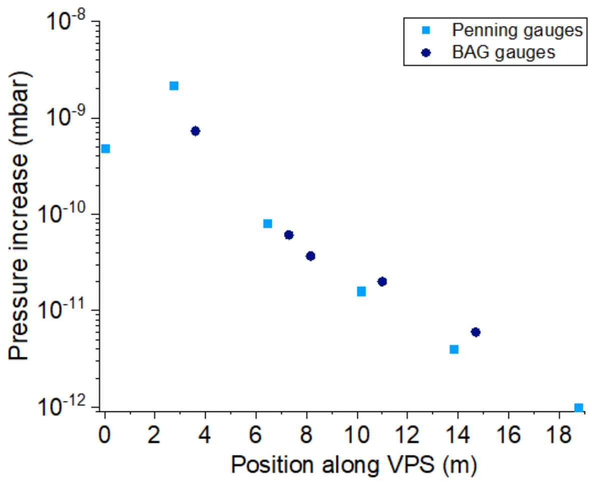

Figure 68: The pressure increase is displayed along VPS during the NEG cartridge injection performed in December 2017.

In this case, the reference spectra were acquired before each injection, leading to a much proper analysis. The first plot (Figure 69) shows the reference and injection spectra acquired at the first station. The gas injection corresponds to a mixture of CO, H_2, CH_4 and CO_2.

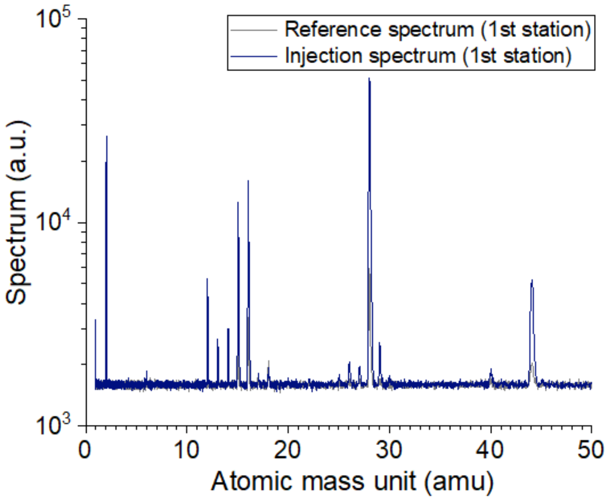

Figure 69: The injection and reference gas spectra performed in December 2017 are displayed for the first station.

The gas mix injected is visible on the four following plots.

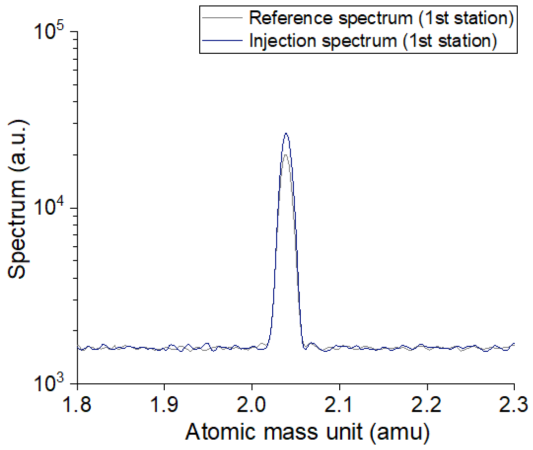

Figure 70: A zoom on mass 2, H_2, is displayed for both injection and reference spectra.

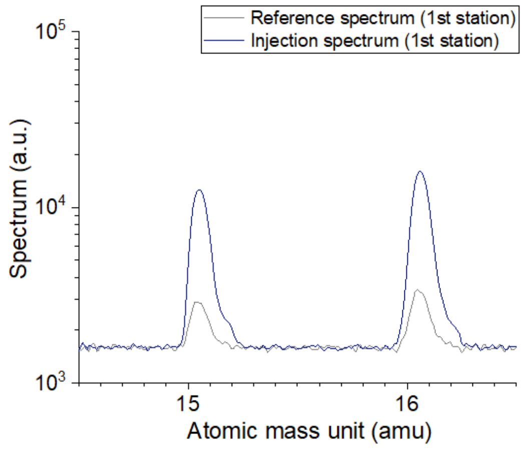

Figure 71: A zoom on masses 15 and 16, signals for CH_4, is displayed for both injection and reference spectra

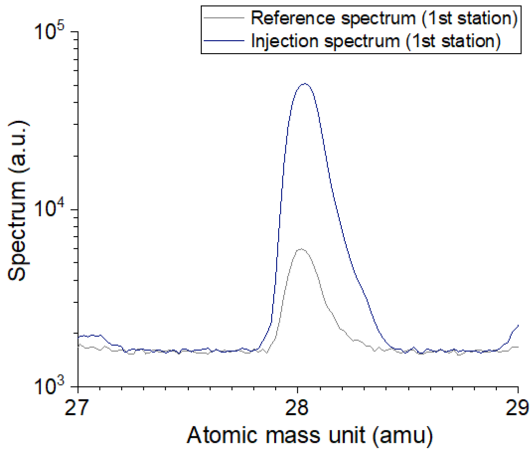

Figure 72: A zoom on mass 28, CO, is displayed for both injection and reference spectra.

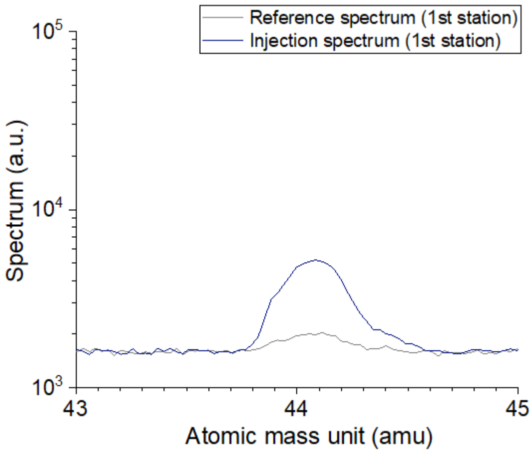

Figure 73: A zoom on mass 44, CO_2, is displayed for both injection and reference spectra.

Figure 74 shows the spectra acquired at the second station. The total pressure reduced of a factor 10 if compared to the first station (see Figure 68). The vacuum is dominated by hydrogen, methane and carbon monoxide.

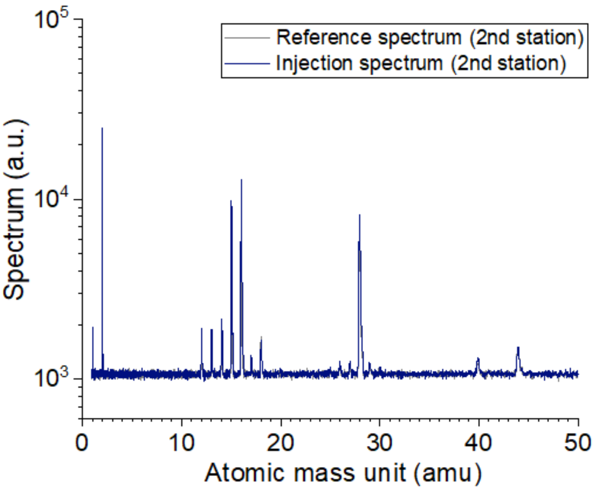

Figure 74: The injection and reference gas spectra performed in December 2017 are displayed for the second station.

The zooms (see Figure 75, Figure 76 and Figure 77) confirm the transmission of mass 2, 16 and 28 into the second station.

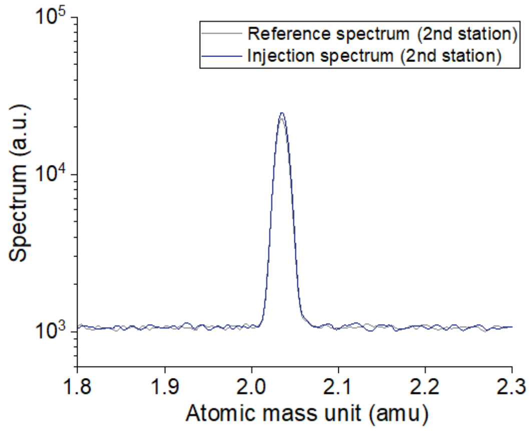

Figure 75: A zoom on mass 2, H_2, is displayed for both injection and reference spectra.

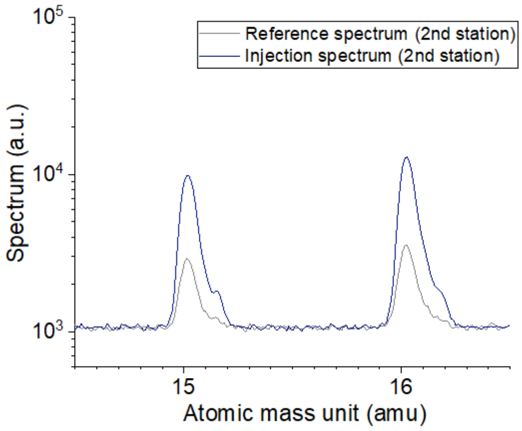

Figure 76: A zoom on masses 15 and 16, signals for CH_4, is displayed for both injection and reference spectra.

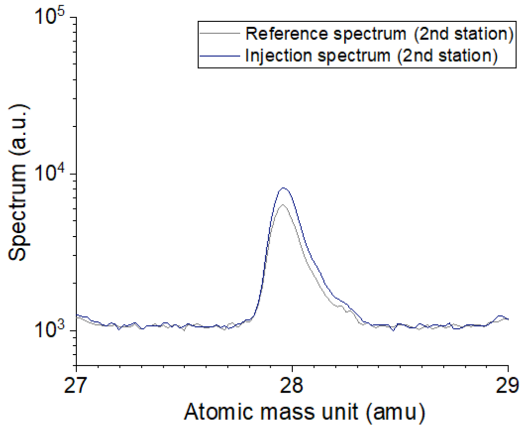

Figure 77: A zoom on mass 28, CO, is displayed for both injection and reference spectra.

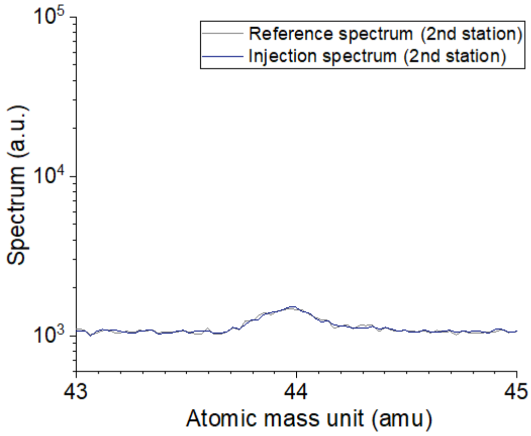

Figure 78: A zoom on mass 44, CO_2, is displayed for both injection and reference spectra.

Figure 79 shows the spectra acquired at the fourth station. The total pressure reduced of a factor 100 if compared to the first station (see Figure 68).

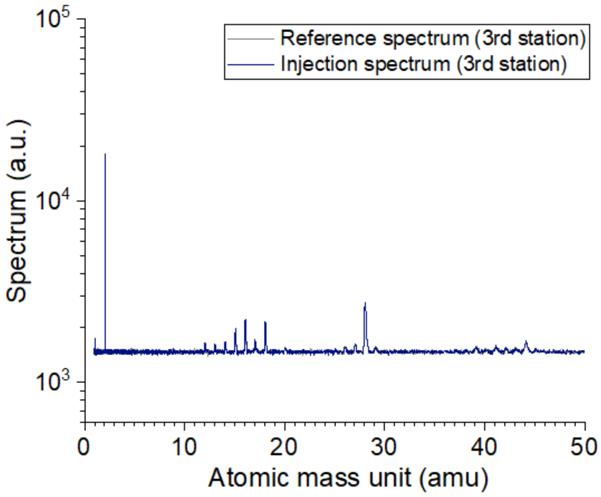

Figure 79: The injection and reference gas spectra performed in December 2017 are displayed for the third station.

The small pressure increase at the fourth station is now only dominated by methane (Figure 80).

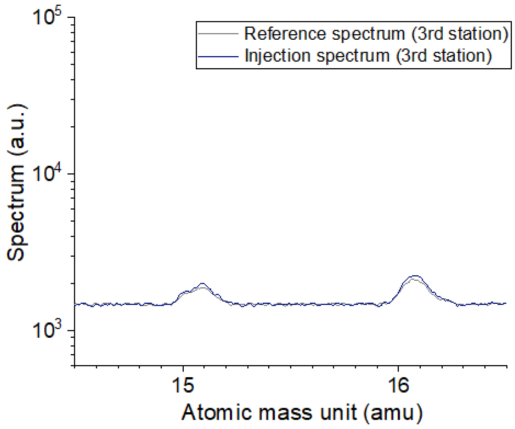

Figure 80: A zoom on masses 15 and 16, signals for CH_4, is displayed for both injection and reference spectra.

In summary, the injection can be considered as hydrogen dominated near the injection point (station 1). Far from the injection point (station 4), only methane is transmitted.

This injection was useful to study the methane influence between stations, in particular between station 2, 3 and 4. The methane transmission is driven by conductance limitations, not being pumped by NEG.

The total pressure ratios measured between station 2 and 3 and between station 3 and 4 is around 3, i.e. a transmission probability of 0.3. A VASCO simulation is carried to cross check that this pressure ratio is linked only to the conductance of the beam pipe and the IP pumping speed. For simplicity, I consider a two-station configuration with a pure methane flux of $1 \cdot 10^{-6}\ mbar\frac{l}{s}$ situated on the left side of the left station and a methane pumping speed of $20\ l/s$ per IP. The pressure ratio between the middle of the first station (at 3 m) and the middle of the second station (at 3.5 m) is exactly 3 (see Figure 81). This confirms that gasses not pumped by NEG easily influence the nearby stations, as CH_4.

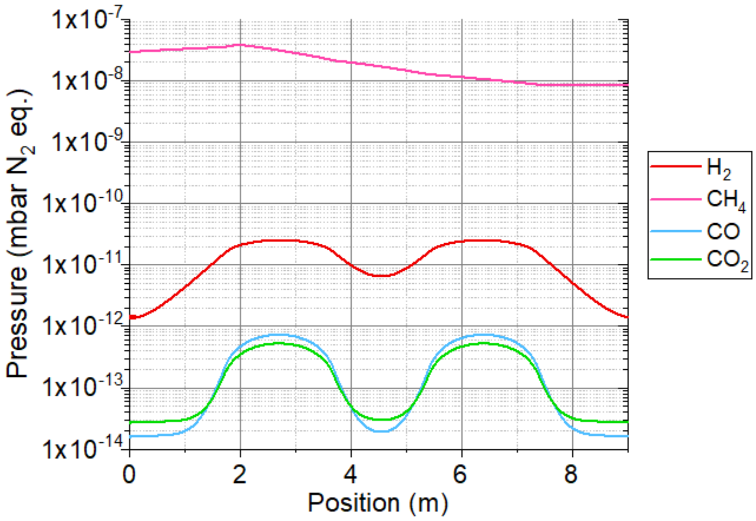

Figure 81: Simulated pressure profile along two stations of VPS, separated with 3 buffers, during a CH_4 injection localised on the left side of the first station.

The gas transmission of methane between stations have been validated by a VASCO simulation. One can consider that a pressure ratio of 3 between near stations can be attributed to pure methane transmission, when a big outgassing occurs in one station.

- **Comparison of the NEG cartridge injections**

Consider the pressure ratio between station 1 and 2, for the two injections. The gas transmitted to the second station was dominated by hydrogen in March, while by a mix of gasses in December. The pressure ratio is around 8-9 for these two cases, as displayed in Figure 60 and Figure 68. This means that the pressure on station 2 is around 11-13% of the pressure reading in station 1 due to the gas transmission, no matter if it is pure hydrogen or a mix of NEG-pumped gasses.

Consider the gas flowing from the second to the third and fourth stations. In this case the gas transmitted was mainly hydrogen and methane in March, while pure methane in December. In this last case, the pressure ratio due to a pure methane transmission is around 3.

In conclusion, one can consider that a pressure ratio between near stations of 10 or 3 can be attributed to hydrogen and methane transmission, respectively. This gas influence explains the pressure reading of a-C surface (station 2) dominated by gas desorption coming from the nearby Cu station (station 3), that will be analysed in *Chapter 4.2*.

3.2.2 GAS analyser calibration

A VQM gas analyser was tested in the laboratory to study its behaviour and compare it with a standard quadrupole mass spectrometer Residual Gas Analyser (RGA). First, I started studying the influence of small changes in the main VQM parameters, as voltage bias (V), filament current (mA) and repeller bias (V). After, I compared a reference VQM spectrum to a standard RGA one, to focus on the VQM limitations concerning qualitative and quantitative gas estimations. The last study presents a VQM signal saturation during injection. In fact, the VQM dynamic range is around 2 to 3 orders of magnitude, much smaller than the one of a standard RGA, that can reach 6 orders of magnitude. This implies that the VQM analyser needs a new auto-tune to avoid saturation of the signal every time the pressure increase is larger than three orders of magnitude. Moreover, this study indicates that the usual RGA sensitivity factors, directly relating the current signals to partial pressures, cannot be employed for the VQM because the signal amplitude of a gas species is not proportional with the partial pressure (see Figure 89).

A reference spectrum of a VQM was studied as a function of the applied voltage bias. The dynamic range was varied between -900 V to -1200 V, with steps of 50 V each. In Figure 82 I plotted the hydrogen peak signal as a function of the bias. The higher the absolute value of the voltage bias is, the higher the signal measured. This behaviour follows an exponential growth for all the main gasses, as displayed in Figure 83.

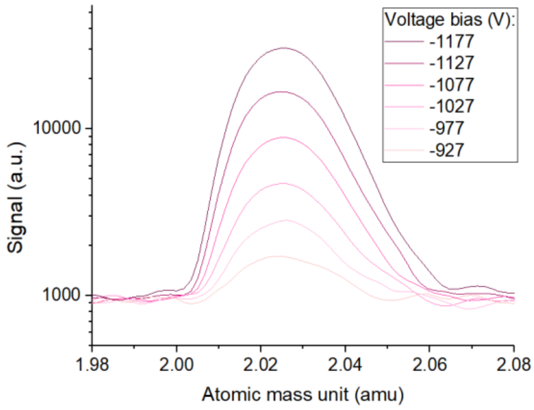

Figure 82: The hydrogen peak signal is shown as a function of the applied voltage bias.

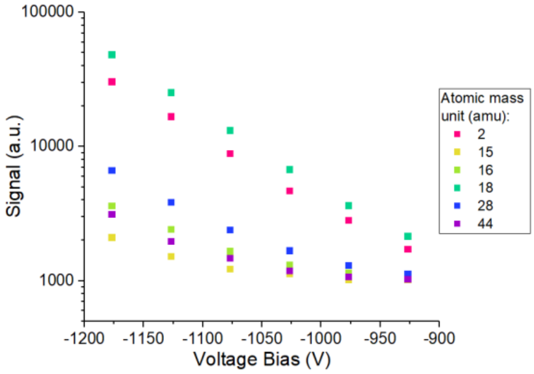

Figure 83: The peak values for hydrogen, methane, water, carbon monoxide and dioxide are displayed as a function of the applied voltage bias.

The VQM signal was also analysed while changing the filament current. The higher the current is, the higher the signal is recorded. This is visible for the hydrogen peak in Figure 84. This behaviour follows a linear increase for all the gas peaks as depicted in Figure 85. The constructor suggests to use 0.07 mA as standard filament current, not to age the instrument.

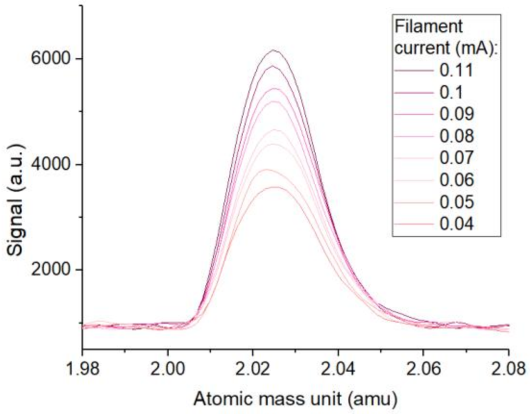

Figure 84: The hydrogen peak signal is shown as a function of the filament current.

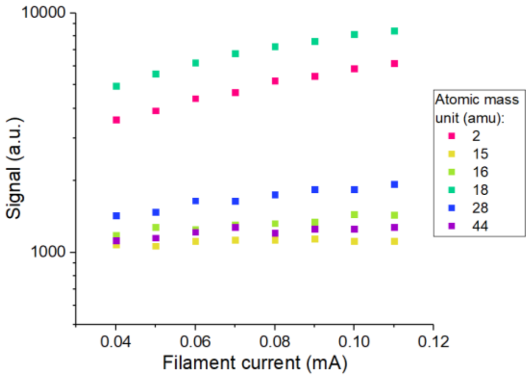

Figure 85: The peak values for hydrogen, methane, water, carbon monoxide and dioxide are displayed as a function of the filament current.

The third test concerns the repeller bias that was varied from -10 V to -25 V. When the bias approaches -10V, the measurement becomes unstable, i.e. the peak can shift as in the case of the hydrogen peak (see Figure 86) or can change shape as the water peak (see Figure 87). Therefore, values above -13 V should be avoided.

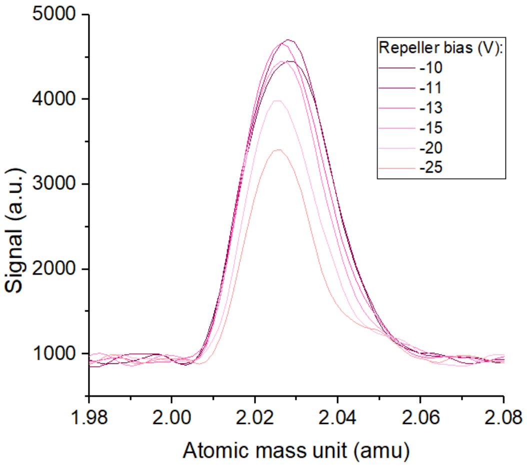

Figure 86: The hydrogen peak signal is shown as a function of the repeller bias.

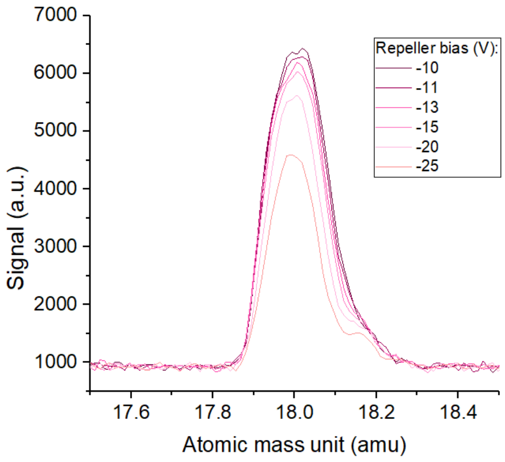

Figure 87: The water peak signal is shown as a function of the repeller bias.

The signal increases with increasing repeller bias value for all the gas peaks as depicted in Figure 88.

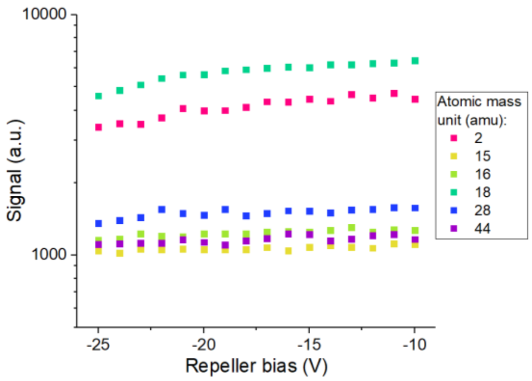

Figure 88: The peak values for hydrogen, methane, water, carbon monoxide and dioxide are displayed as a function of the repeller bias.

The fourth test concerns the comparison between a standard RGA and a VQM. A reference spectrum of the unbaked dome is taken with both instruments and shown in Figure 89. The RGA spectrum shows the highest peak, i.e. water, and all the other main gasses, i.e. hydrogen, methane, carbon monoxide and dioxide in blue. The RGA has a wide dynamic range and can scan the gas composition up to six orders of magnitude. The VQM spectrum shown in pink has a much lower dynamic range, typically 2 to 3 orders of magnitude only. As shown, the VQM appropriately evaluates the gas composition of the main gas species.

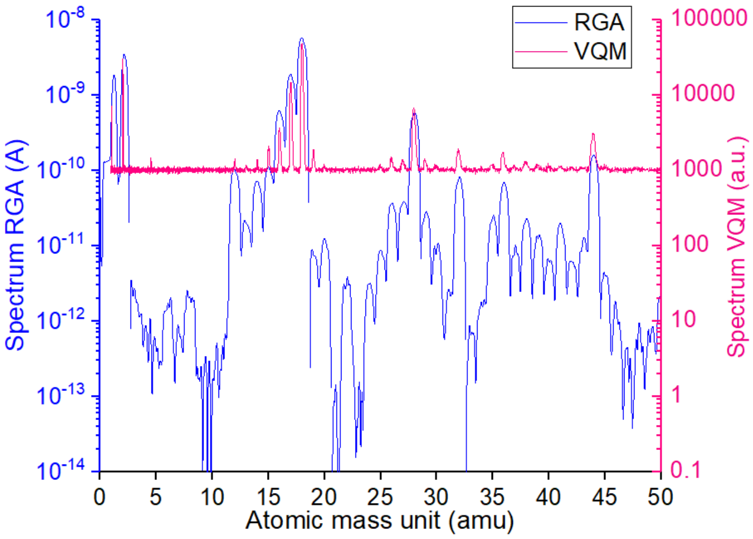

Figure 89: The gas spectra acquired with a RGA and a VQM are displayed in blue and pink, respectively.

In order to quantitatively specify the contribution of each gas species, a normalisation process needs to be applied. Concerning the RGA, I simply scale the spectrum to one, while for the VQM I remove the noise and then I normalise the gas spectrum. In this way I obtain comparable normalised spectra (see Figure 90). For the first two-to-three orders of magnitude, the peaks correspond in quality and quantity. Below 10^{-3} the VQM spectrum is not accurate due to a large background noise. Therefore, the VQM can be used to check for large leaks and to estimate the main gasses present in a vacuum system. It cannot be used, instead, for precise quantitative measurements, as for small leaks or pollutants traces.

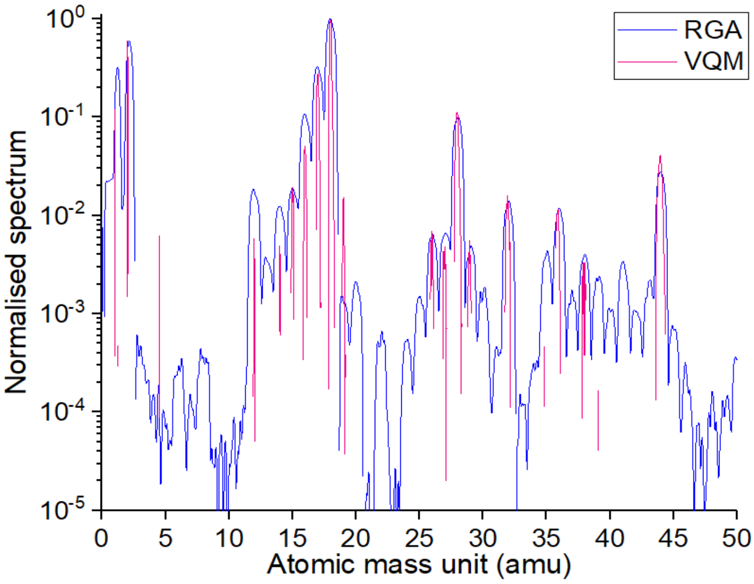

Figure 90: The normalised gas spectra of a RGA and a VQM are compared.

The fifth test presents a VQM signal saturation during hydrogen injection. When the pressure increases more than three orders of magnitude and the highest peak reaches around 60000 counts, the VQM needs to be calibrated again with an automatic auto-tune not to saturate the spectrum signal. A typical example of signal saturation is shown in Figure 91 during a hydrogen injection. The hydrogen saturation happens at around 10^{-9} $mbar$. The same process is displayed as a function of the total pressure in Figure 92, while continuously injecting hydrogen. The pressure is dominated by hydrogen, but all the other gas species signals slightly increase due to the gas cracking at the ion pump and at the gauges during the increased gas flux.

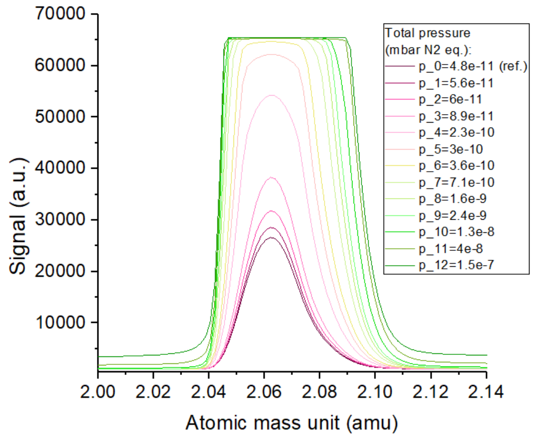

Figure 91: The hydrogen peak saturation is reached for signals above 60000 counts.

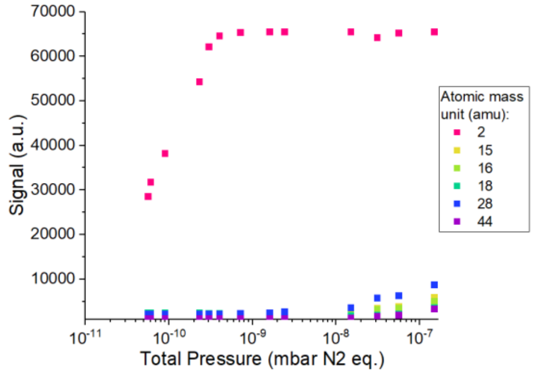

Figure 92: The VQM hydrogen peak saturation is displayed as a function of the total pressure.

Moreover, the last two studies indicate that the standard method used for gas analysers concerning RGA sensitivity factors cannot be used for the analysis of the VQM scans. The standard gas analysis performed with RGA consists on using sensitivity factors that directly relate the spectrum signals, usually in mA, to the partial pressures, in $mbar$, through calibration tests. With the gauge aging, these factors change and a new calibration is, indeed, needed. For the VQM, the signal amplitude is not proportional to the gas partial pressure and depends on the base pressure at which the auto-tune was performed. Therefore, no sensitivity factors for the VQM are presented, nor used. In order to have reliable VQM spectra, one should consider the spectrum automatically acquired and named ''curve'', remove the background and normalise the signal to main peak to get a normalised gas distribution.

3.3 Thermal devices

Ten calorimeters have been installed into VPS since 2014. B. Henrist manufactured two of them (called in this manuscript ''type B''), positioned into the fourth stations (unbaked Cu) since 2014. The type B PT100 sensors were oriented with the beam direction. I have made and installed other eight calorimeters in 2015 (called ''type E''). In these calorimeters, the PT100 have been installed orthogonally with respect to beam direction.

A simplified thermal model of a perfect calorimeter was conceived to evaluate the dynamic temperature response as a function of a localised heat load deposited into the calorimeter plate (*Chapter 3.2.1).* The thermal model defined the main parameters of the equivalent circuit, like thermal resistances and capacitances, and the time constant. This model has been compared against calibration. *A* steady-state ANSYS simulation corroborated the mathematical model, for a defined temperature increase arbitrarily set to $1°C$.

The second part of this study describes the thermal model of the calorimeter during the LHC operation, when the heat load is homogeneously distributed into the system. A distributed heat load calibration test was possible thanks to a fill with no EC, but only a well-known impedance power deposition.

Finally, a preliminary investigation took place to identify the PT100 orientation impact on the measurements. During the operation, the type E calorimeters suffered of additional high-capacitance effect with respect to the calibration tests and are not reliable for the determination of the EC heat load.

3.3.1 Localised heat load

One of the two PT100 sensors attached to each calorimeter plate has been used to deposit a heat load for the localised calibration tests. First, the response of an ideal calorimeter is represented by a simplified model. Secondly, the calibration tests on all the calorimeters are presented and compared with the simplified analytical model. Thirdly, an ANSYS simulation was performed to show a further correspondence between theoretical calculations and tests.

- **Thermal model**

The first model presented concerns the heat transfer between the calorimeter and the liner while applying a localised heat load into the calorimeter plate. The heat from the calorimeter plate can be dissipated mainly by conduction through the stainless steel links and by radiation from both the calorimeter plate and the thermal links. The convection process is not present under vacuum.

The heat is distributed along the circuit depending on the thermal resistances. The equivalent thermal scheme is presented in Figure 93. The mean temperatures are displayed in red (see naming presented at the end of *Chapter 2*), the conductive and radiative resistances measured in $[K/W]$ are shown in black, while the heat fluxes measured in $[W]$ are displayed in orange.

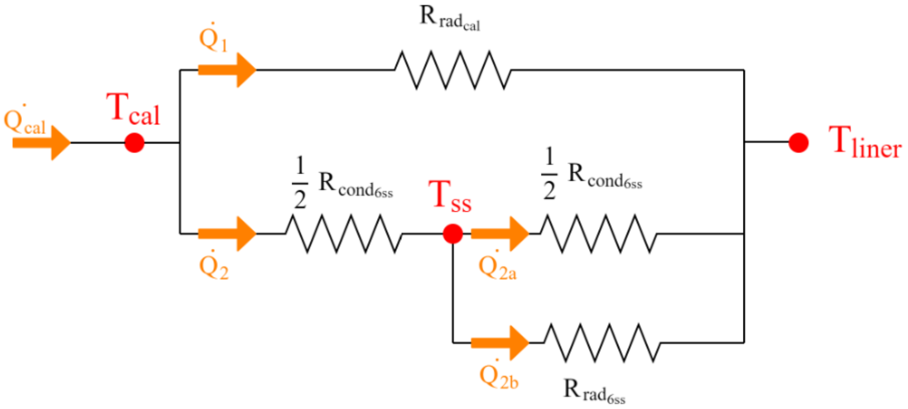

Figure 93: Simplified thermal model during a calorimeter calibration. The mean temperatures are displayed in red, the resistances measured in black, while the heat fluxes in orange.

The main resistances of the equivalent circuit are the following:

- $R_{cond_{6ss}}$ is the equivalent thermal resistance of the parallel of the six stainless steel ribbons.
- $R_{rad_{cal}}$ is the radiative resistance from the calorimeter plate to the chamber. In this simple case, the vacuum chamber has the same mean temperature of the liner.
- $R_{rad_{6ss}}$ is the radiative resistance from the stainless steel ribbons to the chamber and, therefore, the beam pipe.

The distribution of heat loads is respectively defined with:

- $\dot{Q}_{cal}$, the total heat load deposited on the calorimeter plate.
- $\dot{Q}_1$, the heat lost by radiation from the calorimeter plate.
- $\dot{Q}_2$, the heat transported by conduction through the beginning stainless steel links.
- $\dot{Q}_{2a}$, the heat transported by conduction through the last part of the stainless steel links.
- $\dot{Q}_{2b}$, the heat lost by radiation from the stainless steel links.

I considered the average temperature of the thermal links, T_{ss}, hypothetically defined in the middle of each one, for the radiative heat transfer. The conductive resistance of the calorimeter plate is neglected due to a low copper resistivity and, therefore, the temperature distribution on the calorimeter plate is considered homogeneous. The weldings between the stainless steel links and the copper are considered perfect and, so, their resistance.

For the calorimeter plate the only significant resistance is linked to radiation and, for a small temperature increase, it is equivalent to:

$$R_{rad_{cal}} = \frac{\Delta T_{cal-liner}}{\dot{Q}_1} = \frac{1}{\sigma\, \varepsilon\, S\, F\, 4T^3} = \frac{1}{5.67 \cdot 10^{-8} \frac{W}{mK} \cdot 0.04 \cdot 0.03^2\, m^2 \cdot 1 \cdot 4(273+19)^3} = 4919 \frac{K}{W} \tag{76}$$

The conductive and radiative resistances of one stainless steel link are, respectively, $R_{cond_{1ss}}$ and $R_{rad_{1ss}}$:

$$R_{cond_{1ss}} = \frac{R_{el_{1ss}}}{\lambda_{ss}\,\rho_{ss}} = \frac{\rho_{ss}\,L}{S} \cdot \frac{1}{\lambda_{ss}\,\rho_{ss}} = \frac{7 \cdot 10^{-7}\,\Omega m\ \cdot 0.0045\,m}{0.005\,m \cdot 0.00005\,m} \cdot \frac{1}{16\,\frac{W}{mK} \cdot 7 \cdot 10^{-7} \Omega m} = 1125\,\frac{\mathrm{K}}{\mathrm{W}} \tag{77}$$

$$R_{rad_{1ss}} = \frac{\Delta T_{cal-liner}}{\dot{Q}_{2b}/6} = \frac{1}{\sigma\,\varepsilon\,S\,F\,4T^3} = \frac{1}{5.67\ \cdot 10^{-8}\,\frac{W}{mK} \cdot 0.08\ \cdot 0.0045 \cdot 0.005\,m^2 \cdot 1 \cdot 4(273+19)^3} \tag{78}$$

$$= 98387\,\frac{K}{W}$$

I evaluate the values for the parallel of 6 perfect links, $R_{cond_{6ss}}$ and $R_{rad_{6ss}}$ as:

$$R_{cond_{6ss}} = \frac{1}{6}\,R_{cond_{1ss}} = 188\,\frac{K}{W} \tag{79}$$

$$R_{rad_{6ss}} = \frac{1}{6} R_{rad_{1ss}} = 16398\,\frac{K}{W} \tag{80}$$

The conduction resistance is much smaller than the radiative one, therefore the heat flux by conduction dominates. In order to get the equivalent resistance between the calorimeter plate and the liner, I calculate also equivalent resistances, $R_{eq.1}$, $R_{eq.2}$ and $R_{eq.3}$. I define $R_{eq\,1}$ as the parallel of half of the conductive link resistance and the full radiative one:

$$R_{eq.1} = \frac{R_{rad_{6ss}} \cdot \frac{1}{2} R_{cond_{6ss}}}{R_{rad_{6ss}} + \frac{1}{2} R_{cond_{6ss}}} = 93\,\frac{K}{W} \tag{81}$$

The second equivalent resistance is $R_{eq.2}$, corresponding to the series of two resistances, $R_{eq.1}$ and the remaining contribution of the link conduction:

$$R_{eq.2} = R_{eq.1} + \frac{1}{2} R_{cond_{6ss}} = 187\,\frac{K}{W} \tag{82}$$

The total equivalent resistance, $R_{eq.3}$, is the equivalent resistance of the full circuit, from the calorimeter plate to the liner:

$$R_{eq.3} = \frac{R_{rad_{cal}} \cdot R_{eq.2}}{R_{rad_{cal}} + R_{eq.2}} = 180\,\frac{K}{W} \tag{83}$$

I can estimate the relationship between the equilibrium temperature increase, $\Delta T_{cal-liner}$, and the applied heat load, $\dot{Q_{cal}}$, as:

$$\Delta T_{cal-liner} = R_{eq.3}\,\dot{Q}_{cal} = 180 \cdot \dot{Q}_{cal} \tag{84}$$

The heat fluxes are then redistributed along the circuit as presented in Figure 93. The radiative heat load transmitted between the calorimeter and the liner is called $\dot{Q}_1$, while the conductive one between the calorimeter plane and the thermal links is $\dot{Q}_2$. This last heat is divided in two components: $\dot{Q}_{2a}$ transmitted by conduction to the liner and $\dot{Q}_{2b}$ by radiation to the chamber. Their contribution is presented here.

$$\dot{Q}_1 = \frac{R_{eq.2}}{R_{rad_{cal}} + R_{eq.2}}\,\dot{Q}_{cal} = 0.037 \cdot \dot{Q}_{cal} \tag{85}$$

$$\dot{Q}_2 = \frac{R_{rad_{cal}}}{R_{rad_{cal}} + R_{eq.2}}\,\dot{Q}_{cal} = 0.963 \cdot \dot{Q}_{cal} \tag{86}$$

$$\dot{Q}_{2a} = \frac{R_{rad_{6ss}}}{R_{rad_{6ss}} + \frac{1}{2} R_{cond_{6ss}}}\,\dot{Q}_2 = 0.994 \cdot \dot{Q}_2 \approx 0.958 \cdot \dot{Q}_{cal} \tag{87}$$

$$\dot{Q}_{2b} = \frac{\frac{1}{2}R_{cond_{6ss}}}{R_{rad_{6ss}} + \frac{1}{2}R_{cond_{6ss}}}\dot{Q}_2 = 0.006 \cdot \dot{Q}_2 \approx 0.005\,\dot{Q}_{cal} \tag{88}$$

Where $\dot{Q}_{cal} = \dot{Q}_1 + \dot{Q}_2$ and $\dot{Q}_2 = \dot{Q}_{2a} + \dot{Q}_{2b}$. The main heat load component, i.e. 95.8%, is transmitted by conduction from the plate to the liner. I can also describe the temperature difference in a second way, as:

$$\begin{aligned} \Delta T_{cal-liner} &= (T_{cal} - T_{ss}) + (T_{ss} - T_{liner}) = \frac{1}{2}R_{cond_{6ss}}\,\dot{Q}_2 + \frac{1}{2}R_{cond_{6ss}}\dot{Q}_{2a} \\ &= \frac{1}{2}R_{cond_{6ss}}\,\dot{Q}_2\,(1 + 0.994) = \frac{1}{2}\cdot 188 \cdot 0.963 \cdot \dot{Q}_{cal}(1 + 0.994) = \ 180 \cdot \dot{Q}_{cal} \end{aligned} \tag{89}$$

This second formulation is equivalent to Eq. (84). Finally, I can re-write this formula in order to express the heat as a function of the temperature increase during the calibration:

$$\dot{Q}_{cal} \ = \frac{\Delta T_{cal-liner}}{180} \tag{90}$$

A $\Delta T_{cal-liner} = 1^{\circ}C$ corresponds to $\dot{Q}_{cal} = 5.55 \cdot 10^{-3}\ W$ into the calorimeter plate. It is interesting to compare this heat, with an equivalent heat load per unit area distributed on the calorimeter plate. The plate area, A_{cal}, is:

$$A_{cal} = {l_{cal}}^2 = (3 \cdot 10^{-2})^2\ m^2 = 9 \cdot 10^{-4}\ m^2 \tag{91}$$

Where l_{cal} is the dimension of the squared plate. The heat $\dot{Q}_{cal}$ received during the calibration corresponds to an equivalent distributed heat into the calorimeter plate, $\dot{E}\left[\frac{W}{m^2}\right]$:

$$\dot{E} = \frac{\dot{Q}_{cal}}{A_{cal}} = \frac{\Delta T_{cal-liner}}{180\ \cdot 9 \cdot 10^{-4}} = \frac{\Delta T_{cal-liner}}{0.162} \tag{92}$$

A $\Delta T_{cal-liner} = 1^{\circ}C$ corresponds to $\dot{E} = 6.2\ W/m^2$ deposited into the calorimeter plate. These calculations are valid for the steady-state case at equilibrium temperature where a localised heat load is applied only to the calorimeter plate. In order to study the temperature evolution during the transient, I need to introduce the thermal capacitances, C. In general, a thermal capacitance is connected to the material energy storage capacity and is defined as the specific heat, c_p, multiplied by the mass M, as shown in Eq. (93):

$$C = c_p \cdot M \tag{93}$$

For the calorimeter plate the capacitance has the following value:

$$C_{cal} = c_{p_{cu}} \cdot m_{cal} = c_{p\,cu} \cdot \rho_{cu} \cdot V_{cal} = 385\frac{J}{kg\ K} \cdot 8.96 \cdot 10^{-3}\frac{kg}{cm^3} \cdot (3 \cdot 3 \cdot 0.02\ cm^3) = 0.621\frac{J}{K} \tag{94}$$

The six stainless steel links own:

$$C_{6ss} = c_{p_{ss}} \cdot m_{6ss} = c_{p_{ss}} \cdot \rho_{ss} \cdot V_{6ss} = 480\frac{J}{kg\ K} \cdot 7.5 \cdot 10^{-3}\frac{kg}{cm^3} \cdot (6 \cdot 1 \cdot 0.5 \cdot 0.005\ cm^3) = 0.054\frac{J}{K} \tag{95}$$

The contribution of the stainless steel links is much smaller than the plate capacitance, as expected. The equivalent capacitance is:

$$C_{eq} = C_{cal} + C_{6\,ss} = 0.675\frac{J}{K} \tag{96}$$

The time constant of the calorimeter, given by the multiplication of $R_{eq.3}$ and C_{eq}, is:

$$\tau_{cal} = R_{eq.3}\,C_{eq} = 180\frac{K}{W} \cdot 0.675\frac{J}{K} = 122\ s = 2\min 2\ s \tag{97}$$

Finally, I can write the thermal model that describes the dynamic temperature during the calorimeter calibration. The dynamic behaviour is represented by the following differential equation [88]:

$$\dot{Q} - \frac{\Delta T}{R_{eq.3}} - C_{eq}\,\Delta\dot{T} = 0 \tag{98}$$

The solution of this first order differential equation is:

$$\Delta T_{cal-liner} = \dot{Q}_{cal}\,R_{eq.3}\left(1 - e^{-\frac{t}{\tau_{cal}}}\right) = 180\,\dot{Q}_{cal}\left(1 - e^{-\frac{t}{122}}\right) \tag{99}$$

- **Calibration tests**

Calibration tests were performed to measure τ_{cal}, $R_{eq.3}$ and C_{eq} of each calorimeter and cross check the simplified model above-presented. The calibration was performed applying a voltage into a dedicated PT100 sensor installed into each calorimeter plate. The 10 calorimeter responses are displayed in Figure 94, together with the evolution of the thermal model evaluated applying an input of around 1 V. The heat load supplied during the calibration is estimated from the voltage applied into the PT100. The PT100 thermal resistance changes with time and follows the rule given by the constructor:

$$R_{PT100} = 0.398 \cdot\, T + 100 \tag{100}$$

The heat load supplied, $\dot{Q}_{cal_{supplied}}$, can be calculated for $= 21.81\ °C$ and a mean real voltage drop $V_{PT100} = 0.963\ V$:

$$\dot{Q}_{cal_{supplied}} = \frac{V_{PT100}^2}{R_{PT100}(T)} = \frac{0.963^2}{0.398 \cdot\ 21.81 + 100} = 8.53\ mW \tag{101}$$

Therefore, the thermal model response during the calibration is:

$$\Delta T_{cal-liner} = \dot{Q}_{cal}\,R_{eq.3}\left(1 - e^{-\frac{t}{\tau_{cal}}}\right) = 8.53\ mW \cdot 180\frac{K}{W}\left(1 - e^{-\frac{t}{122}}\right) \tag{102}$$

The data and the model follow a similar trend, as plotted in Figure 94. The analytical model overestimates the temperature increase and, therefore, the heat load received by the calorimeter and the equivalent thermal resistance of the circuits. On the contrary, the time constants of calorimeters and model are compatible.

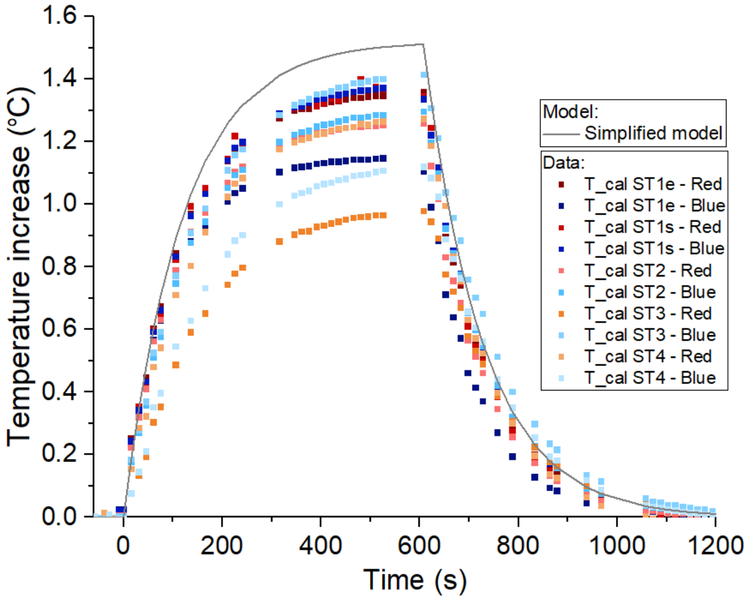

Figure 94: The VPS calorimeter temperature increases are displayed as a function of the time. They are compared with the above-mentioned model calculated for an applied voltage of 0.963 V.

The discrepancy between the calorimeter responses and the model is linked to the manufacturing of the calorimeters. I estimated the parameters for each calorimeter, in terms of thermal resistance and time constant, matching the data with the general model. The first step was to assess the time constants, $\tau_{measured}$, from the data. From these values, I estimated the equivalent thermal resistances, $R_{eq.\ measured}$, considering negligible deviation of the thermal capacitance, C_{eq}, calculated by the model.

The calorimeter parameters are summarised in Table 5 and the results are presented in Figure 95. The name of the calorimeters is encoded starting with the station number (ST1= first station, ST2= second station, etc.), the position along the liner when not in the centre (e = entrance of the liner, s = exit of the liner), and the beam pipe name (Red or Blue).

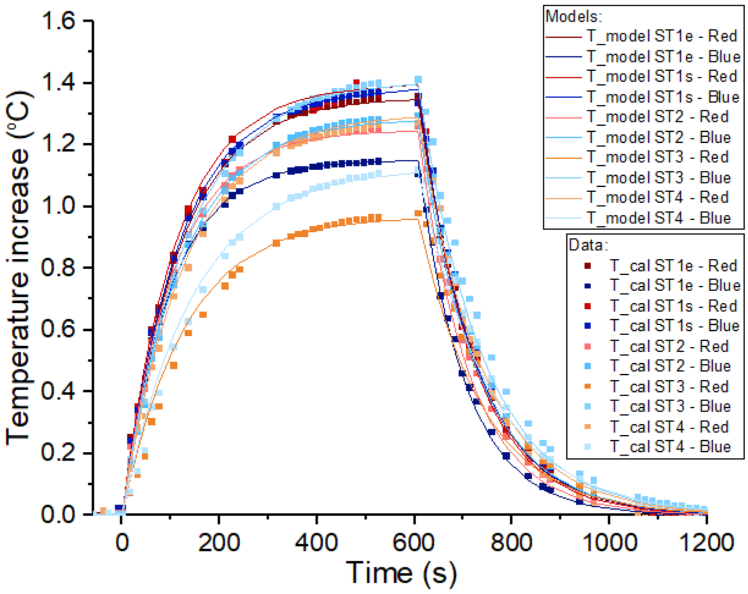

Figure 95: The VPS calorimeter temperature increases and their matched models are displayed as a function of the time, for a 0.963 V calibration test.

The average time constant measured is $\overline{\tau_{measured}} = 120\ s = 2min$ and the equivalent resistance is $\overline{R_{eq.\ measured}} = 178\ \frac{K}{W}$ (see Table 5). These two values are in agreement with the model.

Then, I measured the temperature increases, $\Delta T_{cal-liner}$, and calculated the heat load received by each calorimeter, $\dot{Q_{cal}}$. The mismatch between the heat received and the one supplied indicated a power loss (see calculations summarized in Table 5). This loss can be attributed to the cablings or to the contact of the PT100 into the calorimeter plate. In the following plots the both $\dot{Q}_{cal_{supplied}}$ and $\dot{Q}_{cal}$ are displayed as a function of three different calibration tests, performed respectively with 1 V, 2 V and 3 V for the red calorimeters (see Figure 96) and blue ones (see Figure 97). The heat load supplied are identified by squares and are always higher than the heat received by the calorimeters, identified by triangles.

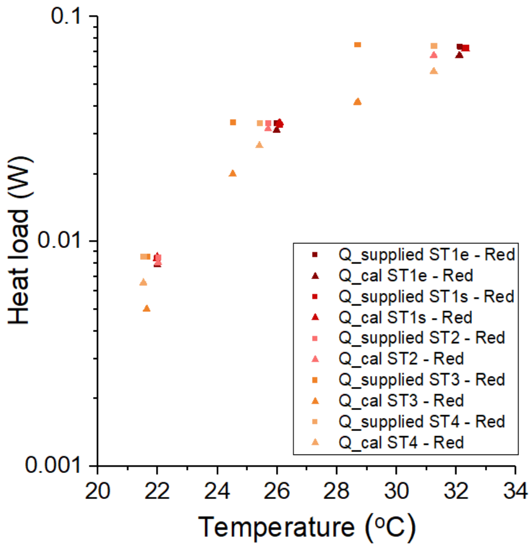

Figure 96: The heat load supplied and received by the red calorimeters are displayed as a function of the temperature.

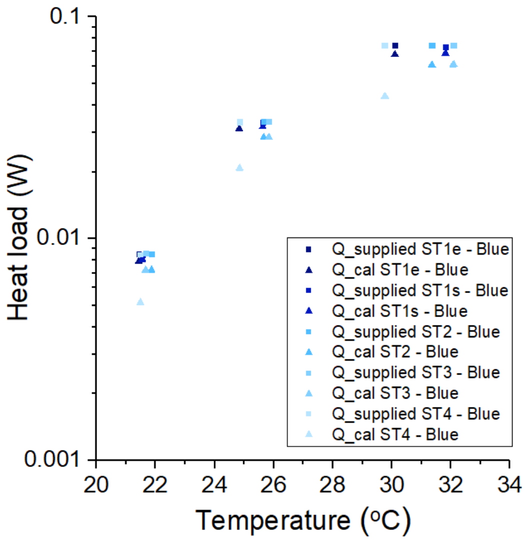

Figure 97 : The heat load supplied and received by the blue calorimeters are displayed as a function of the temperature.

There is a discrepancy between the heat loads, therefore important losses takes place into the calorimeter plate. The wire resistance is around few Ohm per 100 m circuit and this cannot explain the difference between several calorimeter responses. These losses are probably related to the PT100 connection and concern the reproducibility of the calorimeters.

In order to evaluate these losses, I define the power ratio as $r_Q = \frac{\dot{Q}_{cal}}{\dot{Q}_{cal_{supplied}}}$. This parameter is shown as a function of the temperature in Figure 98. Each calorimeter has its own ratio that can be considered constant with temperature at first approximation. This plot shows that a constant percentage of the power is lost in each calorimeter, defined as Q_{lost}=1-r_Q.

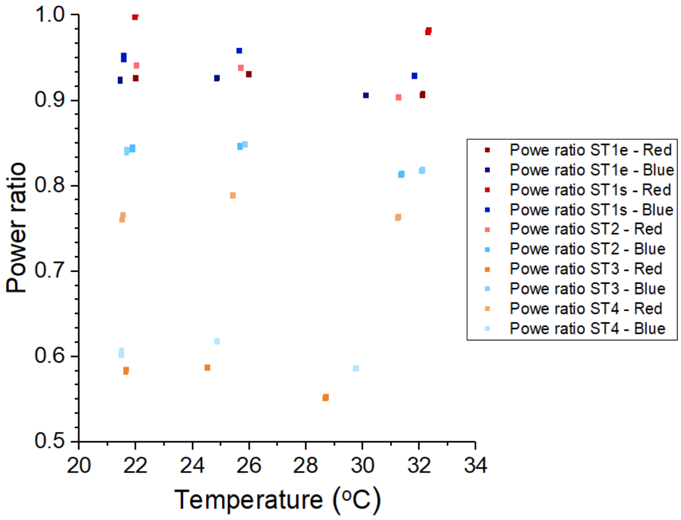

Figure 98: The ratios between the power received by the calorimeter and the supplied one by the source during the calibration tests are displayed as a function of the temperature, for all the calorimeters.

The heat losses must be attributed to additional resistances, R_{add}, that dissipate the remaining heat. R_{add} is calculated solving the following balance for each calorimeter:

$$\dot{Q}_{cal} = \frac{V_{PT100}^2}{R_{PT100}(T) + R_{add}} \tag{103}$$

The additional resistances are displayed as a function of the temperature for the ten calorimeters (see Figure 99). R_{add} varies between 0 Ω and 90 Ω. This additional resistance has a big impact on the estimation of the heat loads from the temperature measurements. Therefore, the calibration tests were needed to assess the real behaviour of each calorimeter.

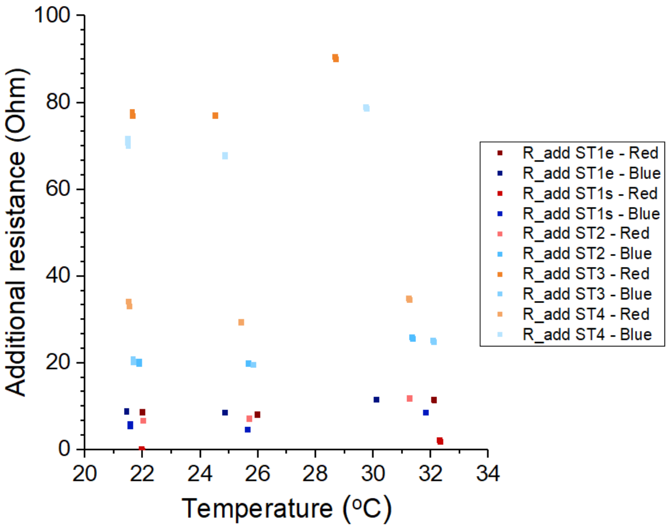

Figure 99: The additional resistance is displayed as a function of the temperature, as a function of the temperature.

In Table 5 the main parameters for the test performed with an input voltage of 1 V are summarised. The heat lost along the circuit on this additional resistance can reach up to 41% (see Q_{lost} of the station 3 – red).

Table 5: Parameters and calculations concerning the calibration tests with 1V for the ten calorimeters implemented into VPS.

Calorimeters:	***ST1e - Red***	***ST1e - Blue***	***ST1s - Red***	***ST1s - Blue***	***ST2 - Red***	***ST2 - Blue***	***ST3 - Red***	***ST3 - Blue***	***ST4 - Red***	***ST4 - Blue***	***Avg.***
$\tau_{mesured}\ [s]$	*115*	*98*	*110*	*115*	*105*	*120*	*130*	*131*	*130*	*145*	***120***
$\boldsymbol{R_{measured}}[\boldsymbol{K/W}]$	*170*	*145*	*163*	*170*	*156*	*178*	*193*	*194*	*193*	*215*	***178***
$\Delta\boldsymbol{T_{measured}}[°\boldsymbol{C}]$	*1.35*	*1.15*	*1.38*	*1.37*	*1.25*	*1.29*	*0.97*	*1.40*	*1.27*	*1.10*	***1.25***
$\boldsymbol{T_{max\,measured}}[°\boldsymbol{C}]$	*22.98*	*21.43*	*21.97*	*21.55*	*22.01*	*21.86*	*21.63*	*21.66*	*21.52*	*21.48*	***21.81***
$\dot{\boldsymbol{Q}}_{\boldsymbol{cal}}\ [\boldsymbol{mW}]$	*7.91*	*7.90*	*8.44*	*8.04*	*8.06*	*7.23*	*5.02*	*7.21*	*6.57*	*5.14*	***7.15***
$\boldsymbol{V_{measured}}[\boldsymbol{V}]$	*0.964*	*0.963*	*0.958*	*0.958*	*0.965*	*0.964*	*0.965*	*0.965*	*0.965*	*0.960*	***0.963***
$\dot{\boldsymbol{Q}}_{\boldsymbol{cal}_{supplied}}\ [\boldsymbol{mW}]$	*8.54*	*8.55*	*8.43*	*8.45*	*8.56*	*8.55*	*8.58*	*8.57*	*8.57*	*8.49*	***8.53***
$\boldsymbol{r_Q}$	*0.927*	*0.924*	*1.000*	*0.951*	*0.942*	*0.846*	*0.585*	*0.842*	*0.766*	*0.605*	***0.839***
$\boldsymbol{Q_{lost}}[\%]$	*7.3*	*7.6*	*0*	*4.9*	*5.8*	*15.4*	*41.5*	*15.8*	*23.4*	*39.5*	***16.1***
$\boldsymbol{R_{add}}[\boldsymbol{\Omega}]$	*9*	*9*	*0*	*6*	*7*	*20*	*77*	*20*	*33*	*71*	***25***

- **ANSYS simulation**

In order to support the thermal model and the measurements for the case $V_{input} = 1\ V$, an ANSYS simulation was carried considering the following boundary conditions:

- The above-mentioned geometry and materials in a 2D model.
- The initial homogeneous temperature: $T_{liner_0} = T_{cal_0} = 19°C$.
- The final temperature at the extremities of the liner: $T_{liner_1} = 19°C$.
- The heat load into the calorimeter plate $\dot{Q}_{cal} = 5.55\ mW$ derived from Eq. (90) for a $\Delta T_{cal-liner} = 1°C$.
- The thermal conductivity of the copper welding electrodes estimated from literature, $C_{cond_{cu}} \cong 385 \frac{W}{m^2K}$.

In Figure 100 I present the temperature distribution around the simplified calorimeter. For $\dot{Q}_{cal} = 5.55\ mW$, the analytical calculations gives $\Delta T_{cal-liner} = 1°C$ and the ANSYS $\Delta T_{cal-liner} = 1.066°C$. Therefore, the ANSYS simulation verifies my analytical calculation and validates the simplified thermal model.

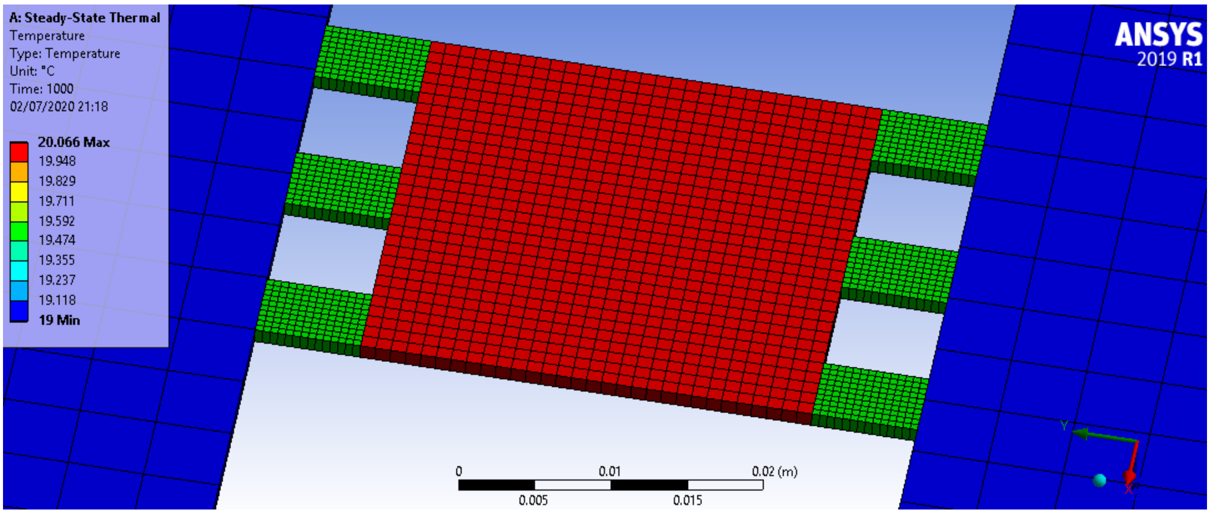
A: Steady-State Thermal
Temperature
Type: Temperature
Unit: °C
Time: 1000
02/07/2020 21:18
20.066 Max
19.948
19.829
19.711
19.592
19.474
19.355
19.237
19.118
19 Min
ANSYS
2019 R1
0
0.01
0.02 (m)
0.005
0.015
Y
X

Figure 100: Temperature distribution on the calorimeter during the calibration with $\dot{Q}_{cal} = 5.55\ mW$.

3.3.2 Distributed heat load

The second analysis concerns a distributed heat load applied into the full system. It was not possible to calibrate with an external heat source, so I chose to use the well-known beam impedance heat load, during a 50 ns fill with no EC and no SR at 450 GeV. The thermal model and the data are here compared.

- **Thermal model**

During the LHC operation, the heat is homogeneously deposited along the liner. For this reason, a more complete thermal model needed to be implemented. Some additional resistances had to be taken into account:

- $R_{cond_{liner}}$ is the thermal resistance of the liner. The heat load can be dissipated in parallel though the two liner extremities where flanges connect the liners to the vacuum chambers.
- $R_{rad_{liner}}$ is the radiative resistance from the liner into the vacuum chamber. It consists of two parallel components, each of them corresponding to half liner.

All the heat received by the liner is transmitted to the vacuum chamber that is cooled down by air convection, radiation and conduction by the mechanical supports. The chamber temperature is around 19 °C all year long. In Figure 101 the equivalent thermal circuit is displayed. The maximum temperature of the liner, $T_{liner_{max}}$, is defined near the calorimeter.

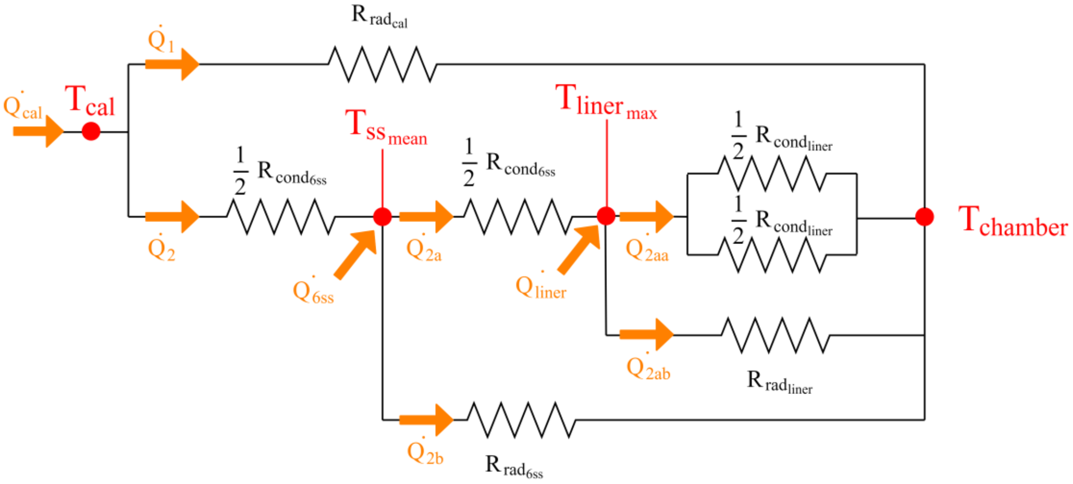
$R_{rad_{cal}}$
$\dot{Q}_1$
$\dot{Q}_{cal}$
T_{cal}
$T_{ss_{mean}}$
$T_{liner_{max}}$
$\frac{1}{2} R_{cond_{6ss}}$
$\frac{1}{2} R_{cond_{6ss}}$
$\frac{1}{2} R_{cond_{liner}}$
$\frac{1}{2} R_{cond_{liner}}$
$T_{chamber}$
$\dot{Q}_2$
$\dot{Q}_{6ss}$
$\dot{Q}_{2a}$
$\dot{Q}_{liner}$
$\dot{Q}_{2aa}$
$\dot{Q}_{2ab}$
$R_{rad_{liner}}$
$\dot{Q}_{2b}$
$R_{rad_{6ss}}$

Figure 101: Equivalent thermal circuit of a calorimeter during the LHC operation, with a distributed heat load.

The resistances previously presented are valid also for this model. The additional conductive and radiative resistances of the liner are respectively:

$$R_{cond_{liner}} = \frac{\overline{R_{el}}}{\lambda_{cu}\,\rho_{cu}} = \frac{\rho_{cu}\,L}{S}\cdot\frac{1}{\lambda_{cu}\,\rho_{cu}} = \frac{1.7\cdot 10^{-8}\,\Omega m\ \cdot 1.378\,m}{0.001\,m\cdot 2\pi\,0.04\,m}\cdot\frac{1}{385\,\frac{W}{mK}\cdot 1.7\cdot 10^{-8}\Omega m} = 14\,\frac{\mathrm{K}}{\mathrm{W}} \tag{104}$$

$$R_{rad_{liner}} = \frac{\Delta T}{\dot{Q}_R} = \frac{1}{\sigma\,\varepsilon\,S\,F\,4T^3} = \frac{1}{5.67\ \cdot 10^{-8}\,\frac{W}{mK}\cdot 0.04\ \cdot 2\pi\,0.04\cdot 1.378\,m^2\cdot 1\cdot 4(273+19)^3} = 51\,\frac{K}{W} \tag{105}$$

I calculated the equivalent resistances of the circuit, through series and parallels. The equivalent resistances are sketched in Figure 102.

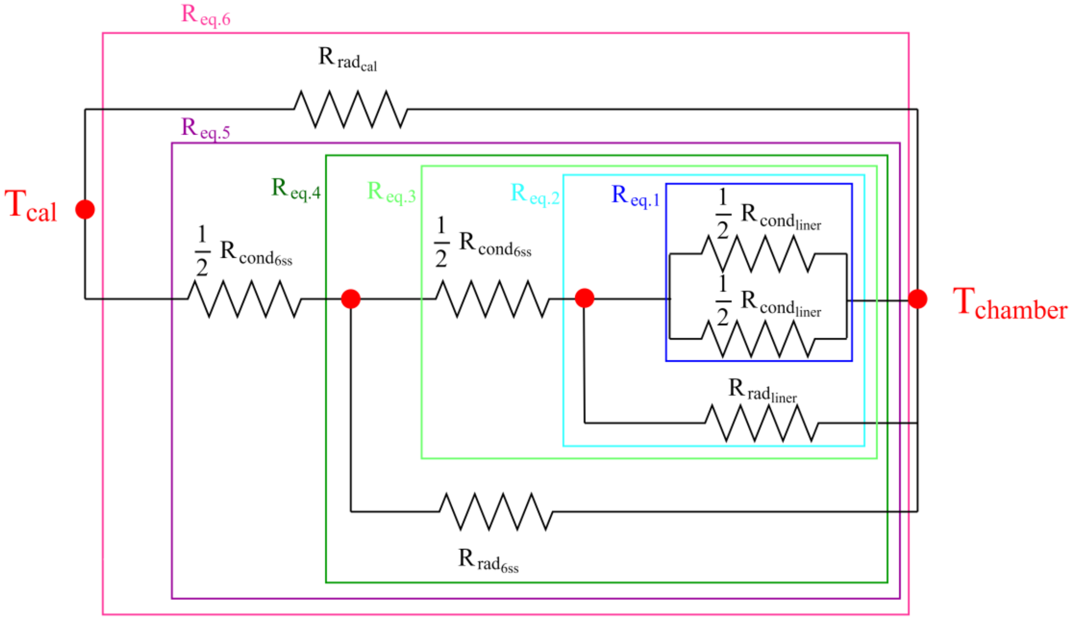
$R_{eq.6}$
$R_{rad_{cal}}$
$R_{eq.5}$
T_{cal}
$R_{eq.4}$
$R_{eq.3}$
$R_{eq.2}$
$R_{eq.1}$
$\frac{1}{2}R_{cond_{liner}}$
$\frac{1}{2}R_{cond_{6ss}}$
$\frac{1}{2}R_{cond_{6ss}}$
$\frac{1}{2}R_{cond_{liner}}$
$T_{chamber}$
$R_{rad_{liner}}$
$R_{rad_{6ss}}$

Figure 102: Simplified thermal scheme of a liner installed in a vacuum chamber, with the final equivalent resistances.

I define $R_{eq\,1}$ as the series of three parallel resistances.

$$R_{eq.1} = \frac{\frac{1}{2}R_{cond_{liner}}\cdot\frac{1}{2}R_{cond_{liner}}}{\frac{1}{2}R_{cond_{liner}} + \frac{1}{2}R_{cond_{liner}}} = 3.50\,\frac{K}{W} \tag{106}$$

$R_{eq.2}$ is equivalent to the parallel of two resistances:

$$R_{eq.2} = \frac{R_{eq.1}\cdot R_{rad_{liner}}}{R_{eq.1} + R_{rad_{liner}}} = 3.28\,\frac{K}{W} \tag{107}$$

I calculate $R_{eq.3}$:

$$R_{eq.3} = R_{eq.2} + \frac{1}{2}R_{cond_{6ss}} = 97.28\,\frac{K}{W} \tag{108}$$

I calculate $R_{eq.4}$, equivalent of a parallel:

$$R_{eq.4} = \frac{R_{eq.3}\cdot R_{rad_{6ss}}}{R_{eq.3} + R_{rad_{6ss}}} = 96.70\,\frac{K}{W} \tag{109}$$

I calculate $R_{eq.5}$, equivalent of a serie:

$$R_{eq.5} = R_{eq.4} + \frac{1}{2} R_{cond_{6ss}} = 190.7 \frac{K}{W} \tag{110}$$

$R_{eq.6}$ is the equivalent resistance of the entire circuit, from the calorimeter until the vacuum chamber:

$$R_{eq.6} = \frac{R_{rad_{cal}} \cdot R_{eq.5}}{R_{rad_{cal}} + R_{eq.5}} = 183.58 \frac{K}{W} \tag{111}$$

In order to calculate the flux reaching each vacuum element, I have to consider the areas exposed to the beam and the homogeneous thermal flux per unit area, $\dot{E}$, measured in $[W/m^2]$. Depending on the area exposed, the calorimeter, the stainless steel links and the liner will receive a different total heat load, respectively identified by $\dot{Q_{cal}}$, $\dot{Q_{6ss}}$ and $\dot{Q_{liner}}$. The areas of the calorimeter, the thermal links, the liner and a 1-m liner are respectively:

$$A_{cal} = {l_{cal}}^2 = (3 \cdot 10^{-2})^2 \, m^2 = 9 \cdot 10^{-4} \, m^2 \tag{112}$$

$$A_{6ss} = 6 \cdot l_1 \cdot l_2 = 6 \cdot 0.005 \cdot 0.005 = 1.5 \cdot 10^{-4} \, m^2 \tag{113}$$

$$A_{liner} = 2\pi \cdot r_{liner} \cdot l_{liner} = 2\pi \cdot 0.04 \, m \cdot 1.378 \, m = 0.35 \, m^2 \tag{114}$$

$$A_{1m\ liner} = 2\pi \cdot r_{liner} \cdot l_{1m} = 2\pi \cdot 0.04m \cdot 1m = 0.25 \, m^2 \tag{115}$$

Therefore, the heat loads in $[W]$ due to the direct effect of the beam into the calorimeter, the stainless steel links and the liner are the followings:

$$\dot{Q}_{cal} = A_{cal}\dot{E} = 9 \cdot 10^{-4} \, \dot{E} \tag{116}$$

$$\dot{Q}_{6ss} = A_{6ss}\dot{E} = 1.5 \cdot 10^{-4} \, \dot{E} \tag{117}$$

$$\dot{Q}_{liner} = A_{liner}\dot{E} = 0.35 \, \dot{E} \tag{118}$$

In particular, the heat loads transmitted between the calorimeter and the steel links, $\dot{Q}_2$, between the steel links and the liner, $\dot{Q}_{2a}$, and between the liner and the chamber, $\dot{Q}_{2aa}$, are:

$$\dot{Q}_2 = \frac{R_{rad_{cal}}}{R_{rad_{cal}} + R_{eq.5}} (\dot{Q_{cal}}) = \frac{R_{rad_{cal}}}{R_{rad_{cal}} + R_{eq.4}} \cdot A_{cal}\dot{E} = 8.66 \cdot 10^{-4} \cdot \dot{E} \tag{119}$$

$$\dot{Q}_{2a} = \frac{R_{rad_{6ss}}}{R_{rad_{6ss}} + R_{eq.3}} (\dot{Q}_2 + \dot{Q}_{6ss}) = 1.01 \cdot 10^{-3} \cdot \dot{E} \tag{120}$$

$$\dot{Q}_{2aa} = \frac{R_{rad_{liner}}}{R_{rad_{liner}} + R_{eq.1}} (\dot{Q}_2 + \dot{Q}_{6ss} + \dot{Q}_{liner}) = 3.34 \cdot 10^{-1} \cdot \dot{E} \tag{121}$$

Therefore, the temperature difference between the calorimeter plate and the chamber is:

$$\begin{aligned} \Delta T_{cal-chamber} = T_{cal} - T_{chamber_{min}} &= \frac{1}{2} R_{cond_{6ss}} \cdot \dot{Q}_2 + \frac{1}{2} R_{cond_{6ss}} \cdot \dot{Q}_{2a} + R_{eq.2} \cdot \dot{Q}_{2aa} = K_1 \cdot \dot{E} \\ &= 1.38 \cdot \dot{E} \end{aligned} \tag{122}$$

Where K_1 is the thermal constant in $\left[K \frac{m^2}{W}\right]$. For a steady-state study, I can finally write the relationship between the temperature increase and the incoming thermal flux per surface unit, $\dot{E}$:

$$\dot{E}\left[\frac{W}{m^2}\right] = \frac{\Delta T_{cal-chamber}\ [K]}{K_1\left[K\,\frac{m^2}{W}\right]} = \frac{\Delta T_{cal-chamber}\ [K]}{1.38\ \left[K\,\frac{m^2}{W}\right]} \tag{123}$$

For example, for a $\Delta T_{cal-chamber} = 1°C,\ \ \dot{E} = 0.72\ W/m^2$. The heat flux per meter of vacuum chamber is linked to the temperature increase in the following way:

$$\dot{q}\left[\frac{W}{m_{chamber}}\right] = \dot{E}\cdot\frac{A_{1m\ liner}}{1\ m_{chamber}} = \frac{\Delta T_{cal-chamber}}{K_1}\cdot\frac{0.25}{1} = \frac{\Delta T_{cal-chamber}}{K_2} = \frac{\Delta T_{cal-chamber}\ [K]}{5.52\left[\frac{K\ m_{chamber}}{W}\right]} \tag{124}$$

Where K_2 is a second thermal constant, measured in $\left[K\,\frac{m_{chamber}}{W}\right]$. A $\Delta T_{cal-chamber} = 1°C$ corresponds to $\dot{q} = 181\ mW/m_{chamber}$.

- **Calibration tests with impedance**

The distributed heat load test was performed during beam operation. This calibration exploits the impedance heat load of a 50 ns beam as source. This particular fill had no EC and SR during the beam injection at 450 GeV. The temperature increases of the ten calorimeters are displayed as a function of the injection time in Figure 103, together with the beam currents. The calorimeters behave differently for the same heat load generated by the impedance between beam pipe and beam. In particular, we can distinguish the two classes of calorimeters, type B and type E. In general, the second group have much smaller temperature increase. This discrepancy can be attributed to the PT100 connection method and orientation to the calorimeter plate.

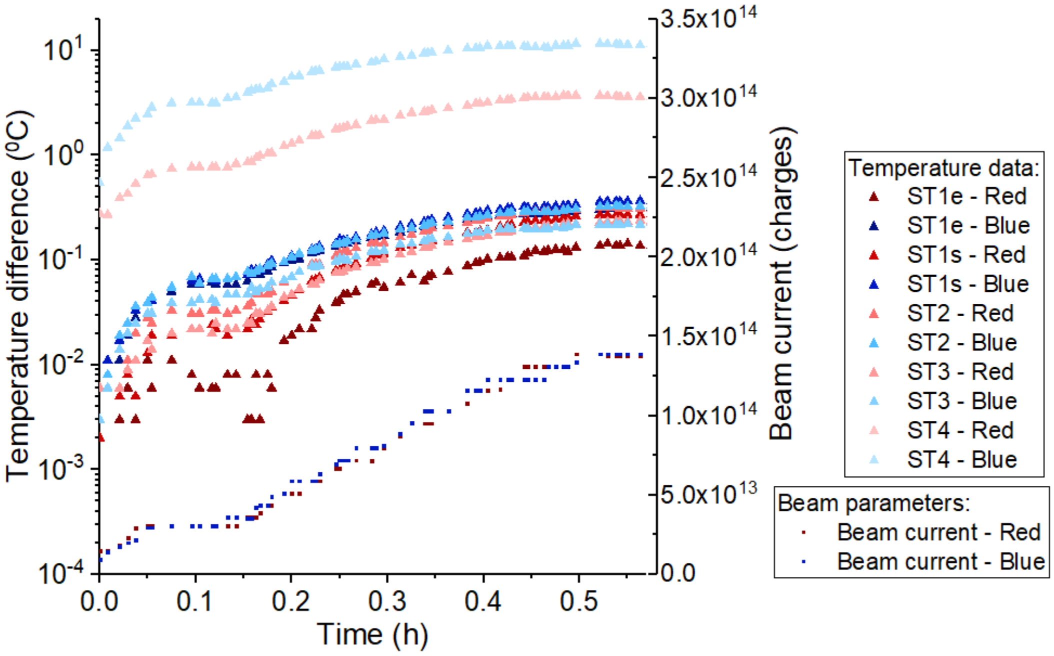

Figure 103: Temperature increases of the ten calorimeters during the injection for a 50 ns LHC beam, at 450 GeV.

The heat load due to wall-beam impedance, homogeneously distributed, can be calculated as following [89]:

$$P_{impedance}\left[\frac{W}{m}\right] = \frac{1}{2\pi R}\,\Gamma\left(\frac{3}{4}\right)\frac{N_b}{r}\left(\frac{\mathrm{nb}\ e}{2\pi}\right)^2\sqrt{\frac{c\ \rho\ Z_0}{2}}\ \sigma_t^{-\frac{3}{2}} \tag{125}$$

Where $2\pi R$ is the LHC storage circumference, Γ is the Gamma function, N_b is the number of bunches injected, r is the beam pipe radius, n_b e is the bunch charge that in the LHC case is simply the number of protons per bunch ppb, ρ is the resistivity of the beam pipe, Z_0 is the free space impedance, σ_t is the r.m.s. bunch length in time. The parameters of a 50 ns LHC beam are summarised in Table 6. For this beam, the beam-wall impedance heat load per unit of length is around $66.8\ mW/m_{chamber}$ after injection.

Table 6: Standard parameters for a 50 ns LHC beam, applied to calculate the distributed heat load due to beam-wall impedance.

Fill number		5980
Date		22/07/2017
$C = 2\pi R$	*[m]*	26659
$\Gamma(3/4)$		1.225416702
N_b		1284
r	*[m]*	0.04
n_b	*[protons]*	$1.98 \cdot 10^{11}$
e	*[C/proton]*	$1.6 \cdot 10^{-19}$
c	*[m/s]*	299792458
ρ	*[Ωm]*	$1.68 \cdot 10^{-8}$
Z_0	*[Ω]*	376.87
$4\,\sigma_t$	*[s]*	$1.19 \cdot 10^{-9}$
σ_t	*[s]*	$2.98 \cdot 10^{-10}$
$P_{impedance}$	*[W/m]*	0.0668

As depicted in Figure 104, for the same heat load, $P_{impedance}$, the equilibrium temperatures reached by each calorimeter differ. The temperature difference at equilibrium for a distributed heat load of 66.8 $mW/m_{chamber}$ are summarised in Figure 104 for the ten calorimeters as a function of VPS layout.

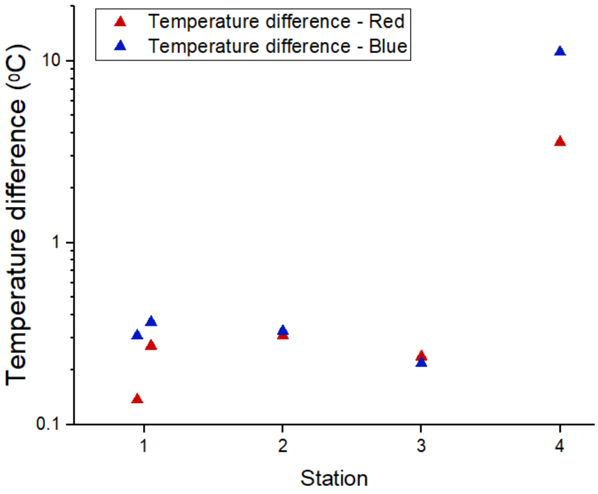

Figure 104: Steady-state temperature increases reached for a distributed heat load of 66.8 $mW/m_{chamber}$.

From the temperature increase measurements and the distributed heat load calculated with the formula, I can obtain the thermal constants per length of chamber, $K_{2_{calibration}}$, characteristics of each calorimeter:

$$K_{2_{calibration}} = \frac{\Delta T_{cal-chamber}\ [K]}{\dot{q}\left[\frac{W}{m_{chamber}}\right]} \tag{126}$$

These constants are useful to determine the steady-state heat loads applied into the calorimeter. Being the chamber temperature stable at 19 ºC during the LHC operation, the $\Delta T_{cal-chamber}\ [K]$ is consistent with the time evolution of the calorimeter plate. The $K_{2_{calibration}}$ values are summarised in Table 7 for the ten different calorimeters. The mean value of the first 8 calorimeters, type E, is around 4 $[K\,\frac{m_{chamber}}{W}]$. This is not far from the K_2 value calculated in Eq. (124). The type B calorimeters have a much higher thermal constant. The discrepancy is given by the PT100 orientation.

Table 7: Thermal constants, $K_{2_{calibration}}$, for the ten calorimeters.

Station	$K_{2_{calibration}}$ $[K\frac{m_{chamber}}{W}]$
ST1e - Red	2.05
ST1e - Blue	4.61
ST1s - Red	4.06
ST1s - Blue	5.48
ST2 - Red	4.61
ST2 - Blue	4.90
ST3 - Red	3.55
ST3 - Blue	3.25
ST4 - Red	53.52
ST4 - Blue	167.65

In order to study the time dependence, one can focus on the temperature increase all along the beam injections. In particular, during this 50 ns fill there were 20 injections, up to a total of 1284 bunches. The data of station 3 (blue pipe) can be compared to a thermal model (see Figure 105). To build this thermal model, I considered the steady-state temperature increase after the full injection and I attributed it to the impedance heat load of the 1284 bunch injection. Therefore, I found a mean value of temperature increase per bunch, considering a uniform bunch population among the injection. Then, I implemented the injection pattern in terms of timing and number of bunches injected. In this way, I could estimate the heat load contribution of each injection in a transient regime, i.e. considering the calorimeter time constant. . All the injection contributions are displayed with colourful lines on the bottom of the graph. It was possible to reconstruct the full time evolution of the calorimeter plate temperature increase as sum-up of all the injections, as displayed with a blue line in Figure 105. This model matches very well the time evolution of the calorimeter plate during injection. Note that the first injection is made only of 1 pilot and 12 bunches, while the other injections consisted of trains composed of 48 and 72 bunches per batch. Each additional bunch composed of $9.13 \cdot 10^{10}\, protons$ corresponds to $0.052\, mW/m_{chamber}$, equal to a temperature increase of $0.00017\ {}^{0}C$ for the ST3 - Blue.

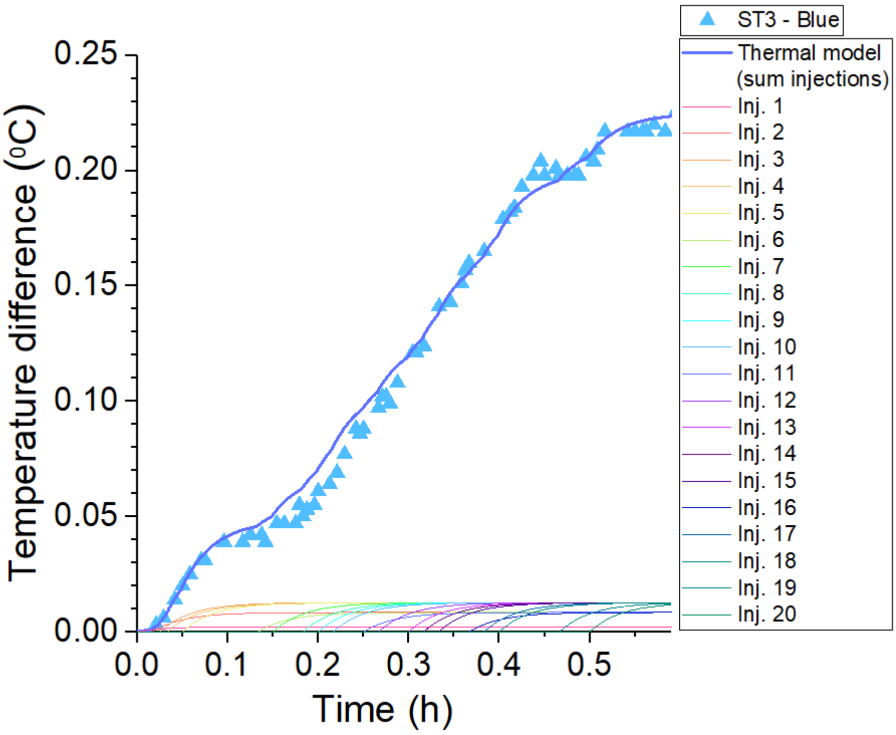

Figure 105: Temperature evolution of ST3 – Blue as a function of time for a 50 ns beam injection. The thermal model, sum-up of the 20 injection contributions, matches with the data.

The distributed power calibration has been performed with the impedance heat load of a 50 ns filling scheme at 450 GeV. The calibration allows to determine the values of thermal constants for the calorimeters, in terms of $K\,\frac{m_{chamber}}{W}$. These parameters are useful to convert the temperature increase into a power deposition value measured in W/m. Each calorimeter needs its own calibration to derive its real thermal constant. The behaviour of the calorimeters follows the model presented, if the heat load deposited is not extended for a long time (i.e. hours). During the LHC operation, the majority of the type E calorimeters suffered of high-capacitance effects, with much longer time constant. For this reason an investigation took place on the PT100 to determine if the orientation of the sensors could compromise the measurements.

3.3.3 Investigation on PT100 sensors

An investigation on the PT100 installation direction was performed. It was not possible for the company to provide the drawing of the PT100 inner circuit, therefore I decided to break few of them to see the electrical circuit. As shown in Figure 106 and Figure 107, the circuit is similar to the one of a strain gage, and the windings are positioned in transverse position. Their installation direction, together with the weak contact of the PT100 to the calorimeter plate, influenced the measurements and the discrepancy between type B and E installations.

Both type B and type E calorimeters had installed this model of PT100, but connected with different orientations. The type E calorimeter has the PT100 installed in transversal position with respect to the beam motion, therefore a long part of the windings is parallel to the beam direction and, so, to the image current running on the beam pipe. An effect could be induced on this kind of detectors.

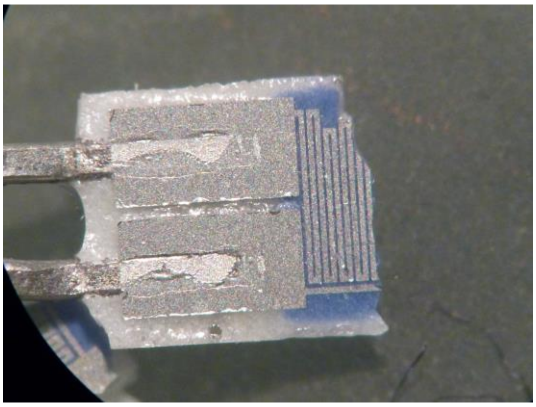

Figure 106: A zoom of a broken PT100, to illustrate the inner circuit of the sensor used for both type B and type E calorimeters.

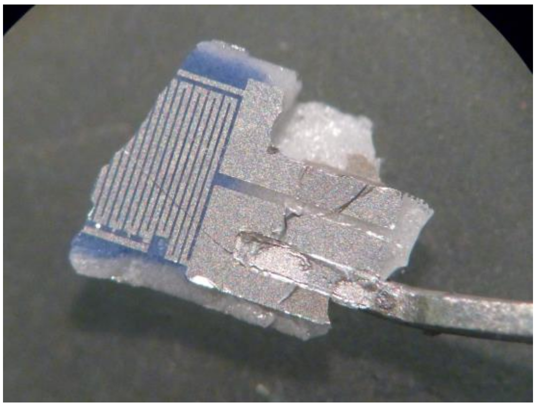

Figure 107: A zoom of a second broken PT100, to illustrate the inner circuit of the sensor used for both type B and type E calorimeters.

Chapter 4 Electron Cloud and Synchrotron Radiation signals

Electron cloud and synchrotron radiation generate heat loads, pressure increase and beam instabilities around the LHC machine. In particular, the most crucial effect of EC is the heat load deposited on different arcs around the LHC machine, exceeding the cooling system capacity and, therefore, limiting the machine operation, as in 2017.

The study of the gas desorption due to the EC is quite difficult to be performed inside magnets. The pressure measurements carried out with pressure gauges is affected by a big temperature difference between their installation at room temperature and the superconducting magnet temperature. This limitation reduces the information on the real EC behaviour.

For this reason, it has been decided to install the VPS system in a room temperature and field-free area to easily measured the EC dynamics in terms of electrical, pressure and thermal signals and compare it with simulations, the same used to foreseen the EC behaviour in the most challenging parts of machine.

The EC and SR monitoring with the VPS simultaneously allows to characterize the dependency with beam parameters and beam pipe properties, to infer the contribution of photoelectrons due to SR on the seed generation, to determine the energy kick received by the electrons due to the bunch passage acceleration, to study the surface conditioning with accumulated electron dose and the key role of a low surface SEY parameter. This study measures, as well, the composition of the desorbed gasses following the EC activity and the heat loads due to EC, SR and beam-wall impedance. This complete overview on the EC evolution will be useful to validate the existing simulating codes.

This chapter has three parts. In the first part, the electrical signals acquired with the shielded pick-ups are analysed. The EC signals are studied as a function of the beam parameters for the three surfaces. Oscilloscope measurements show the real time shape of the EC, along a batch and over the entire machine. Then, the electron energy spectrum is derived using a dedicated detector. This part concludes with the analysis of the evolution of the surface properties with the accumulated electron dose. The main results were presented in different conferences or published [22] [90] [91].

The second part concerns the pressure measurements. Attention is given to the signals as a function of beam pipe properties and beam parameters. The pressure influence between stations is also discussed for the a-C surface [22] [90]. Conditioning effect during the scrubbing and along few months of operation is discussed and the Electron Stimulated Desorption parameter is estimated for Cu. The composition of the gas released during beam operation is analysed at 450 GeV and 6.5 TeV. The last paragraphs are dedicated to an indirect measurement of EC from pressure profiles.

The third part analyses the temperature evolution of the beam pipe along a fill in order to estimate the heat loads and their origin. Not only can the electron activity and the SR heat up the beam pipe, but also the beam-wall impedance contribution must be taken into account. The analysis of the power deposition into the beam pipe for different LHC beams is presented comparing the electrical and pressure measurements, with the calorimeter. Particular importance is given to the bunch length parameter, whose dynamics influences the impedance and EC heat loads.

4.1 Electrical signals

The first analysis considers the EC signals (acquired by shielded pick-ups and the energy spectrum analysers) and the beam signals (recorded by unshielded pick-ups). The shielded pick-ups signals were acquired with picoammeters and oscilloscopes, to track the integrated activity and the real time behaviour, respectively. Firstly, the evolution of EC as a function of beam parameters (i.e. number of bunches, bunch population, bunch length, bunch spacing, beam energy and filling pattern) is presented for the three surfaces. Secondly, the fast-time signals recorded with the oscilloscopes are shown. Thirdly, the energy spectra of the EC are provided at 6.5 TeV. Last, the evolution of the surfaces properties is studied as a function of the accumulated electron dose along the scrubbing period and during two years of LHC operation.

4.1.1 Beam parameter influence on EC

During the injection phase of a standard 25-ns fill, the influence of the number of bunches on the EC was studied. At the end of the injection phase at 450 GeV, the influence of the bunch population was measured. At the beginning of the energy ramp-up the bunch length was analysed. The bunch spacing (25 ns and 50 ns) was analysed comparing two fills. The contribution of photoelectrons due to SR was disentangled from the total EC phenomenon. Finally, different filling schemes are compared.

- **Influence of the number of bunches**

A typical LHC beam (fill 5800) is chosen to study the EC signal as a function of the number of bunches, N_b. This fill was performed at the beginning of 2017, during the scrubbing run at 450 GeV. This beam was made of 2820 bunches, with an average of $1.19 \cdot 10^{11}$ protons per bunch at injection. Since the beginning of the 2017 operation the electron doses accumulated until this fill were significantly large, around $1.5 \cdot 10^{-3}\ C/mm^2$ for the Cu surface, $3 \cdot 10^{-4}\ C/mm^2$ for the ex-situ NEG and $1.2 \cdot 10^{-7}\ C/mm^2$ for the a-C surface. Therefore, each electron dose accumulated during the successive fill can be neglected with respect to the total accumulated one.

The EC signals for the three surfaces are shown in Figure 108 and Figure 109 as a function of N_b. The collected signals increase linearly with N_b. As expected, the higher the SEY, the larger the EC signal. Copper shows the largest EC signal, followed by the ex-situ NEG and the a-C coated beam pipes. The linear behaviour seen in the a-C station was only observable at the beginning of 2017.This is probably linked to an initial surface contamination following the end of the year stop (2016).

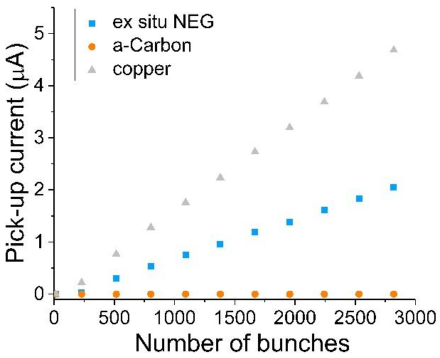

Figure 108: Electrical signals (A) as a function of the number of bunches during the injection phase of a 25-ns standard LHC beam in linear scale.

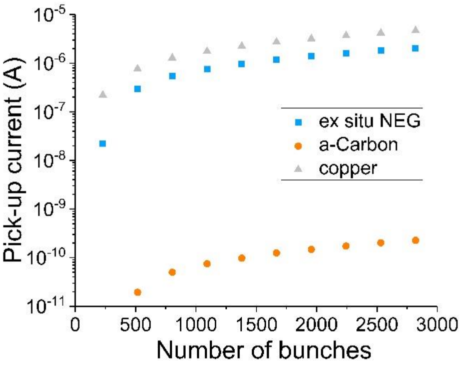

Figure 109: Electrical signals (A) as a function of the number of bunches during the injection phase of a 25-ns standard LHC beam in logarithmic scale.

The slope of the linear signals are reported in Table 8.

Table 8: Slopes of the EC increase as a function of the number of bunches, for the three surfaces.

Surface	$slope\ [A_{EC}/bunch]$
Copper	$1.7 \cdot 10^{-9}$
Ex situ NEG	$7.5 \cdot 10^{-10}$
a-Carbon	$8.5 \cdot 10^{-14}$

- **Influence of the bunch population**

At the end of the injection phase, the bunch population decreases due to proton losses. The initial value was around $1.19 \cdot 10^{11}$ protons per bunch (fill 5800). After several hours of beam circulation, the bunch population was halved. The effect of bunch population on the EC is linked to the beam electromagnetic field that accelerates the free electrons. The beam electric field is proportional to the bunch charges and the electron energy kick depends on the electron position at the time of the bunch passage [40].

The EC signals are shown as a function of the number of protons per bunch, ppb, in Figure 110 and Figure 111. Above the multipacting thresholds, the three signals increase linearly. The SEY influences significantly the EC magnitude. The highest current is reached by the Cu sample, followed by ex-situ NEG and a-C coatings. The threshold, visible in linear scale, corresponds to the curve inflection point in the logarithmic scale. The slopes and the thresholds are reported in Table 9.

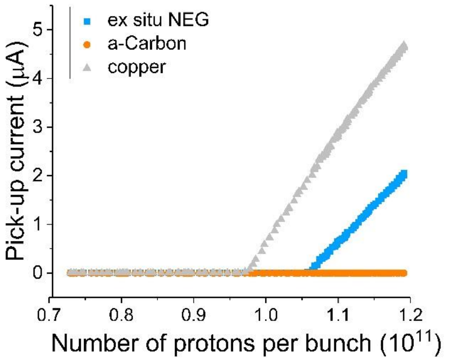

Figure 110: Electrical signals as a function of the number of protons per bunch after the injection phase of a 25-ns standard LHC beam in linear scale.

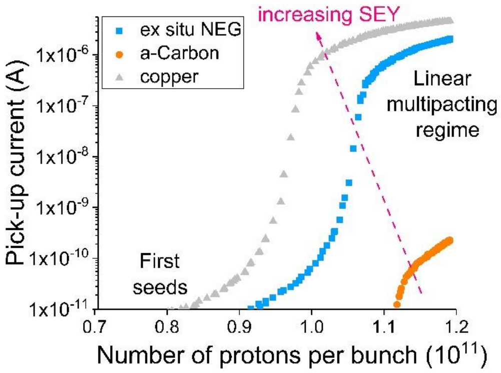

Figure 111: Electrical signals as a function of the number of protons per bunch after the injection phase of a 25-ns standard LHC beam in logarithmic scale.

Table 9: Slopes of the linear EC increase as a function of the bunch population and multipacting threshold values for the three surfaces.

Surface	$\boldsymbol{slope\ [A_{EC}/proton]}$	$\boldsymbol{Threshold\ [protons/bunch]}$
Copper	$2.0 \cdot 10^{-16}$	$9.6 \cdot 10^{10}$
Ex situ NEG	$1.5 \cdot 10^{-16}$	$1.06 \cdot 10^{11}$
a-Carbon	$2.9 \cdot 10^{-20}$	$1.12 \cdot 10^{11}$

- **Influence of the bunch spacing**

Here I present the comparison between two bunch spacings, the first with 50 ns (fill 5980) and a standard LHC fill performed with 25 ns (fill 5979). These two fills are consecutive so one can assume no change in the electron dose. The parameters of the two fills are summarised in the following table.

Table 10: Beam parameters of the two analysed fills.

Fill No.	***Bunch spacing [ns]***	***Number of bunches***	***Protons per bunch***	***Beam current [A]***
5980	50	1284	$9.13 \cdot 10^{11}$	0.25
5979	25	2556	$1.12 \cdot 10^{11}$	0.51

With 50 ns bunch spacing, no EC build up is expected during the injection phase. Even if the first electron seeds are accelerated during the bunch passage, the bunch distance is so large that the number of survival electrons, i.e. the electrons reflected or backscattered until the next bunch arrives, is negligible and no EC multipacting occurs.

As shown in Figure 112, during a fill with 50 ns bunch spacing there is no EC current at injection energy. However, above 2.8 TeV, photoelectrons are detected because a significant fraction of impinging photons from synchrotron radiation have an energy above the work function of Cu ($4 \div 5$ eV). In the absence of multipacting, the electron currents measured at 6.5 TeV correspond to the number of photo-electrons generated and are directly related to the PEY of the surfaces.

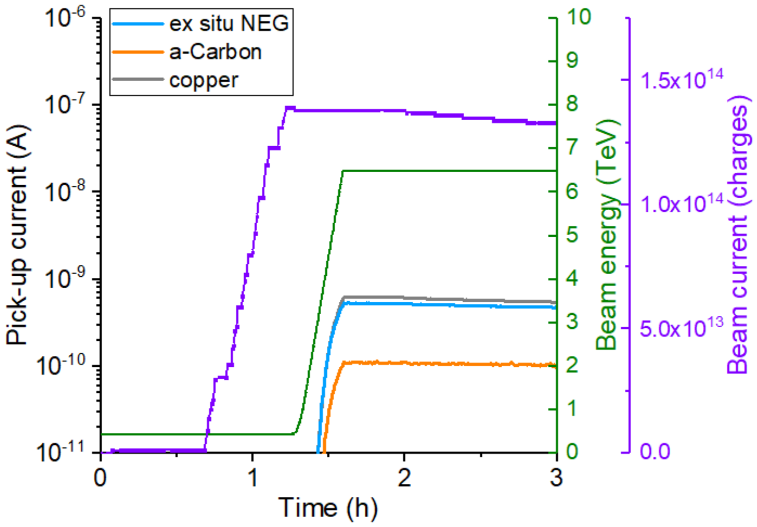

Figure 112: The photoelectron signals of a 50 ns bunch spacing beam are displayed in logarithmic scale. The beam current and the beam energy are displayed in dark purple and green, respectively.

Table 11: Photoelectric currents measured at 6.5 TeV and the estimation of the PEY (see Eq.(7)) for the three materials.

Surface	**Photoelectron current [A]**	**Photon Yield (PEY)**
Copper	$1.25 \cdot 10^{-9}$	0.05
Ex situ NEG	$1.06 \cdot 10^{-9}$	0.04
a-Carbon	$2.16 \cdot 10^{-10}$	0.01

With 25 ns bunch spacing, the EC build-up due to multipacting is expected for a surface with a large enough SEY. During the beam injection phase, once the multipacting regime starts, the EC current is proportional to the number of bunches as presented above and therefore to the beam current (see Figure 110). When the beam injection finishes, the EC signal decreases due to proton losses. This is the case for ex situ NEG and Cu, while a-C has no visible signal, thanks to its low SEY.

With the energy ramp-up, the EC multipacting signal is influenced by the bunch length, which is inversely proportional to the square root of the beam energy [92]. In the LHC, when the bunch length reaches a value below 8 10^{-10} s, longitudinal instabilities starts. As consequence, RF noise is injected in the superconducting cavities to increase the length of the bunches. In the meantime, the beam energy continues to rise, still contracting the bunch. The impact of the bunch length dynamics is observed on the EC signals, in particular on the Cu surface. The shorter the bunch length, the stronger the electron energy kick. If the average electron gain were above few hundreds eV, the electrons would tend to penetrate into the surface so deeply that the number of secondary electrons would decrease, reducing the multipacting effect.

As previously explained for the 50 ns fill, above 2.8 TeV, photoelectrons provide an additional contribution to the EC signals in all the surfaces, a-C included.

At the collision energy, once the LHC is in stable beam phase, the proton-proton collisions start. The EC current behaviour is mainly driven by beam losses, i.e. the bunch population decay due to the physic collisions at the IPs. On average, each standard collision consists of 40 protons per bunch lost.

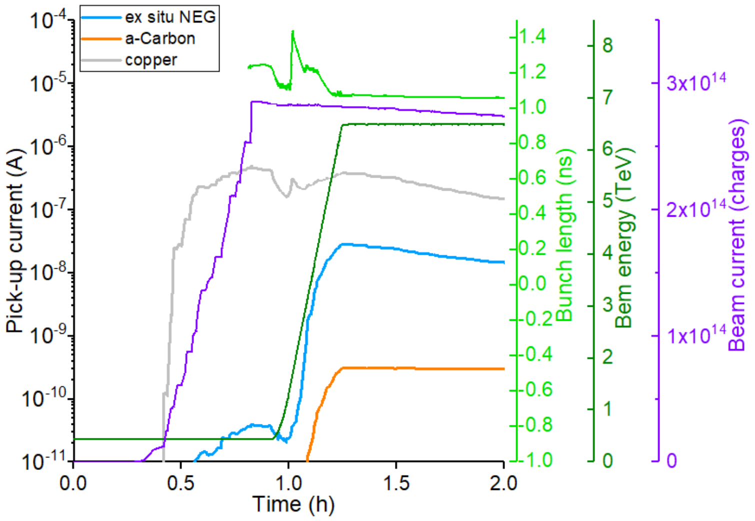

Figure 113: The EC signals of a 25 ns bunch spacing beam are displayed in logarithmic scale. The bunch length, the beam current and the beam energy are displayed in light green, dark purple and dark green, respectively.

- **Influence of the bunch length**

For the same fill, the bunch length was studied at the beginning of the energy ramp-up, as described in the previous paragraph. In Figure 114 the EC signal measured on Cu is displayed as a function of the bunch length. The Cu signal was chosen because its variation was significant if compared to that of the other surfaces. The EC behaviour is linear with increasing bunch length even if the data are scattered due to the time interpolation. Shorter the bunch, higher the linear proton bunch density, higher the EM field, higher the mean electron energy kick. The electron distribution along the radial position can change. The high-energy electron ring around the bunch might become closer the bunch centre and the electron current read at the beam pipe wall may decrease.

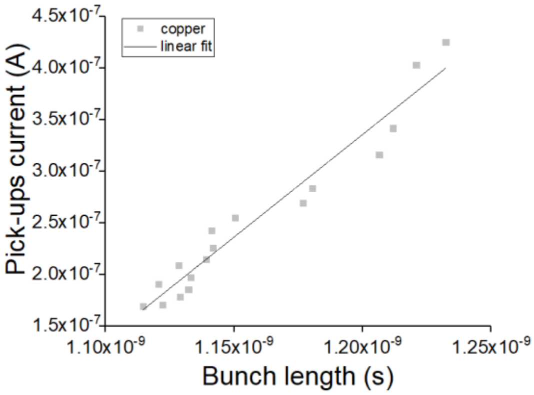

Figure 114: Electrical signal on Cu as a function of the bunch length at the beginning of the energy ramp-up of a 25-ns standard LHC beam in linear scale.

- **Influence of the filling scheme**

During 2017, different filling schemes were adopted. The energy was ramped up to 6.5 TeV. In addition to the 50 ns beam spacing, three beam schemes were investigated: 8 bunches 4 empty (8b4e), 12 and 48 bunches per batch. For each beam, the signals were normalised to the standard beam current of 2556 bunches (48 bunches fill). The contributions of photoelectrons are also calculated normalising the collected signals obtained with the 50 ns beam to the beam current. The relevant beam parameters are summarized in Table 12.

Table 12: Information related to the different filling scheme.

Fill No.	***Bunch spacing (ns)***	***Number of bunches***	***Bunches per batch***	***Protons per bunch***
6174	25	1916	8b4e	$1.06 \cdot 10^{11}$
5717	25	75	12	$1.18 \cdot 10^{11}$
5887	25	2556	48	$1.17 \cdot 10^{11}$
5980	50	1824	24	$9.13 \cdot 10^{10}$

The EC and photoelectron signals of Cu are shown in Figure 115, Figure 116 and Figure 117, for 8b4e, 12 and 48 bunches per batch fills. The beam energy and the beam current are also displayed as a function of time. Time $t = 0$ is arbitrarily set at the beginning of the energy ramp-up to align the measurements. During the beam injection at 450 GeV, the EC increases linearly with the number of bunches for the Cu surface only with the standard 48 bunches per batch structure. No EC is detected at injection energy for the other two cases. Above 2.8 TeV, the photoelectron production becomes visible in all the three schemes. The multipacting is then driven by the photoelectron seeds, as presented in dark colours on the plots. The higher the number of consecutive bunches, the higher the multipacting of photoelectrons. At collision energy, the collected current for the standard 48 bunches per bunch decays following the bunch population evolution as explained in the first paragraph of this chapter.

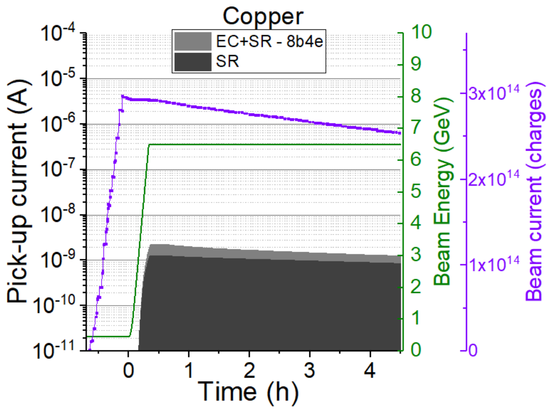

Figure 115: EC dynamics along a 8b4e fill, comparing the total EC build-up with of the effect of photoelectrons for Cu.

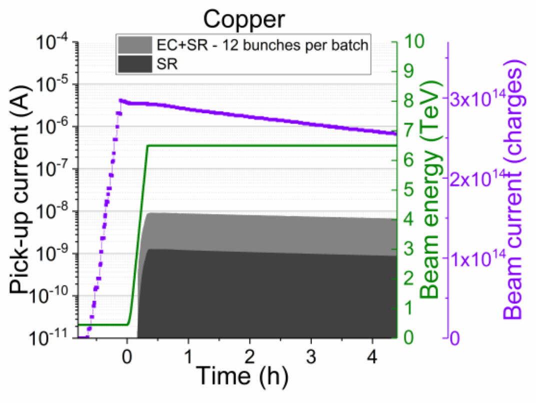

Figure 116: EC dynamics along a 12 bunches per batch fill, comparing the total EC build-up with of the effect of photoelectrons for Cu.

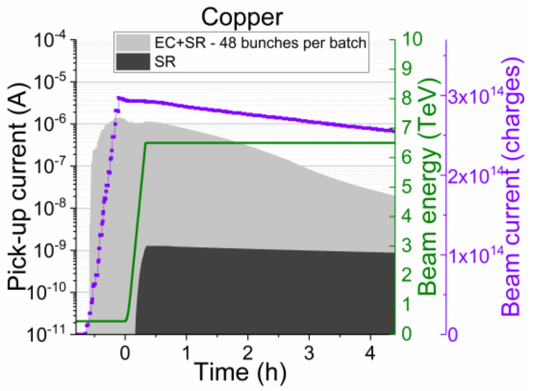

Figure 117: EC dynamics along a 48 bunches per batch fill, comparing the total EC build-up with of the effect of photoelectrons for Cu.

Similar plots are shown for the ex- situ NEG. At injection energy, EC signals appears only for the 48 bunches per batch fill. This might be explained by the need of 6 to 10 bunches for the EC build-up process to start and stabilize, as the oscilloscope measurements will show in the following section. With batches of less than 12 bunches, the EC multipacting mechanism is interrupted as soon as generated at the end of each batch, so the cloud is not sustained and is not measurable by the VPS pick-ups. Above 2.8 TeV, the photoelectron contribution is detected. The three signals are higher than the photoelectron currents but follow its trend. A weak multipacting is present at collision energy for 8b4e, an higher signal is detected for the 12 bunches per batch filling schemes, while the standard 48 bunches per batch has an important multipacting already at 450 GeV (see Figure 120).

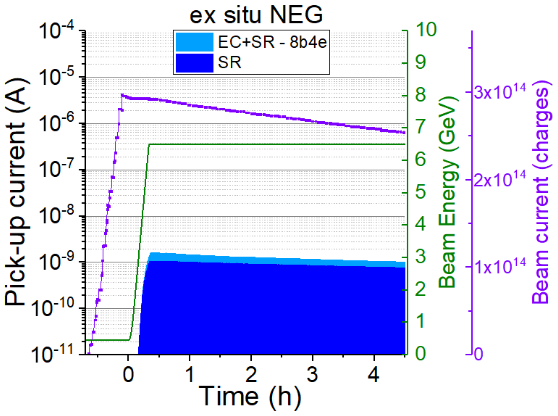

Figure 118: EC dynamics along a 8b4e fill, comparing the total EC build-up with of the effect of photoelectrons for ex situ NEG.

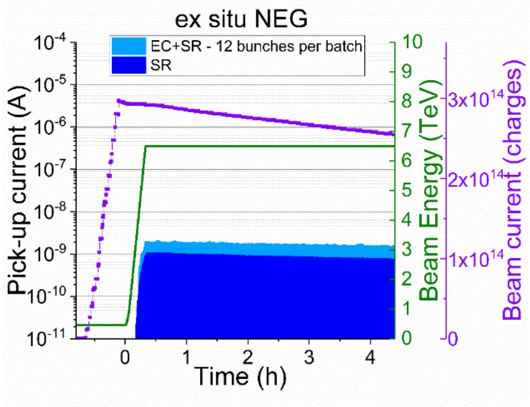

Figure 119: EC dynamics along a 12 bunches per batch fill, comparing the total EC build-up with of the effect of photoelectrons for ex-situ NEG.

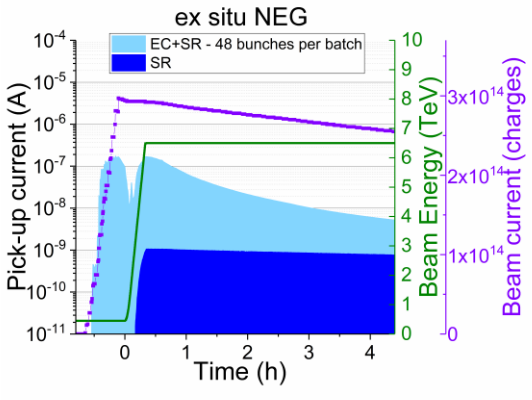

Figure 120: EC dynamics along a 48 bunches per batch fill, comparing the total EC build-up with of the effect of photoelectrons for ex-situ NEG.

The a-C coating shows electrical signals only related to the photoelectron activity (see Figure 121, Figure 122 and Figure 123). In any case, after the scrubbing period, no signal on a-C was detected at 450 GeV. The small mismatch between the estimation of photoelectrons and the acquired signals could be attributed to a measurement error propagation due to the normalisation process or to a real tiny photoelectron multipacting. Hence, the value of the a-C surface SEY can be estimated to be very close to 1.

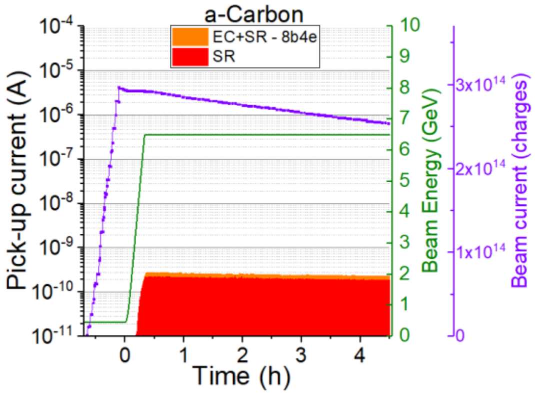

Figure 121: EC dynamics along a 8b4e fill, comparing the total EC build-up with of the effect of photoelectrons for a-Carbon.

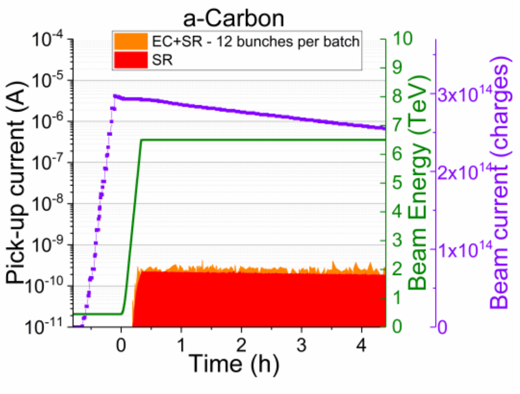

Figure 122: EC dynamics along a 12 bunches per batch fill, comparing the total EC build-up with of the effect of photoelectrons for a-Carbon.

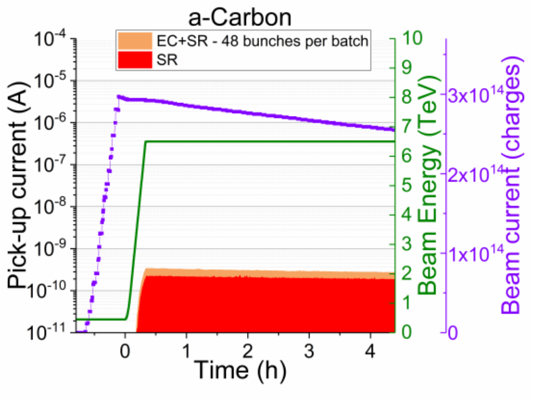

Figure 123: EC dynamics along a 48 bunches per batch fill, comparing the total EC build-up with of the effect of photoelectrons for a-Carbon.

4.1.2 Oscilloscope measurements

This paragraph presents beam and EC signals, respectively measured by shielded and unshielded pick-ups connected to two oscilloscopes. As for the picoammeter measurements, the shielded pick-ups connected to the oscilloscopes have a +9 V bias applied to the electrode. Four different oscilloscope measurements are presented in see Table 13. The fills have different numbers of bunches, bunches per batch, bunch population and beam energy.

Table 13: The fill parameters of the beams analysed below are here presented.

Fill No.	*Bunch spacing (ns)*	*Number of bunches (Blue)*	*Number of bunches (Red)*	*Bunches per batch*	*Initial bunch Population (Blue)*	*Initial bunch Population (Red)*	*Beam energy reached (GeV)*
5765	25	2040	2100	72	$1.03 \cdot 10^{11}$	$1.01 \cdot 10^{11}$	450
5794	25	2820	2820	48	$1.16 \cdot 10^{11}$	$1.17 \cdot 10^{11}$	450
5878	25	2460	2460	48	$1.10 \cdot 10^{11}$	$1.11 \cdot 10^{11}$	6500
6594	25	339	339	12	$1.13 \cdot 10^{11}$	$1.13 \cdot 10^{11}$	6500

- **First EC signals on Cu at 450 GeV**

The first signal was acquired during 2017 and the first data refers to the fill 5765, acquired on the blue pipe that was connected to the oscilloscope 2. The beam was made of 2100 bunches and kept at 450 GeV (scan taken on 07/06/2017 at 14:08). There were 8 trains of batches, composed of 72 bunches. The EC signal was measured only on the copper station. No signals were detected on the other surfaces, probably due to too large background noise. The beam and EC signals of the full machine are displayed in Figure 124 in black and grey, respectively. The EC signal is negative because negatively charged particles, i.e. electrons, are collected. The first batches do not register any EC signal. This is linked to a different bunch population, visualized by the amplitude of the black signal. Once the n_p threshold is reached and the EC stimulated, the EC signal dies at the end of each batch.

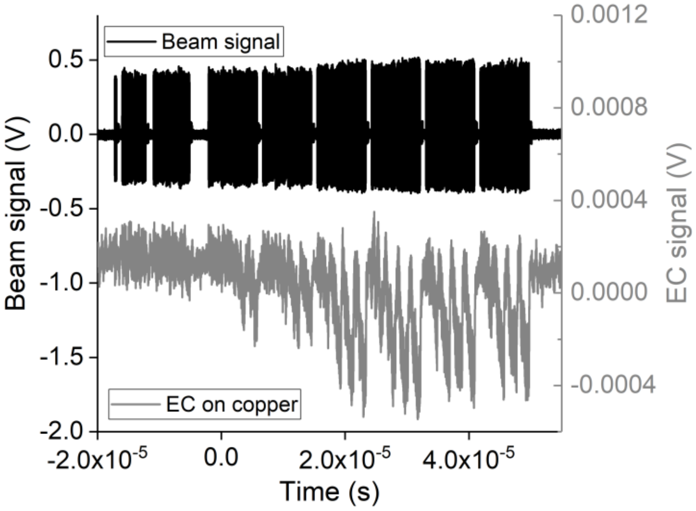

Figure 124: EC signal of the full ring (trains 1 to 8) is measured on Cu with an oscilloscope.

Figure 125 zooms on the last four batches of this fill. At the beginning of a new train the EC signal is weaker than at the end of the same train. At the end of the last trains, the EC seems to reach an equilibrium when the EC multipacting regime takes place.

Figure 126 presents a zoom of the third batch, composed of 72 bunches. The EC signal increases linearly bunch after bunch. The multipacting regime seems to be reached at the end of the batch, when the signal stabilizes at -0.4 mV.

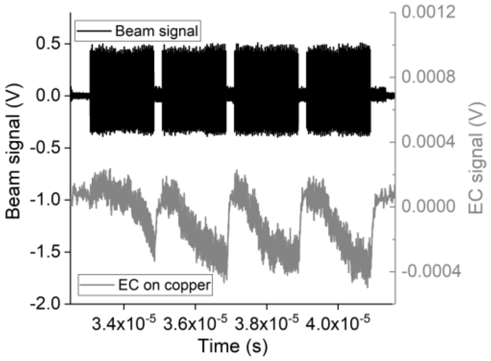

Figure 125: EC detail taken on the last train (#8) of this fill.

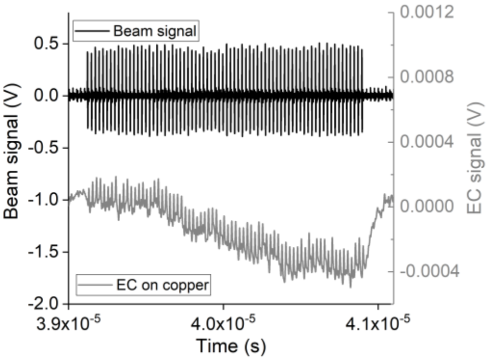

Figure 126: EC detail taken on one batch (batch xx of train xx) of this fill.

- **Comparison of ex-situ NEG and Cu signals at 450 GeV**

A second oscilloscope measurement is here presented, for fill 5794, acquired on the red pipe that was connected to the oscilloscope 1. This beam was kept at 450 GeV (scan taken on 10/06/2017 at 13:08). A signal was visible on the Cu and the ex-situ NEG stations (see Figure 127), while no signal was visible on a-Carbon.

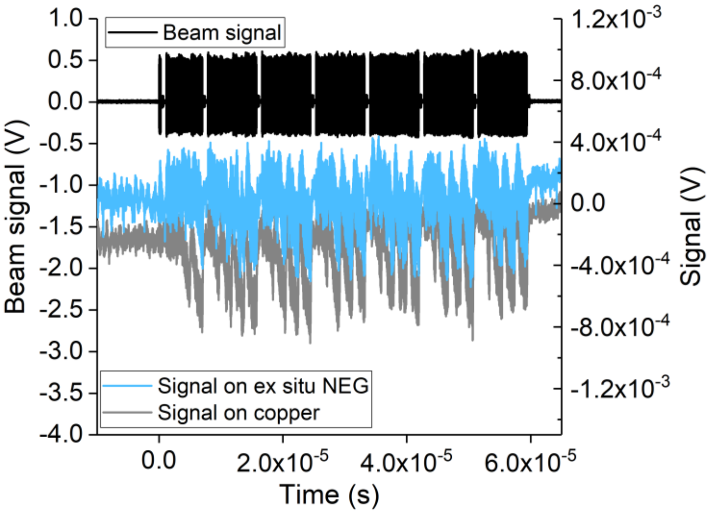

Figure 127: EC signals of the full ring (trains 1 to 7) are measured on Cu and ex-situ NEG with an oscilloscope.

Figure 128 zooms on the beginning of the fill, in particular on the pilot bunches and the first train. The EC signal is visible on the two batches on the Cu beam pipe, while only on the third batch for the ex-situ NEG coating. For this reason the surface SEY of this second material must be smaller than for Cu.

In Figure 129 a zoom of the last train is presented. The EC signal starts increasing at the end of the first batch for Cu and then for the following batched it starts much before. The ex situ NEG surface behaves slightly better than Cu due to a lower SEY.

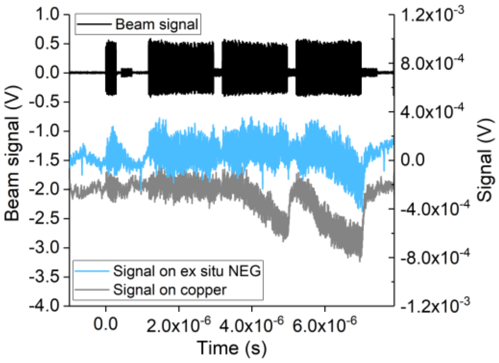

Figure 128: EC signals taken on the first train of this fill for ex-situ NEG and Cu.

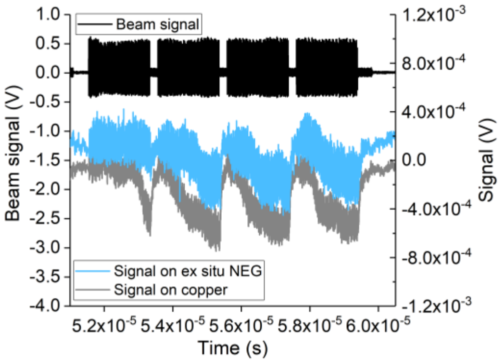

Figure 129: EC signals taken on the last train of this fill for ex-situ NEG and Cu.

- **EC multipacting signals on Cu at 6.5 TeV**

The third observation concerns a fill at 6.5 TeV (fill number 5878, performed on 27/06/2017 at 17:00) consisting of 2460 bunches separated by 25 ns. Figure 130 shows the EC signal measured only on Cu, for a full machine turn. The signal is much larger than in Figure 135 because also SR takes part into the EC seed generation, sustaining the EC multipacting regime.

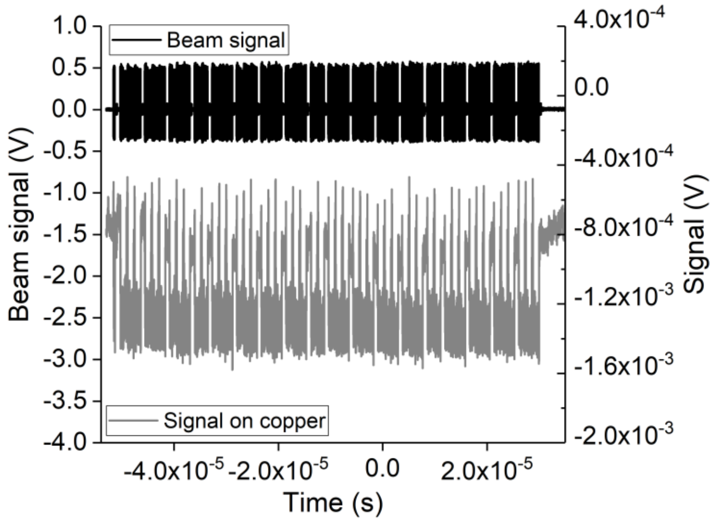

Figure 130: EC signals of the full ring are measured on Cu and ex-situ NEG with an oscilloscope.

Figure 131 zooms on the beginning of the fill, in particular on the 12-bunches batch followed by the first two trains of three batches each. The EC signal is visible everywhere on the Cu beam pipe. The EC multipacting regime is reached starting from the pilot bunches and it dies after each batch.

In Figure 132 a zoom of the last two trains is shown. The EC signal are similar to those registered at the beginning of the fill. At 6.5 TeV, the multipacting regime is then sustained all along the fill.

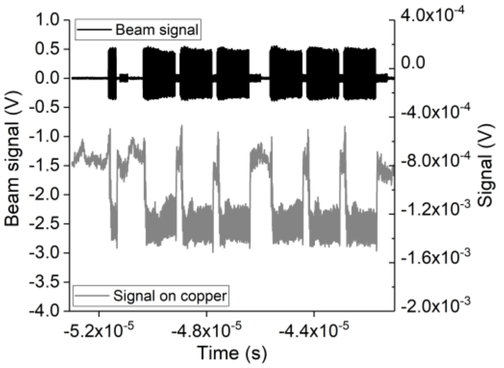

Figure 131: EC signals taken on the first two train of a 6.5 TeV fill on a Cu surface.

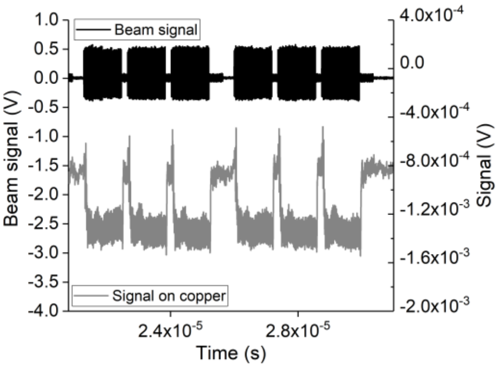

Figure 132: EC signals taken on the last two train of a 6.5 TeV fill on a Cu surface

For the same fill, other two zooms are presented here. The first focuses on the EC activity along a single batch (see Figure 133). The equilibrium is clearly visible and it corresponds to the multipacting regime. The second one, Figure 134, shows the beginning of the same batch. A delay of around 30 ns is present between the beam signal and the EC, due to different cabling length. Nevertheless, 6-to-8 bunches are needed to reach EC multipacting equilibrium. For this reason, the so-called 8b4e filling scheme is applied to the LHC when the EC signal is too strong. In this latter case, the EC growth is stopped before the multipacting regime is established. Please note that the 25 ns bunch distance is also clearly visible on the beam signal (Figure 134).

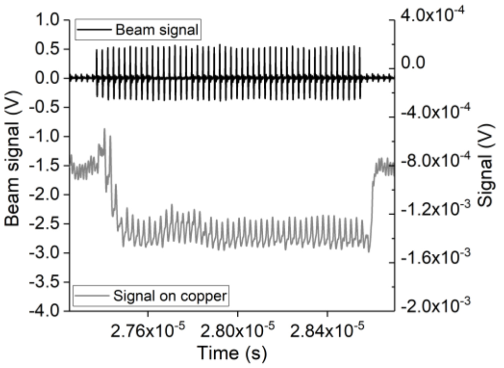

Figure 133: EC signal along a batch (batch no. 2 of the last train) for a Cu surface at 6.5 TeV.

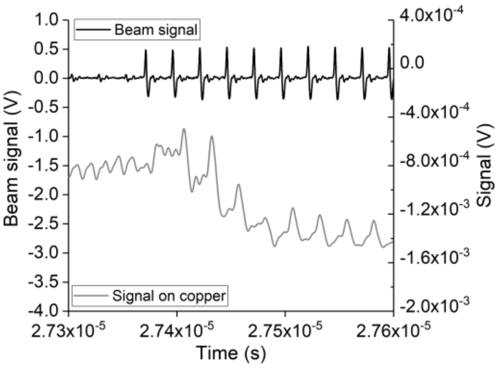

Figure 134: EC signal at the beginning of a batch (batch no. 2 of the last train) for a Cu surface at 6.5 TeV.

- **EC multipacting signals on Cu at 450 GeV and 6.5 TeV**

The last observation presents the EC signal on Cu at 450 GeV and at 6.5 TeV. The scans were performed on 22/04/2018 at 8:17 and 10:34, respectively (fill number 6594). Before these measurements, amplifiers and filters were applied at the signal output to amplify and smooth the readings. This was possible thanks to the collaboration with M. Gasior and M. Wendt from the CERN Beam Department. The amplifiers have a gain of 650 (equivalent to 56 dB), a bandwidth between 5 kHz and 10 MHz, 50 Ω input impedance, a 9 V input bias through 1 MΩ, and reversed the signals.

The fill analysed consisted of 339 bunches separated by 25 ns bunch spacing, divided in 31 beam injections of 12 bunches each. Figure 135 shows the EC signal measured on Cu for the first seven batches. The light signals refer to the 450 GeV measurements, while the dark grey to the 6.5 TeV. In both case, the signals reach equilibrium, i.e. the EC multipacting regime. Figure 136 presents a zoom along one batch. The signal at 6.5 TeV is higher due to the contribution of photoelectrons. The oscillations between bunches are wider.

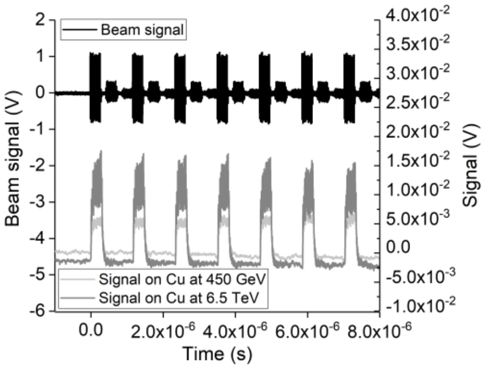

Figure 135: EC multipacting signals along seven batches for a Cu surface at 450 GeV and at 6.5 TeV.

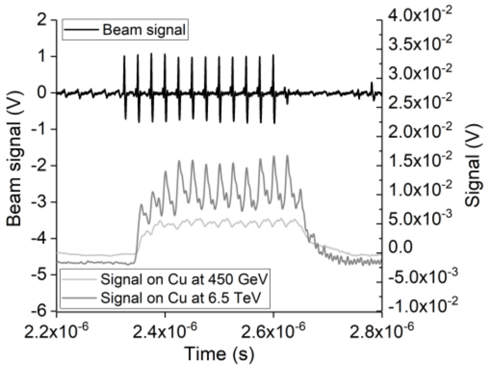

Figure 136: EC multipacting signals along one batch (batch no.2) for a Cu surface at 450 GeV and at 6.5 TeV.

4.1.3 Electron energy spectrum

Not only the EC electrical signals, but also its energy spectra were measured for the first time in the LHC machine thanks to the VPS system. The energy detectors are installed only on station 4 (Cu surface), for both beam pipes. The two electron energy detectors are composed of a double grid to accelerate the electrons, as presented in the *Chapter 2*. The voltage is varied from 0 to -1250 V and vice versa. For each voltage value applied to the grid, a current, proportional to the electron flux impinging on the pick-up is read. This current is proportional to the number of electrons with an energy (eV) above the applied bias (V). The measurements presented refers to the fill 4528 (25ns bunch spacing beam, $N_b = 1825\,bunches$, $I_{beam} = 1.8 \cdot 10^{14} charges$) performed at 6.5 TeV. The measurements were not automatic and they required a long time to be performed. For this reason, it was not possible to perform scans at 450 GeV. Later, an automatic scan was applied but the measurements were not precise and not significant.

The measured currents are negative due to the electron charges entering the picoammeter. The absolute value of the currents is displayed as a function of the absolute value of the voltage (see Figure 137). The current decreases with increasing voltage bias because the detectors collect the electrons with an energy above the applied bias. Note that the x-axis is displayed in logarithmic scale.

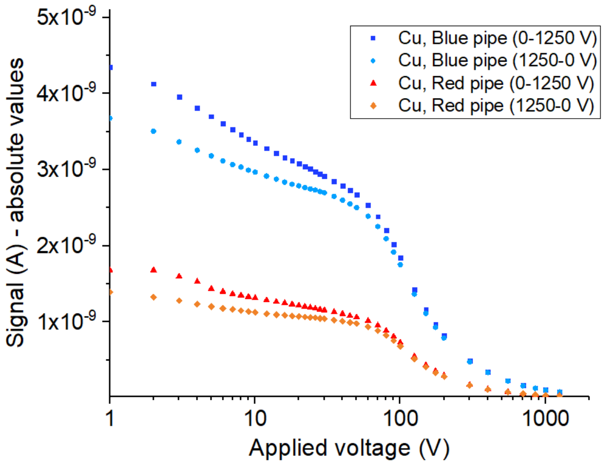

Figure 137: The absolute value of the EC signals are displayed as a function of the absolute value of the applied bias, for blue and red copper detectors. The voltage is scanned from 0 V to 1250 V and vice versa.

This is not the spectrum, it is the integral of all the charges collected as a function of the applied voltage, i.e. particle energy in eV. The derivation of each curve gives a electron energy spectrum, as defined in Eq. (47). The spectra were afterwards normalised at 2 eV to allow the comparison. The normalised spectra are displayed as a function of the electron energy in Figure 138. At stable beam, the spectra present two regions, one at few eV and the second one at around 90-100 eV. The low-energy part corresponds to the secondaries; the high-energy electrons corresponds to the accelerated electrons by the bunch passages. In between, the minimum of the curve is reached at around 50 eV. The mean energy of this spectrum is around 3 eV.

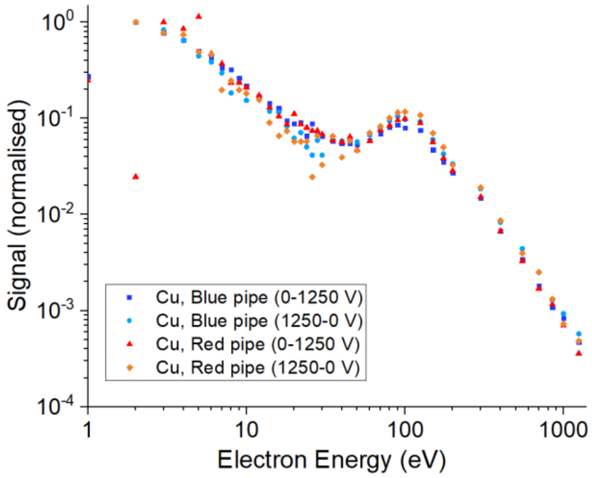

Figure 138: EC energy spectra normalised at 2 eV, of a 25 ns stable beam at 6.5 TeV (fill 4528).

The amount of electrons above 50 eV, i.e. the integral of the electron distribution above this energy, is around 6-7% of the total number of electrons. An energy value of 50 eV value corresponds to the minimum electron energy gained from the EM field of the bunch when the electrons are located at the beam pipe wall (see the calculation of ΔE_{wall} on Eq. (21)). Above 50 eV, the accelerated electrons are located closer to the bunch.

Considering the limits of the energy spectrum detector explained in *Chapter 2*, the reflected electrons are not all measured and the low energy peak could be much larger than the measured one. For this reason, a simulation was run with PyECLOUD by G. Iadarola. The comparison between the data and the simulation for an 80 mm diameter beam pipe is shown in Figure 139. The signals are normalised to the 90 eV peak value. The data and the spectrum have a similar behaviour, despite a small shift on the accelerated peak.

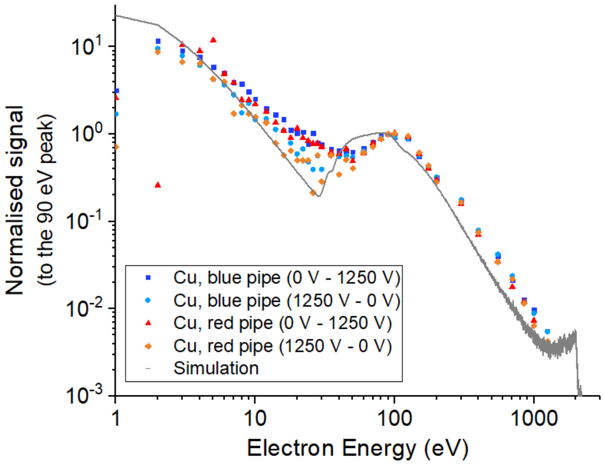

Figure 139: EC energy spectra normalised at 90 eV. The data are compared with a simulation performed by G. Iadarola with PyECLOUD.

At this point, it would be interesting to extract the electron distribution along the radius. To do so, I can consider just the accelerated peak on the energy spectrum, i.e. the peak centred at 90-100 eV. These electrons are responsible for the multi-pacting process and are the source of secondaries. Therefore, I consider only the electrons with an energy above 50 eV, equivalent to the electron kick at the wall, and 1250 eV, i.e. the maximum signal measured. Following the kick approximation [40], each energy corresponds to a certain distance from the beam pipe centre. Therefore, I can estimate the position where the electrons were at the time of the kick. The integrated distributions of the electrons as a function of their radial position are shown in Figure 140 and Figure 141, in linear and logarithmic scale. These signals are normalised to the 90 eV signal, corresponding to a distance or radius of 3.15 cm. The maximum electron energy measured by the spectrum, 1250 eV, corresponds to a radius of around 0.8 cm. The LHC transverse beam size at the VPS location is around 0.5 mm. These signals are proportional to the integrated number of electrons per defined radius; the larger the radius is, the larger is the ring area where the electrons are distributed. The signals have a maximum corresponding to around 90-100 eV, positioned at around 3 cm from the beam pipe centre.

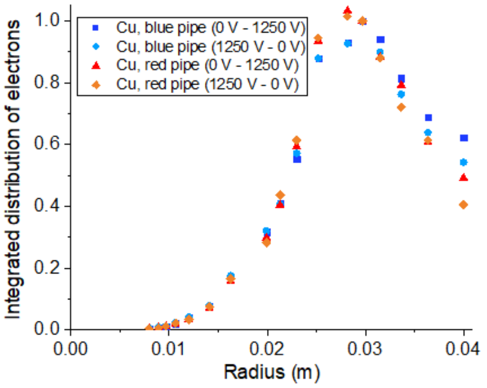

Figure 140: Integrated distribution of the high-energy electrons as a function of the radius in logarithmic scale.

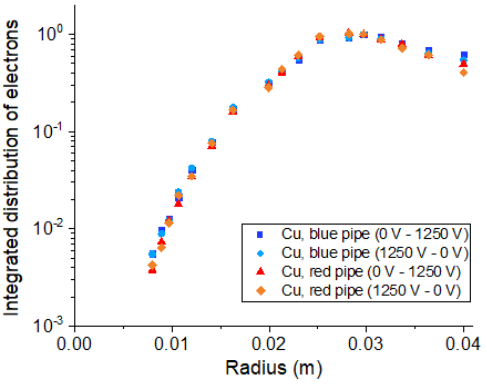

Figure 141: Integrated distribution of the high-energy electrons as a function of the radius, in logarithmic scale.

The above graphs shows the integrated radial distribution. To derive the radial distribution, one should consider the area of each radial element. The ring elements where electrons can stand at a given distance far from the beam pipe centre are much larger than near the bunch. Therefore to compute the electron density along the radius, I need to divide the previous data by the increasing area as a function of r. The area difference between r_1 and r_2 can be linearly described as ΔA:

$$\Delta A = A_2 - A_1 = \pi(r_2^2 - r_1^2) = \pi((r_1 + dr)^2 - r_1^2) = \pi(r_1\, dr + dr^2) = \pi\, dr\, (r_1 + dr) \tag{127}$$

Where $dr = r_2 - r_1$. The area of ring elements increases linearly with the distance from the centre. Dividing the integrated radial distribution by the ring area, I get the real electron distribution along r.

$$D = \frac{D_{int}}{\Delta A} \tag{128}$$

Where D is the electron distribution, D_{int} the integrated distribution above presented, ΔA the area increase as a function of the radial position. Figure 142 and Figure 143 represent the distribution in linear and logarithmic scales, respectively. A plateau is visible between 2.13 cm and 3.15 cm. This was predicted by Eq. (33), confirming that a dense halo of high-energy electrons reaches a maximum at 3.3 cm away from the centre of the beam pipe for a VPS chamber dimension (4 cm radius).

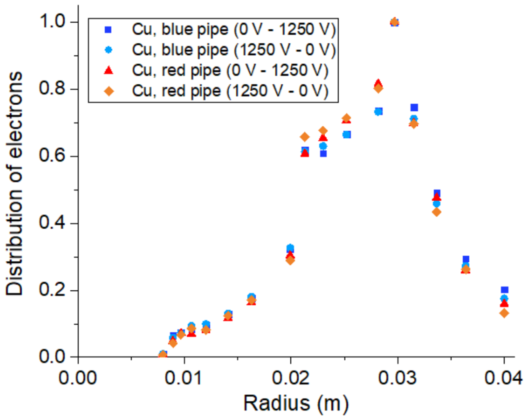

Figure 142: Linear distribution of the high-energy electrons normalised to the maximum value at 3 cm, i.e. 90 eV.

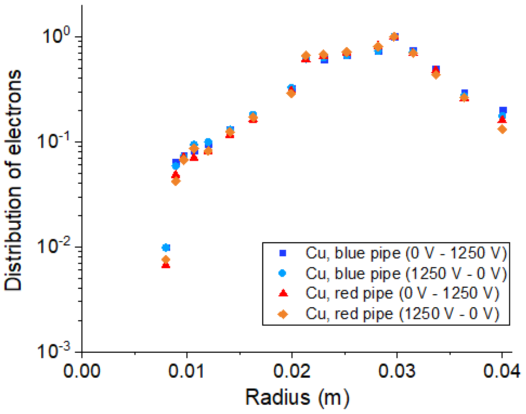

Figure 143: Logarithmic distribution of the high-energy electrons normalised to the maximum value at 35 cm, i.e. 90 eV.

4.1.4 Influence of the surface conditioning on the EC

During the scrubbing run performed in 2017, the mitigation of the EC was monitored as a function of the accumulated electron dose. The electron dose was calculated by integrating the electrical signals of EC registered by pick-ups at both 450 GeV and 6.5 TeV. The second analysis concerns the EC evolution of the standard fills during 2017 and 2018.

- **Influence of the electron dose accumulated during the scrubbing run 2017**

During the scrubbing run performed in 2017, beams of 2820 bunches were injected in the LHC. The fill numbers analysed go from 5788 to 5821. The scrubbing run increased the accumulated dose from $6 \cdot 10^{-4}\ C/mm^2$ to $2 \cdot 10^{-3}\ C/mm^2$ for the Cu surface, $6 \cdot 10^{-5}\ C/mm^2$ to $4 \cdot 10^{-4} C/mm^2$ for the ex-situ NEG surface, and $1 \cdot 10^{-7}\ C/mm^2$ to $1.3 \cdot 10^{-7}\ C/mm^2$ for the a-C surface.

Figure 144 and Figure 145 show the electrical signals at different accumulated doses as a function of n_p. They are similar to Figure 110 and Figure 111, while increasing the electron dose. The n_p thresholds increase and a small reduction of the slopes is visible. These shifts are signs of surface conditioning.

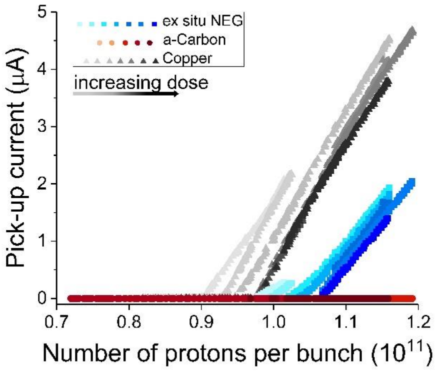

Figure 144: Accumulated electron dose effect on the electrical signals as a function of the number of protons per bunch, in linear scale.

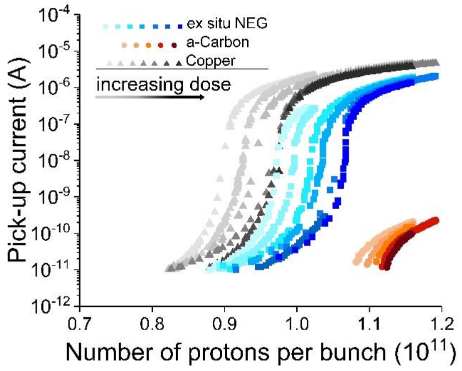

Figure 145: Accumulated electron dose effect on the electrical signals as a function of the number of protons per bunch, in logarithmic scale.

The threshold can be displayed as a function of the electron dose accumulated during the scrubbing run (see Figure 146). The three samples accumulated different electron doses owing to the different electron activities.

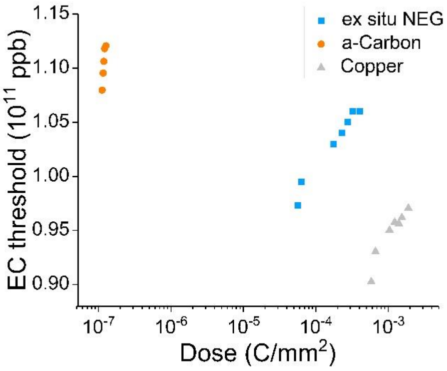

Figure 146: Bunch population threshold to trigger electron multipacting as a function of the accumulated electron dose during the 2017's scrubbing run.

- **Influence of the electron dose accumulated during two years of LHC run**

Three standard 48 bunches per batch fills are compared: fill 5887 two weeks after the scrubbing run 2017, fill 5979 five weeks after the scrubbing and 7334 the last fill after two years of operation. The electron doses accumulated before these three fills are presented in Table 14.

Table 14: Information related to three fills exploited in this paragraph.

Fill No.	***Accumulated electron doses***		
	Ex situ NEG	a-C	Cu
5887	$5.8 \cdot 10^{-4}$	$1.8 \cdot 10^{-6}$	$3.7 \cdot 10^{-3}$
5979	$6 \cdot 10^{-4}$	$2 \cdot 10^{-6}$	$4 \cdot 10^{-3}$
7334	$> 10^{-3}$	$\sim 10^{-5}$	$> 10^{-2}$

The evolution of the pick-up signal at the Cu beam pipe is shown in Figure 147, Figure 148 and Figure 149 for the three fills presented in chronological order. The EC activity is reduced with time, i.e. with accumulated electron dose. At 450 GeV the EC signal decreases from $10^{-6}A$ (fill 5887) to 10^{-11} A (fill 7334). At 6.5 TeV the maximum signal still decreases from $10^{-6}A$ (fill 5887) to 10^{-8} A (fill 7334) but it is limited by the photoelectron multipacting.

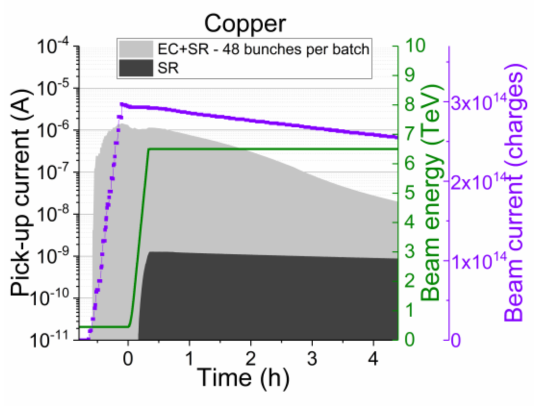

Figure 147: EC dynamics along a 48 bunches per batch fill, comparing the total EC build-up with of the effect of photoelectrons for Cu (fill 5887).

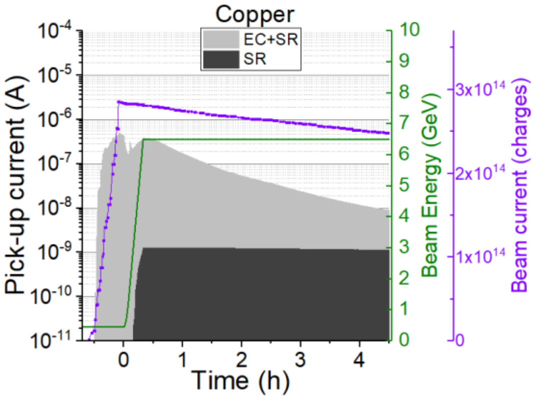

Figure 148: EC dynamics along a 48 bunches per batch fill, comparing the total EC build-up with of the effect of photoelectrons for Cu (fill 5979).

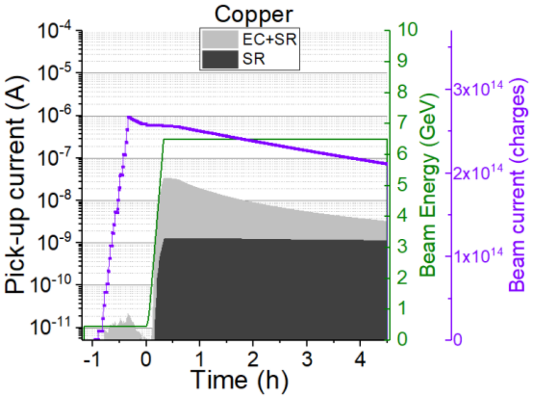

Figure 149: EC dynamics along a 48 bunches per batch fill, comparing the total EC build-up with of the effect of photoelectrons for Cu (fill 7334).

The evolution of the pick-up signal at the ex-situ NEG beam pipe is presented in Figure 150, Figure 151 and Figure 152, for the three fills. At 450 GeV the EC signal decrease significantly from $10^{-7}A$ to an undetected value below $10^{-11}A$. At 6.5 TeV the signal still decreases with electron dose but it is limited by the photoelectron emission and multipacting. Please note that the behaviour of Cu in Figure 149 and ex-situ NEG in Figure 151 are comparable, therefore the SEY at these two different instants are probably similar. The use ex-situ NEG beam pipes, therefore, could be useful to get a lower SEY. The EC signals tend to the photoelectron component with the decay of the multipacting regime after several hours of beam circulation.

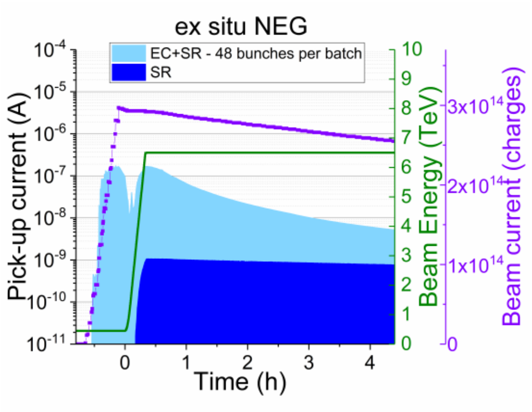

Figure 150: EC dynamics along a 48 bunches per batch fill, comparing the total EC build-up with of the effect of photoelectrons for ex-situ NEG (fill 5887).

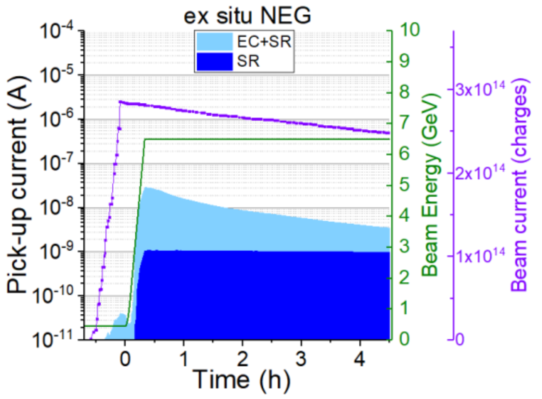

Figure 151: EC dynamics along a 48 bunches per batch fill, comparing the total EC build-up with of the effect of photoelectrons for ex-situ NEG (fill 5979).

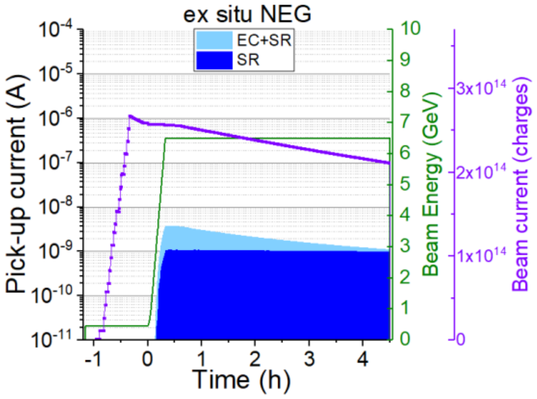

Figure 152: EC dynamics along a 48 bunches per batch fill, comparing the total EC build-up with of the effect of photoelectrons for ex-situ NEG (fill 7334).

The evolution of the pick-up signal of the a-Carbon coating beam pipe is displayed in Figure 153, Figure 154 and Figure 155, for the three fills. All the signals are compatible with the only photoelectron component, no matter the dose received by the surface. The slight difference between the signals and the photoelectron computations is attributed to a propagation of the measurement errors following the normalisation process and hence can be neglected.

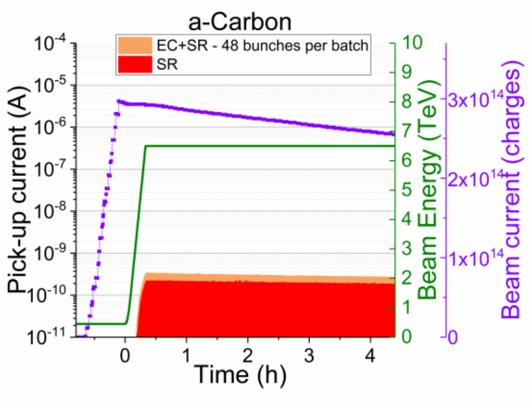

Figure 153: EC dynamics along a 48 bunches per batch fill, comparing the total EC build-up with of the effect of photoelectrons for a-Carbon (fill 5887).

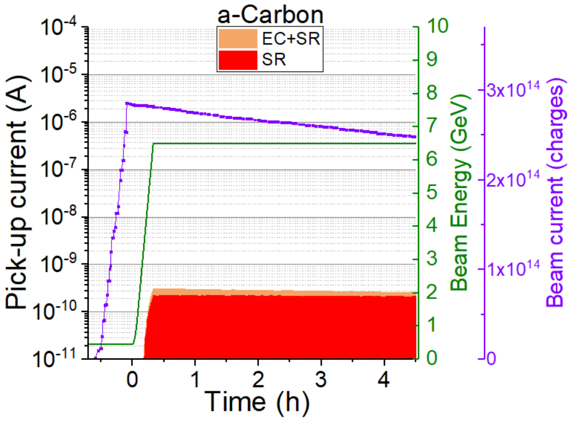

Figure 154: EC dynamics along a 48 bunches per batch fill, comparing the total EC build-up with of the effect of photoelectrons for a-Carbon (fill 5979).

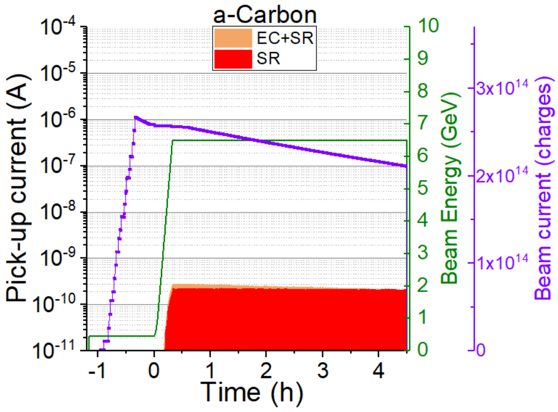

Figure 155: EC dynamics along a 48 bunches per batch fill, comparing the total EC build-up with of the effect of photoelectrons for a-Carbon (fill 7334).

4.1.5 Summary of the electrical analysis

The EC mechanism has been studied as a function of several beam pipe properties and surface properties. The evolution of the electron signal is linear with the number of injected bunches, with the bunch population above a certain multipacting threshold, and with the bunch length. The bunch spacing is a crucial parameter for the multipacting process. The EC is avoided with the 50 ns scheme. The electron seeds in between bunches are not accelerated by the following bunch and the multiplication process is not sustained. Only photoelectrons are visible on the pick-ups above 2.8 TeV.
The oscilloscope measurements present the EC dynamic along a full turn of the machine for ex-situ NEG and copper in Section 4.1.2. The EC multipacting begins after several batches. With the energy ramp-up, the multipacting was stimulated along all the batches, and it required 6-to-10 bunches to go to the equilibrium regime.

The energy spectrum measurements show two classes of electrons (Section 4.1.3): the electron seeds accelerated by the beam field with an energy gain of around 90-100 eV, and the secondaries generated at the beam pipe surface at few eV. The measurements are in agreement with the PyECLOUD simulation for an 80 mm diameter beam pipe. The radial distribution of the electrons shows that a dense halo of electrons is present at around 0.02-0.03 m from the beam pipe centre, as stated by the theoretical calculations performed in Chapter 1.

The evolution of the surface, i.e. the shift of the bunch population threshold with the accumulated electron dose, has been shown in Section 4.1.4: higher the dose, lower the surface SEY, higher the multipacting threshold. The conditioning of the surface thanks to the electron bombardment itself is a key point for the machine scrubbing. Along two years of operation the EC signal on standard fills at 450 GeV decreased of several orders of magnitude thanks to the reduction of the surface SEY on cu pipes.

4.2 Pressure signals

The second analysis considers the pressure signals acquired with the Bayard Alpert and Penning gauges. Firstly, the evolution as a function of some of the previous beam parameters (i.e. number of bunches, bunch population, bunch spacing, beam energy) is presented for the three surfaces. Secondly, the evolution of the surfaces properties is studied as a function of the accumulated electron dose along the scrubbing period and the ESD is evaluated along few months of the 2017's LHC operation.

The parallelism with the electrical analyses is kept when possible. The pressure evolution is a less precise indicator of the electron cloud activity with respect to the electrical signals because of the possible gas transmission between stations the evolution of the static pressure between fills: the gas travels along VPS and it is not instantaneously pumped after the beam dump, influencing the pressure measurement of the following fill.

The third part is dedicated to the composition of the gas released during beam operation at 450 GeV and 6.5 TeV. The last paragraph shows an application for the routine LHC operation: an indirect measurement of the EC activity from the pressure observation.

4.2.1 Beam parameter influence on EC as seen on pressure signals

The pressure is studied as a function of number of bunches, bunch population, bunch spacing and beam energy, for the same fills presented for the electrical measurements, see section 4.1.1.

- **Influence of the number of bunches**

The pressure evolution is studied at injection of the fill 5800. The pressure increase as a function of the number of bunches is plotted in Figure 156. The pressure increases linearly, similarly to the electron current signals. The pressure on a-C increases much more than the electrical measurement. This is linked to the pressure influence between the stations, as discussed in *Chapter 3*. Therefore, the pressure measurement alone cannot be a unique indicator of the EC in situ.

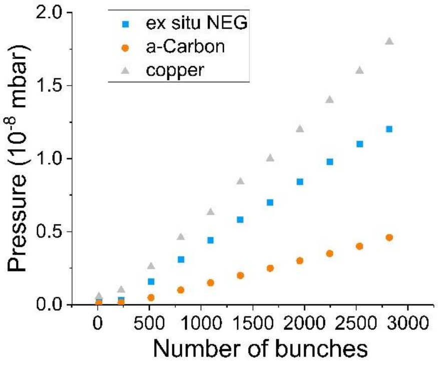

Figure 156: Pressure trends as a function of the number of bunches during the injection phase of a 25-ns standard LHC beam in linear scale.

The pressure signal can be fitted with lines, whose slopes are presented in Table 15.

Table 15: Linear coefficients of the pressure increase as a function of the number of bunches.

Surface	$slope\ [mbar/bunch]$
Copper	$6.4 \cdot 10^{-12}$
Ex situ NEG	$4.5 \cdot 10^{-12}$
a-Carbon	$1.7 \cdot 10^{-12}$

- **Influence of the number of protons per bunch**

The pressure measurements are plotted as a function of the bunch population in Figure 157. The vacuum dynamics linearly follows the electron signals. The Cu station has the largest pressure signal, in the order of 10^{-8} mbar. The pressure thresholds match with the electrical thresholds (see Figure 110 and Figure 111) for Cu and ex-situ NEG.

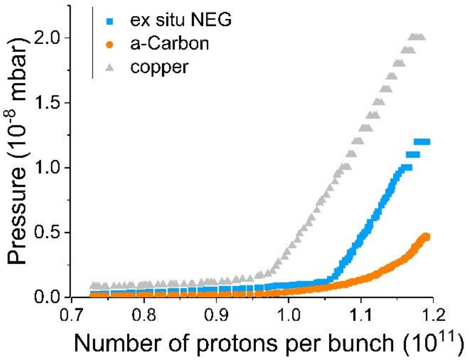

Figure 157: Pressure trends as a function of the number of protons per bunch after the injection phase of a 25 ns standard LHC beam in linear.

The slopes are reported in Table 16.

Table 16: Linear coefficients of the pressure increase as a function of the bunch population. The value for a-C coating will be discuss in the results.

Surface	***slope*** $[\boldsymbol{mbar/ppb}]$
Copper	$9.5 \cdot 10^{-19}$
Ex situ NEG	$8.6 \cdot 10^{-19}$
a-Carbon	$4.4 \cdot 10^{-19}$

- **Influence of the bunch spacing**

The pressure evaluation along a 50 ns fill (fill 5980) is depicted in Figure 158. At 450 GeV no signal increase is visible in any of the surfaces. With the energy ramp-up, the effect of SR and photoelectrons generate a small bump on a-C and ex-situ NEG. The background pressure on Cu is larger hence no bump is visible at 6.5 TeV. A second important bump is present for a-C and ex-situ NEG few minutes after the energy ramp-up, linked to the adjustments of the optics.

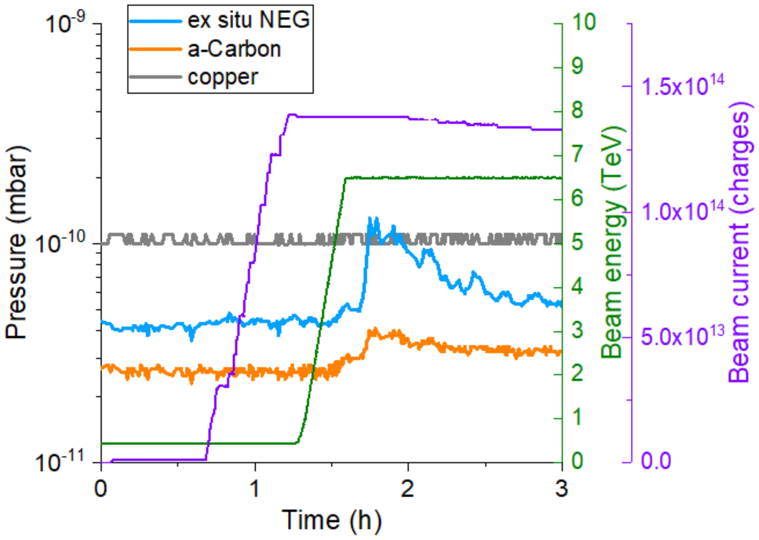

Figure 158: The pressure signals of a 50 ns bunch spacing beam are displayed in logarithmic scale. The beam current and the beam energy are displayed in dark purple and green, respectively.

For a standard 25 ns beam (fill 5979), the pressure of the three surfaces increase already at 450 GeV due to the EC. The carbon coating has an increase, due to gas transmission, as described in *Chapter 3,* of one order of magnitude lower than Cu. The ex-situ NEG is two stations away from the Cu one, so the observed pressure increase is really related to the EC activity. During the energy ramp-up the bunch length dynamic is evident, followed by the SR and photoelectron contribution at 6.5 GeV.

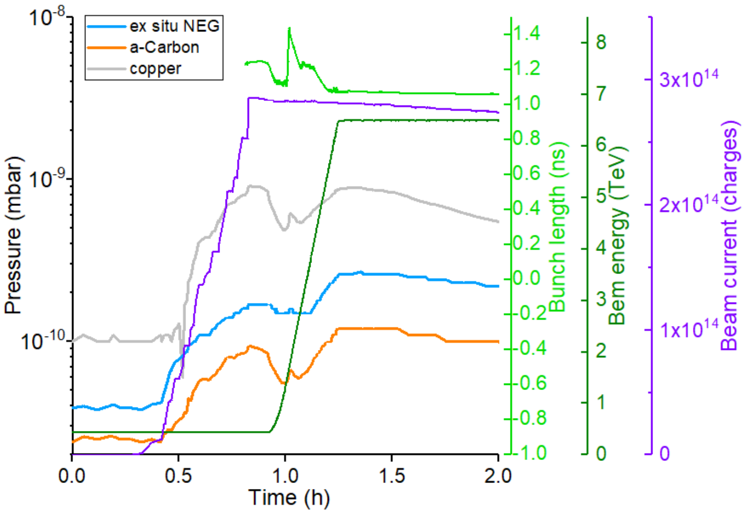

Figure 159: The pressure signals of a 25 ns bunch spacing beam are displayed in logarithmic scale. The bunch length, the beam current and the beam energy are displayed in light green, dark purple and dark green, respectively.

4.2.2 Influence of surface conditioning on the EC

The mitigation of the EC effect on gas dynamics was monitored during the scrubbing run 2017 as a function of the accumulated electron dose. The second analysis concerns the maximum pressure evolution of standard fills along the first two months of machine operation in 2017.

- **Influence of the electron dose accumulated during the scrubbing run 2017**

The pressure values are displayed as a function of the bunch population and the accumulated electron dose in Figure 160 and Figure 161. These graphs are in agreement with the electrical measurements: there is a shift of the threshold to higher bunch populations while increasing the electron dose.

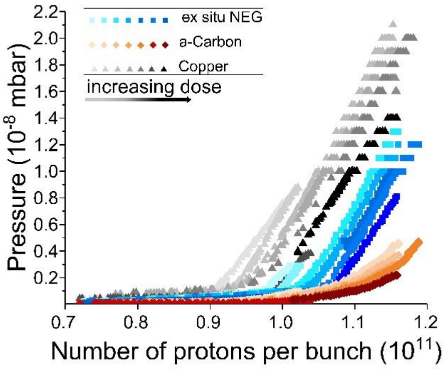

Figure 160: Accumulated electron dose effect on the pressure trends as a function of the number of protons per bunch, in linear scale.

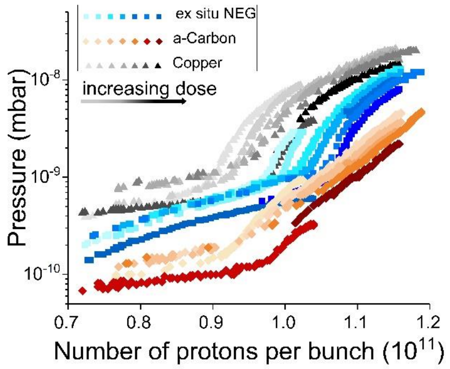

Figure 161: Accumulated electron dose effect on the pressure trends as a function of the number of protons per bunch, in logarithmic scale.

- **ESD as a function of the electron dose accumulated during the first two months of 2017 LHC operation**

During the LHC operation in June and July 2017 the EC activity was particularly strong. The evolution of the maximum pressure reached during each fill has been studied along these two months. The pressure increase due to the EC activity is linked to a surface parameter called Electron Stimulated Desorption (ESD) yield, i.e. the number of gas molecules released per impinging electron. Higher the ESD parameter, higher the gas desorption for a defined electron flux. This parameter is calculated from both electrical and pressure measurements. The maximum pressure and electrical signal measured at 450 GeV are considered for each fill.

$$ESD = \frac{P \cdot 2(C + S_{IP+NEG\,buffer}) \cdot G}{\left(\frac{I_{pick-up} \cdot l_{chamber}}{A_{pick-up}\ e}\right)} \tag{129}$$

Here P is the pressure [Pa], C is the conductance of half liner equivalent to 434 for hydrogen [l/s], $S_{IP+NEG\,buffer}$ is the pumping speed at one extremity due to ion pump and NEG buffer ($S_{IP+NEG\,buffer} = S_{IP} + S_{NEG\,buffer} \approx 30 + 600\ l/s$), G is the constant converting gas quantities to a number of molecules, equivalent to $2.4\ 10^{19}\ [\text{molecules/Pa} \cdot \text{l}]$ at 293 K, $I_{pick-up}$ is the electrical signal from the pick-up [A], $l_{chamber}$ is the chamber length equal to 1.378 [m], $A_{pick-up}$ is the surface of the pick-up considering the transparency equal to 0.0078 $[m^2]$, e is the electron charge [C] [93].

The ESD yield is calculated as a function of the accumulated dose only for Cu (see Figure 162) due to gas transmission issues that partially influenced also the ex-situ NEG station. The ex-situ NEG pressure measurements sometimes suffered of gas transmission from Q5, therefore not displayed. The ESD yield reduction is related to the conditioning effect on the Cu surface. With three order of magnitude of accumulated dose, the ESD yield decreases by a factor 100.

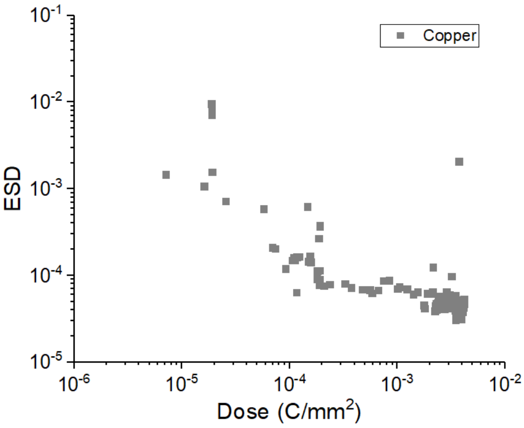

Figure 162: The evolution of the ESD parameter calculated for the Cu surface as a function of the accumulated electron dose in two months of LHC operation.

4.2.3 Gas composition during the beam operation

This paragraph is dedicated to the composition of the gas released during beam operation along the VPS. Two examples are reported. The total and partial pressure are acquired at 450 GeV and at 6.5 TeV.

- **Gas desorption due to EC at 450 GeV and the additional contribution of photoelectrons at 6.5 TeV**

The first scans concern a fill with 2460 bunches (fill no. 6860) acquired at 450 GeV and 6.5 TeV, respectively on 28/06/2018 at 17:07 and 17:30. At 450 GeV EC signal were recorded for ex-situ NEG and Cu surfaces. At 6.5 TeV, the photoelectrons multipacted also on a-C, as described for the standard fills along the LHC run. The first three plots show the gas spectrum as a function of the atomic mass, acquired for Cu, ex-situ NEG and a-C coatings (see Figure 163, Figure 164 and Figure 165). When the beam is circulating, the main peaks are hydrogen (2) and carbon monoxide (28) for all the surfaces. As well, other peaks are visible: methane (16), water (18), carbon dioxide (44) and a heavier mass centered at 69.

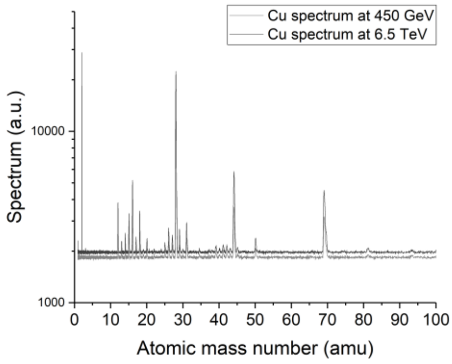

Figure 163: Gas spectra read on the Cu station during beam operation at 450 GeV and 6.5TeV.

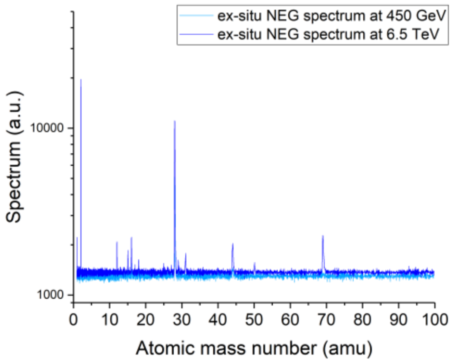

Figure 164: Gas spectra read on the ex-situ NEG station during beam operation at 450 GeV and 6.5TeV.

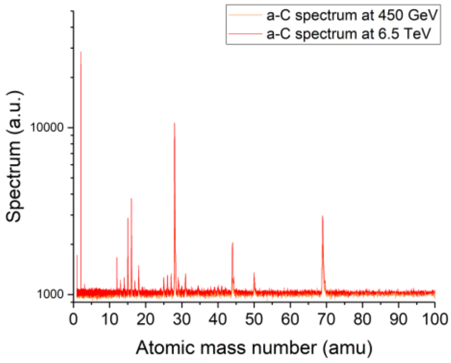

Figure 165: Gas spectra read on the a-C station during beam operation at 450 GeV and 6.5TeV.

The mass 69 can be related to different compounds. Following the cracking pattern visible on the spectrum, one can identify two peaks at masses 31 and 51. Among the materials, I identify two possible substances: fluoroform (CHF_3) and 2-Propynenitrile 3-fluoro (C_3FN). Their cracking pattern are taken from the NIST database and shown in Figure 166 and Figure 167, respectively [94]. The presence of mass 51 for fluoroform is quite important if compared to the one in C_3FN.

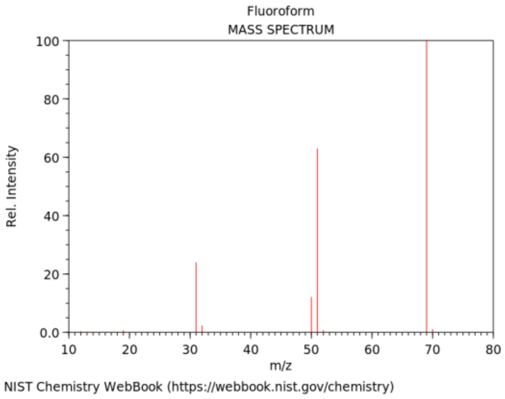

Figure 166: Cracking pattern of fluoroform (CHF_3) taken from NIST database [94].

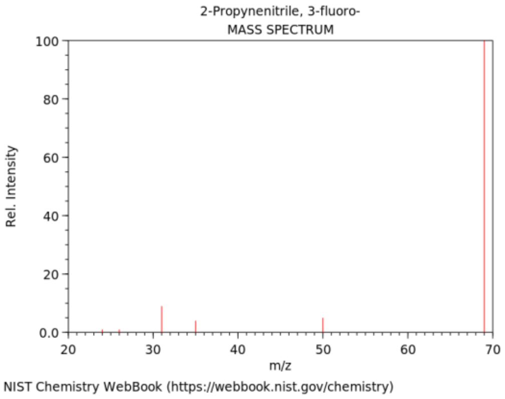

Figure 167: Cracking pattern of 2-Propynenitrile 3-fluoro (C_3FN) taken from NIST database [94].

In order to understand which of the two substances is detected, the acquired spectra are normalized and, so, the gas quantities converted into percentages. The normalized spectra are displayed as a function of the atomic mass in Figure 168, Figure 169 and Figure 170. The mass 51 is much lower than the mass 31 in every spectrum, therefore the above-mentioned 69-

mass signal may be linked to C_3FN. A very small peak is also visible on mass 26, confirming the presence of C_3FN. This unexpected signal can be explained by the presence of kapton wires used for pick-ups and calorimeters which under electron and photon bombardment generate these gas species.

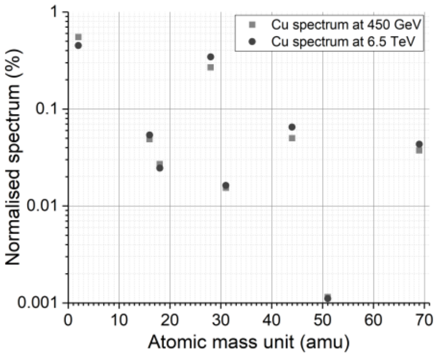

Figure 168: Normalised gas spectra read on the Cu station during beam operation at 450 GeV and 6.5TeV.

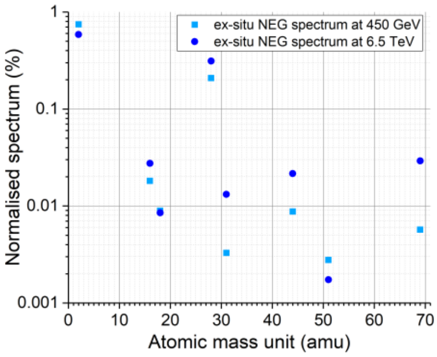

Figure 169: Normalised gas spectra read on the ex-situ NEG station during beam operation at 450 GeV and 6.5TeV

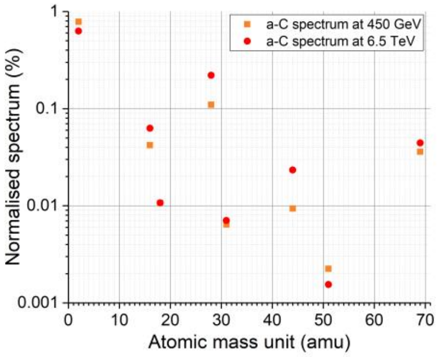

Figure 170: Normalised gas spectra read on the a-C station during beam operation at 450 GeV and 6.5TeV.

The total pressure profile in nitrogen equivalent is plotted in Figure 171 for the VPS measurements performed at 450 GeV. The data are presented and compared with a related vacuum simulation performed with VASCO (see *Annex 4*). The partial pressures of the main four standard gasses are plotted in Figure 172 and compared with the partial pressure simulations. The VASCO code can simulate only these four gas species. This simulation was carried to cross check the buffer performance, i.e. the standard sticking factors.

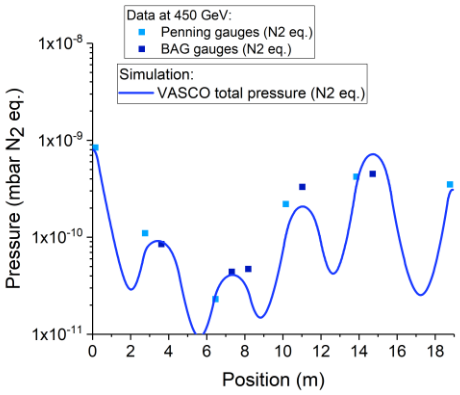

Figure 171: Data and simulation of the total pressure profile in nitrogen equivalent for the 450 GeV measurement.

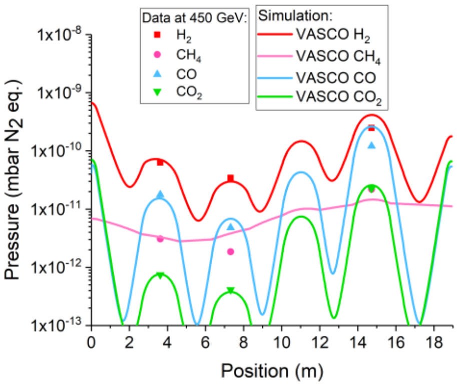

Figure 172: Data and simulation of the partial pressures for the 450 GeV measurement.

The total pressure profile is plotted in Figure 173 for the measurements performed at 6.5 TeV with the related VASCO simulation. The partial pressures are plotted and simulated Figure 174. The measurements and the simulations agree within an error of 30%, typical for standard pressure gauges.

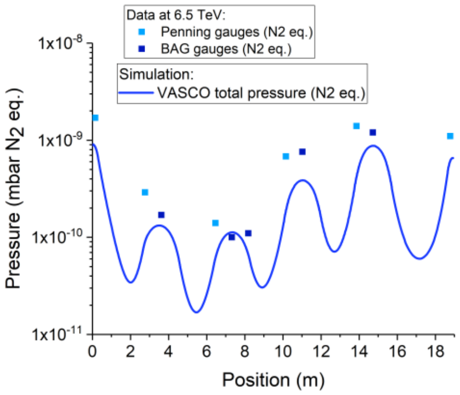

Figure 173: Data and simulation of the total pressure profile in nitrogen equivalent for the 6.5 TeV measurement.

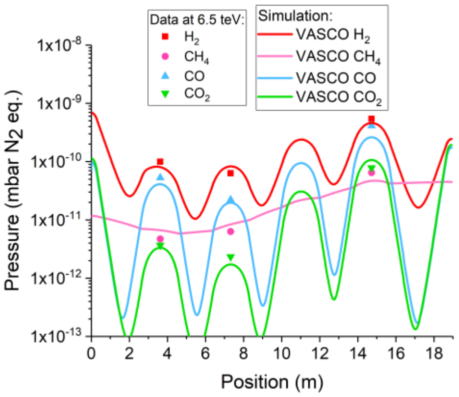

Figure 174: Data and simulation of the total pressure profile in nitrogen equivalent for the 6.5 TeV measurement.

- **Gas desorption due to only photons and photoelectrons at 6.5 TeV**

The second example concerns the fill 7013 (2556 bunches spaced of 25 ns) acquired at 450 GeV and 6.5 TeV, respectively on 02/08/2018 at 15:55 and 16:19. At 450 GeV a weak EC signal was recorded on the Cu surface only. At 6.5 TeV, the photoelectrons signal was visible for the three surfaces. The plots show the gas spectrum as a function of the atomic mass for the three surfaces (see Figure 175, Figure 176 and Figure 177). When the beam is circulating, the main peaks are hydrogen (2) and carbon monoxide (28) for all the surfaces. Even with a much lower electron activity, the 69 peak is still visible.

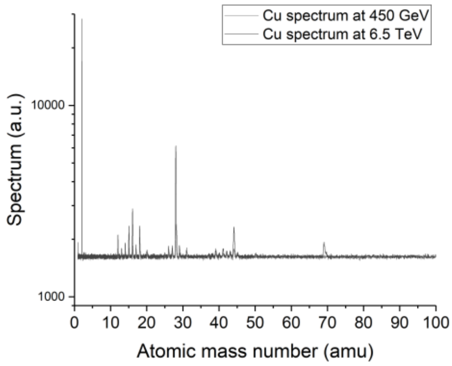

Figure 175: Gas spectra read on the Cu station during beam operation at 450 GeV and 6.5TeV.

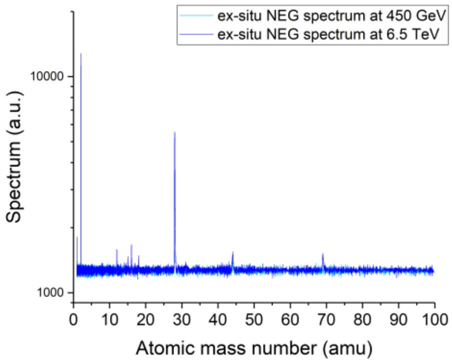

Figure 176: Gas spectra read on the ex-situ NEG station during beam operation at 450 GeV and 6.5TeV.

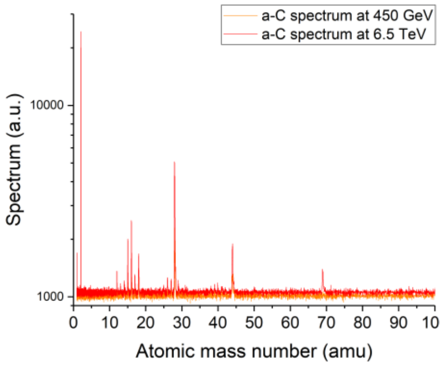

Figure 177: Gas spectra read on the a-C station during beam operation at 450 GeV and 6.5TeV.

The normalized spectra are displayed in Figure 178, Figure 179 and Figure 180. As before, the mass 51 is lower than the mass 31 in every spectrum, therefore the above-mentioned 69-mass signal can be attributed to C_3FN.

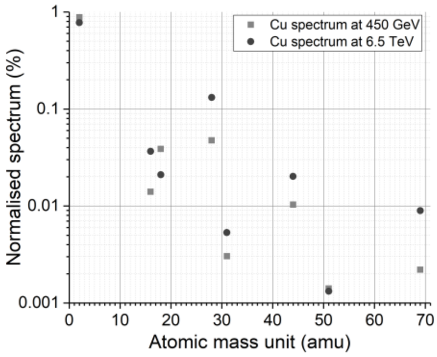

Figure 178: Normalised gas spectra read on the Cu station during beam operation at 450 GeV and 6.5TeV.

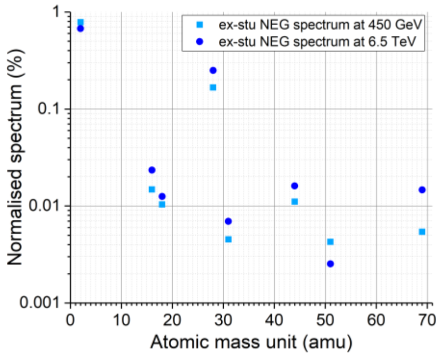

Figure 179: Normalised gas spectra read on the ex-situ NEG station during beam operation at 450 GeV and 6.5TeV.

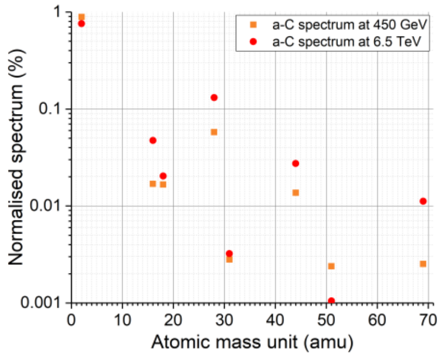

Figure 180: Normalised gas spectra read on the a-C station during beam operation at 450 GeV and 6.5TeV.

The total pressure profile data and simulation is displayed in Figure 181 for the measurements at 450 GeV. The partial pressures of the main four standard gasses are plotted in Figure 182 and compared with the simulations. They still agree with the literature data sticking factors, i.e. 0.8% for H_2, 70% for CO and CO_2 [86].

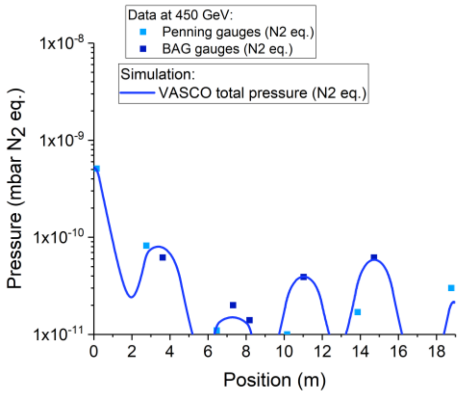

Figure 181: Data and simulation of the total pressure profile in nitrogen equivalent for the 450 GeV measurement

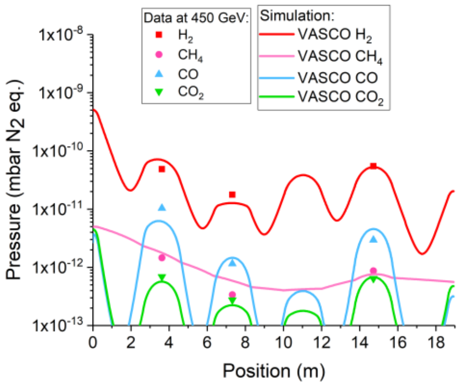

Figure 182: Data and simulation of the partial pressures for the 450 GeV measurement.

The total pressure profile is plotted in Figure 183 for the measurements performed at 6.5 TeV, along with the related VASCO simulation. The partial pressures are displayed in Figure 184. The measurements and the simulations agree quite well considering only the presence of the standard four gasses, i.e. H_2, CO, CO_2, CH_4. The total pressure simulated is lower than the measured one because it does not include other molecules, such as water.

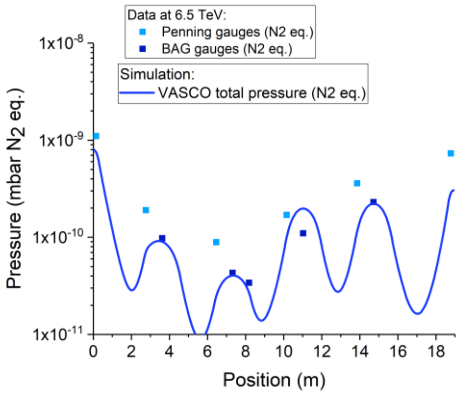

Figure 183: Data and simulation of the total pressure profile in nitrogen equivalent for the 6.5 TeV measurement.

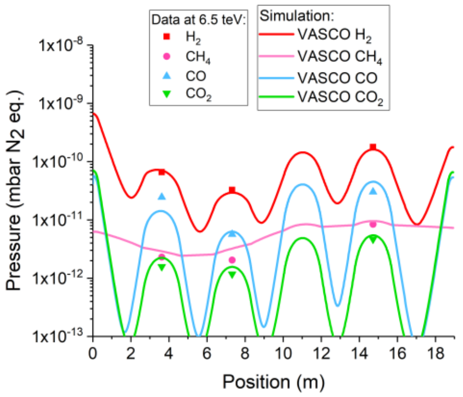

Figure 184: Data and simulation of the total pressure profile in nitrogen equivalent for the 6.5 TeV measurement.

4.2.4 Application for routine LHC operation: indirect measurements of EC

This section focuses on the comparison of the pressure profile in different positions around the LHC machine. The electrical pick-ups are installed only on VPS, while pressure gauges are placed everywhere. The pressure can be used as a proxy for detecting EC, even if the precision is reduced because of the gas influence from the nearby elements.

Consider the fill 6610, during the scrubbing run 2018. The beam was composed of 2316 bunches with the standard bunch distance of 25 ns. The beam energy was kept at 450 GeV. In the VPS system the EC was visible in both electrical and pressure measurements for the copper surface, as displayed in Figure 185. The bump in the electron signal corresponds to the pressure bump.

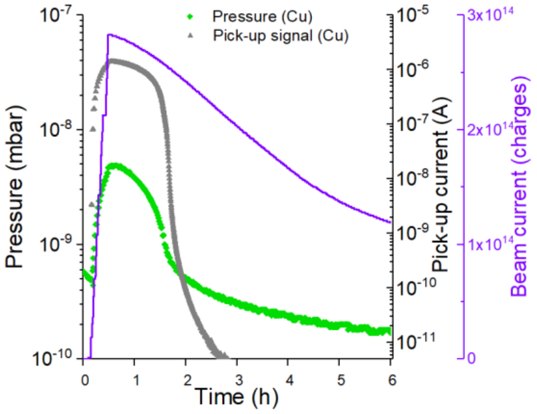

Figure 185: Electrical and pressure signals of EC on the copper station on VPS during the fill 6610.

Let us consider other thee locations around the machine, at equivalent positions in point 1, 2 and 5 of the LHC. A sketch of the corresponding positions is represented in Figure 186. The chosen beam pipes are 80-mm diameter copper pipes installed in the LSS similar to the VPS.

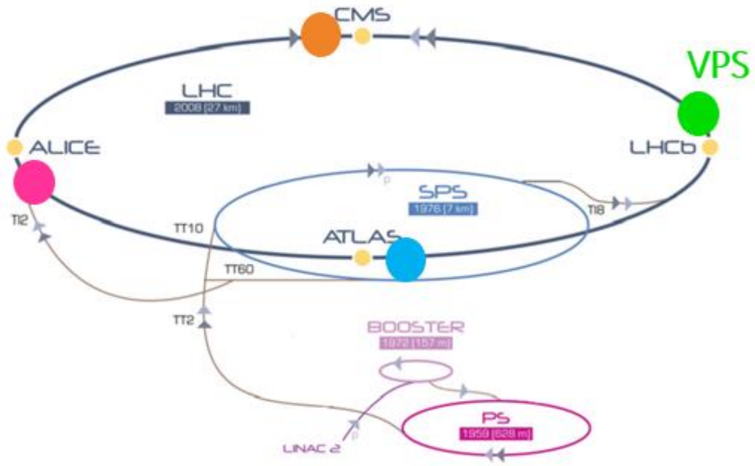

Figure 186: Position of the four different vacuum gauges compared.

The pressure profiles of the four vacuum gauges are displayed in Figure 187. The VPS station reaches the highest pressure because it is the only beam pipe with unbaked copper, while the other three pipes are baked copper surfaces.

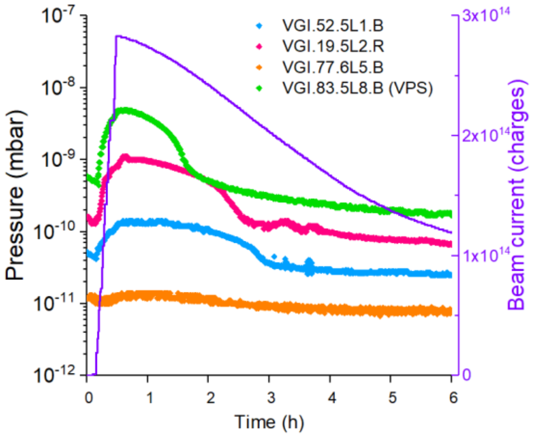

Figure 187: Pressure profiles of four vacuum gauges around the LHC during the fill 6610.

To understand the difference between them, one has to look into the layout of each location. In point 8, i.e. the VPS system, the unbaked Cu is positioned between NEG buffers and its EC activity was confirmed by Figure 187. Its layout is displayed in Figure 188. The second highest pressure is registered at point 2, where the Cu insert is between a 1-m NEG buffer an Injection Kicker Magnet (MKI). Around them two sector valves are positioned (see Figure 189).

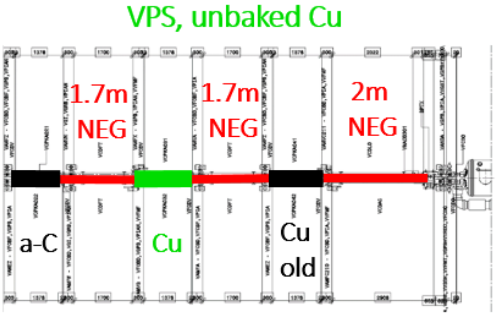
VPS, unbaked Cu
1.7m NEG
1.7m NEG
2m NEG
a-C
Cu
Cu old

Figure 188:Layout of the chosen system positioned near point 8, in the VPS system.

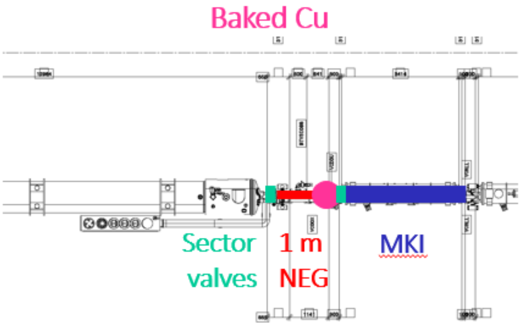
Baked Cu
Sector valves
1 m NEG
MKI

Figure 189: Layout of the chosen system positioned near point 2.

The third highest pressure among the chosen gauges is recorded near point 1 (see Figure 190). The gauge is surrounded by long NEG buffers. At the end of the 2.6-m right buffer a stainless steel pick-up called Beam Pick-up Timing system for Experiments (BPTX) is positioned. The gas measured at the gauges is probably related to EC activity at this electrode. In fact, stainless steel has a very high SEY. The lower pressure is measured in point 5, where a similar system is installed, without BPTX. In this case, the pressure does not significantly increase (see Figure 191).

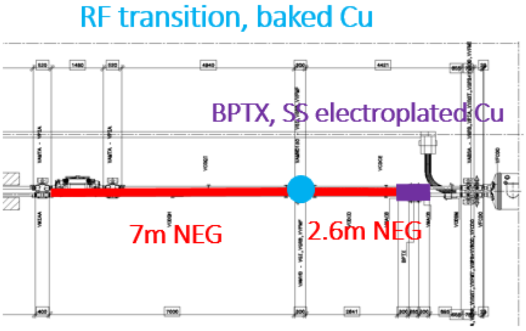
RF transition, baked Cu
BPTX, SS electroplated Cu
7m NEG
2.6m NEG

Figure 190: Layout of the chosen system positioned near point 1.

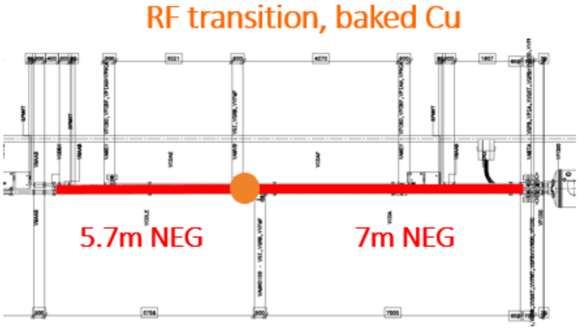
RF transition, baked Cu
5.7m NEG
7m NEG

Figure 191: Layout of the chosen system positioned near point 5.

It is clear that a regular pressure monitoring can be used to detect the EC activity in situ or in the nearby elements. However, one must be aware that the pressure increase cannot be always attributed to the EC activity itself but also from surrounding elements.

4.2.5 Summary of the pressure analysis

The pressure evolution has been studied as a function of the same beam parameters and beam pipe properties analysed for the electrical signals. The pressure increase is linear with the number of bunches and bunch population. The gas transmission can be a non-negligible contribution when very different EC activities are present in nearby vacuum chambers. The bunch spacing is confirmed to be a crucial parameter also for the gas dynamics. The gas desorption due to SR and photoelectrons is negligible on 50 ns bunch spacing fills (Section 4.2.1).

The evolution of the pressure with dose validates the threshold increase due to conditioning, measured already with the pick-ups. The ESD parameter could be calculated for the Cu surface during several months of beam operation. The conditioning is achieved thanks to the electron activity (Section 4.2.2).

The gas composition was studied using VQM analysers. Their signals confirm the presence of standard vacuum gasses, such as hydrogen, carbon monoxide and dioxide, methane. Traces of water are also detected because the mild bake out process performed at 80 °C was not enough to remove all the water. Traces of C_3FN are visible due to the interaction between SR with the kaptop wires used for the measurements (Section 4.2.3).

The pressure dynamics has been evaluated in other parts of the machine and compared with the VPS system. The pressure measurements can be an indicator of the EC activity and its multipacting threshold. The EC can be localised in situ, near the pressure reading, or indirectly in nearby machine components, due to the gas transmission (Section 4.2.4).

4.3 Thermal signals

The thermal signals of the calorimeters give complementary information on the EC phenomenon. In particular, I will discuss the thermal behaviour of a copper calorimeter as a function of the beam parameters. Three main heat loads are discriminated for several fills: the beam wall heat load due to the beam passage, called impedance; the photoelectrons and the SR component above 2.8 TeV; the EC itself. These heat loads are compared with the electrical measurements, i.e. the electron flux and the electron energy spectrum.

The thermal behaviour of all the second batch of calorimeters distributed along the VPS stations, the type E calorimeters, is driven by self-heating and high-capacity effects, with a much larger time constant than the ones defined during both calibrations, in the order of hours, that prevents a meaningful comparison between stations.

4.3.1 Beam parameter influence on EC as seen on thermal signals

Similar analyses to those presented for the pick-up signals and the pressure measurements are here reported for the copper calorimeter. These analyses focus on the calorimeter installed in station 4 on the red beam pipe. The influence of the main beam parameters is discussed for 450 GeV and 6.5 TeV.

- **Thermal dynamics at 450 GeV**

Here, I consider the fill 5800, the first fill of the scrubbing run 2017. During this fill, the energy was kept at 450 GeV and no SR contribution was present. Therefore, the origin of the observed heat load is related to impedance and to the EC. This is visible in Figure 192, where the temperature of the calorimeter during the fill is displayed in grey, the impedance contribution calculated with Eq. (125) is plotted in pink, and the electron pick-up signal acquired on the same station in black. It is evident that when the multipacting regime decays and the pick-up current decreases by six orders of magnitude, the calorimeter temperature decreases asymptotically towards the impedance contribution. This measurement confirms that a strong EC activity has an impact on the power deposited on the beam pipe.

In order to evaluate the heat loads, the temperature is converted in power using the thermal constant, presented during the calorimeter calibrations. For this calorimeter, $k = 53.52\ \mathrm{K \cdot m_{chamber}/W}$. The power is plotted in Figure 193. The maximum EC power is deposited at the end of the beam injection, at around 0.5 h, it corresponds to the difference between the grey and pink curves and equals to 49 mW/$m_{chamber}$.

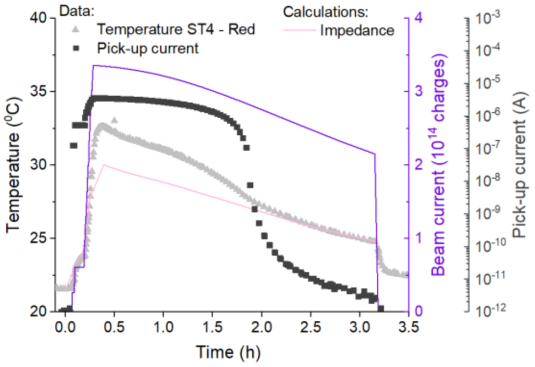

Figure 192: The temperature of the Cu calorimeter and the pick-up current are displayed as a function of time for the fill 5800 in grey and black, respectively. The impedance contribution is calculated and plotted in pink.

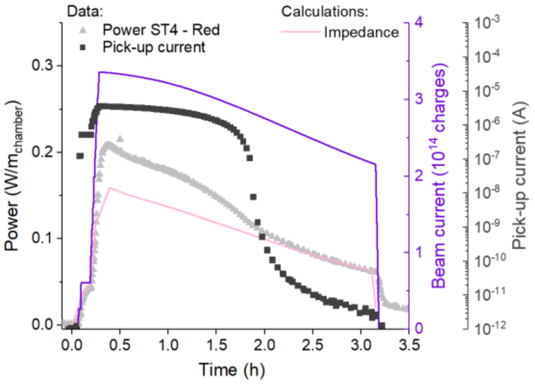

Figure 193: The power deposited on the Cu calorimeter is displayed as a function of time for the same fill. The impedance contribution is calculated and plotted in pink.

- **Influence of the number of bunches**

The evolution of the power as a function of the number of bunches is presented for the Cu surface during the same previous fill (see Figure 194). The power data are shown in grey, while the impedance heat load is calculated following Eq.(125) and displayed in pink. The behaviour is linear for both the data and impedance calculations. The difference between the two curves can be attributed to EC. The error for a small temperature difference between pink and grey curves is quite large; this is why the slope of the EC power calculation is not perfectly linear. At the beginning of the scrubbing run, the impedance contribution for 2820 bunches is 161 mW/$m_{chamber}$ and the total heat load measured is around 210 mW/ $m_{chamber}$. The EC heat load from 2820 bunches is, therefore, around 49 mW/$m_{chamber}$. The EC slope is $1.74 \cdot 10^{-5} \frac{mW}{m_{chamber}\, bunch}$.

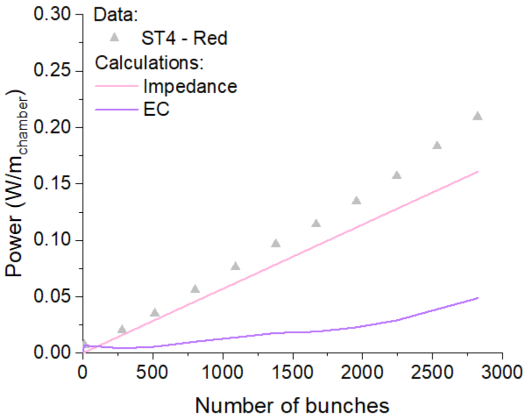

Figure 194: The total power deposited on a copper surface is displayed in grey as a function of the number of bunches. The computations of the impedance component is drawn in pink. The remaining power, attributed to EC, is displayed in purple

- **Influence of the bunch population**

The evolution of the power as a function of the bunch population for the same fill after the injection phase is presented in Figure 195. The power data are shown in grey, while the temperature increase due to impedance heat is calculated and displayed in pink. The impedance calculation follows the square of the bunch population and this is visible for high n_p values in both measurements and calculations. The missing component is the EC contribution.

The error on the temperature difference is large and the EC power estimation is affected, but the behaviour is still almost linear. The EC power slope is $1.81 \cdot 10^{-12} \frac{mW}{m_{chamber} \cdot proton}$, and the multipacting threshold is around 9.23 10^{11} protons per bunch while interpolating the data with a linear fit. The EC threshold agrees with the one measured with electrical and pressure detectors, i.e. 9.6 10^{10} protons per bunch, with an error of 4%.

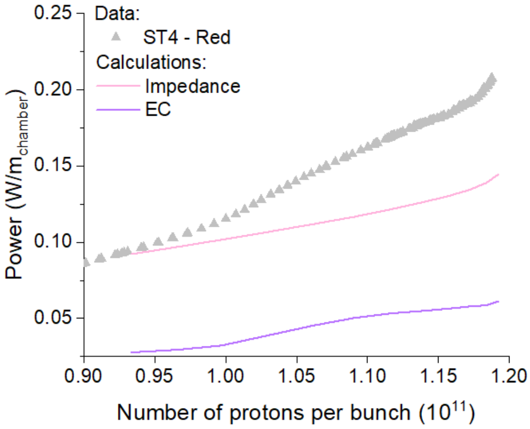

Figure 195: The total power deposited on a copper surface is displayed in grey as a function of the bunch population. The computations of the impedance component is drawn in pink. The remaining power, attributed to EC, is displayed in purple.

- **Relationship between the EC heat load and pick-up current**

For the same fill, it is interesting to plot the EC heat load versus the pick-up currents measured after the injection phase. With the decrease of the electron activity, the EC power deposition decreases as well (see Figure 196). Below the bunch population threshold, the electrical signals decrease dramatically due to the loss of the multipacting regime. At this point, the power curve cannot follow this rapid change as fast as the electrical measurements due to the thermal time constant of the calorimeter. For this reason, if one displays the data in logarithmic scale, there is a plateau visible below $10^{-7}A$ (see Figure 197). The electrical measurements are essentially instantaneous (with an integration time of 20 ms), while the thermal ones have an intrinsic time constant of around $\tau = 120\ s$ and they need around 5τ to get to the equilibrium. For this reason, during a fast transient, it is difficult to relate the proper heat load from the temperature measurement points acquired every 30 seconds. The behaviour is linear for the steady-state regime above $10^{-7}A$, with a slope of $9.15 \cdot 10^{-3} \frac{mW}{m_{chamber}\,\mu A}$.

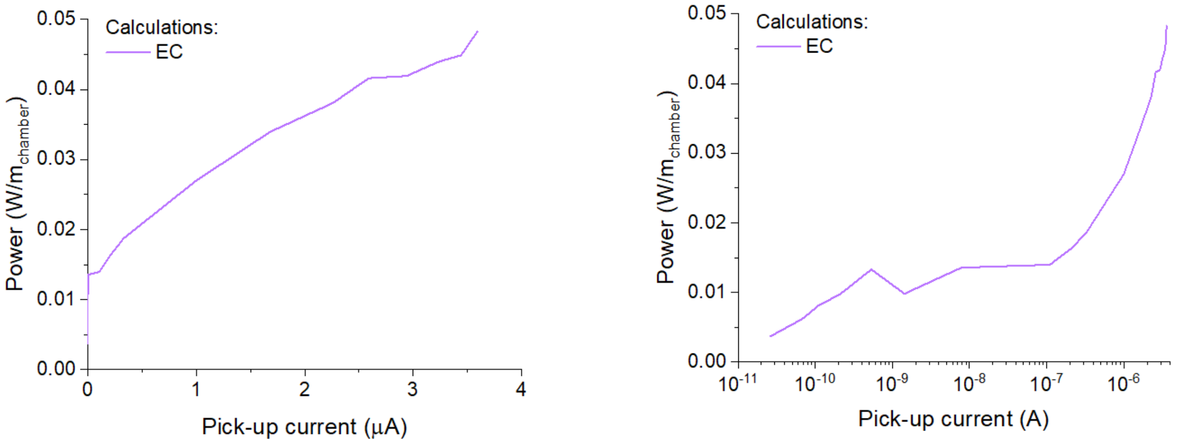

Figure 196: The computation of the power deposited on a copper surface is displayed in linear scale as a function of the total beam current, after the injection phase.

Figure 197: The computation of the power deposited on a copper surface is displayed in logarithmic scale as a function of the total beam current, after the injection phase

- **Mean electron energy as a function of the bunch population at 450 GeV**

From the electrical and the thermal measurements, it is possible to compute the mean electron energy. The mean energy can be computed from the slope of the previous curve in the steady-state regime, when the time constant of the calorimeter does not compromise the calculation, i.e. for a pick-up current above $10^{-7}A$. The mean electron energy, $\bar{E}$, is equivalent to:

$$\bar{E}\ [eV] = \frac{Q_{EC}\left[\frac{W}{m}\right]}{I_{EC}\ [A]} \cdot \frac{A_{detector}}{A_{1-m\ chamber}} \tag{130}$$

Where P_{EC} is the EC heat load and I_{EC} is the electrical current read by the pick-up, that must be normalised by the full surface of 1-m chamber. In Figure 198 I present the mean energy computations in linear and logarithmic scales. Higher the multipacting process, higher the pick-up current, and, therefore, lower the average electron energy due to a larger number of secondaries. With a large electron current at a bunch population of $1.2 \cdot 10^{11}\ protons\ per\ bunch$, the mean electron energy calculated from the heat load measurements is around $\bar{E} = 4\ eV$. With $1 \cdot 10^{11}\ protons\ per\ bunch,\ \ \bar{E} = 40\ eV$, still in multipacting regime.

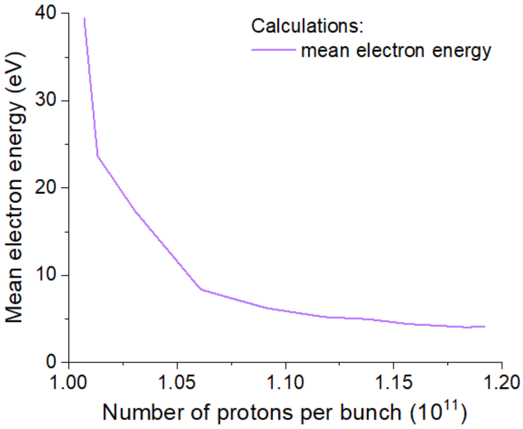

Figure 198: The mean electron energy as a function of the protons per bunch.

It is important to underline that in multipacting regime the majority of the electrons have low energy. Therefore, in order to simulate and to study the surface behaviour and parameters in the laboratory, one must set the electron gun to a much lower energy than the energy kick received at the time of the bunch passage. I would recommend a 2-phase conditioning to represent what happens in a LSS pipe of the LHC: the first part done with electrons at around 100 eV, as the accelerated peak visible on the spectrum I measured; the second below 10 eV to describe the action of the secondaries, much less effective.

- **Influence of the bunch spacing**

Consider the fill 5980, run with 50 ns and previously studied in terms of electrical signal and pressure signals. The power behaviour of the Cu surface (station 4) is displayed in grey in Figure 199 as a function of time. Two computations are compared to the measurement: the power losses from impedance (in pink), the SR and the photoelectron heat loads (in dark grey).

The impedance heat load is given by the Eq. (125). After the injection, this value is equivalent to 68 mW/m$_{\text{chamber}}$. The impedance heat load drastically changes with the bunch length and the bunch population. During the energy ramp up this effect is strongly visible. The SR heat load cannot be calculated with the standard formula because the SR is not generated in situ, but it comes from the arc 7-8, located hundred meter upstream and can be highly reflected due to a grazing angle. In order to match the missing component, the SR and photoelectron contributions per meter of chamber corresponds to 48 mW/m$_{\text{chamber}}$. This value can be compared with the total amount of SR heat generated in the arc.

$$Q_{SR}\left[\frac{W}{m}\right] = \frac{U_0 \cdot \mathrm{I_{beam}}}{2\pi\rho} = \frac{4}{3}\pi\alpha\ \hbar c\ \frac{\gamma^4}{\rho} \cdot \frac{\mathrm{I_{beam}}}{2\pi\rho} \tag{131}$$

Where U_0 is the power loss per turn, $\mathrm{I_{beam}}$ the beam current, ρ the bending radius equivalent to 2803.95m, α is a constant, equal to 1/137, $\hbar c$ is equal to 197 MeV·fm, γ the Lorentz factor equal to the energy divided by the mass in GeV. For a beam current of 0.25 A at 6.5 TeV, the SR power losses are equal to 70 mW/m$_{\text{chamber}}$. Therefore, the value measured is consistent, but still a big part of the SR power generated in the arc is partially transferred to the LSS due to reflection mechanisms. In order to complete this analysis, I calculate the contribution of photoelectrons on the total missing heat load measured. From previous analysis, we know the photoelectron current of 10^{-9} A is measured during this fill on Cu. From the energy spectrum, I know that the electron kick is around 100 eV. Therefore, their energy deposition per meter of chamber is equivalent to:

$$Q_{photoelectrons}\left[\frac{W}{m}\right] = I_{photoelectron} \cdot \frac{\dot{A}_{chamber}}{A_{detector}} \cdot \overline{E_{k\imath ck}} \qquad (132)$$

Where the $I_{photoelectron}$ is the electrical current read by the pick-up, $A_{chamber}$ is the surface of a meter of chamber equal to 0.2512 m^2, $A_{detector}$ is the surface os the detector, $\overline{E_{k\imath ck}}$ the mean energy kick that photoelectrons receive. The photoelectron power results to be around 0.3 mW/$m_{chamber}$, negligible if compared to 48 mW/$m_{chamber}$ measured. Therefore, the missing heat load at 6.5 TeV is mainly attributed to SR power deposition and not to photoelectrons. After the energy ramp-up, the heat load decreases with time following the bunch population decay.

In a second plot, a zoom of the energy ramp-up is presented (Figure 200). The two peaks related to the bunch length dynamics are visible, but the amplitude of the temperature profile exceeds the maximum temperature increase foreseen by the impedance calculations. In fact, the formula used to calculate the impedance heat load is derived for the case of Gaussian bunches. During the energy ramp-up, the bunch shape changes due to beam shaking and this could explain the discrepancy of around 30% between data and impedance calculations. At first approximation, one can notice that the heat load due to impedance and SR are in the same order of magnitude for a 50 ns fill at 6.5 TeV.

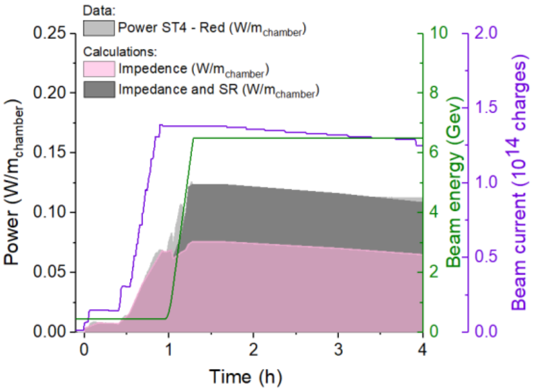

Figure 199: The power deposited on a Cu calorimeter (Station 4, Blue pipe) as a function of the time (fill 5980) for a 50 ns LHC beam.

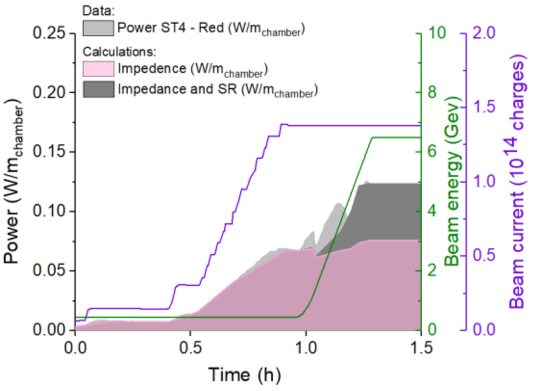

Figure 200: A zoom of the power deposited on a Cu calorimeter (Station 4, Blue pipe) as a function of the time (fill 5980) for a 50 ns LHC beam

Consider the fill 5887, run with 25 ns and previously studied in terms of electrical signals. The power deposited on the Cu surface (station 4) is displayed in grey in Figure 201.

After the injection, the impedance heat load is equivalent to 148 mW/$m_{chamber}$. The impedance heat load was calculated considering both bunch length and bunch population; the impedance contribution of this 25 ns fill is more than double of the 50 ns fill. During the beam injection, the impedance heat calculated corresponds to the measurements. The EC at 450 GeV seems to have no effect on the power deposition into the beam pipe. This could be attributed to a different energy kick and spectrum than the one measured at 6.5 TeV (see Figure 198 and Figure 203). The mean energy of the EC should be smaller at 450 GeV not to be measured after the scrubbing.

The third heat load, the SR power, is calculated from the previous case, considering the increased beam current. The SR power contribution becomes 103 mW/$m_{chamber}$. To compare with the arc, the maximum SR losses of a standard beam current of 0.58 A at 6.5 TeV would be 163 mW/$m_{chamber}$. The SR power contribution measured in the LSS is lower than the maximum SR heat deposited into the arcs.

The impedance and SR components are not sufficient to explain the heat load at 6.5 TeV, therefore the EC seems to have a visible impact at 6.5 TeV (see Figure 201). This is in agreement with the pick-up and pressure measurements.

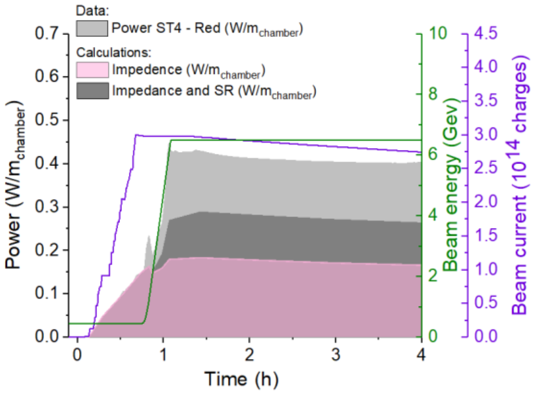

Figure 201: The heat loads on a Cu calorimeter (Station4, red pipe) as a function of the time (fill 5887) for a standard LHC beam.

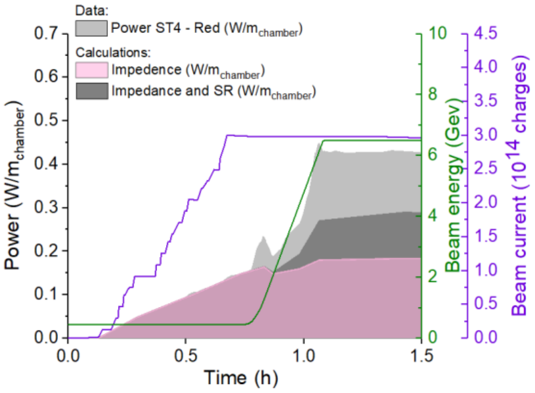

Figure 202: A zoom of the heat loads on a Cu calorimeter (Station4, red pipe) as a function of the time (fill 5887) for a standard LHC beam.

The missing heat load measured with the calorimeters at 6.5 TeV is around 142 mW/$\text{m}_{\text{chamber}}$ (see Figure 201). The three heat loads have the same order of magnitude. The total heat load reaches a maximum of 450 mW/$\text{m}_{\text{chamber}}$.

- **Mean electron energy as a function of the bunch population at 6.5 TeV**

Based on the data presented above, it is possible to compute the mean electron energy at 6.5 TeV. The mean electron energy, $\bar{E}$, can be calculated with Eq. (130). In Figure 203, I present the mean electron energy in linear and logarithmic scales. As at 450 GeV, the higher the multipacting process, the lower the average electron energy. With a high current of around $I_{EC} = 1 \cdot 10^{-6} A$, the mean electron energy calculated from the heat load measurements is around $\bar{E} = 130\ eV$. With $I_{EC} = 1.1 \cdot 10^{-7} A$, $\bar{E} = 1096\ e$, still in multipacting regime.

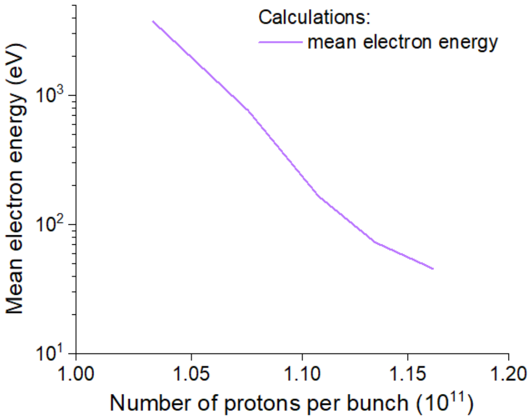

Figure 203: The computation of the mean electron energy from the power deposition as a function of the pick-up current in logarithmic scale at 6.5 TeV.

4.3.2 Influence of surface evolution on EC (conditioning effect)

During the scrubbing run performed in 2017, the mitigation of the EC heat load was monitored as a function of the accumulated electron dose. Consider the first and the last fill of the scrubbing run, respectively fills 5800 and 5821. The first fill was analysed in Figure 195. The last fill is here analysed to compare the EC power contribution. During the scrubbing run the cu surface passed from $6 \cdot 10^{-4}\, C/mm^2$ to $2 \cdot 10^{-3}\, C/mm^2$ of accumulated electron dose. The maximum electron signal of the cu surface passed from $5 \cdot 10^{-6}\, A$ to $4 \cdot 10^{-6}\, A$, with a reduction of 20%.

Consider the fill 5821, the last fill of the scrubbing run 2017. This power profile is visible in Figure 204, together with the impedance contribution plotted in pink and the pick-up signal acquired in black. As for the fill 5800, when the multipacting regime and the pick-up current decay, the power profile drops towards the impedance contribution. In this case, the maximum EC power deposited at the end of the injection corresponds to 39 mW/m$_{\text{chamber}}$. This value corresponds to a reduction of 20% of the heat load of the fill 5800, i.e. 49 mW/m$_{\text{chamber}}$, in agreement with the current decay of 20%.

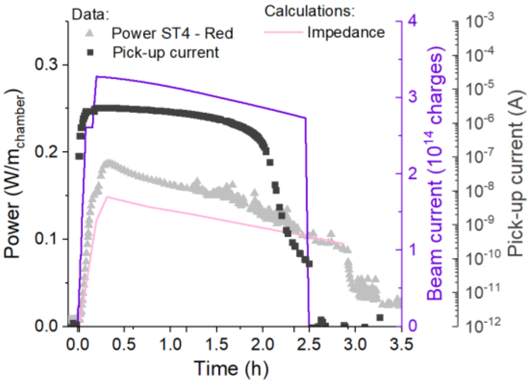

Figure 204: The power deposition on the Cu calorimeter and the pick-up current are displayed as a function of time for the same fill. The impedance contribution is calculated and plotted in pink.

As expected, the EC power deposition decreased along the scrubbing run thanks to the decrease of the multipacting, i.e. the reduction of the electron flux into the wall. The 2017 scrubbing run performed in the LHC reduced the EC phenomenon of about 20%. Afterwards, the EC generated during the standard LHC fills continued to condition the beam pipe walls.

4.3.3 Summary of the thermal analysis

The thermal measurements has been analysed as a function of the beam parameters and beam pipe properties as for electrical and pressure signals. The temperature increase is linear with the number of bunches and bunch population. The evolution of the power deposited by EC has been linked to the electrical activity to determine the mean electron energy deposition into the beam pipe (Section 4.3.1). The contribution of impedance and SR has been inferred for a 50 ns and a standard 25 ns fills. For the 50 ns beam, the impedance and the SR heat loads describe well the heat load measurements. The remaining heat load measured on the 25ns fill is attributed to the EC activity. A higher mean electron energy has been detected for a fill at 6.5 TeV, due to a lower electron activity and a smaller SEY, with machine operation. During the scrubbing the heat load scaled with the lower electron activity. The mean electron energy was, therefore, constant (Section 4.3.2).

Chapter 5 Future HL-LHC operation, analytical model of EC and conclusions

Chaper 5 presents the future EC behaviour of the HL-LHC LSS, with increased bunch population. With higher beam current, the EC activity at the beam pipe walls will change, because of the increased beam electromagnetic field. The electron energy gain as a function of bunch length and bunch population is discussed in *Section 5.1*. This allows to infer the future electron flux and gas desorption behaviour of the surfaces installed into VPS. The energy spectra derived for higher energy kicks and bunch populations allow to estimate the mean electron energy and , therefore, the EC power deposition. The heat load is then compared with a PyECLOUD simulation for similar beam pipe conditions [95]. One of the main purposes of this study is the validation of the PyECLOUD estimations with experimental data.

The above-mentioned data and the extension for higher bunch intensities allow to described the EC with an analytical model, presented for different case studies at 450 GeV and 6.5 TeV. The EC description uses the coefficients determined during the data analysis and the main beam parameters, such as bunch population, number of bunches and bunch length. Also the beam pipe properties are taken into account. The goal of *Section 5.2* is to provide experimental inputs for the analytical description of the EC dynamics for the long straight sections of the LHC.

The last two sections summarize the results and the main outcomes, and discuss the implications of this work and the future operation of the VPS system.

5.1 Future EC behaviour on the LSS during HL-LHC operation

Not only the LHC, but also the future HL-LHC will be affected by EC issues. The main upgrade between the LHC and the HL-LHC is that the bunch population will pass from an average value of $1.15 \cdot 10^{11}$ to $2.2 \cdot 10^{11}$ protons per bunch. In order to estimate the future behaviour of EC on the LSS of the machine, one has to consider the increased electron energy gain [39].

For a standard LHC fill with $1.15 \cdot 10^{11}$ protons per bunch, the energy gain is displayed in Figure 205 as a function of the radial position and the bunch length. As measured with the energy spectrum detector, for a standard fill with $1.15 \cdot 10^{11}\ n_p$ and a bunch length $\sigma = 1.1$ ns, the average kick at a radial position of 3 cm, where the electron density is higher (see Figure 142 and Figure 143) is around 100 eV. A zoom of the energy gain for the most populated region around the bunch is presented in Figure 206.

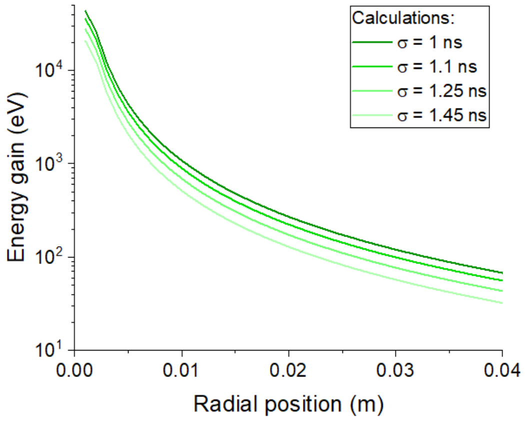

Figure 205: The energy gain is displayed as a function of the radial position for different bunch lengths.

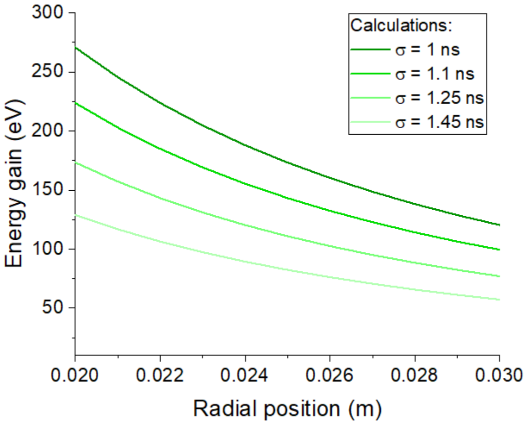

Figure 206: A zoom of the energy gain is displayed as a function of the radial position for different bunch lengths.

I can study the evolution of the mean energy kick for increased bunch populations. For a bunch length of $\sigma = 1.1$ ns, typical at 6.5 TeV, the energy gain is plotted in Figure 207 as a function of the radial position and bunch population. The number of protons per bunch is varied from $1.15 \cdot 10^{11}$ to $2.5 \cdot 10^{11}$. At a radial position of 3 cm, the energy gain for $2.2 \cdot 10^{11}$ protons per bunch is around 363 eV (see Figure 208).

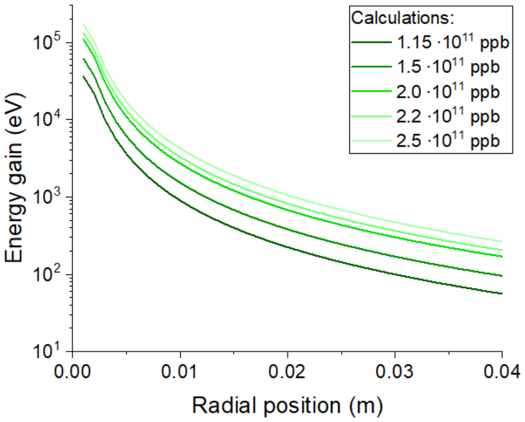

Figure 207: The energy gain is displayed as a function of the radial position for different bunch populations.

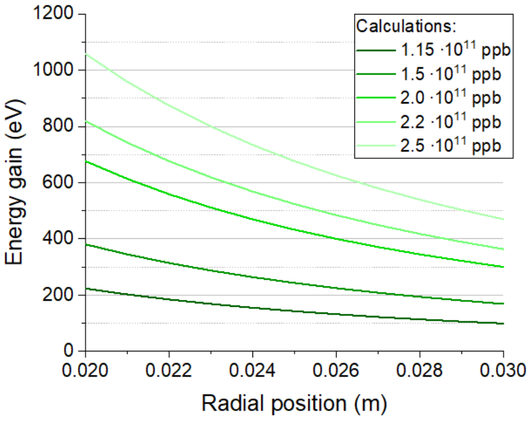

Figure 208: A zoom of the energy gain is displayed as a function of the radial position for different bunch populations.

One can compare this value with the energy at which the surface SEY reaches its maximum. For a Cu surface, it is typically around 200-300 eV (see Figure 9). The SEY decrease between 300 eV and 400 eV is negligible. This means that for the LSS of the HL-LHC, the electrons will get an energy kick at around 363 eV, that is near the maximum of the SEY curve. The electron activity will produce the maximum number of secondaries and the multipacting will not strongly decrease. Therefore, the estimation of the LSS behaviour for HL-LHC can be calculated from the LHC data presented above.

The pick-up currents and pressure that will be measured at the beginning of the HL-LHC run, can be estimated for the surfaces installed. The maximum pick-up current is displayed as a function of the bunch population in Figure 209. Its linear behaviour is extrapolated from Figure 110, also for the case of a-C. The maximum pressure is plotted as a function of the n_p in Figure 210. Its linear behaviour is derived from Figure 157. The maximum values estimated for HL-LHC are around $3 \cdot 10^{-5}$ A and $1.3 \cdot 10^{-7}$ mbar for the Cu surface. The pressure values are still acceptable for the LHC operation.

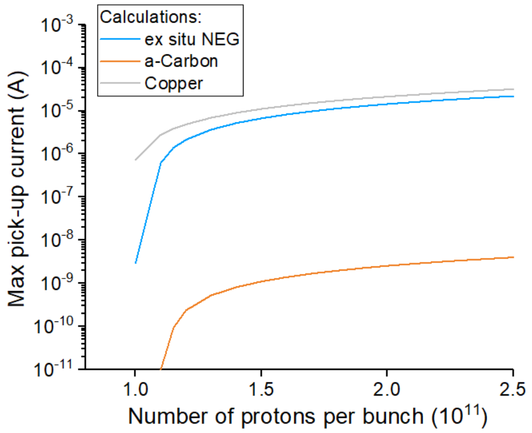

Figure 209: The maximum EC pick-up current estimated for the operation of HL-LHC.

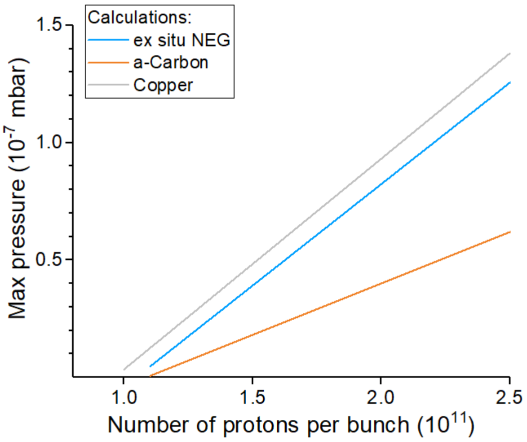

Figure 210: The maximum EC pressure increase estimated for the operation of HL-LHC.

The power computation is more complex. The mean electron energy decreases up to a certain bunch population and then it should increase when the contribution of the high-energy electrons above the maximum SEY is significant. To compute the mean electron energy change, I took the energy spectrum acquired at 6.5 TeV and I estimated the spectra for increasing bunch population and, therefore, with higher electron energy kick. I estimated five cases, from $1.15 \cdot 10^{11}$ to $2.3 \cdot 10^{11}$ protons per bunch, corresponding to mean energy kicks as calculated in Table 17.

Table 17: The mean energy kick received by electron for 80-mm diameter beam pipes as a function of the bunch population for HL-LHC estimations.

Bunch population (protons)	***Energy kick (eV)***
$1.15 \cdot 10^{11}$	100
$1.7 \cdot 10^{11}$	200
$2.0 \cdot 10^{11}$	300
$2.2 \cdot 10^{11}$	363
$2.3 \cdot 10^{11}$	400

The calculated spectra are shown in Figure 211 as a function of energy kick, i.e. bunch population. Above 300 eV the SEY decreases and the secondary electron peak centered at 2 eV decreases.

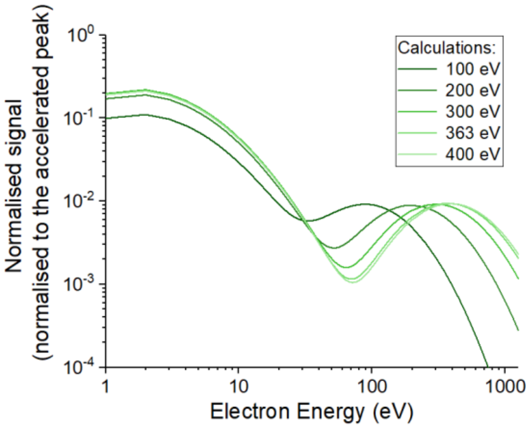

Figure 211: Estimation of energy spectra at different bunch population, i.e. electron energy kick.

The mean electron energy can be estimated for different bunch populations. This is displayed in Figure 212, together with the data measured and presented in Figure 198.

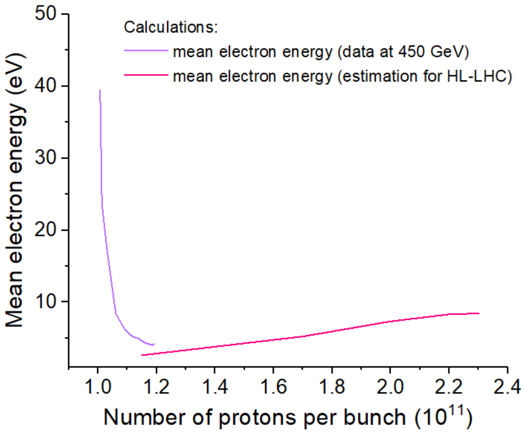

Figure 212: The mean electron energy data and calculations as a function of the bunch population.

The mean electron energy at 2.2 10^{11} is around 8 eV. The EC heat load for the initial HL-LHC operation with an electron current of around $3 \cdot 10^{-5}$ A, is equivalent to 770 mW/m$_{\text{chamber}}$. This computation is valid for a maximum SEY around 1.8-2 for a new Cu surface.

The EC heat load has been simulated with PyECLOUD as a function of bunch population and SEY by colleagues [95]. For a standard 25 ns filling scheme at 450 GeV, the EC behaviour on a 84-mm diameter drift is presented in Figure 213. For an SEY included between 1.5 and 2 and a HL-LHC bunch population of 2.2 10^{11}, the EC heat load simulated is below 8 W/m$_{\text{chamber}}$. Due to a large uncertainty on the SEY estimation of my Cu sample, the PyECLOUD simulation and my heat load estimation can be considered compatible for an SEY around 1.8.

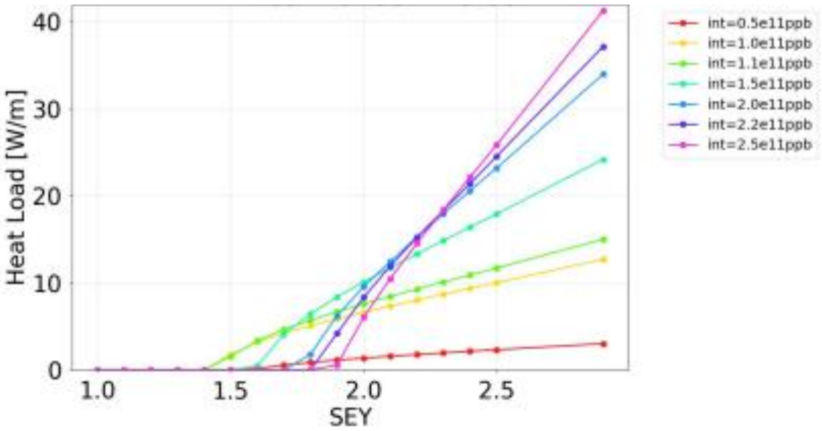

Figure 213: The EC heat load as a function of SEY and bunch population for a drift of LHC [95].

In summary, the EC phenomenon at the beginning of the HL-LHC operation will increase by a factor 10 the electron density and pressure in the LSS (see Figure 209 and Figure 210). The associated EC heat load could reach 1 W/m$_{\text{chamber}}$, with a precise value that will depend on the maximum surface SEY value and the energy at which it is positioned.

In terms of impedance, the HL-LHC operation will be affected by a quadruple heat load, because this component scales with the square of the bunch population. It will pass from 148 mW/m$_{\text{chamber}}$ to around 600 mW/m$_{\text{chamber}}$. In addition, the HL-LHC will register a double SR power deposition because it scales with the bunch population, passing from 103 mW/m$_{\text{chamber}}$ to around 200 mW/m$_{\text{chamber}}$. Finally, the maximum power deposition expected for a LSS of the HL-LHC machine at 6.5 TeV will be around 1.5-1.6 W/m$_{\text{chamber}}$.

5.2 Analytical model of EC

This experimental study showed the evolution of the electron flux, pressure and heat load as a function of several beam pipe parameters and surface properties. The general analytical description of the EC phenomenon and its effects in terms of gas desorption and power deposition is presented here. I considered four different case studies: 50 ns and 25 ns filling scheme at 450 GeV and 6.5 TeV. This simplified description is useful to provide important inputs for the analytical EC model. The electron dynamics in the LSS is linear with bunch population, number of bunches and bunch length at 450 GeV. At collision energy, the EC dynamics is also determined by the photoelectron contribution, whose activity dominates for low SEY surfaces. The surface parameters considered in the description are the secondary electron yield (SEY), the photon electron yield (PEY), the electron stimulated desorption (ESD) and the photon stimulated desorption (PSD).

The experimental values of the coefficients used for the linear interpolations, presented in *Chapter 4,* are valid for the above-mentioned surfaces at a given accumulated electron dose. The status of the surfaces evolves with time, therefore the coefficients decrease with conditioning. This is also valid for the initial a-C coating behaviour due to a surface contamination.

- **50 ns bunch spacing fill at 450 GeV**

The first one concerns the case of a 50 ns bunch spacing and a beam energy of 450 GeV. No EC signals is present no matter the surface SEY value and the EC is avoided. Unfortunately, this filling scheme cannot be used as standard filling scheme to reach the LHC luminosity target, i.e. the number of collision desired. The pressure reading is linked only to the background pressure. The heat load on the beam pipe is deposited due to beam-wall impedance.

- **50 ns bunch spacing fill at 6.5 TeV**

The second case regards a 50 ns bunch spacing filling scheme at 6.5 TeV. The photoelectrons are present but do not multipact. The electron signal is therefore related to the photon flux $\dot{\Gamma}_{ph}$ and the PY of the surface. The photon flux is proportional to the beam current and to the fourth power of the beam energy.

$$I_{EC} = I_{photoelectrons} = PY \cdot \dot{\Gamma}_{ph} \tag{133}$$

In this case, the pressure reading is linked to the background pressure, to a possible in-situ desorption due to SR and photoelectrons, and to gas transmission between different components of the machine. It can be expressed by:

$$\begin{aligned} P &= P_{background} + P_{gas\ transmission} + P_{SR} + P_{photoelectrons} \\ &= P_{background} + P_{gas\ transmission} + PDS \cdot \dot{\Gamma}_{ph} + ESD \cdot PY \cdot \dot{\Gamma}_{ph} \end{aligned} \tag{134}$$

The pressure is dominated by the background also in this case. The SR and photoelectron contributions measured are almost negligible, and so no big gas transmission between different parts of the machine is expected. The heat load on the beam pipe is linked to beam-wall impedance and to SR. The photoelectron heat load is negligible, see the calculation carried with Eq. (132). Therefore:

$$Q = Q_{impedance} + Q_{SR} + Q_{photoelectrons} \approx Q_{impedance} + Q_{SR} \tag{135}$$

The impedance and SR components at 6.5 TeV resulted to be in the same order of magnitude.

- **25 ns bunch spacing fill, with 48 bunches per batch, at 450 GeV**

The third case considers a standard 25 ns fill at 450 GeV. The EC multipacts following the proportionality with the number of bunches (N_b), the bunch population (n_p) and the bunch length (σ), as described in *Chapter 4*.

$$I_{EC} = a_i\, N_b \cdot (b_i\, ppb + c_i) \cdot (d_i\, \sigma + f_i) \tag{136}$$

Where a_i, b_i, c_i, d_i and f_i are slopes and coefficients of the linear interpolations. The bunch population threshold above which the EC multipacting takes place is defined by $th_{ppb} = -c_i/b_i$. The pressure reading in this standard 25 ns case is a sum up of background, EC and gas transmission.

$$P = P_{background} + P_{gas\,transmission} + P_{EC} \tag{137}$$

If the electron activity in situ is strong, the pressure measurement is dominated by the local EC phenomenon and can be used as EC detector. The EC component is expressed by the proportionality with number of bunches, bunch population and bunch length, as for the electron current:

$$P_{EC} = a_p\, N_b \cdot \left(b_p\, ppb + c_p\right) \cdot \left(d_p\, \sigma + f_p\right) = ESD \cdot \dot{\Gamma}_{electrons} \tag{138}$$

Where $a_p, b_p, c_p, d_p$and f_p are slopes and coefficients of the linear interpolations of the pressure trends. The heat load on the beam pipe is linked to beam-wall impedance and to the EC phenomenon.

$$Q = Q_{impedance} + Q_{EC} \tag{139}$$

The EC component is linked to the number of bunches injected and to the bunch population. It can also be expressed using the electron current calculated in Eq. (136) multiplied by the mean electron energy, $\bar{E}$, defined on the map at 450 GeV (see Figure 198).

$$Q_{EC} = a_q\, N_b \cdot \left(b_q\, ppb + c_q\right) = I_{EC} \cdot \frac{A_{chamber}}{A_{detector}} \cdot \bar{E} \tag{140}$$

The EC component at 450 GeV results to be smaller than the impedance contribution.

- **25 ns bunch spacing fill, with 48 bunches per batch, at 6.5 TeV**

The last case is the standard LHC fill at 6.5 TeV. The photoelectron multipacting effect is added to the electron current measured at 450 GeV. It behaviour can be described as:

$$I_{EC} = a_i\, N_b \cdot (b_i\, ppb + c_i) \cdot (d_i\, \sigma + f_i) + I_{photoelectrons} \cdot \varepsilon_i \tag{141}$$

Where ε_i corresponds to the multipacting effect of photoelectrons. In all the cases, the coefficients ($PY, a_i, b_i, c_i, d_i, f_i$ and ε_i) decrease with electron bombardment, i.e. surface conditioning. The multipacting threshold, th_{ppb}, instead, increases with electron dose. The pressure reading in this standard 25 ns case is linked to the background, to the EC, to the SR, to the photoelectrons and to the gas transmission.

$$P = P_{background} + P_{gas\,transmission} + P_{EC} + P_{SR} + P_{photoelectrons} \tag{142}$$

Also at this energy, if the electron activity in situ is strong, the pressure is dominated by the EC phenomenon. The SR contribution is, in fact, negligible (see Figure 158). The photoelectrons participate to the multipacting process together with the other electron seeds and its component in not neglected. If the local electron activity is strong, the pressure is, therefore, dominated by the Electron Stimulated Desorption mechanism. The EC component is expressed by the proportionality with number of bunches, bunch population and bunch length, as before, together with the effect of photoelectrons:

$$P_{EC} = a_p\, N_b \cdot \left(b_p\, ppb + c_p\right) \cdot \left(d_p\, \sigma + f_p\right) + I_{photoelectrons} \cdot \varepsilon_p \tag{143}$$

Where ε_p corresponds to the gas released by the photoelectrons and their multipacting. The heat load on the beam pipe is attributed to beam-wall impedance, to EC, to SR and to photoelectrons. The photoelectrons participate to the EC multipacting and their contribution is taken into account into the total EC component.

$$Q = Q_{impedance} + Q_{EC} + Q_{SR} \tag{144}$$

The EC component is linked to the number of bunches injected and to the bunch population. It can also be expressed using the electron current calculated in Eq. (141) multiplied by the mean electron energy.

$$Q_{EC} = I_{EC} \cdot \frac{A_{chamber}}{A_{detector}} \cdot \bar{E} \tag{145}$$

The EC component at 6.5 TeV for a copper LSS is in the same order of magnitude of impedance and SR contributions.

5.3 Discussion of the main results

I have shown that the VPS is able to detect electron cloud signals with different detectors. This system is now a perfect operational test-bench to validate future materials for accelerator installations.

Among the installed surfaces, the copper station has the highest electron currents and pressure signals in all conditions reported in this thesis, as expected from the SEY studies present in literature. The EC currents increase linearly with the number of bunches, the bunch population in multipacting regime and the bunch length. The electron bombardment has a conditioning effect on the surfaces, reducing the SEY parameter and therefore the multipacting. Along two years, the electrical signal on Cu reduced of five orders of magnitude. At 450 GeV, EC is detected for standard filling schemes, composed of 48 bunches per batch. With 8b4e or 12 bunches per batch, the multipacting is correlated only to the photoelectron activity due to SR above 2.8 TeV. The implementation of 8b4e or 12 bunches per batch could reduce drastically the EC around the EC ring, but with a reduced luminosity. The fast measurements performed with the oscilloscope allowed to detect the ns evolution of the EC build-up mechanism. For a multipacting regime, less than 10 bunches are sufficient to reach multipacting equilibrium on high SEY surfaces, as Cu.

Amorphous carbon coating reduces drastically the EC multipacting, thanks to a low SEY. At the beginning of the LHC operation, the a-C surface can suffer of small EC activities due to gas contaminants on the surface. The a-C pressure measurements suffer from gas transmission between the nearby stations. This transmission effect has been shown with NEG cartridge injections. With the injection of hydrogen and methane, a pressure reduction of a factor 10 and 3, respectively, has been measured and simulated with VASCO and Monte Carlo between different stations. This ratio depends on the gas type, its sticking factor on the NEG buffers, and on the beam pipe geometry. The photoelectron current in the a-C surface is about 5 times lower than the one of Cu and 4 times smaller than ex-situ NEG. The implementation of a low SEY a-C would reduce the EC build-up in the most critical parts of the machine.

The ex-situ NEG station shows a lower EC activities if compared with Cu, therefore, it has a lower initial SEY. The same SEY conditions are reached in two years for the Cu surface (see Figure 149) and 5 weeks for the ex-situ NEG one (see Figure 151). Therefore, the installation of NEG with ex-situ activation can be a solution to lower the EC activity for in-situ unbakeable systems.

The contribution of photoelectrons is negligible for high SEY surfaces, while it triggers the electron cloud signal for low SEY surfaces. The gas desorption due to SR and photoelectrons is anyway negligible from all the tested surfaces. The main gas desorption mechanism is triggered by the EC activity.

The power deposition is equally distributed between beam-wall impedance, SR and EC for standard 25 ns filling schemes. The mean electron energy can be measured through the ratio of heat load deposited by EC and the electrical signal, or thanks to the electron energy spectrum. The kick received by the electrons is around 100 eV for s 80-mm beam pipe installed in room temperature and field free LSS, while the mean electron energy is dominated by the presence of secondaries at few eV.

The estimation for HL-LHC are carried thanks to an analytical model that described the EC as a function of beam parameters and surface properties. The measurements and the estimations are useful to validate the simulating codes used to estimate the EC behaviour for the future operation of the most crucial components of the machine. In terms of electrical, pressure and thermal loads the LSS will register higher signals, still acceptable for the operation.

5.4 Conclusions

This work studies the EC behaviour in terms of electrical, pressure and thermal physical quantities acquired in a LSS of the LHC ring. The results of this study describe the influence of beam parameters and beam pipe properties into the EC and SR phenomena and estimate the future operation of the HL-LHC machine.

The Vacuum Pilot Sector (VPS) system is able to detect EC and SR signals in the LHC. The electrical signals have a higher resolution and precision if compared with the pressure and thermal ones. For a high electron activity in multipacting regime, the pressure signals are also good indicators of the presence of the EC phenomenon.

In multipacting regime, the EC is linearly dependent with the number of bunches (N_b). EC is linearly dependent with the number of protons per bunch (n_p) above a certain multipacting threshold that defines the multipacting regime. The bunch spacing has an enormous impact on the EC phenomenon. With 50 ns, the EC disappears and only photoelectrons are measured. With the standard 25 ns the EC is visible at both 450 GeV and 6.5 TeV. The EC is also linear with the bunch length in the LHC drifts. The filling scheme, in particular the number of bunches per batch, strongly influences the EC dynamics. The 12 bunches per batch only shows the photoelectron multipacting at 6.5 TeV. The 8b4e filling scheme has the lowest activity, triggered by photoelectrons. The implementation of these two filling schemes, i.e. 8b4e or 12 bunches per batch, reduces drastically the EC and its effects, also for beam pipe surfaces with a high SEY.

In multipacting regime, 6 to 10 bunches are needed to reach the equilibrium. The energy spectrum performed at 6.5 TeV identifies a peak at 100 eV for a RT chamber (d=80 mm) and it agrees with simulations and calculations. The energy kick depends on beam parameters as the beam energy and emittance, and on surface parameters, as beam pipe SEY. The electron distribution as a function of the radius shows a high-dense ring with a maximum at around 3 cm, as foreseen by the analytic calculations. The surface evolution confirms the beam conditioning effect, with the reduction of the EC signals and the increase of the the protons-per-bunch multipacting threshold with accumulated electron dose. In 2 years, the EC multipacting reduced of five orders of magnitude at 450 GeV in the copper surface. The EC decreases of 20% during the scrubbing run and the conditioning effect continues along the years. The comparison between different surfaces shows that amorphous carbon coating reduces drastically the EC build-up, thanks to its low SEY. The amorphous carbon coating surface is stable with time, therefore a good candidate for future installations. In fact, thanks to its good performances confirmed by this study, it was chosen and installed in 2019 in several parts of the LHC machine.

The pressure signals reproduce the behaviour measured with the electrical pick-ups. The EC multipacting threshold can be identified in both electrical and pressure signals for ex situ NEG and copper surfaces. A regular pressure monitoring can be used to detect the EC threshold in multipacting regime, but a pressure increase cannot be always attributed to EC activity. The ESD parameter was inferred for the Cu surface and its decrease is attributed to the conditioning effect. The gas composition studies define a possible presence of C_3FN, probably generated by the SR impinging into the kapton cables between the beam pipe and the vacuum chamber.

The thermal signals were more complex to analyse, because the calorimeters were responding with different time constants than the ones measured during the calibration tests. The only calorimeters that seemed to work properly were the two installed before my arrival at CERN and installed on cu. The temperature profile was analysed for a copper surface at 450 GeV and 6.5 TeV, as a function of beam parameters, and followed the above-mentioned behaviours. The thermal behaviour was inverse to the one read by pick-up currents only in the case of the bunch length dynamic. These thermal measurements allow to calculate the evolution of the mean electron energy, changing along the fill. The impedance, EC and SR components are disentangled and the EC heat load component is derived for several fills.

The estimations for the LSS of the HL-LHC machine confirm that the increase of the bunch population will have a big impact on the machine operation. The electrical and pressure signals will increase of an order of magnitude, up to 10^{-5} A and 10^{-7} mbar, respectively. The deposited power due to EC will increase up more than 770 mW/$m_{chamber}$. The contribution of SR and impedance will raise up the total power to 1.5-1.6 mW/$m_{chamber}$ for unbaked copper beam pipes in field free and room temperature areas of the machine.

As consequence, the VPS system has been confirmed to be a valid test bench for future surface installations before the implementation in the most critical parts of the machine. The modularity of the system will allow the replacement of the stations in the following years, for testing new possible surface candidates and to carry new EC studies. For the first time in the LHC history, this system is able to detect different signals and effects of the EC activity with direct measurements. New studies have been planned for the future of VPS:

- the implementation of another low SEY surface as the Laser Engineered Surface Structures (LESS) coating;
- the upgrades of the type E calorimeters, for a better understanding of the thermal transients;
- the follow-up of the radiation-resistant amplifiers and filters applied into the pick-ups connected to the oscilloscopes (designed and build by M. Gasior);
- the update of the spectrum detector acquisition system to reduce the signal-to-noise ratio.

The experimental data acquired with VPS validates the EC simulation code used at CERN (PyECLOUD), in particular the EC energy spectra and the heat load estimations. This validation allows to trust the simulation code and its results in the other parts of the machine where it is difficult to directly measure the EC activity. Another upgrade of the system could involve the implementation of a electromagnetic coil to trap the electrons near the beam pipe and study the effective reduction of the EC, or, in alternative, the application of an external magnet to drive the electron motion and to simulate the dipoles.

Concerning the good performance of the a-C coatings, an installation campaign took place starting from 2019. The a-C coating has been applied in some magnets of the LHC, but with not excellent results. Some more studies needs to be carried to evaluate the hydrogen content during the in situ coating process, responsible for a high SEY, up to around 1.6. The CERN Vacuum, Coatings and Surface group will invest lots of energies and manpower to reach the prefix target of coating 4 quadrupoles in the following years. The implementation of a low SEY surface in the most critical components of the machine is crucial for the LHC operation without cryogenic EC limitations in the upcoming years.

Annex 1: Physical constants

$\hbar$	Reduced Planck constant	$6.58 \cdot 10^{-16}\ eV\ s$
c	Light speed	$299\,792\,458 \frac{m}{s}$
m_p	Proton mass	$1.67 \cdot 10^{-27}\ kg$
e	Electron charge	$-1.60 \cdot 10^{-19}\ C$
ε_0	Vacuum permittivity	$8.85 \cdot 10^{-12} \frac{F}{m}$
m_e	Electron mass	$9.11 \cdot 10^{-31}\ kg$
Z_0	Impedance of free space	$376.73\ \Omega$
k_B	Boltzmann constant	$1.38 \cdot 10^{-23} \frac{m^2 kg}{s^2\ K}$
r_e	Classical electron radius	$2.82 \cdot 10^{-15}\ m$

Annex 2: Beam pipe properties

This section is a brief literature overview of the beam pipe properties as a function of impinging particles, energy, angle, surface conditioning, thermal treatments and temperature, mentioned in *Chapter 1.4*.

A.2.1 Electron Stimulated Desorption (ESD)

The evolution of the electron stimulated desorption, ESD or η_e, was analysed as a function of several parameters. For different gasses, the ESD increases with higher electron energy (see Figure 214) and decreases with accumulated electron dose, measured in electrons per cubic centimetre (see Figure 215) [13].

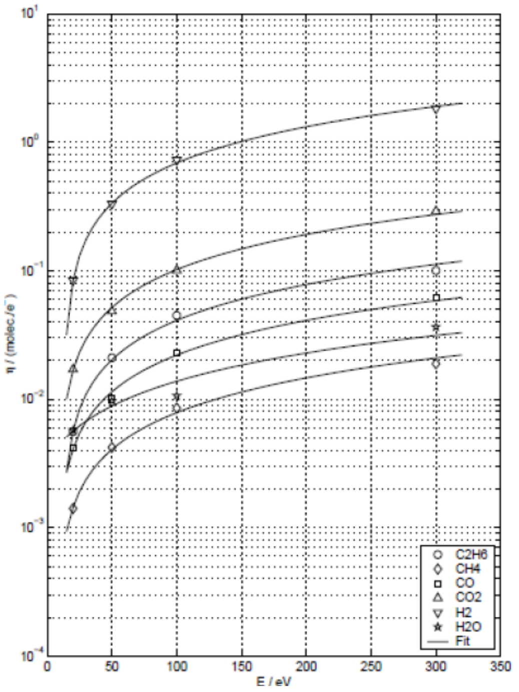

Figure 214: The η_e as a function of electron energy, for an unbaked OFHC copper with a dose $D = 1.4 \cdot 10^{14}\ \frac{electrons}{cm^2}$ [13].

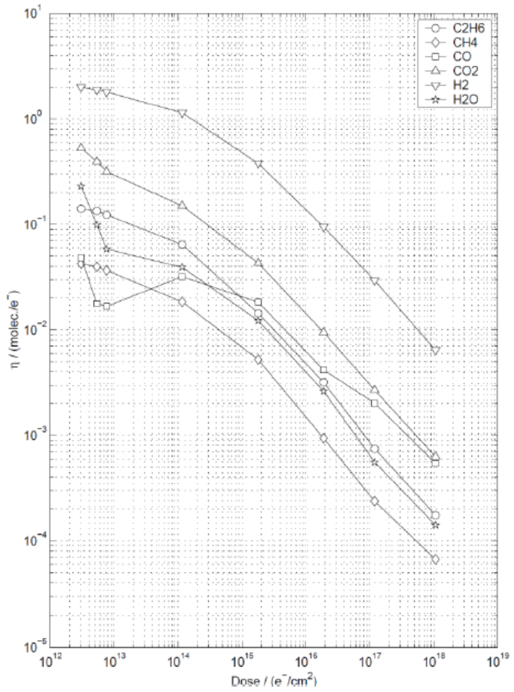

Figure 215: The η_e as a function of accumulated electron dose, for an unbaked OFHC copper after 24 hours with an electron gun set at $E = 300\ eV$ [13].

The ESD decreases if the vacuum firing process (VF) is performed on a vacuum component (see Figure 216). Moreover, the ESD increases with the temperature (see Figure 217) [67, 68].

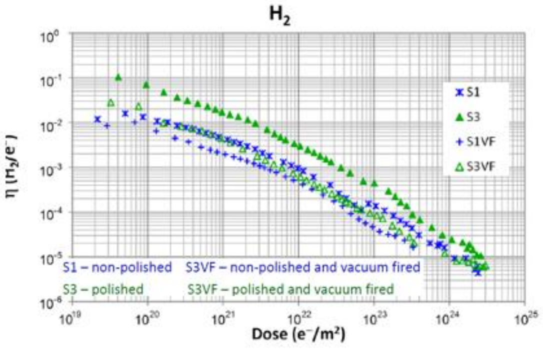

Figure 216: The η_e in presence of the vacuum firing (VF) [67].

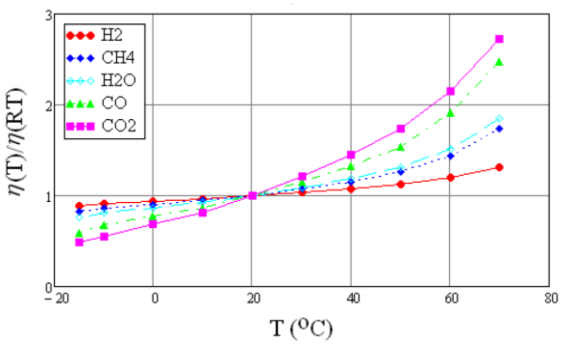

Figure 217: The η_e as a function of the temperature [68].

A.2.2 Photon Stimulated Desorption (PSD)

The photons stimulated desorption η_γ decreases with dose (see Figure 218) and increases with photon energy (see Figure 219) [61, 62].

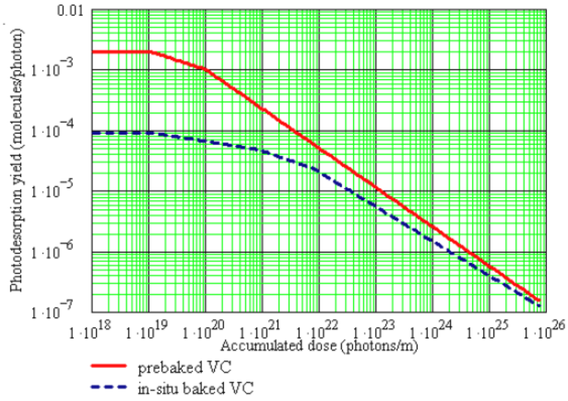

Figure 218: The η_γ as a function of accumulated photon dose [61].

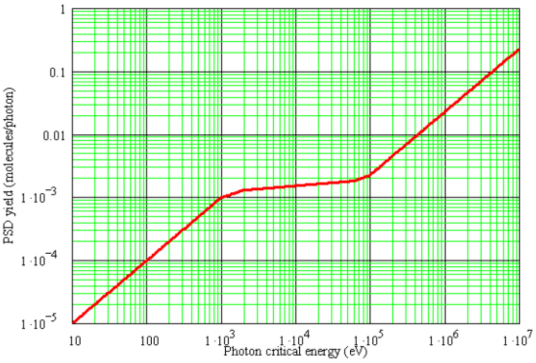

Figure 219: The η_γ as a function of photon critical energy. [62].

The η_γ is displayed as a function of the absorber angle in Figure 220. The impinging angle correspond to 0 with grazing radiation and 90 degrees with perpendicular photon. The higher the angle, the higher the desorption [63].

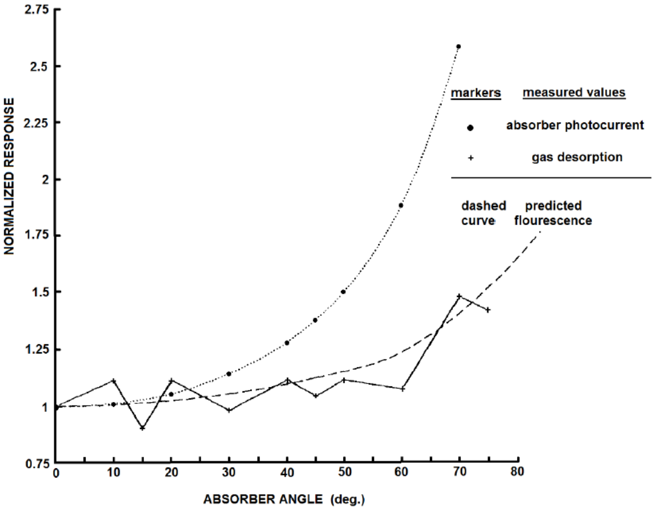

Figure 220: The η_γ as a function of the absorber angle [63].

Annex 3: High Voltage Bias measurement

This section describes the analytical reasoning used to derive the Eq. (45), describing the measurement performed with a High Voltage Bias (HVB) pick-up, shown in *Chapter 2.4.2*.

In this paragraph I explore the influence of positive bias only, from 0 V to few hundreds Volts. The higher is the bias, the more secondary, reflected and back-scattered electrons are trapped at the electrode, and so the more reliable the measurement. The measurement is summarised in Figure 29.

$$I_{pick-up\ (V_x)} = I_{E<V_x} + I_{E>V_x} - I_{refl>V_x,E>V_x} - I_{sec>V_x,E>V_x} \tag{146}$$

If one varies the bias with a defined input source and compares the values with the 9-10 eV measurement usually applied to the electrode with a battery, the difference should give the information on the reflected, back-scattered and secondary components. The higher the applied bias, the bigger the amount of secondaries trapped at the electrode, so the higher the absolute value of the current read:

$$\begin{aligned}
&I_{pick-up\ (V_x)} - I_{pick-up\ (+9V)} \\
&\qquad = \left(I_{E<V_x} + I_{E>V_x} - I_{refl>V_x,E>V_x} - I_{sec>V_x,E>V_x}\right) - \left(I_{E<+9V} + I_{E>+9V}\right. \\
&\qquad \left. - I_{refl>+9V,E>+9V} - I_{sec>+9V,E>+9V}\right) \\
&\qquad = \left(I_{input} - I_{refl>V_x,E>V_x} - I_{sec>V_x,E>V_x}\right) - \left(I_{input} - I_{refl>+9V,E>+9V}\right. \\
&\qquad \left. - I_{sec>+9V,E>+9V}\right) \\
&\qquad = \left(I_{refl>+9V,E>+9V} - I_{refl>V_x,E>V_x}\right) + \left(I_{sec>+9V,E>+9V} - I_{sec>V_x,E>V_x}\right)
\end{aligned} \tag{147}$$

Here $I_{refl>V_x,E>V_x}$ are the electrons reflected and the back-scattered with more than V_x and not trapped by the bias, $I_{refl>+9V,E>+9V}$ are the electrons reflected and the back-scattered with more than $9eV$, not trapped. This last element corresponds to the sum of the reflectivity between $9V$ and V_x and the reflectivity above V_x. The same is valid for $I_{sec>V_x,E>V_x}$ and $I_{sec>+9V,E>+9V}$ that are respectively the secondaries with more than V_x and $9eV$. Therefore, it is possible to write the elastic component as:

$$\begin{aligned}
I_{refl>+9V,E>+9V} - I_{refl>V_x,E>V_x} &= \delta_{elastic} \cdot I_{E>9eV} - \delta_{elastic} \cdot I_{E>V_x} \\
&= \delta_{elastic}\left(I_{9eV<E<V_x} + I_{E>V_x}\right) - \delta_{elastic} \cdot I_{E>V_x} \\
&= \delta_{elastic} \cdot I_{9eV<E<V_x} + \delta_{elastic} \cdot I_{E>V_x} - \delta_{elastic} \cdot I_{E>V_x} = \delta_{elastic} \cdot I_{9eV<E<V_x}
\end{aligned} \tag{148}$$

And the true secondary generation is similarly described as:

$$\begin{aligned}
I_{sec>+9V,E>+9V} - I_{sec>V_x,E>V_x} &= \delta_{true} \cdot I_{E>9eV} - \delta_{true} \cdot I_{E>V_x} \\
&= \delta_{true}\left(I_{9eV<E<V_x} + I_{E>V_x}\right) - \delta_{true} \cdot I_{E>V_x} \\
&= +\delta_{true} \cdot I_{9eV<E<V_x} + \delta_{true} \cdot I_{E>V_x} - \delta_{true} \cdot I_{E>V_x} = \delta_{true} \cdot I_{9eV<E<V_x}
\end{aligned} \tag{149}$$

Considering the previous equations and a voltage $V_x > 9V$, the final expression becomes:

$$I_{pick-up\,(V_x)} - I_{pick-up\,(+9V)} = \left(I_{refl>+9V,E>+9V} - I_{refl>V_x,E>V_x}\right) + \left(I_{sec>+9V,E>+9V} - I_{sec>V_x,E>V_x}\right) =$$

$$= \delta_{elastic} \cdot I_{9eV<E<V_x} + \delta_{true} \cdot I_{9eV<E<V_x} = (\delta_{elastic} + \delta_{true}) \cdot I_{9eV<E<V_x}$$

$$= \delta \cdot I_{9eV<E<V_x} \qquad (150)$$

Annex 4: VASCO simulation code

The Vacuum Stability Code (VASCO) has been developed at CERN. This code simulates the stability of vacuum systems for particle accelerators estimating the gas density distribution. The mathematical model consider several mechanisms:

- the molecular diffusion due a pressure difference, $c_{spec}\frac{\partial^2 n}{\partial x^2}$
- ion stimulated desorption, $\sum_{gas}\eta_{ion-gas}\sigma\ \frac{I}{e}\ n_{gas}$
- electron stimulated desorption, $\eta_e N_e$
- photon stimulated desorption, $\eta_{ph}\Gamma_{ph}$
- linear pumping, $S_{dis}n$
- beam pumping, $\eta_i\sigma\ \frac{I}{e}\ n$
- thermal outgassing, aq

The model takes into account all these mechanisms that desorb or pump gas molecules to calculate the equilibrium gas density. For a given temperature and gas sensitivity, it is possible to convert the gas density estimation (molecules/m^3) into mbar$_{\text{N2 equivalent}}$.
The program calculates the steady-state density, reached by equilibrium between gas sources and pumping systems.
The program solve the following equation, expressed by the time variation of the volumetric density in volume V per unit of length, $V\frac{\partial n}{\partial t}$, that is equal to the sum up of the above-mentioned mechanisms:

$$V\frac{\partial n}{\partial t} = c_{spec}\frac{\partial^2 n}{\partial x^2} + \sum_{gas}\eta_{ion-gas}\sigma\ \frac{I}{e}\ n_{gas} - \eta_i\sigma\ \frac{I}{e}\ n - S_{dis}n + \eta_{ph}\Gamma_{ph} + \eta_e N_e + aq \approx 0 \qquad (151)$$

A typical overview of these mechanisms is here presented:

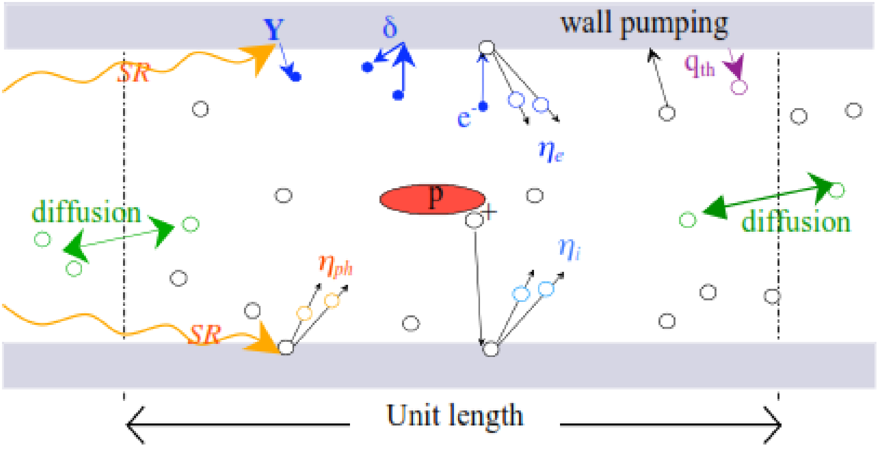

Figure 221: Representation of several mechanisms affecting the vacuum dynamic [96].

The model uses cylindrical geometry to allow one dimensional approximation, time invariant parameters, multi-gas model and finite elements with boundary conditions ensuring the continuity between elements. Typical coefficients and examples can be found in [96].

Annex 5: Beam parameters of the main fills

The beam parameters of the main fills analysed in this work are summarised below. The follow-up of the different LHC beams was presented in the CERN operation logbook [97].

Fill No.	*Bunch spacing (ns)*	*Number of bunches (Blue)*	*Number of bunches (Red)*	*Bunches per batch*	*Initial bunch Population (Blue)*	*Initial bunch Population (Red)*	*Beam energy reached (GeV)*	*Page*
4528	25	1825	1824	72	$1.17 \cdot 10^{11}$	$1.15 \cdot 10^{11}$	6500	86-87
5717	25	75	75	12	$1.18 \cdot 10^{11}$	$1.16 \cdot 10^{11}$	6500	80-82
5765	25	2040	2100	72	$1.03 \cdot 10^{11}$	$1.01 \cdot 10^{11}$	450	82-83
5794	25	2820	2820	48	$1.16 \cdot 10^{11}$	$1.17 \cdot 10^{11}$	450	82-84
5800	25	2820	2820	48	$1.19 \cdot 10^{11}$	$1.19 \cdot 10^{11}$	450	75-76, 94, 105, 110-111
5821	25	1820	1820	48	$1.17 \cdot 10^{11}$	$1.16 \cdot 10^{11}$	450	89, 110
5878	25	2460	2460	48	$1.10 \cdot 10^{11}$	$1.11 \cdot 10^{11}$	6500	82, 84
5887	25	2556	2556	48	$1.17 \cdot 10^{11}$	$1.17 \cdot 10^{11}$	6500	80, 90-92, 109-110
5979	25	2556	2556	48	$1.12 \cdot 10^{11}$	$1.11 \cdot 10^{11}$	6500	77, 90-92, 96
5980	50	1824	1824	24	$9.1 \cdot 10^{10}$	$9.1 \cdot 10^{10}$	6500	77, 80, 95, 108-109
6174	25	1916	1916	8b4e	$1.06 \cdot 10^{11}$	$1.07 \cdot 10^{11}$	6500	80
6594	25	339	339	12	$1.13 \cdot 10^{11}$	$1.13 \cdot 10^{11}$	6500	82, 86
6610	25	2316	2316	48	$1.23 \cdot 10^{11}$	$1.22 \cdot 10^{11}$	450	102-103
6860	25	2460	2460	48	$1.12 \cdot 10^{11}$	$1.14 \cdot 10^{11}$	6500	97
7013	25	2556	2556	48	$1.06 \cdot 10^{11}$	$1.06 \cdot 10^{11}$	6500	100
7334	25	2556	2556	48	$1.05 \cdot 10^{11}$	$1.05 \cdot 10^{11}$	6500	90-93

References

[1] H. Fukuma, Electron Cloud Observations and Predictions at KEKB, PEP-II and SuperB Factories, in Proceeding of ECLOUD12: Joint INFN-CERN-EuCARD-AccNet Workshop on Electron-Cloud Effects, La Biodola, Isola d'Elba, Italy, 2012.

[2] W. Fischer et al., Electron cloud observations and cures in the relativistic heavy ion collider, Phys. Rew. Special Topics Accelerators and Beams, vol. 11, no. 4, p. 041002, 2008.

[3] M. G. Billing et al., Update on Electron Cloud Mitigation Studies at Cesr-TA, in IPAC Conf. Proc. C 796-798, 2011.

[4] M. Zobov et al., Operating experience with electroncloud clearing electrodesat DEFNE, in Proceedings ofECLOUD12: Joint INFN-CERN-EuCARD-AccNet Workshop on Electron-Cloud Effects, La Biodola, Isola d'Elba, Italy, 2012.

[5] J. M. Jimenez, B. Henrist, N. Hilleret, J. M. Laurent, D. Schulte, LHC and SPC Electron Cloud Studies, AIP. Conf. Proc., no. 773, pp. 211-215, 2005.

[6] O. Brüning, P. Collier, P. Lebrun, S. Myers, R. Ostojic, J. Poole, P. Proudlock, LHC Design Report, CERN-2004-003, Geneva, 2004.

[7] L. A. Rossi, G. Apollinari, M. Lamont, High-Luminosity Large Hadron Collider (HL-LHC): Preliminary Design Report, United States, 2015.

[8] Benedikt, "FCC: colliders at the energy frontier," in 9th International Particle Accelerator Conference (IPAC), Vancouver, Canada, 2018.

[9] B. Henrist, V. Baglin, G. Bregliozzi, P. Chiggiato, The LHC Vacuum Pilot Sector Project, Proceedings of IPAC2014, Dresden, Germany, 2014.

[10] G. Rumolo, F. Ruggiero, and F. Zimmermann, Simulation of the electron-cloud build up and its consequences on heat load, beam stability, and diagnostics, Physical Review Special Topics - Accelerator and Beams, vol. 4, p. 012801, Jan 2001.

[11] G. Iadarola, Electron Cloud studies for CERN particle accelerators and simulation code development, CERN-THESIS-2014-047, 2014.

[12] R. Cimino, G. Rumolo, F. Zimmermann, Proceedings of ECLOUD'12: Joint INFN-CERN-EuCARD-AccNet Workshop on Electron-Cloud Effects, as CERN Yellow Report, La Biodola, Isola d'Elba, Italy, 2013.

[13] F. Billard, N. Hilleret, G. Vorlaufer, Some results on the electron induced desorption yield of OFHC copper, Vacuum Technical Note 00-32, Geneva, 2000.

[14] G. Peach, Ionization of atoms and positive ions by electron and proton impact, Journal of Physics B: Atomic and Molecular Physics, vol. 4 (no 12), no. 1971, p. 1670.

[15] M. E. Rudd, Y. -K. Kim, D. H. Madison, J. W. Gallagher, Electron production in proton collisions: total cross sections, Review of Modern Physics, vol. 57, p. 965-994, 1985.

[16] A. Hofmann, The Physics of Synchrotron Radiation, C. U. Press, Ed., Cambridge: Cambidge Monographs on Particle Physics, Nuclear Physics and Cosmology, 2004.

[17] F. Zimmermann, Synchrotron radiation in the LHC Arcs - Monte Carlo Approach, LHC-Project-Note-237, 2000.

[18] J. Jackson, Classical electrodynamics, 3rd rd. ed., New York: Wiley, 1999.

[19] V. Baglin, G. Bregliozzi, J. M. Jimenez, G. Lanza, Synchrotron radiation in the LHC vacuum system, in IPAC, San Sebastian, Spain, 2011.

[20] H. Wiedemann, Particle Accelerator Physics, Stanford, USA: Springer, 2015.

[21] G. N. Derry, M. E. Kern and E. H. Worth, Recommended values of clean metal surface work functions, JVST A, vol. 33, p. 060801, 2015.

[22] E. Buratin, V. Baglin, B. Henrist, Preliminary results obtained with the LHC Vacuum Pilot Sector, Proceedings of ECLOUD'18, La Biodola, Isola d'Elba, Italy, 2018.

[23] V. Baglin, I.R. Collins, O. Gröbner, Photoelectron Yield and Photon Reflectivity from Candidate LHC Vacuum Chamber Materials with Implications to the Vacuum Chamber Design, Proceedings of the 6th European Particle Accelerator Conference, Stockholm, Sweden, 1998.

[24] M. Lamont, Yearly beam losses in past and future operation, presentation at the LHC Collimation Working Group - 142th meeting, 4 Juin 2012.

[25] L. Mether, Multispecies simulations withcross-ionization: investigation on numerical, Electron cloud meeting n.71, CERN, 2019.

[26] S. Bilgen et al., Dynamic pressure in the LHC: influence of ions induced by ionization of residual gas by both the proton beam and the electron cloud, Journal of Physics: Conference Series, vol. 1350, p. 012171, 2019.

[27] A. G. Mattewson and S. Zhang, “Beam-Gas Ionisation Cross Sections at 7.0 TeV,” CERN Vacuum Technical Note 96-01, 1996.

[28] R. Cimino, Interaction between Beams and Vacuum System Walls, presentation at the CERN Accelerator School (CAS) - Vacuum for Particle Accelerators, 2017.

[29] P.O. Gartland, S. Berge, B. J. Slagsvold, Photoelectric Work Function of a Copper Single Crystal, Physical Review Letters, vol. 28 (12), 1972.

[30] P. A. Anderson, The Work Function of Copper, Physical Review, vol. 76 (3), 1949.

[31] B. Henrist, N. Hilleret, M. Jimenez, C. Scheuerlein, M. Taborelli and G. Vorlaufer, Secondary electron emission data for the simulation of electron cloud, Mini workshop on Electron Cloud Simulations for Proton and Positron Beams, CERN, Geneva, Switzerland, 2002.

[32] R. Cimino and I. R. Collins, Vacuum chamber surface electron properties influencing electron cloud phenomena, Applied Surface Science, vol. 235, p. 231-235, 2004.

[33] M. A. Furman and M. T. Pivi, Probabilistic model for the simulation of secondary electron emission, Phys. Rew. Special Topics: Accelerators & Beams, vol. 5, p. 124404, 2002.

[34] V. Baglin, J. Bojko , O. Gröbner, B. Henrist, N. Hilleret, C. Scheuerlein, M. Taborelli, The secondary electron yield of technical materials and its variation with surface treatments, Proceedings of EPAC, Vienna, Austria, 2000.

[35] B. Henrist, N. Hilleret, C. Scheuerlein, M. Taborelli, The secondary electron yield of TiZr and TiZrV, Applied Surface Science, vol. 172, pp. 95-102, 2001.

[36] C. Yin Vallgren, G. Arduini, J. Bauche, S. Calatroni, P. Chiggiato, K. Cornelis, P. Costa Pinto, B. Henrist, E. Metral, H. Neupert, G. Rumolo, E. Shaposhnikova and M. Taborelli, Amorphous carbon coatings for the mitigation of electron cloud in the CERN Super Proton Synchrotron, Physical Review Special Topics - Accelerators and Beams, vol. 14, 071001, 2011.

[37] P. Costa Pinto, T. Basso, A. Bellunato, P. Edwards, M. Mensi, Implementation of carbon thin film coatings in the super proton synchrotron (SPS) for electron cloud mitigation, in Proc. of IPAC2014, Dresden, Germany.

[38] R. Cimino, M. Commisso, DR. Grosso, T. Demma, V. Baglin, R. Flammini, R. Larciprete, Nature of the Decrease of the Secondary-Electron Yield by Electron Bombardmenet and its Energy Dependence, Physical Review Letters, vol. 109, 064801, 2012.

[39] O. Gröbner, Beam Induced Multipacting, in Proceedings of the 1997 Particle Accelerator Conference, Vancouver, Canada, 1997.

[40] J. S. Berg, Energy Gain in an Electron Cloud During the Passage of a Bunch, LHC Project Note 97, Geneva, Switzerland, 1997.

[41] M. A. Furman, The Electron-Cloud Effect in the Arcs of the LHC, LHC Project Report 180, Geneva, Switzerland, 1998.

[42] L. Vos, Electron Cloud: an Analytic View, LHC Project Note 150, 1998.

[43] M. Ferraio, M. Migliorati, and L. Palumbo, Space Charge Effects, CERN Yellow Report CERN-2014-009, pp.331-356, Geneva, Switzerland, 2014.

[44] O. Bruning, Simulations for the beam-induced electron cloud in the LHC beam screen with magnetic field and image charges, CERN LHC Project Report 158, Nov 1997.

[45] S. Heifets, Electron cloud at high beam currents, in Mini-Workshop on Electron Cloud Simulations for Proton and Electron Beams, Geneva, Switzerland, 2002.

[46] S. Heifets, Qualitative Analysis of the e-Cloud Formation, in Mini-Workshop on Electron Cloud Simulations for Proton and Positron Beams, Geneva, Switzerland, 2002.

[47] K. Kanazawa, H.Hukuma, H. Hisamatsu, and Y. Suetsugu, Measurement of the electron cloud density around the beam, in Particle Accelerator Conference, Knoxville, Tennessee, 2005.

[48] M. A. Furman, Formation and dissipation of the electron cloud, in Particle Accelerator Conference, 2003.

[49] F. Zimmermann, G. Rumolo, K. Ohmi, Electron Cloud Build Up in Machines with Short Bunches, ICFA Beam Dyn. Newslett., no. 33, pp. 14-24, 2004.

[50] G. Iadarola, G. Rumolo, PyECLOUD and build-up simulations at CERN, in Prodeedings for ECLOUD'12, 2012.

[51] G. Iadarola et al., Electron Cloud and scrubbing studies for the LHC, in Proc. of IPAC2013, Shangai, China, 2013.

[52] Y. Papaphilippou et al., Operational beams for the LHC, CERN Yellow Report (YR), Geneva, 2014.

[53] V. Baglin, O. Brüning, R. Calder, F. Caspers, I.R. Collins,O. Gröbner, N. Hilleret, J.-M. Laurent, M. Morvillo, M. Pivi, F. Ruggiero, Beam-induced electron cloud in the LHC and possible remedies, LHC Project Report 188, CERN, 1998.

[54] N. Mahne, V. Baglin , I. R. Collins, A. Giglia, L. Pasquali, M. Pedio , S. Nannarone and R. Cimino, Photon reflectivity distributions from the LHC beam screen and their implications on the arc beam vacuum system, LHC Project Report 668, CERN, Geneva, 2003.

[55] V. V. Anashin et al., Experimental Investigations of the Electron Cloud Key Parameters, LHC Project Report 313, 1999.

[56] P. Costa Pinto et al., Carbon coatings with low secondary electron yield, Vacuum, vol. 98, pp. 29-36, 2013.

[57] M. Zobov et al., Impact of Ion Clearing Electrodes on beam dynamics in Dafne, Journal of Instrumentation, vol. 2, p. PO8002, 2007.

[58] K. Zapfe, “Commissioning of large vacuum systems,” in CAS CERN Accelerator School - Vacuum in accelerators, Plaja d'Aro - Spain, 2007.

[59] P. Chiggiato, Materials and Properties IV Outgassing, presentation at CERN Accelerator School (CAS) - Vacuum for Particle Accelerators, 2017.

[60] M. L. Stutzman, P. A. Adderley, Md A. A. Mamun, and M. Poelker, Nonevaporable getter coating chambers for extreme high vacuum, Journal of Vacuum Science & Technology A, vol. 36 (3), 2018.

[61] O. Malyshev, Beam induced desorption, presentation at CERN Accelerator School (CAS) - Vacuum for Particle Accelerators, 2017.

[62] O.B. Malyshev, D.J. Scott, I.R. Bailey, D.P. Barber, E. Baynham, T. Bradshaw, A. Brummitt, S. Carr, J.A. Clarke, P. Cooke, J.B. Dainton, Y. Ivanyushenkov, L.I. Malysheva, G.A. Moortgat-Pick, J. Rochford, Vacuum systems for the ILC helical undulator, Journal of Vacuum Science & Technology A, vol. 25, p. 791, 2007.

[63] B. A. Trickett. D. Schmied and E. M. Williams, Hard synchrotron radiation and gas desorption processes at a copper absorber, Journal of Vacuum Science & Technology A, vol. 10, p. 217, 1992.

[64] N. Hilleret, “Non-thermal outgassing,” presentation at CERN Accelerator School (CAS) - Vacuum for Particle Accelerators, 2017.

[65] O. Gröbner, Beam vacuum interactions II, in CAS presentation, Playa d'Or, Spain, 2006.

[66] O. Malyshev, Vacuum in Particle Accelerators: Modelling, Design and Operation of Beam Vacuum Systems, Wiley, 2019.

[67] O. B. Malyshev, B. T. Hogan and M. Pendleton, Effect of surface polishing and vacuum firing on electron stimulated desorption from 316LN stainless steel, Journal of Vacuum Science & Technology A, vol. 32, p. 051601, 2014.

[68] O. B. Malyshev, C. Naran, Electron stimulated desorption from stainless steel at temperature between -15 and +70 C, Vacuum, vol. 86, pp. 1363-1366, 2012.

[69] E. Buratin, Commissioning of the CERN Large Hadron Collider Vacuum Pilot Sector, Master Thesis at the University of Padua (Italy), 2016.

[70] M. Taborelli, Cleaning and Surface Properties, in Proceedings of the 2017 CERN–Accelerator–School, Glumslöv (Sweden), 2017.

[71] A. Sapountzis, X-ray photoelectron spectroscopy (XPS) report, ‘’Quality control of TiZrV NEG coatings by X-ray electron spectroscopy'', EDMS 630214, CERN internal report, 2015.

[72] A. Sapountzis, X-ray photoelectron spectroscopy (XPS) report - Job No: S0115_b_XPS-TE-VSC-SCC-20151210, EDMS: 1568128 v.1, CERN internal report, Geneva, 2015.

[73] P. Costa Pinto e. al., Thin film coatings to suppress electron multipacting in particle accelerators, in PAC'11, New York, 2011.

[74] M. Himmerlich, 683_ LHC Pilot Sector VPS a-C coating #1_SEY_TE-VSC-SCC_2020-07-31, EDMS: 2402765 v.1, CERN internal report, Geneva, 2020.

[75] Manual - Cold Cathode Gauge, Metal sealed, IKR 070, Pfeiffer Vacuum.

[76] Manual - Bayard-Alpert Ionization Gauges, Stanford Research System (SRS) company.

[77] Quick Installation and Startup Guide for the 835 Vacuum Quality Monitor System, Granville-Philippes, 2013.

[78] Instruction Manual - Series 835 Vacuum Quality Monitor, mks, Granville-Phillips, 2016.

[79] J.-M. Laurent, U. Iriso Ariz, Particle collectors for electron cloud studies, CERN Vacuum Technical Note 03-05, EDMS: 374712, Geneva, 2003.

[80] J. Sikora, Y. Li, M. Palmer, S. De Santis, D. Munson, A shielded pick-up detector for electron cloud measurements in the CESR-TA ring, Proceedings of BIW10, Santa Fe, New Mexico, US, 2010.

[81] L. Wang, A. Chao, H. Fukuma, Energy spectrum of an electron cloud with short bunch.

[82] J.-M. Laurent and H. Song, Electron cloud energy and power measurements in SPS, Vacuum Technical Note, CERN, 2004.

[83] M. Commisso, T. Demma, S. Guiducci, L. Ping, A. Raco, V. Tullio, G. Viviani and R. Cimino, P. Vilmercati, A retarding field detector to measure the actual energy of electrons partecipating in e-cloud formation in accelerators, Proceedings of EPAC08, Genoa, Italy, 2008.

[84] D. Saez de Jauregui, S. Casalbuoni, A. Grau, M. Hagelstein, R. Cimino, M. Commisso, M. Mashkina, R. Weigel, Spectrum of the low energy electrons bombarding the wall in the ANKA storage ring, Proceedings of PAC09, Vancouver, 2009.

[85] W. M. H. Sachtler, G. J. H. Dorgelo, A. A. Holscher, The work function of gold, Surface Science, vol. 5, pp. 221-229, 1966.

[86] P. Chiggiato, P. Costa Pinto, Ti–Zr–V non-evaporable getter films: From development to large scale production for the Large Hadron Collider, Thin Solid Films, vol. 515, pp. 382-388, 2006.

[87] G. Lewin and G. Smith, Free Molecular Conductance of a Cylindrical Tube with Wall Sorption, Journal of Vacuum Science and Technology, vol. 3, no. 92, 1966.

[88] V. Baglin and B. Jenninger, SPS Electron-Cloud Heat Load Measurements with WAMPAC and Simulations, in Proc. ECLOUD'02, CERN, Geneva, Switzerland, 2002.

[89] G. Iadarola, E. Metral, G. Rumolo, Beam induced heat loads on the beam-screens of the twin-bore magnets in the IRs of the HL-LHC, CERN-ACC-2016-0112, Geneva, 2016.

[90] E.Buratin, V.Baglin, B. Henrist, P. Chiggiato, A. Fasoli, Electron flux and pressure dynamic in the LHC vacuum pilot sector as a function of the beam parameters and beam pipe properties, Phys. Rev. Accel. Beams 23, 114802, November 2020.

[91] E.Buratin, V.Baglin, B. Henrist, P. Chiggiato, G. Iadarola, A. Fasoli, Energy spectrum of the Electron Cloud measured in the LHC Vacuum Pilot Sector, under review process, 2020.

[92] F.Perez, I. Birkel, E.Huttel, A.S.Müller and M.Pont, Beam size and bunch length measurements et the ANKA storage ring, in 0-7803-7739-9 2003 IEEE, January 2003.

[93] F. Le Pimpec, O. Gröbner, J.M. Laurent, “Electron Stimulated Molecular Desorption of a NEG St 707 at Room Temperature,” Nuclear Instruments and Methods in Physics Research Section B: Beam Interactions with Materials and Atoms, vol. 194, no. 4, pp. 434-4424, 2002.

[94] NIST database, www.nist.gov.

[95] E. Wulff, Dependence of electron cloud build-up on beam position, Presentation at the Electron Cloud meeting no. 62, CERN, Geneva (CH), 2018.

[96] A. R. a. N. Hilleret, “Residual gas density estimations in the LHC experimental interaction regions,” LHC Project Report 674, Geneva (CH), 2003.

[97] Logbook of LHC page one, https://op-webtools.web.cern.ch/index.html

Curriculum Vitae

ELENA BURATIN

BORN: PADOVA (ITALY), 6 SEPTEMBER 1991

NATIONALITY: ITALIAN

EXPERIENCE

- **February 2019 – August 2020:** Lecturer at EPFL (Lausanne, Switzerland).
- **February 2017 – November 2020:** PhD studentship at CERN (Geneva, Switzerland), Vacuum, Surfaces and Coatings group, and at EPFL (Lausanne, Switzerland), Swiss Plasma Center group.
- **May 2016 – January 2017:** Engineering support for CERN, MANPOWER SA. (Geneva, Switzerland).
- **March 2015 - April 2016:** Technical studentship at CERN (Geneva, Switzerland), TE department, Vacuum, Surfaces and Coatings group.
- **June 2013 - September 2013**: Internship at CNR - Consorzio RFX - Istituto IGI (Padova, Italy).

EDUCATION

- **February 2017 – December 2020:** ***PhD in Applied Physics*** (Ecole Polytechnique Fédérale Lausanne, Switzerland).
  Thesis subject: Electron Cloud and Synchrotron Radiation characterization of technical surfaces with the Large Hadron Collider Vacuum Pilot Sector.
- **October 2013 - March 2016:** ***MSc in Energy Engineering*** (Universita' degli Studi di Padova, Italy).
  Thesis subject: Commissioning of the CERN Large Hadron Collider Vacuum Pilot Sector.
- **October 2010 - September 2013:** ***BCs in Energy Engineering*** (Universita' degli Studi di Padova, Italy).
  Thesis subject: Characterization of atmospheric plasma torch for thin films deposition from liquid precursors.